

Towards Understanding Molecule-Based Spintronics Systems from First-Principles Calculations

Dissertation

with the aim of achieving a doctoral degree
at the Faculty of Mathematics, Informatics and Natural Sciences
Department of Chemistry
Universit of Hamburg

Haitao Zhang

May 2022

The present work was carried out in the period from May 2018 to May 2022 in the Institute of Inorganic and Applied Chemistry at the Universität Hamburg in the group of Prof. Dr. Carmen Herrmann.

Dissertation accepted on the recommendation of
Prof. Dr. Carmen Herrmann
Prof. Dr. Gabriel Bester

Date of admission: 01/05/2018
Date of submission: 31/05/2022
Date of oral defense: 15/07/2022
Approval of dissertation: 15/07/2022

Contents

Zusammenfassung	i
Abstract	v
1. Introduction	1
2. Theoretical background	5
2.1. Basic concepts in quantum mechanics	5
2.2. Molecular systems	6
2.3. Slater determinant	7
2.4. The Hartree-Fock method	9
2.5. Basis functions	11
3. Global optimization of reactive force-field (ReaxFF) parameters	13
3.1. Introduction	13
3.2. Fitting reactive force-field: development of a python script	17
3.2.1. Introduction to the classes in REAXFFFITTING	17
3.2.2. The score function	18
3.2.3. Preparing a set of ReaxFF parameter vectors	21
3.2.4. The optimization process: machine learning-assisted genetic algorithms	23
3.3. Example: C ₂₀	25
3.4. Dimensionality reduction	28
3.4.1. Contractive autoencoder	29
3.4.2. Limitations	33
3.4.3. Locally linear embedding (LLE)	35
3.5. Components segmentation	39
3.6. Conclusion and outlook	44
4. Radical interfaces	47
4.1. TEMPO radicals on gold surfaces	47
4.1.1. Introduction	47
4.1.2. Verifying the reliability of the exchange–correlation functional	49

4.1.3.	The atomic structures of TEMPO on gold surfaces	52
4.1.4.	Chemical bonding analysis of the TEMPO–gold cluster complexes	56
4.1.4.1.	The functional dependence of the complexing energy	56
4.1.4.2.	Partial density of states analysis	58
4.1.4.3.	Extended transition state – natural orbitals for chemical valence	61
4.1.4.4.	Interaction region indicator	65
4.2.	TEMPO–OPE in double tunnel junctions	66
4.2.1.	Introduction	66
4.2.2.	Methodology	69
4.2.3.	The adsorption energies on the surfaces	69
4.2.4.	The structure of the embedded TEMPO–OPE	71
4.3.	Conclusion	72
5.	The conduction mechanism of switchable valence tautomer complexes	75
5.1.	Background	75
5.2.	Geometrical Structure	76
5.3.	Experimental results	80
5.4.	Methodology	81
5.5.	A photochromic bridging ligand (DAEpy)	82
5.6.	The neutral monomer of the tautomeric building block (CoL_2)	84
5.7.	The charged monomer of the tautomeric building block ($\text{CoL}_2^+ / \text{CoL}_2^-$)	87
5.8.	Determining a suitable U for the systems	89
5.9.	CoL_2DAEpy	91
5.10.	The dimer of the tautomeric building block ($[\text{CoL}_2]_2$)	93
5.11.	Band structures of c-CoDAE and o-CoDAE	94
5.12.	Electron transfer matrix elements between CoL_2 units	96
5.13.	Discussion	99
6.	The conduction behavior of CoBO_4	101
6.1.	Background	101
6.2.	Geometrical structure	104
6.3.	Experimental results	105
6.4.	Methodology	106
6.5.	The monomer of the organic conductor (BO)	107
6.6.	The dimer of the organic conductor (BO)	108
6.7.	The single-molecule magnet ($[\text{Co}(\text{pdms})_2]^{2-}$)	115

6.8. The electronic structure in bulk CoBO_4	117
6.9. Discussion	121
7. Conclusion and outlook	127
A. Supporting information for theoretical background	131
A.1. Creation and annihilation operators	131
A.2. Operators in second quantization	132
A.3. Wick's theorem	134
A.4. Fermi vacuum and hole-particle formalism	136
A.4.1. Decomposition of the operators	140
A.5. Configuration interaction	141
A.6. Many-body perturbation theory	143
A.6.1. Reduced resolvent	144
A.7. Coupled cluster theory	149
B. Supporting information for reactive force-field fitting	153
B.1. The data structure of ReaxFF parameters files	153
B.2. LAMMPS	158
B.2.1. Installation	158
B.2.2. The structures of normal LAMMPS input files	160
B.2.3. Simulations with reactive force fields (ReaxFF)	161
B.3. C_{20} mechanical learning test results	163
B.4. Components segmentation for a 4,4'-bis(thiol)benzil system	171
C. Supporting information for TEMPO	173
D. Supporting information for CoDAE	193
E. Supporting information for CoBO_4	217
F. List of publications	229
F.1. Published	229
F.2. In preparation	229
G. List of chemicals	231
Bibliography	232
Acknowledgements	249
Declaration on Oath	251

Zusammenfassung

Die Spintronik basiert auf der Idee, den Freiheitsgrad des Spins zusätzlich zur Ladung von Ladungsträgern zu nutzen. Dieser Forschungsbereich entwickelt sich seit Jahrzehnten mit großer Dynamik, hat erste Fortschritte z.B. auf dem Bereich der Informationsspeicherung in unser tägliches Leben gebracht und hat großes Potential für zukünftige Entwicklungen.

Es gibt mehrere Möglichkeiten, spintronische Anwendungen zu konstruieren, z. B. Spin-Ventile auf der Grundlage von Multimetallschichten, Halbleiter-Heteroübergängen, Quantenpunkten oder ähnliches. Die molekülbasierte Spintronik hat viel Aufmerksamkeit auf sich gezogen. Bei den Molekülen kann es sich um rein organische Radikale oder um offenschalige Koordinationskomplexe mit Übergangs- oder Lanthanidmetallzentren handeln. Die ungepaarten Elektronen in diesen Molekülen bilden Spin-Zentren, welche zur Realisierung von spintronischen Anwendungen verwendet werden können. Bestimmte Moleküle weisen bistabile Spinzustände auf, die als Bits für potenzielle Anwendungen von Quanteninformationsprozessen genutzt werden könnten. Darüber hinaus können die Orbitalenergieniveaus organischer Moleküle durch Hinzufügen oder Modifizieren funktioneller Gruppen mit Hilfe von Synthesemethoden angepasst werden, um so ihre Eigenschaften präzise zu modifizieren. Um experimentelle Ergebnisse zu erklären und die zugrunde liegenden Mechanismen aufzudecken, sind die Konstruktion theoretischer Modelle und die entsprechenden Simulationen unerlässlich. Spintronikssysteme decken einen breiten Bereich von Zeit- und Längenskalen ab, so dass verschiedene Näherungen gewählt werden müssen, um geeignete Modelle zu konstruieren. In dieser Arbeit werden theoretische Untersuchungen angewendet und entwickelt, die sich auf die Moleküldynamik und die Elektronenstrukturen molekülbasierter Spintronikssysteme konzentrieren.

Im ersten Teil schlagen wir einen durch maschinelles Lernen unterstützten genetischen Algorithmus für die Neuparametrisierung des reaktiven Kraftfelds (ReaxFF) vor. Dies ist ein erster Schritt in Richtung flexibler Kraftfelder für organische Radikale auf Oberflächen. ReaxFF ist sehr flexibel, da es im Gegensatz zu konventionellen Kraftfeldern die topologischen Informationen des Systems (z.B. Bindungen, Winkel, Flächenwinkel) nicht vordefinieren muss. Dadurch ist es in der Lage,

Prozesse der Bindungsbildung und des Bindungsbruchs zu beschreiben, die für die Vorhersage von Reaktionswegen und für die Dynamik von einzelnen Molekülen in elektronischen Bauteilen relevant sind. Aufgrund der großen Anzahl von Parametern sind herkömmliche Optimierungsmethoden jedoch unzureichend. Daher haben wir herkömmliche genetische Algorithmen und Modelle des maschinellen Lernens kombiniert. Zwei verschiedene Ansätze werden untersucht: Einer davon besteht darin, die Fehlerfunktion der Parameter direkt zu lernen und das Modell dann für die Parametersuche zu verwenden. Andererseits könnten Modelle des maschinellen Lernens zum Erlernen der Verteilung von Parametern mit guter Leistung und geringer Abweichung von der Referenz verwendet werden, was zur Verringerung der Dimension der Parameter genutzt werden könnte. Darüber hinaus wird eine Methode zur Segmentierung der Parameter auf der Grundlage von Korrelationen zwischen den Parametern vorgeschlagen, die mit den oben genannten Methoden kombiniert werden könnte, um den Optimierungsprozess zu vereinfachen.

Bei Anwendungen auf der Basis einzelner Moleküle ist die geometrische Information des Moleküls entscheidend für das Verständnis des Mechanismus der elektrischen Leitung. Ein Beispiel sind Spintronik-Systeme, die durch organische radikalische Moleküle in mechanisch kontrollierten Break-Junctions realisiert werden. Diese Bauelemente weisen einen starken Magnetowiderstand auf, der mit konventionellen Simulationen nicht erklärt werden kann. In einem idealisierten Fall sind die organischen Moleküle durch Thiolgruppen an Goldelektroden verankert, und die Nitroxylradikale (2,2,6,6-tetramethylpiperidin-1-yl)oxidanyl (TEMPO)-Gruppen sind von den Elektroden entfernt. Gold wird aufgrund seiner hervorragenden Duktilität und chemischen Inertheit häufig als Elektrode für molekulare Verbindungen verwendet. Die erwähnten TEMPO-Gruppen kommen häufig in organischen Spintroniksystemen als Spin-Zentrum vor. Die Wechselwirkung zwischen einem TEMPO-Radikal und Gold könnte die Wechselwirkung zwischen dem gesamten Molekül und der Oberfläche beeinflussen, zusätzlich zu den funktionellen Gruppen, die zur Verankerung des Moleküls dienen. Um einen möglichen Einfluss zu finden, haben wir die TEMPO-Gold-Systeme mit theoretischen Methoden analysiert. Auf der Grundlage der verschiedenen Bindungsanalysen gehen wir davon aus, dass die Wechselwirkung zwischen TEMPO und Gold nicht vernachlässigbar ist und sogar mit einigen üblicherweise verwendeten Ankergruppen (z. B. Aminogruppen) vergleichbar ist, was bei den nachfolgenden Simulationen berücksichtigt werden muss. Darüber hinaus wurde die geometrische Struktur eingebetteter (2,2,6,6-tetramethylpiperidin-1-yl)oxidanyl-oligo(p-phenyleneethynylene) (TEMPO-OPE)-Moleküle in Doppeltunnelübergängen (sogenannten double tunnel junctions) untersucht. Der Übergang besteht aus isolierenden SiO_2 - und Al_2O_3 -Schichten. Die offenschaligen organischen

Moleküle bilden die Spin-Zentren. In dieser Arbeit wird gezeigt, dass die adsorbierten TEMPO–OPE-Moleküle in der *trans*-Konfiguration eine niedrigere Energie aufweisen, da sie eine größere Kontaktfläche mit der Oberfläche haben. Der Spin der TEMPO-Gruppe diffundiert nicht in das Rückgrat oder in die isolierenden Schichten, was für diese Struktur als konkurrenzfähiger Kandidat für die Anwendung in spintronischen Bauteilen entscheidend ist.

Auch kristalline Materialien sind eine vielversprechende Klasse der Spintronik, die es zu erforschen gilt. Im letzten Teil dieser Arbeit werden zwei Arten von Kristallen mit ungewöhnlichem Leitfähigkeitsverhalten diskutiert. Der erste Typ ist eine Hybridverbindung, die aus photochromen Linkern und Valenztautomeren besteht und einen synergistischen Leitfähigkeitsübergang mit Spin-Crossover zeigt. Der zweite Typ ist eine Hybridverbindung, die aus organischen Leitern und Einzelmolekülmagneten besteht, die oberhalb der Temperatur von flüssigem Helium (bei 6.5 K) eine hohe metallische Leitfähigkeit und unterhalb dieser Temperatur einen Abfall der Leitfähigkeit aufweist. Zur Erklärung der experimentellen Ergebnisse wurden die Bandstrukturen auf der Grundlage der Dichtefunktionaltheorie (DFT) und elektronischer Kopplungsmatrixelemente berechnet und ein möglicher Mechanismus für beide Typen von Kristall vorgeschlagen.

Anhand mehrerer praktischer Beispiele zeigen wir die Anwendung und Weiterentwicklung der theoretischen Chemie im Bereich der Spintronik. Mit ihrer Hilfe können wir einige Eigenschaften erforschen, die im Experiment nur schwer zugänglich sind, und die möglichen Mechanismen hinter den experimentellen Ergebnissen erkunden. Die Aufstellung solcher Theorien und Methoden kann die Entwicklung der Spintronik fördern.

Abstract

Spintronics as a discipline based on the spin degree of freedom has been vigorously developing for decades. It has provided great advances in the field of information storage for everyday life, and its numerous branches provide ample technological reserves for the future.

There are multiple ways to achieve spintronic devices, like spin valves based on multi-metal layers, semiconductor heterojunctions, quantum dots, *etc.* In particular, molecule-based spintronics have been drawing a lot of attention. The molecules can be purely organic radicals or open-shell coordination complexes with transition or lanthanide metal centers. The unpaired electrons in those molecules provide spin centers to realize spintronic functionality. Some particular molecules show bistable spin states, which could be tried as bits for potential applications of quantum information processes. Moreover, the orbital energy levels of organic molecules can be adjusted by adding or modifying functional groups through synthetic methods, with the final goal of regulating spintronics performance. In order to explain experimental results and to reveal the underlying mechanisms, the construction of theoretical models and the corresponding simulations are essential. Spintronics systems cover a broad range of time and length scales, thus different approximations need to be chosen to construct appropriate models. In this thesis, theoretical investigations focusing on the molecular dynamics and electronic structures of molecule-based spintronic systems are applied and developed.

In the first part, we propose a machine-learning-assisted genetic algorithm for the reactive force-field (ReaxFF) reparameterization, as the first step towards flexible force fields for organic radicals on surfaces. ReaxFF has great flexibility in that it does not need to pre-define the topological information of the system (*e.g.*, bonds, angles, dihedral angles, *etc.*), in contrast to conventional force fields. Thus, it is able to describe bond formation and breaking processes, which are important for predicting reaction paths and for the dynamics of single-molecule junction devices. However, the large number of parameters makes conventional optimization methods inadequate. Therefore, we combined genetic algorithms and machine learning models for this purpose. We explored two different types of approaches. One of them is to directly learn the error function of the parameters, and then to use the machine

learning model for parameter searching. On the other hand, machine learning models can be used for learning the distribution of parameters with good performance and low deviation from the reference, which can be used for reducing the dimension of the parameter space. In addition, we also proposed a method for parameter segmentation based on correlations between parameters, which could be combined with the above methods to simplify the optimization process.

For single-molecule systems, the geometric information of the molecule is crucial for understanding the mechanism of electrical conduction. For instance, organic radical molecules in mechanically controlled break junctions have been reported by our collaborators. The devices exhibit strong magnetoresistance which could not be explained by straightforward conductance simulations. It is usually assumed that the organic molecules are anchored to the gold electrodes by linker thiol groups with the nitroxyl radical (2,2,6,6-tetramethylpiperidin-1-yl)oxidanyl (TEMPO) substituents far from the electrodes. However, the interaction between a TEMPO radical and gold could influence the interaction between the whole molecule and the surface, in addition to the functional groups designed for anchoring the molecule. To find a possible influence, we analyzed the TEMPO–gold systems by theoretical methods. Based on the various bonding analyses, we believe that the interaction between TEMPO and gold is not negligible and is even comparable to some commonly used anchoring groups (*e.g.*, amino groups), which needs to be considered in the subsequent simulations. Furthermore, the geometrical structure of embedded (2,2,6,6-tetramethylpiperidin-1-yl)oxidanyl-oligo(p-phenyleneethynylene) (TEMPO–OPE) molecules in double tunnel junctions were explored. The junction consists of insulating SiO_2 and Al_2O_3 layers. The open-shell organic molecules provide the spin centers. We found that the adsorbed TEMPO–OPE molecules have lower energy in a *trans* configuration, due to a larger area contacting with the surface. The spin on the TEMPO group does not diffuse into the backbone or into the insulating layers, which is crucial for this structure to be a competitive candidate for the application in spintronics devices.

Crystalline materials are also a promising class to explore for spintronics applications. In the final part of this thesis, two types of crystals with unusual conductive behaviors are discussed. The first type is a hybrid compound consisting of photochromic linkers and valence tautomer units. It shows a synergistic conductivity transformation with spin crossover at 330 K. The second type is a hybrid compound consisting of organic conductors and single-molecule magnets, which shows a high metallic conductivity above liquid helium-temperature (6.5 K) and a drop of conductivity below this temperature. The band structures based on density-functional theory (DFT) and electronic coupling matrix elements were calculated for explain-

ing the experimental results, and a possible mechanism for each type of crystal was proposed.

Through several practical examples, we show the application of theoretical chemistry in the direction of spintronics. We explore properties that are difficult to obtain through conventional experiments and explore possible mechanisms behind the experimental results. We provide steps towards improving the theoretical methodology for such studies. Based on this, we hope to contribute to the further development of spintronics.

1. Introduction

With the fast burst of the semiconductor industry in the past half century, the ability to deal with complex and massive numerical calculations has profoundly changed people's life. According to Moore's Law [1, 2], the potential of a classical computer appears to be unlimited. Within the existing framework of semiconductor manufacturing, increasing the performance of chips relies on reducing the size of transistors to increase integration. But the size reduction hits a fundamental limit set by the quantum behavior of matter at the nanoscale. At this scale, the de Broglie wavelength of electrons becomes comparable with the gate size, and the insulating character provided by insulator layers is no more reliable [3, 4]. Moreover, the high frequency operations of charging and discharging a capacitor also limit the clock speed, due to the waste heat, which mainly comes in the form of Joule heating. The power density of chips is drastically increased by reducing the size of transistors, which will eventually exceed the thermal stability of semiconductor gates [5]. Photolithography is currently the main manufacturing method, in which the light source plays the main role. In principle, the shorter the wavelength, the smaller the transistor can be manufactured. The light source has switched from mercury lamps (436 nm) to microdroplet-tin plasma (13.5 nm) [6, 7]. Finding light sources with shorter wavelengths and high conversion efficiency is challenging. Therefore, gaining performance and reducing power consumption by reducing the size of transistors is not sustainable, a new paradigm must be explored.

As an elementary particle, the electron has several conserved properties, such as mass, spin, charge. In a large part of established information technology, the electron's charge is exploited. With the limitation of our knowledge, to build a balance-like computer by taking advantage of the electron's mass is nearly impossible. The spin is an obviously better-suited property to manipulate and measure. Spintronics has a great potential for data storage and information processing.

Spin in molecules, semiconductors, and other materials has the potential to build spin qubit quantum computers [8, 9]. According to Landauer's principle, any irreversible operation on information, such as erasing a bit, must be accompanied by a corresponding information entropy increase in its environment [10]. For a modern classical computer, the waste heat contribution from the information entropy is mil-

lions of times smaller than the Joule heating. But the information entropy is critical for a quantum computer, which is a natural barrier not able to be overcome [11]. Therefore, quantum gates are desired to be reversible to preserve the unitarity. The well established pulse-sequence methods of electron paramagnetic resonance (EPR) and nuclear magnetic resonance (NMR) realize robust reversible quantum gates in electron and nuclear spin systems [12, 13].

Since the giant magnetoresistance (GMR) effect was discovered by Albert Fert and Peter Grünberg [14], the sensitivity of the hard disk head has largely improved, which has led to a rapid development of the storage density of a hard disk drive [15]. Therefore, today we do not have to use a storage device as big as a refrigerator. The GMR effect is observed in multilayers composed of alternating ferromagnetic and non-magnetic conductive layers (*e.g.*, Fe-Cr-Fe layers) [14]. In such structures, spin-polarized electrons exhibit a very different scattering rate in different directions of a magnetic field from ferromagnetic layers, which results in a magnetic-field dependent electro-conductivity. This effect can be used to detect the magnetic orientation from a tiny magnetic domain of a hard disk.

As a possible approach towards the miniaturization of information technology, single-molecule junctions enable the research of quantum transport phenomena for a single molecule connected between two electrodes [16, 17]. Such systems provide an opportunity to unveil the quantum features of a single molecule, which are related to its orbital and spin degrees of freedom. The conductivity can be studied considering the coupling of electronic degrees of freedom with vibrational modes (phonons), light excitation (photons), or magnetic fields, which are able to tune electron transport [18–21]. Furthermore, switchable groups can be introduced by chemical modification, enabling switching of conductivity under certain conditions [22–25]. The conductive experiments are normally performed in mechanically controlled break junctions (MCBJ) [26, 27], where the distance between two electrodes can be adjusted.

In many cases, due to the limitation of measurement technology, we are not able to figure out the atomistic configuration of a nanoscale system, especially, for a device based on a single molecule. Another challenge for the case of nanoscale spintronics is the fact that the state of a spin is easy to decohere as a typical quantum system, and the carried information could thus be lost due to the environmental noise [28–30]. To deal with such challenges, theory and simulations can provide valuable guidance.

The systems and phenomena we are dealing with may have different spatial sizes and time scales, which requires us to make corresponding assumptions at different levels to build different models [31]. In general, the smaller the scale of the system, the fewer assumptions are required. For a single-molecule system, the de-

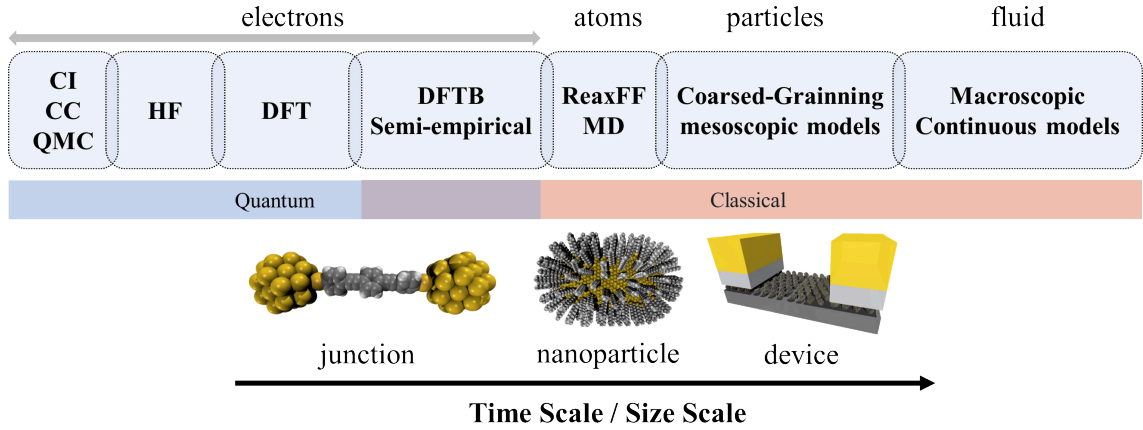


Figure 1.1.: A hierarchy of modeling. Here, the abbreviations indicate configuration interaction (CI), coupled cluster (CC), quantum Monte Carlo (QMC), Hartree–Fock (HF) theory, density functional theory (DFT), density functional based tight binding (DFTB), reactive force field (ReaxFF), molecular dynamics (MD).

tails of the electrons can be obtained by *ab initio* quantum chemistry methods, like Hartree–Fock (HF) theory or correlated wavefunction methods (*e.g.*, configuration interaction, coupled cluster) [32]. The above methods only require physical constants like the speed of light, the Planck constant, the electron mass, *etc.* For larger systems, parametrized methods are more feasible, like density functional theory (DFT) or semi-empirical methods [33, 34]. DFT is in principle exact, but in practice contains approximations to exchange and correlation. It is often referred to as a first-principles method. Semi-empirical methods are based on quantum mechanics, but system-specific parameters of the model need to be obtained by fitting to certain properties of selected test systems from high level calculated or measured references. Force field methods (the basis of molecular dynamics simulations) neglect the electronic details. The forces between two atoms or particles are calculated based on their position and on parameters depending on the selected force field. Force-field based MD only has to deal with atomic degrees of freedom, thus it is possible to simulate systems with larger size and also longer time scales. If the scale of a system is beyond the ability of MD, it is necessary to group multiple atoms into a single particle by a coarse-graining method and to construct a suitable force field.

The quantum chemistry methods (*e.g.*, HF, DFT) are able to give a relatively reliable description, which enables us to consult the behavior of the system to explain the experimental results obtained, *e.g.*, by UV-Vis, IR, Raman, or NMR spectroscopy. Also, the conductivity characteristics of single-molecule junctions can be predicted by the post-processing of the corresponding wavefunction of the system [35].

MD simulations can provide dynamical and statistical information about the system.

For example, during a conductivity measurement of a single-molecule junction, the system can transition between several configurations. The system could show very different conductivity behaviors for different such configurations. By taking snapshots from MD simulations, conductance histograms can be obtained and compared to the experiment [31].

In this thesis, we mainly focus on three topics corresponding to central issues in molecular spintronics: In the first place, this is a machine-learning-assisted reactive force-field reparameterization. For many cases, to understand a spintronic system, a simulation that spans a certain time scale with a large number of atoms is required. Conventional force fields preserve the topology of a system and a new bond is not allowed to form or to break [36–38]. For chemical reactions or for molecular break junction systems, the force field should be reactive and flexible. A reactive force-field (ReaxFF) has been proposed for those reasons [39], however, there are too many parameters, which make common methods for parameter optimization (gradient descent, genetic algorithm, simulated annealing, covariance matrix adaptation evolution strategy (CMA-ES)) challenging [40]. Two possible solutions are using machine learning methods to reduce the dimension of parameter space or grouping the components of the parameters by the correlations between them, then optimizing separately. In both cases, a machine learning model could be trained for the score prediction based on the simplified parameter sets obtained from the parameter space dimension reduction or the grouping of components. Then, a grid search can be used to find the best parameter with the help of the machine learning model.

Organic radical molecules are a competitive candidate in spintronics. We study a system in which the electron spin is confined in a localized molecular orbital, which is easy to be addressed and manipulated by common techniques, *e.g.*, electron paramagnetic resonance (EPR) [41]. In a system experimentally studied by Elke Scheer and collaborators, this orbital is placed on a side chain [21]. Therefore, it is necessary to look into the interaction between such side chains and the environment in a device. Here we discussed a possible interaction between a commonly used nitroxyl radical (2,2,6,6-tetramethylpiperidin-1-yl)oxidanyl (TEMPO) with the gold electrode surfaces by various methods. The geometrical structures of the TEMPO derivative in experimentally studied double tunnel junctions were also explored.

As another research focus, there have been many discoveries in the field of condensed matter [42, 43]. Especially the spin-related electron conductivity has attracted a lot of attention. Our collaborators have synthesized two kinds of novel crystalline materials with conductive transitions whose nature was unexplained [44]. Here, two compounds were studied, and the electronic structure and the corresponding conductivity mechanism were discussed.

2. Theoretical background

2.1. Basic concepts in quantum mechanics

In the above systems, the dynamics of the material at such a small scale are non-classical and must be described using quantum mechanics. A fundamental assumption in quantum mechanics is that a system can be described by a state ψ , which can be represented by a nonzero state vector $|\psi\rangle$. The space containing the above states is a special *complex vector space*, which is called *Hilbert space* (\mathcal{H}). It may have either a finite or an infinite number of dimensions. The Hermitian inner product $\langle \cdot, \cdot \rangle$ is defined in \mathcal{H} , thus the ‘angle’ between any two of the states can be calculated. So, the state vectors also naturally contain the properties of the elements of a vector space.

Another assumption of quantum mechanics is that information has to be preserved (unitarity) [45]. This requires the inner product of any two vectors to be conserved at any time.

To derive the dynamics of the system, suppose that there are two state vectors in a Hilbert space at time zero, $|\Psi(0)\rangle, |\Phi(0)\rangle \in \mathcal{H}$. The time evolution of states is described by a unitary transformation $\hat{U}(t)$, thus the two state vectors at time t are as follows,

$$|\Psi(t)\rangle = \hat{U}(t) |\Psi(0)\rangle \quad ; \quad |\Phi(t)\rangle = \hat{U}(t) |\Phi(0)\rangle \quad .$$

According to the law of information conservation, the inner product between two vectors $\langle \Psi | \Phi \rangle$ should be conserved. This yields

$$\langle \Psi(t) | \Phi(t) \rangle = \langle \Psi(0) | \hat{U}^\dagger(t) \hat{U}(t) | \Phi(0) \rangle = \langle \Psi(0) | \Phi(0) \rangle \iff \hat{U}^\dagger(t) \hat{U}(t) = \hat{I} = \text{Identity}.$$

For an infinitesimal small time step ($\epsilon \rightarrow 0$), a Taylor expansion of \hat{U} and \hat{U}^\dagger can be performed. Only the terms linear with time are considered (neglecting $\mathcal{O}(\epsilon^2)$ or

higher),

$$\begin{aligned}
 & \begin{cases} \hat{U}(\epsilon) &= \hat{I} + \epsilon \hat{X} \\ \hat{U}^\dagger(\epsilon) &= \hat{I} + \epsilon \hat{X}^\dagger \end{cases} \\
 & \Rightarrow (\hat{I} + \epsilon \hat{X})(\hat{I} + \epsilon \hat{X}^\dagger) = \hat{I} \\
 & \Rightarrow \epsilon(\hat{X} + \hat{X}^\dagger) = 0 \quad \text{Neglect the } \epsilon^2 \text{ term} \\
 & \Rightarrow -\hat{X} = \hat{X}^\dagger .
 \end{aligned}$$

Here, \hat{X} is skew-Hermitian (skew-adjoint). It can be converted to a Hermitian (self-adjoint) form by $\hat{H} = i\hat{X}$, and we have $\hat{H} = \hat{H}^\dagger$. Thus we can write down the state $|\Psi(0)\rangle$ after time ϵ evolution,

$$\begin{aligned}
 |\Psi(t)\rangle &= (\hat{I} - i\epsilon \hat{H}) |\Psi(0)\rangle \\
 \frac{1}{\epsilon}(|\Psi(\epsilon)\rangle - |\Psi(0)\rangle) &= -i\hat{H} |\Psi(0)\rangle \\
 i\frac{\partial}{\partial t} |\Psi\rangle &= \hat{H} |\Psi\rangle .
 \end{aligned} \tag{2.1}$$

Equation 2.1 is the Schrödinger equation, \hat{H} is the generator under time evolution, so called *Hamiltonian*. The corresponding observable $\langle \Psi | \hat{H} | \Psi \rangle$, which is invariant under time evolution, is called the *energy* of the system. Therefore, energy conservation can be derived based on information conservation.

If we want to know the magnitude of $|\Psi\rangle$ at the point \mathbf{x} in real space, the state vector $|\Psi\rangle$ can be projected on the position state vector \mathbf{x} , resulting in $\langle \mathbf{x} | \Psi \rangle$, which is usually written as $\Psi(\mathbf{x})$ and called the *wavefunction*.

While the state vector $|\Psi\rangle$ is abstract, the wavefunction $\Psi(\mathbf{x})$ is a function of the arrays of real numbers, which could be handle by a computer.

2.2. Molecular systems

In the world of chemistry, a system consists of a variety of atomic nuclei and electrons. In principle, the state of the system with M nuclei and N electrons could be represented by a wavefunction as follows, where \mathbf{r}_n is the vector of the n^{th} electron consisted of the Cartesian coordinates (x_n, y_n, z_n) and the spin label σ_n which could either be up (α) or down (β), \mathbf{R}_m is the Cartesian coordinate vector of the m^{th} nucleus.

$$\begin{aligned}\Psi &= \Psi(\mathbf{r}_1, \dots, \mathbf{r}_N; \mathbf{R}_1, \dots, \mathbf{R}_M) = \Psi(\mathbf{r}; \mathbf{R}) \\ \mathbf{r}_n &= (x_n, y_n, z_n, \sigma_n) \quad \sigma_n \in \{\alpha, \beta\} \\ \mathbf{R}_m &= (X_m, Y_m, Z_m)\end{aligned}$$

Due to the fact that even a single proton is 1836 heavier than a electron, according to the Born-Oppenheimer approximation [46], the movement of electrons and nuclei happen on very different time scales and can be separated (Equation 2.2). Here, $\Psi_{\mathbf{R}}(\mathbf{r})$ is the electrons' wavefunction with the fixed nuclei positions \mathbf{R} , and $\chi(\mathbf{R})$ is the wavefunction of the nuclei. It is worth noting, that the variation of the nuclei positions could be seen as a perturbation for the electrons. This can lead to a mixing of different electronic states, as seen in triatomic hydrogen (H_3) system [47]. In following, we focus the electrons' wavefunction only.

$$\Psi = \Psi_{\mathbf{R}}(\mathbf{r})\chi(\mathbf{R}) \quad (2.2)$$

2.3. Slater determinant

For a system containing multiple electrons, the N -particle many-body state Φ need to be constructed based on the single particle states ψ_{p_n} , here the subscript p_n is a label indicating the state. Intuitively, the many-body state could be obtained by the direct product over the selected N single particle states, $|\psi_{p_1}\rangle \otimes |\psi_{p_2}\rangle \otimes \dots \otimes |\psi_{p_N}\rangle$. But it does not obey the Pauli principle.

A vector in the Hilbert space can be represented by a general formula, with a summation over all possible combination of the p_1, \dots, p_N array, where p_n could be any single particle states,

$$|\Psi\rangle = \sum_{p_1, \dots, p_N} d_{p_1, \dots, p_N} |\psi_{p_1}\rangle \otimes \dots \otimes |\psi_{p_N}\rangle .$$

However, not all vectors in the Hilbert space are legitimate. For a Fermion system, the antisymmetric condition need to be satisfied. Here a projection operator \mathcal{A} is required to project the vector to a subspace for the Fermion system, \mathcal{A} is an idempotent antisymmetrizer, where S_N is the n -permutation group, π is a group element (and also a representative operation), $\#\pi$ indicates the number of transpositions for the π operation,

$$\mathcal{A} = \frac{1}{N!} \sum_{\pi \in S_N} (-1)^{\#\pi} \pi .$$

Therefore, a state vector for a Fermion system could be written as follow, which is a linear combination of the antisymmetric state vectors $|\Phi_{p_1, \dots, p_N}\rangle$. $|\Phi_{p_1, \dots, p_N}\rangle$ vectors form a set of basis of the Fermion subspace.

$$\begin{aligned} |\Psi\rangle &= \mathcal{A}|\Psi\rangle = \sum_{p_1, \dots, p_N} d_{p_1, \dots, p_N} \mathcal{A}(|\psi_{p_1}\rangle \otimes \dots \otimes |\psi_{p_N}\rangle) \\ &= \sum_{p_1, \dots, p_N} \frac{1}{\sqrt{N!}} d_{p_1, \dots, p_N} \sqrt{N!} \mathcal{A}(|\psi_{p_1} \dots \psi_{p_N}\rangle) \\ &= \sum_{p_1, \dots, p_N} D_{p_1, \dots, p_N} |\Phi_{p_1, \dots, p_N}\rangle \end{aligned}$$

For an antisymmetric state vector, the corresponding wavefunction could be written, here the perturbation operation is is acted on the single particle states, thus the corresponding label changed from p_n to $p_{\pi(n)}$. It is easy to observe that the summation can be written in the form of a determinant, normally called the *Slater determinant*,

$$\begin{aligned} \langle \mathbf{r}_1 \dots \mathbf{r}_N | \Phi_{p_1, \dots, p_N} \rangle &= \frac{1}{\sqrt{N!}} \sum_{\pi \in S_N} (-1)^{\# \pi} \pi(\psi_{p_1}(\mathbf{r}_1) \dots \psi_{p_N}(\mathbf{r}_N)) \\ &= \frac{1}{\sqrt{N!}} \sum_{\pi \in S_N} (-1)^{\# \pi} \psi_{p_{\pi(1)}}(\mathbf{r}_1) \dots \psi_{p_{\pi(N)}}(\mathbf{r}_N) \\ &= \frac{1}{\sqrt{N!}} \begin{vmatrix} \psi_{p_1}(\mathbf{r}_1) & \psi_{p_2}(\mathbf{r}_1) & \dots & \psi_{p_N}(\mathbf{r}_1) \\ \psi_{p_1}(\mathbf{r}_2) & \psi_{p_2}(\mathbf{r}_2) & \dots & \psi_{p_N}(\mathbf{r}_2) \\ \vdots & \vdots & \ddots & \vdots \\ \psi_{p_1}(\mathbf{r}_N) & \psi_{p_2}(\mathbf{r}_N) & \dots & \psi_{p_N}(\mathbf{r}_N) \end{vmatrix}. \end{aligned}$$

For example, an antisymmetric state vector of the two Fermion system could be written as $\frac{1}{\sqrt{2}} (\psi_{p_1}(\mathbf{r}_1)\psi_{p_2}(\mathbf{r}_2) - \psi_{p_1}(\mathbf{r}_2)\psi_{p_2}(\mathbf{r}_1))$

There are other commonly used notations for a basis vector, which could be the labels of the occupied states, or the occupation numbers for all states. In the case that the p_1, \dots, p_N states are occupied, it could be indicated by the occupation numbers, 1, and leaving other empty states with 0. In the occupation number notations, if all states are unoccupied $|00 \dots 0\rangle = |0\rangle$, then the system is in the *true vacuum state*. It is worth noting that, $|0\rangle$ is not the zero vector, $\langle 0|0\rangle = 1$. It spans the vacuum subspace, which is isomorphic to complex number, $\text{span}(|0\rangle) = \mathcal{H}_0 \cong \mathbb{C}$.

$$\begin{aligned}
 |\Phi_{p_1, \dots, p_N}\rangle &= |\{p_1, \dots, p_N\}\rangle = \left| 0 \dots 0 \underset{\substack{\uparrow \\ p_1}}{1} 0 \dots 0 \underset{\substack{\uparrow \\ p_N}}{1} 0 \dots 0 \right\rangle \\
 &= |n_1 n_2 \dots \textcolor{red}{n}_{p_1} \dots \textcolor{red}{n}_{p_2} \dots \textcolor{red}{n}_{p_N} \dots\rangle
 \end{aligned}$$

2.4. The Hartree-Fock method

To find the optimized state of a system, the energy needs to be minimized by the variation of the trial function $\tilde{\Phi}$,

$$E[\Phi] = \min_{\tilde{\Phi}} E[\tilde{\Phi}] \quad ; \quad E[\tilde{\Phi}] = \frac{\langle \tilde{\Phi} | \hat{H} | \tilde{\Phi} \rangle}{\langle \tilde{\Phi} | \tilde{\Phi} \rangle} .$$

Thouless theorem tells [48], if $\exists |\Phi\rangle, |\tilde{\Phi}\rangle$, where $\langle \Phi | \tilde{\Phi} \rangle \neq 0$, then

$$|\tilde{\Phi}\rangle \propto e^{\hat{C}_1} |\Phi\rangle \quad ; \quad \hat{C}_1 = \sum_{a,i} \langle a | \hat{c}_1 | i \rangle X_a^\dagger X_i .$$

Therefore,

$$E[\tilde{\Phi}] = \frac{\langle \Phi | e^{\hat{C}_1^\dagger} \hat{H} e^{\hat{C}_1} | \Phi \rangle}{\langle \Phi | e^{\hat{C}_1^\dagger} e^{\hat{C}_1} | \Phi \rangle} ,$$

$$\begin{aligned}
 |\tilde{\Phi}\rangle - |\Phi\rangle &= e^{\hat{C}_1} |\Phi\rangle - |\Phi\rangle = \left(1 + \hat{C}_1 + \frac{1}{2} \hat{C}_1^2 + \dots \right) |\Phi\rangle - |\Phi\rangle \\
 &= \hat{C}_1 |\Phi\rangle + \mathcal{O}(\hat{C}_1^2) \\
 &\Rightarrow \delta\Phi = \hat{C}_1 |\Phi\rangle .
 \end{aligned}$$

The linear variation of the wavefunction is corresponding to the single excitation,

which could mix the occupied and the unoccupied states,

$$\begin{aligned}
 E[\tilde{\Phi}] - E[\Phi] &= \frac{\langle \Phi | \left(1 + \hat{C}_1^\dagger + \frac{1}{2}\hat{C}_1^{\dagger 2} + \dots\right) \hat{H} \left(1 + \hat{C}_1 + \frac{1}{2}\hat{C}_1^2 + \dots\right) | \Phi \rangle}{\langle \Phi | \left(1 + \hat{C}_1^\dagger + \frac{1}{2}\hat{C}_1^{\dagger 2} + \dots\right) \left(1 + \hat{C}_1 + \frac{1}{2}\hat{C}_1^2 + \dots\right) | \Phi \rangle} - E[\Phi] \\
 &= \frac{\langle \Phi | \hat{H} | \Phi \rangle + \langle \Phi | \hat{C}_1^\dagger \hat{H} | \Phi \rangle + \langle \Phi | \hat{H} \hat{C}_1 | \Phi \rangle + \mathcal{O}(\hat{C}_1^2)}{\langle \Phi | \Phi \rangle + \langle \Phi | \hat{C}_1^\dagger | \Phi \rangle + \langle \Phi | \hat{C}_1 | \Phi \rangle + \mathcal{O}(\hat{C}_1^2)} - E[\Phi] \\
 &= \left(\langle \Phi | \hat{H} | \Phi \rangle + \langle \Phi | \hat{C}_1^\dagger \hat{H} | \Phi \rangle + \langle \Phi | \hat{H} \hat{C}_1 | \Phi \rangle + \mathcal{O}(\hat{C}_1^2) \right) \left(1 - \mathcal{O}(\hat{C}_1^2)\right) - E[\Phi] \\
 &= \langle \Phi | \hat{C}_1^\dagger \hat{H} | \Phi \rangle + \langle \Phi | \hat{H} \hat{C}_1 | \Phi \rangle + \mathcal{O}(\hat{C}_1^2) \\
 &\Rightarrow \delta E[\Phi] = \langle \Phi | \hat{C}_1^\dagger \hat{H} | \Phi \rangle + \langle \Phi | \hat{H} \hat{C}_1 | \Phi \rangle .
 \end{aligned}$$

According to the variation principle, the solution should be a stationary point, thus $\forall \hat{C}_1$, $\langle \Phi | \hat{C}_1^\dagger \hat{H} | \Phi \rangle = 0$,

$$\begin{aligned}
 \langle \Phi | \hat{C}_1^\dagger \hat{H} | \Phi \rangle &= 0 \\
 \langle \Phi | \hat{C}_1^\dagger \left(\hat{F}_N + \hat{V}_N \langle \Phi | \hat{H} | \Phi \rangle \right) | \Phi \rangle &= 0 \\
 \langle \Phi | \hat{C}_1^\dagger \hat{F}_N | \Phi \rangle + \langle \Phi | \hat{C}_1^\dagger \hat{V}_N | \Phi \rangle + \langle \Phi | \hat{H} | \Phi \rangle \langle \Phi | \hat{C}_1^\dagger | \Phi \rangle &= 0 \\
 \langle \Phi | \hat{C}_1^\dagger \hat{F}_N | \Phi \rangle &= 0 \\
 \sum_{a,i} \sum_{p,q} \langle a | \hat{c}_1 | i \rangle^* \langle p | \hat{f} | q \rangle \langle \Phi | X_i^\dagger X_a N [X_p^\dagger X_q] | \Phi \rangle &= 0 \\
 \sum_{a,i} \sum_{p,q} \langle a | \hat{c}_1 | i \rangle^* \langle p | \hat{f} | q \rangle \delta_{pa} \delta_{qi} &= 0 \\
 \sum_{a,i} \langle a | \hat{c}_1 | i \rangle^* \langle a | \hat{f} | i \rangle &= 0 \quad ; \quad \forall \langle a | \hat{c}_1 | i \rangle \\
 \Rightarrow \langle a | \hat{f} | i \rangle &= 0 \quad ; \quad \forall i \in \text{occ.} , \forall a \in \text{unocc.} .
 \end{aligned}$$

$\langle \Phi | \hat{C}_1^\dagger \hat{V}_N | \Phi \rangle = 0$ can not fully contracted. It easy to find, $\forall i \in \text{occ.}$, $\hat{f} | i \rangle$ is orthogonal to the any of the unoccupied $|a\rangle$, thus $|i\rangle$ is closed under the action of \hat{f} . Here, \hat{f} is the Fock operator, and the derivation is shown in Section A.4.1.

$$\hat{f} | i \rangle = \sum_{j=1}^N \lambda_{ji} | j \rangle \quad ; \quad \lambda_{ji} = \langle j | \hat{f} | i \rangle \quad (2.3)$$

Due the hermiticity of the Fock operator \hat{f} , the corresponding matrix $\mathbf{\Lambda}$ is also Hermitian, $\mathbf{\Lambda}^\dagger = \mathbf{\Lambda}$, so it can be diagonalized by a unitary matrix, $\mathbf{U}^\dagger \mathbf{\Lambda} \mathbf{U}$. Then eigenstates $(\{\varepsilon_i\})$ of \hat{f} are obtained with a form of $\hat{f} | i \rangle = \varepsilon_i | i \rangle$.

It is worth noting, Equation 2.3 is not an typical eigenvalue problem, since \hat{f} is dependent on the occupied states $\{|i\rangle\}$. As a consequence, an initial guess of the states $\{|i\rangle^{(0)}\}$ is needed in the first step, which is normally done by the extended Hückel method. Then, the initial Fock operator is constructed by $\hat{f}^{(0)} = \hat{f} \left[\{|i\rangle^{(0)}\} \right]$. Diagonalizing $\hat{f}^{(0)}$, yields a the new set of states $\hat{f}^{(0)} |i\rangle^{(1)} = \epsilon_i^{(1)} |i\rangle^{(1)}$. The new Fock operator $\hat{f}^{(1)}$ can be constructed based on the new set of states. This process needs to be iterated to achieve convergence, where the energy or the density matrix of the states does not change any more. It is call the self-consistent-field (SCF) method [49].

To calculate the matrix elements, the the spatial part of single particle wavefunctions can be obtained by linear combination of atomic orbitals (LCAO),

$$\varphi_i(\mathbf{x}) = \langle \mathbf{x} | i \rangle = \sum_{\mu} d_{\mu i} \phi_{\mu}(\mathbf{x}) .$$

Here, $d_{\mu i}$ are the LCAO coefficients, and $\phi_{\mu}(\mathbf{x})$ are the basis functions. Normally the number of the basis functions need to be far more larger than the number of states.

2.5. Basis functions

In all these years of development, there are many types of basis function, the plane waves for the extended system, the contracted Gaussian-type orbitals (CGTO) and Slater-type orbitals (STO) for the isolated system [50, 51]. If the size of the nucleus is disregarded and reduced to a geometric point, then the wavefunction close to the nucleus should have a cusp shape, in which is close to the STO. However STO has difficulties with numerical calculations. The Gaussian-type functions are much more easy to handle. But a single GTO is not sharp enough at the center and decays too fast at the edges. As a consequence, the combination of different Gaussian-type functions are employed to construct the single-particle wavefunction of the atom.

$$\phi_{abc}^{\text{CGTO}}(x, y, z) = N \sum_{i=1}^n c_i x^a y^b z^c e^{-\zeta_i r^2}$$

As an example, the 1s orbital of hydrogen based on the STO-3G basis set. This basis set is combining three Gaussian-type functions to construct the 1s orbital, as shown in Equation 2.4. The red ‘S’ indicates its symmetry, b_i are the Gaussian orbital exponents, and c_i are the expansion coefficients. As shown in Figure 2.1, the CGTO approximates the behavior of the STO.

H	0		
S	3	1.00	
0.3425250914D+01	(b_1)	0.1543289673D+00	(c_1)
0.6239137298D+00	(b_2)	0.5353281423D+00	(c_2)
0.1688554040D+00	(b_3)	0.4446345422D+00	(c_3)

$$\phi_{H_{1s}}^{\text{CGTO}} = c_1(2b_1/\pi)^{3/4}e^{-b_1r^2} + c_2(2b_2/\pi)^{3/4}e^{-b_2r^2} + c_3(2b_3/\pi)^{3/4}e^{-b_3r^2} \quad (2.4)$$

$$\phi_{H_{1s}}^{\text{STO}} = (1.24^3/\pi)^{1/2}e^{-1.24r} \quad (2.5)$$

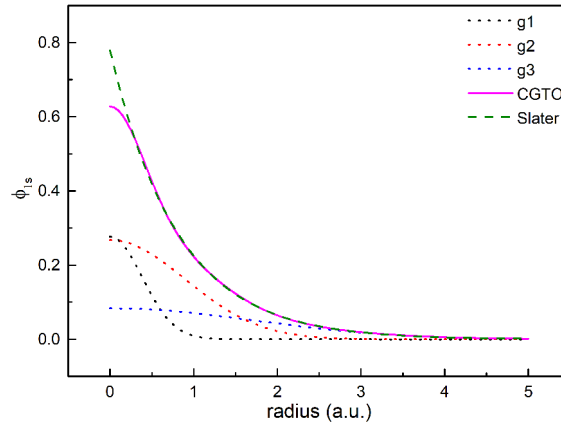


Figure 2.1.: The comparison between the CGTO and the STO of the 1s orbital of hydrogen.

3. Global optimization of reactive force-field (ReaxFF) parameters

3.1. Introduction

With the vibrant development of the semiconductor industry, the abundant and easily accessible computational capability allow us to use wave function methods and DFT to study a molecular system with a resolution as fine as electron level. Unfortunately, the time or resource requirements for such highly accurate methods grows with the size of system in a polynomial way (*e.g.*, $\mathcal{O}(n^3)$ for DFT) [52]. Therefore, the system size is usually limited to under few thousand atoms. For most biomolecules (*e.g.*, ferritin, DNA), this is nowhere near large enough. But in most of the cases (*e.g.*, proteins), we do not really have to know the exact electronic structures at every point in time. We may only care about the geometrical structures' evolution, because the dynamic of electrons (from attoseconds to femtoseconds) is far more faster than atoms. Thus, the fluctuations of electronic configuration could be smeared by time, and the energy of the system could be represent by some local, simplified, functions of the remaining atomic degree of freedoms, which is called a force field.

A force field could be treated as a function giving the potential energy with respect to atomic positions. In principle, if the initial conditions (velocities, positions) and the potential function are given, then the system is deterministic, and the trajectory in the phase space could be predicted by Newton's laws. The system's evolution in time is called molecular dynamics (MD) [31]. Due to the locality nature of most of the force fields, the system could be easily segmented into smaller parts. Thus, the calculation can be parallelized and accelerated [53]. The molecular dynamics method allows us to track the geometrical evolution (from picoseconds to nanoseconds) of a large biomolecular system, which is commonly used in, *e.g.*, drug design, protein target-search, or DNA self-assembly [52–58].

Generally, a conventional force field (*e.g.*, AMBER, CHARMM, OPLS) includes terms for bond, angle, dihedral, improper torsion, Coulomb and van der Waals

interactions [36–38]. The last two terms sometimes also are called non-covalent interaction (NCI) terms. In such a framework, the topology of the molecule needs to be defined in the first step. This is both a blessing and a handicap. Because for these force fields, the topology is fixed, calculations can be performed in an efficient way, and we do not have to be worried that the molecule flies into parts. But on the other hand, rearrangements, cleaving of bonds or even bond creation is not possible.

As one approach to overcome these shortcomings, reactive force-field (ReaxFF) was proposed [39]. The main idea is, that the bond strength is able to vary depending on the surrounding coordination environment by altering the bond order. The detail of the ReaxFF parameters file can be found in Section B.1. From the initial idea, ReaxFF could be universal, but this has been proven hard to implement. A set of force field parameters with excellent performance on a certain system may behave erroneously on another system. The force field parameters need to be optimized for the system to be explored. In principle, a set of optimized parameters could be found by minimizing the deviation from a reference data, which is based on high-level calculation methods or experimental results. However, the large number of the parameters often prevents finding the global minimum by standard methods, like grid search, gradient descent. Fruitful results in this field have been made by many groups. As some traditional methods for finding the global minima, the particle swarm optimization [59], the genetic algorithms (GA) [60, 61], the multiple objective evolutionary strategies algorithm [62, 63], hill climbing methods [64], covariance matrix adaptation evolution strategy (CMA-ES) [40, 65], and Monte Carlo methods [66] have been explored. Some methods of above are based on evolutionary algorithms. However, for evolutionary algorithms, the optimization process may not be ideal when dealing with parameter spaces with very high dimension, or functions in the parameter space with pathological behavior [67, 68].

From another point of view, machine learning (ML) has been a great success since its inception, especially in the field of pattern recognition [69]. With right training process, machine learning models can be given the ability to extract information from complicated data, which could be used for predicting. Therefore, by using this predictive capability, ReaxFF parameter optimization processes can be accelerated. A variety of machine learning methods have been applied to this topic [70–73]. For instance, whole parameter space can be efficiently explored by a Latin hyper design algorithm rather than being stuck at the beginning regions [73].

In this work, a machine-learning-assisted ReaxFF reparameterization was explored with three different methods: direct learning, parameter space dimension reduction, and the grouping of parameter components by the correlations between them (Figure 3.1) .

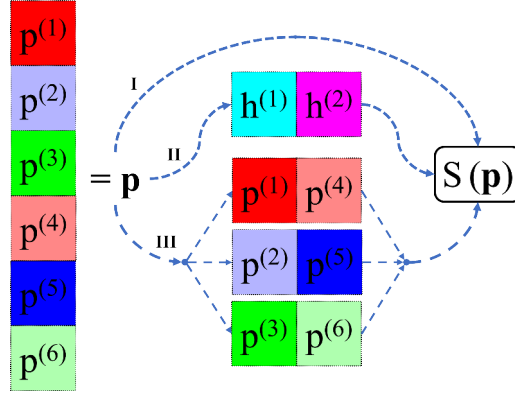


Figure 3.1.: Illustration of the three methods in this work. For a set of force field parameters \mathbf{p} , the score of each subsystem can be calculated based on the ReaxFF MD results and the references. A machine learning model could be used for directly predicting a score based on a parameter. For instance, a parameter vector (\mathbf{p}) consists of six components, in which correlations between components are represented by colors. In the first approach, we try to get the score ($S(\mathbf{p})$) directly based on a model. In the second approach, a dimension reduction method is applied, and the original parameter vector is converted to a code (\mathbf{h}) with a lower dimension. Then, the score is predicted by the code based on a model. In the third approach, six components are segmented by the correlations between them, and optimizations are performed on each segmented group of components sequentially.

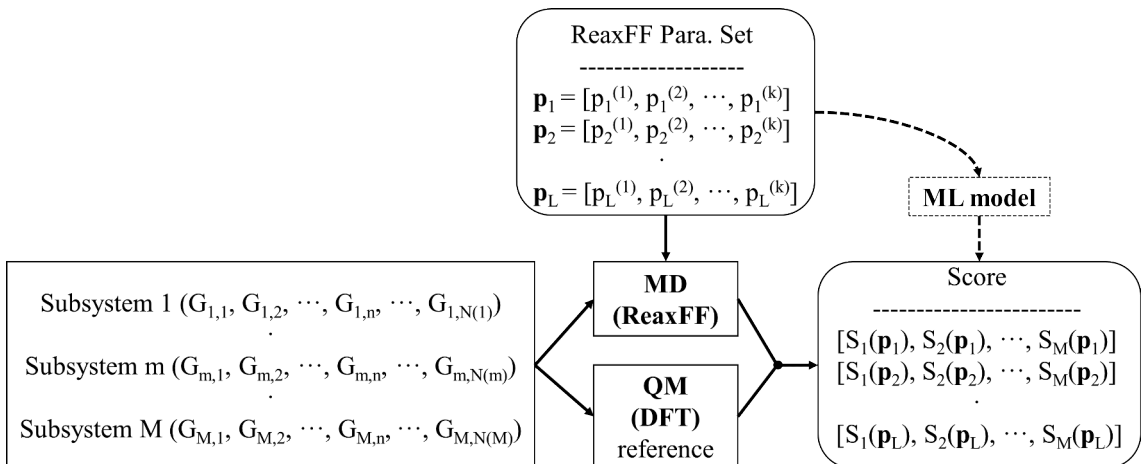


Figure 3.2.: The conceptual work flow of fitting a reactive force-field.

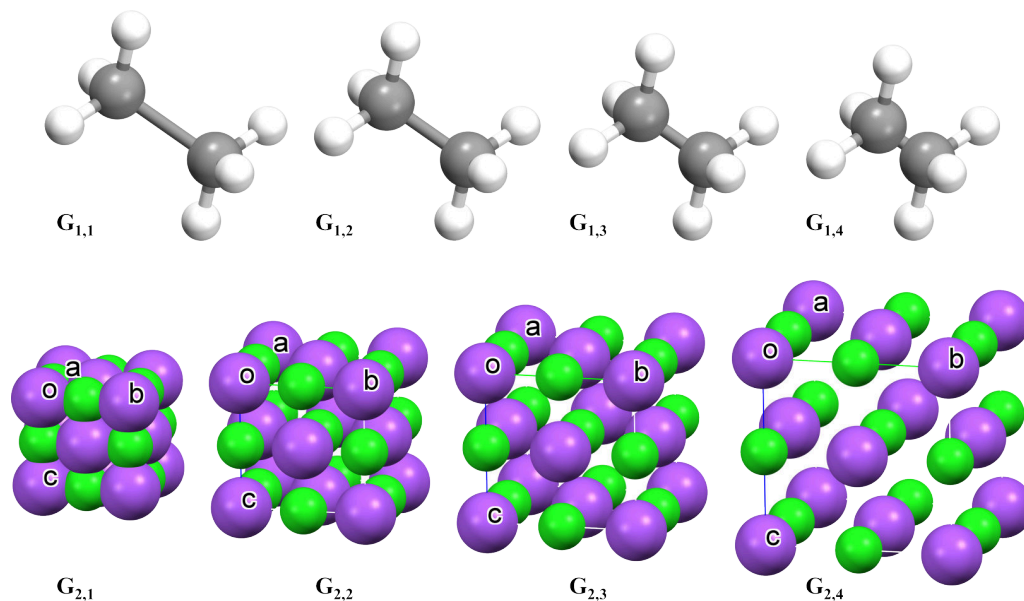


Figure 3.3.: The frames of two subsystems are represented by ball-and-stick models of ethane (top) and ball models of a NaCl unit cell (bottom). The ethane subsystem (G_1) consists of four frames with different C-C bond lengths. The NaCl subsystem (G_2) consists of four frames with different C-C lengths of a unit cell. The correspondence between atoms and colors, carbon (gray); hydrogen (white); sodium (violet); chlorine (green).

In order to cover as much as possible the mechanical properties of the desired system using as few calculations as possible, the whole system can be approximated by using multiple subsystems containing a small number of atoms. Each subsystem is focused on one property, *e.g.*, stretching of carbon-hydrogen bonds, a vibrational mode, *etc.* A subsystem consists of several frames with a geometrical structure $G_{m,n}$. Here, m and n are the indices of the subsystem and the frame respectively (Figure 3.2, Figure 3.3).

The frames can be obtained by various ways, including but not limited to the scanning of bond, angle, dihedral, improper torsion, reaction path, the movement along a vibrational normal mode and the snapshots from a MD simulation based on pre-optimized parameters or a semi-empirical method (*e.g.*, PM7). To build a standard, the mechanical properties (*e.g.*, energy, force) of each frame in each subsystem can be calculated as a reference based on a high level method, like HF, DFT, or coupled cluster theory. Based on a set of force field parameters \mathbf{p} , the corresponding properties could be calculated by ReaxFF MD, and the deviations from the references could be evaluated by a score function $S(\mathbf{p})$. In this work, the defined score is positively correlated with the deviations, thus lower the better (the lower bound being zero).

3.2. Fitting reactive force-field: development of a python script

To implement the above idea, we have written a small program REAXFFFITTING in PYTHON3.

GAUSSIAN 16B01 and VASP 5.4.4 are used for getting reference data [74, 75]. The ReaxFF MD simulations rely on the Large-scale Atomic/Molecular Massively Parallel Simulator (LAMMPS 15APR2020 program package) [76]. The installation and setting can be found in Section B.2. Due to possible differences in the input and output files of different versions of the software, using other versions requires verification of the formats (here we checked for the listed version only).

3.2.1. Introduction to the classes in ReaxFFFitting

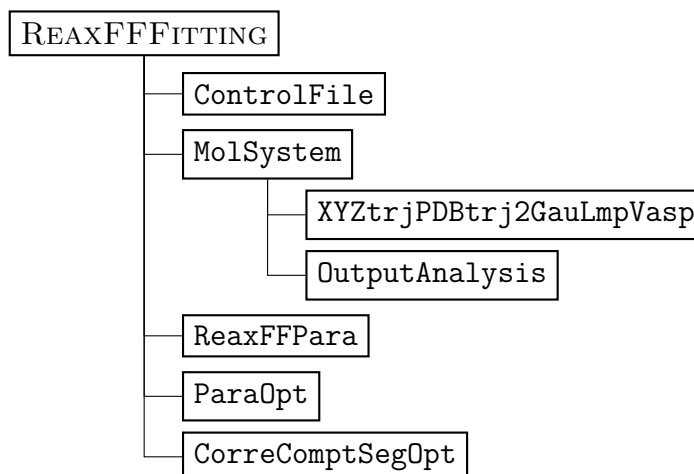


Figure 3.4.: The class structure of REAXFFFITTING.

Main creates an instance, and starts the main function, as the entry point. **REAXFFFITTING** defines the main class. **ControlFile** reads in the control file (*e.g.*, **ReaxFF-Fitting_control**), which defines the subsystems, the hardware information (*e.g.*, the number of cores, memory, *etc.*), the setting for the quantum chemistry and molecular dynamics programs, the configuration for the parameter-optimization process (*e.g.*, the number of the optimization cycles, the mutation rate in the genetic algorithm, the boundary conditions, *etc.*). **MolSystem** defines the class which will be implemented for each subsystem. There are two interfaces for writing the input files and reading the results. **XYZtrjPDBtrj2GauLmpVasp** converts the molecular structure files (in *.xyz or *.pdb format) to the inputs of the corresponding softwares. **OutputAnalysis** reads out the calculated results (*e.g.*, energy, force, ten-

sion) and convert the units (Table 3.1). For a periodical system, tension refers to the stress tensor (pressure) acting on the unit cell. The reason for using this name is to avoid confusion between its abbreviated symbol and the others. In particular LAMMPS has various unit systems, and here the **real** style units are used. **ReaxFFPara** reads and writes the ReaxFF parameter file (***.ff**), and produces the new parameters. **ParaOpt** defines the machine learning models and the grid searching function. **CorreComptSegOpt** defines the functions for segmenting parameter components based on the correlations between them.

Table 3.1.: The standard units used in the different programs.

	Energy	Force	Tension
REAXFFFITING	eV	eV/Å	kB
LAMMPS(real)	kcal/mol	(kcal/mol)/Å	atmospheres
GAUSSIAN	Hartrees	Hartrees/Bohr	
VASP	eV	eV/Å	eV/Å ³

3.2.2. The score function

In order to describe the deviation between the ReaxFF simulated results and the references, a scalar score, $S(\mathbf{p})$, is required for the following optimization steps, which is a function of the ReaxFF parameter vector (\mathbf{p}).

An ideal MD simulation should be able to reproduce the potential energy surface (PES) like the reference method. Thus, the energy and its derivatives (*e.g.*, force, tension) are naturally taken into account. Here, tension indicates a pressure in a unit cell of a periodical system.

Suppose there are M number of subsystems containing $|\mathbb{A}|$ types of atoms, where \mathbb{A} is the set of atom types in the whole system (*e.g.*, $\{\text{C}, \text{H}, \text{N}, \text{O}\}$) and $|\mathbb{A}|$ is the number of elements (cardinality) in \mathbb{A} (*e.g.*, 4). Each subsystem contains N_m frames which have different geometrical structures. However, the ReaxFF MD simulations could fail for some ReaxFF parameter vectors, thus the *failed frames* need to be removed and only the remaining $\tilde{N}_m^{\mathbf{p}}$ *available frames* will be used for the score. Here, the function σ maps an index of an available frames to the original index of the frame. For example, a subsystem G_m has three frames ($N_m = 3, \{1, 2, 3\}$). For a certain ReaxFF parameter, if the 2nd frame fails in the MD simulation, then $\{2\}$ is the failed frame and $\{1, 3\}$ are the available frames, and $\tilde{N}_m^{\mathbf{p}} = 2$. The σ function behaves like: $\sigma(1) = 1$ and $\sigma(2) = 3$.

To evaluated the deviation of energy for a certain \mathbf{p} , we do the following steps:

Here, $E_{m,\sigma(n)}^{\text{MD}}(\mathbf{p})$ represents the ReaxFF MD energy of the $\sigma(n)$ frame in the m subsystem based on the ReaxFF parameter vector \mathbf{p} , and $E_{m,\sigma(n)}^{\text{Ref}}$ represents the corresponding reference energy. Because MD calculations and reference calculations could have very different absolute values, and only the energy difference between frames is critical. The MD energies and the reference energies in a subsystem are shifted by their average values, where the average of the MD energies is $\overline{E_m^{\text{MD}}(\mathbf{p})} = \frac{1}{\tilde{N}_m^{\mathbf{p}}} \sum_{n=1}^{\tilde{N}_m^{\mathbf{p}}} E_{m,\sigma(n)}^{\text{MD}}(\mathbf{p})$ and the average of the reference energies is $\overline{E_m^{\text{Ref}}} = \frac{1}{\tilde{N}_m^{\mathbf{p}}} \sum_{n=1}^{\tilde{N}_m^{\mathbf{p}}} E_{m,\sigma(n)}^{\text{Ref}}$. The energy deviation between the MD simulations and the references for the m subsystem based on \mathbf{p} is given by the root mean square (RMS) of the differences over the available frames, which is

$$\Delta E_m(\mathbf{p}) = \frac{1}{\sqrt{\tilde{N}_m^{\mathbf{p}}}} \sqrt{\sum_{n=1}^{\tilde{N}_m^{\mathbf{p}}} \left[E_{m,\sigma(n)}^{\text{MD}}(\mathbf{p}) - \overline{E_m^{\text{MD}}(\mathbf{p})} - E_{m,\sigma(n)}^{\text{Ref}} + \overline{E_m^{\text{Ref}}} \right]^2}. \quad (3.1)$$

For the deviation of force, we have: $\mathbf{F}_{m,\sigma(n),i}^{\text{MD}}(\mathbf{p})$ represents the atomic force on the atom i of the $\sigma(n)$ frame in the m subsystem by MD simulation with a ReaxFF parameter vector \mathbf{p} . It has three components, on along the three Cartesian coordinate axes. $\mathbb{E}_{m,a}$ is a set of indices for the a type atoms in the m subsystem, where a is an element of A , $a \in \mathbb{A}$. For the m subsystem, the force deviation of the all a type atoms between the MD simulations and the references, $\Delta F_m^{(\mathbb{E}_{m,a})}(\mathbf{p})$, is given by the RMS of the differences over the available frames and the possible atom indices, which is

$$\Delta F_m^{(\mathbb{E}_{m,a})}(\mathbf{p}) = \frac{1}{\sqrt{|\mathbb{E}_{m,a}| \tilde{N}_m^{\mathbf{p}}}} \sqrt{\sum_{i \in \mathbb{E}_{m,a}} \sum_{n=1}^{\tilde{N}_m^{\mathbf{p}}} \left\| \mathbf{F}_{m,\sigma(n),i}^{\text{MD}}(\mathbf{p}) - \mathbf{F}_{m,\sigma(n),i}^{\text{Ref}} \right\|^2}. \quad (3.2)$$

For a periodical system, the tension of the unit cell is crucial when altering the cell size (by expansions or compressions) without changing the cell shape and the atoms' fractional coordinates, where the net force on an atom would not be changed during the process but the tension can be varied significantly. The deviation of tension could be calculated as follows: $\mathbf{T}_{m,\sigma(n)}^{\text{MD}}(\mathbf{p})$ represents the unit cell tension of the $\sigma(n)$ frame in the m subsystem by MD simulation with a ReaxFF parameter vector \mathbf{p} . The tension deviation for the m subsystem could be calculated by the average of the normal of the differences over the available frames, which is

$$\Delta T_m(\mathbf{p}) = \frac{1}{\tilde{N}_m^{\mathbf{p}}} \sum_{n=1}^{\tilde{N}_m^{\mathbf{p}}} \left\| \mathbf{T}_{m,\sigma(n)}^{\text{MD}}(\mathbf{p}) - \mathbf{T}_{m,\sigma(n)}^{\text{Ref}} \right\|. \quad (3.3)$$

The scores are calculated from the deviations (s) with a penalty function f^P , which penalizes the failed frames,

$$f^P(s, \gamma) = (s + 100\gamma)e^{5\gamma} . \quad (3.4)$$

Here, γ is the rate of the failed frames, which is defined by $\gamma = 1 - \frac{\tilde{N}_m^P}{N_m}$. If it is too high (the default threshold is 50%), the ReaxFF parameter vector \mathbf{p} will be discarded. The selected penalty function contains an additive term (100γ) and a multiplication term ($e^{5\gamma}$), which are targeted at a small and large input deviation, respectively. It is necessary to use a penalty function. First, by taking the strictest standard, in which \mathbf{p} is discarded if there is any error in any frame in any subsystem, a lot of data points of \mathbf{p} could be wasted, especially the parameters are far from optimized. Second, if there is no measure regarding the frame failure, then the optimization process will only optimize a single frame ignoring the others, and the final optimized \mathbf{p} will only work on that single frame.

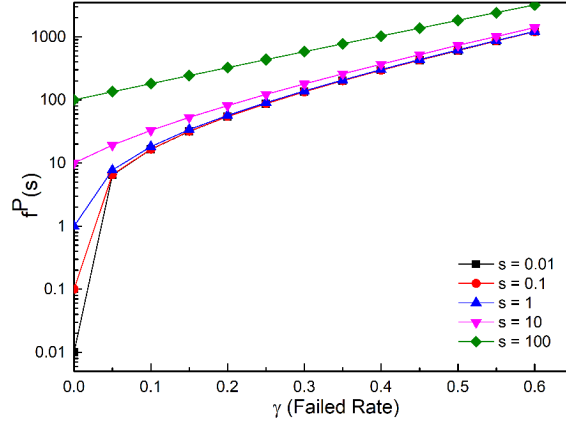


Figure 3.5.: The penalty function behavior under different original values (s).

The energy, force, and tension components of the score for each subsystem are calculated by f^P with the corresponding deviations (s) and γ .

$$S_m^{(E)}(\mathbf{p}) = f^P(\Delta E_m(\mathbf{p}), \gamma) \quad (3.5)$$

$$S_m^{(F)}(\mathbf{p}) = \sum_{a \in \mathbb{A}} f^P(\Delta F_m^{(\mathbb{E}_{m,a})}(\mathbf{p}), \gamma) \quad (3.6)$$

$$S_m^{(T)}(\mathbf{p}) = f^P(\Delta T_m(\mathbf{p}), \gamma) \quad (3.7)$$

The summation over the products of the score components with the weights gives the score for a subsystem. Here, the default values of the weights are 0.01 for an energy component, 1.0 for a force component, and 0.002 for a tension component.

$$S_m(\mathbf{p}) = w_{(E)}S_m^{(E)}(\mathbf{p}) + w_{(F)}S_m^{(F)}(\mathbf{p}) + w_{(T)}S_m^{(T)}(\mathbf{p}) \quad (3.8)$$

The score of the whole system is given by the summation over all products between the subsystems' scores and the corresponding weights. The default weight for a subsystem is 1.0.

$$S(\mathbf{p}) = \sum_{m=1}^M w_m S_m(\mathbf{p}) \quad (3.9)$$

Both two kinds of weights can be modified in the control file, and the key point in choosing the weights is to keep the corresponding components of score in a same order of magnitude.

3.2.3. Preparing a set of ReaxFF parameter vectors

When running the program for the first time, the `ReaxFFPara` module reads in the original ReaxFF parameter file (`*.ff`) and vectorizes all parameters into the original parameter vector \mathbf{p}^0 . In fact, there could be many fixed components by the setting from the `ReaxFFFitting` control file and also some constants (*e.g.*, atomic masses, types of hydrogen bond) which do not need to be optimized. Thus, the module will generate a mask according to the limitation conditions, which removes the fixed components from the original parameter vector resulting in a new vector \mathbf{p} with fewer components. The mask will be recorded into a file (`ReaxFFPara.Mask`) for restarting an interrupted task. From here, we will refer to the new vector as the parameter vector.

For the generation of new parameter vectors, it is not possible to use a grid mesh in the entire parameter space, due to the high dimensionality of this space. For instance, a very simple ReaxFF parameter file of carbon has 114 components, and even 44 components are left after removing the unnecessary parts. By taking two values on each component, although to evaluate a parameter vector would not cost a second, 2^{44} vectors will take around sixty thousand years. For a slightly more complicated system containing gold, sulfur, carbon, hydrogen, and oxygen, the dimension of the parameter vector is 907 (originally 1561).

During an optimization process, when there are no *a priori* assumptions about the structure of the parameter space, a deterministic algorithm (*e.g.*, gradient descent) is easy to be converged to a local stationary point, but the process could jump out of the local stationary point and explore the other part of the space by introducing some randomness (*e.g.*, evolutionary algorithm). Here, a genetic algorithm (GA) is used for the new vectors generation. It is important to note that the `ReaxFFPara` module only plays a part of the role of GA, the reproduction. The selection part is executed by the optimization module (`ParaOpt`).

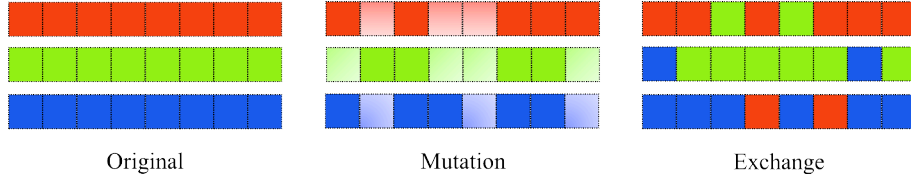


Figure 3.6.: The schematic diagram representing the mutation and the exchange process of the parameter vectors in a genetic algorithm. On the left side, there are three different vectors colored by red, green, and blue. A small dashed box corresponds to a component of the vector. In the mutation process (middle), the values of components can be changed, illustrated by lighter colors. In the exchange process (right), the components on one vector can be replaced by the position-equivalent components of the other vector. In a case of ReaxFF parameter \mathbf{p} , a vector is a real number array.

In the reproduction process of GA, a new parameter vector could be generated by mutating the vector's components or by exchanging components with other vectors (Figure 3.6). The ratio between the new vectors generated by mutation and exchange can be adjusted by the keyword (`InterParaExchangeRate`), the default value is 0.20. If 1000 new vectors will be generated (as in the default setting), then 800 vectors are generated by self mutation and 200 vectors are generated by inter-vector exchange. The ratio of the changed components for a vector can also be set in the control file, where the default value is 50%.

In order to limit the search area, the upper and lower bounds of each component need to be defined in the control file. For the implemented mutation process, the selected k component $\mathbf{p}^{(k)}$ will be altered as described by,

$$\mathbf{p}'^{(k)} = \mathbf{p}^{(k)} + L^k \mu x, \quad (3.10)$$

where L^k is the difference between the upper and lower bounds of the k component, μ is an amplitude factor to adjust the magnitude of the mutation, and x satisfies a normal distribution with a standard deviation σ ,

$$p(x) = \frac{1}{\sqrt{2\pi}\sigma^2} e^{-\frac{x^2}{2\sigma^2}}. \quad (3.11)$$

If the generated $\mathbf{p}'^{(k)}$ is out of the bounds, then it will be reset to a randomly selected value between the two bounds, which satisfies a uniform distribution.

By running such a process, the majority of the new components are distributed in the vicinity of the original value, which provides convergence and stability. It also gives the possibility to disperse the component far away from the original point, which enables finding a new stationary point.

In the first optimization loop of the program, only the mutation process will be executed, due to the lack of other optimal parameter vectors. After the program has run at least one round of optimization steps, it will produce multiple parameter vectors with good performance and those vectors can be used as seeds to generate new vectors. They will also be recorded as a file (`Seed.sum`). For the implemented exchange process, the components to be changed in the selected seed vectors will be replaced by the components of another seed vector. This process may merge the strengths of both vectors or jump into another part in the parameter space.

After getting the generation process, the corresponding MD simulations will be made, and the score for each parameter vector can be calculated by comparing the MD results and the references according to the score definition above.

If some parameters with good performance are chosen as the seed vectors for the next generation cycle, then it is a conventional genetic optimization method. Here we want to speed up the process by using machine learning methods.

3.2.4. The optimization process: machine learning-assisted genetic algorithms

In this optimization process, there are three steps, first clustering of parameter vectors, second fitting the machine learning model(s), finally searching local minimum points by the model(s) predicted scores.

After several rounds of parameter generation, these vectors could be widely distributed in the parameter space, but some of them may form clusters. For vectors belonging to the same cluster, the distances between them are significantly shorter than the distances between a vector out of the cluster. Each cluster could represent a type of parameter vectors which have some good properties to reliably describe a characteristic of a subsystem.

Here, k -means clustering is used for the parameter vectors. This method is implemented by using the `SCIKIT-LEARN 0.23.0` package [77]. The number of clusters needs to be defined in advance. After the clustering process, the parameter vectors with the best score in each cluster are selected.

For the machine learning models, there are many options, like random forest regression (RFR), Gaussian process regression (GPR), neural network (NN), *etc.* [78–82]. Here, the random forest regression is implemented in the `ParaOpt` module firstly, since it can partially solve the overfitting problem. The random forest is a combination of two methods, bootstrapping and decision tree. Bootstrapping is a kind of resampling method. The statistical distribution of the desired charac-

teristic (*e.g.*, the mean value) can be calculated from the bootstrapping data set which is built from the original sample data set. For instance, if there are a data points in the sample set $\{s_1, s_2, \dots, s_i, \dots, s_a\}$, then the bootstrapping data set could be built by using random sampling a points with replacement, giving a set like $D_m = \{s_1, s_1, s_2, s_3, \dots, s_{a-1}\}$. The desired characteristic then be calculated according to the D_m , by repeating this process several times, and the distribution of the characteristic can be given based on the original sample data set.

A decision tree is built from the given data set. Data points are split into two at each judgment node according to a certain feature (a component of a parameter vector). The splitting condition should minimize the error. For a classifier, it should minimize the Gini impurity (a measure of the misclassified ratio), and for a regressor, it should minimize the mean-square error (MSE) between the real and estimated data values. In principle, by repeating such a process, eventually each data point will be assigned to their own node, which is not able to be split. Such terminal nodes are also called leaves. In this case, each leaf contains only one data point, so the final decision tree is 100% precise for the given training set, but with very high variance for other test points. The common practice is to limit the amount of the selected features, the minimum number of samples required to split a node, the minimum number of samples in a leaf, *etc.* Such a pruning decision tree has more generalizability [83, 84].

A model consisting of a single decision tree is not reliable in terms of stability, due to the tree being highly sensitive to the selected data points. As an improvement, the random forest is an ensemble containing multiple decision trees as the estimators. A bootstrapping data set based on the original data is used for building a single decision tree with the randomly selected features. Normally, not all of the features will be used to build a tree, that will lead to a large similarity between any two of trees in the forest. The predicted value is given by a voting from all estimators. Such a process is also called aggregating. Thus, random forest is a bootstrapping aggregating (bagging) method.

In the **ParaOpt** module, each subsystem instantiates a RFR model. The parameter vectors ($\{\mathbf{p}\}$) and the scores for the corresponding subsystems ($\{S_m(\mathbf{p})\}$) are split into the training set and the test set. The models are trained by the given training set and tested by the test set after the training process. The accuracy of the models could be evaluated by some functions of the actual data and the predicted data, like the Pearson product-moment correlation coefficient (PPMCC), the R^2 score.

The final step is to find the local minimum for each seed vectors, which is the local minimum of each cluster. The optimization sequence of the vector components (fea-

tures) are sorted by the PPMCC evaluated correlations between the corresponding components ($\{\mathbf{p}^{(\alpha)}\}$) and the score of subsystems ($\{S_m(\mathbf{p})\}$).

The first few components (the default value is 12) are selected and divided into several groups, and a $\underbrace{k \times k \times \cdots \times k}_l$ search grid for those components is generated by those components (default, $l = 4$, $k = 20$) in a group. The search grid covers the subspace spanned by the components' intervals with a certain length (default, 10%) with the original value as the midpoint. The scores of the search grid points are estimated by the corresponding subsystem model, and the best vector is selected for the following step. The grid searching processes are repeated on the other group components, the other systems, and the other seed vectors hierarchically. Finally, all seed vectors are optimized by the grid searching processes, and verified by actual MD simulations. The seed vectors optimized by machine learning grid searching will be accepted if the actual scores are better than the original seed vector. The obtained seed vectors will be used for the next round of parameter vector generation and optimization.

3.3. Example: C₂₀

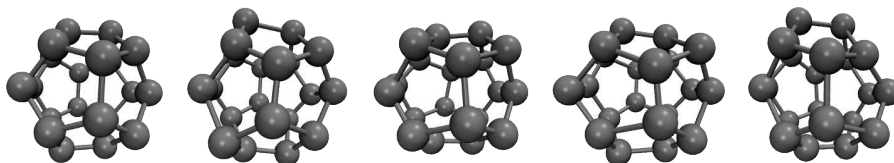


Figure 3.7.: A part of frames of the C₂₀ subsystem obtained by the snapshots from a molecular dynamics simulation.

The C₂₀ molecule was used to verify the REAXFFFITTING module. The system only contains one subsystem, in which the 20 frames were captured by the snapshots of the PM7 semi-empirical based MD simulation (Figure 3.7). The optimization process was run for a total of seven cycles, and 10000 new parameter vectors were generated for each cycle. The vectors have 44 components excluding the fixed ones.

According to the energy curves (Figure 3.8), the MD simulated energies based on the optimized parameters are closer to the reference than the original parameters. As an example, the value distribution of the bond energy parameter (p_{be2}) in the odd-number cycles are illustrated in Figure 3.9. At the beginning, almost all values are concentrated around the original value with a sharp peak and a mutated broadened peak. In the next cycle, the component is extended to a wider range in the allowed interval, and a new value around 45 is found with good performance. Gradually,

more distribution around the new value and less around the original value is found. Finally, the components are converged at the new value.

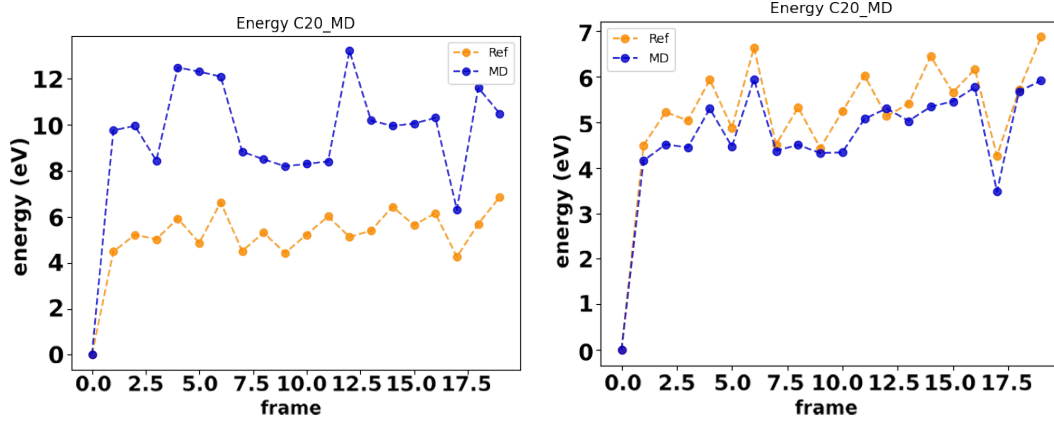


Figure 3.8.: The energies of the C₂₀ subsystems' frames before (left) and after (right) the optimization of the parameters. The yellow and the blue lines represent the reference and the ReaxFF MD simulation results respectively.

The behavior of the random forest model are shown in Figure 3.8, suggesting a fairly good performance in this simple example. Both the test data and the training data were close to the ideal line, which means the model did not exhibit over-fitting.

However, the adoption rate of the optimized seed vectors by the model is not really satisfying (Figure B.1). It was around 10% in this case, which means the accuracy of the model is not ideal when exploring in the new area of the parameter space. But it is worth noting that the adoption rate is slightly higher when the number of generated vectors for each cycle is small.

To verify the effect of the model's hyperparameters on performance, six million data points were prepared by actual MD simulations. Here, a cut-off was used to exclude the pathological-behavior data points with very high errors. One hundred thousand benign data points (their scores are under a certain threshold) were selected, the first 80% points ranked by their scores were used to build the sample data set, the 70% samples were used to train the model (56000 points), and the rest for testing (24000 points). The verified random forest model consisted of 1000 estimators. From results shown in Figure B.2 and Figure B.3, it is clear to see that the unpruned trees (the left side of the figures) well perform on the training data set, but the performance on the test data set showed the model was overfitted. By the pruning of decision trees, the performance on the two data sets behavior more similar. But excessive pruning can cause the model to lose its predictive power (the right side of the figures). In this case, the vectors have 44 components (also called features). By increasing the number of the features to build a decision tree, the performance on the two data sets

became better. However, this does not guarantee that the model could be valid as well for other data points.

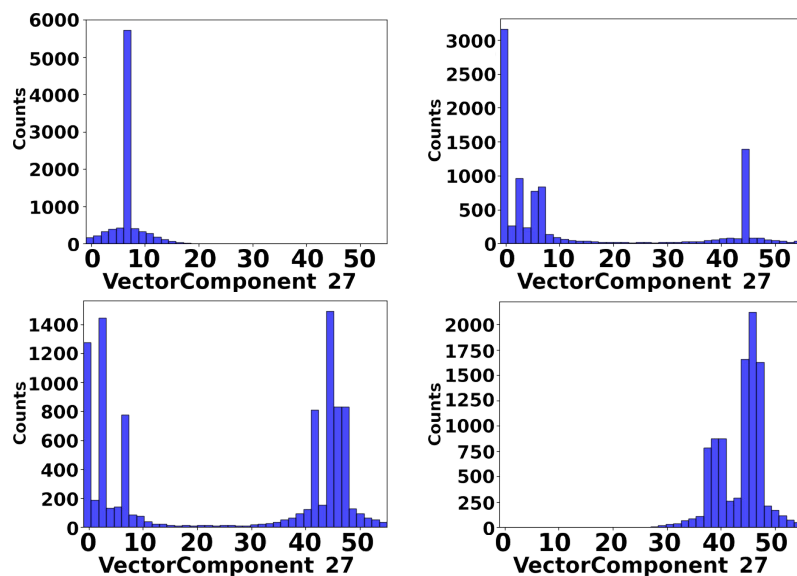


Figure 3.9.: For the C_{20} system, the variation of the value distribution of the p_{be2} component over the 1st (top left), 3rd (top right), 5th (bottom left), 7th (bottom right) optimization cycles of the parameters.

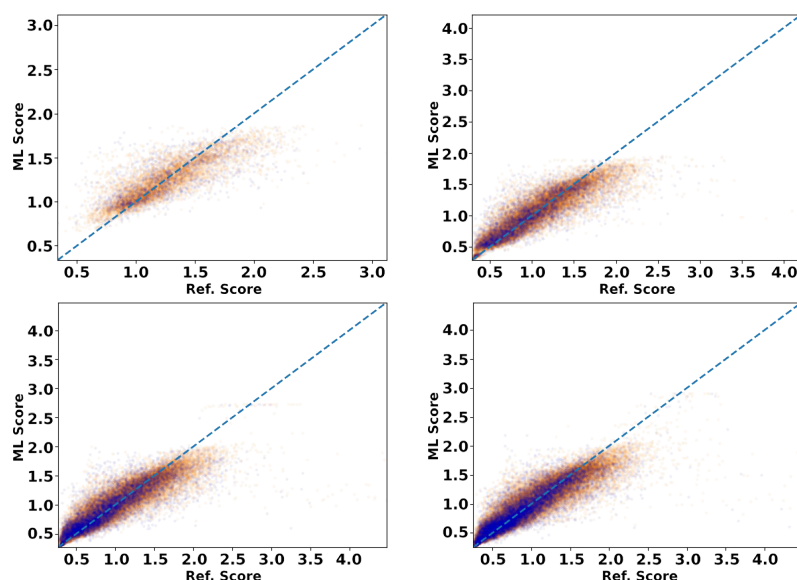


Figure 3.10.: For the C_{20} system, the comparison between the actual scores and the scores predicted by the machine learning model in the 1st (top left), 3rd (top right), 5th (bottom left), 7th (bottom right) optimization cycles of the parameters. Here the yellow and the blue points represent the training and the test data respectively.

As one advantage of the random forest regressor, the working process tries to divide the parameter space into different areas based on the scores. Thus, it is not sensitive to the preprocessing of the data points, like normalization or logarithmisation (Figure B.5). Furthermore, it requires fewer data to give a predictive results on the test set compared with a neural network (Figure B.6, Figure B.9). In other words, this system is suitable for small amounts of new vectors generation and many times of optimization cycles. The time required for the model training and grid search is usually an order of magnitude less than the actual score calculations, by improving the generalisation and the accuracy of the model is a direction worth trying.

3.4. Dimensionality reduction

In the above method, the machine learning model is used to learn the score function in the parameter space $S(\mathbf{p})$, which learns the geometrical structure of the function. As another approach, since we are only interested in parameter vectors that perform well, a model also could be used to learn the distribution of the vectors with benign performance in the parameter space.

Without any criterion for selecting parameter vectors, they will be evenly distributed in the parameter space which normally is isomorphic to an Euclidean space. A selection removes the bad performing vectors and the remaining vectors form a set. In general, normally the score function is continuous and the real world will not behave too badly. Thus, for a vector in the set, it should have a similar score to its neighbourhood. Thus, the set should satisfy a topological condition as a manifold, which should have a lower dimension compared with the original parameter space. If the properties of the score functions are good enough, the manifold could even be smooth.

For example, a hat-like score function $f(x, y) = (x^2 + y^2 - 1)^2$ in the xy parameter space has low scores in the vicinity of a points in the set $\{(x, y) | (x^2 + y^2 = 1)\}$. The original xy parameter space is two-dimensional, but the manifold formed by the vectors with the lowest score is isomorphic to a circle S^1 , which is one-dimensional (Figure 3.11).

This gives a hint that, the information carried by the benign parameter vectors ($\{\mathbf{p}\}$) have redundancy, and the vectors could be represented by fewer components by dimensionality reduction. It offers a great advantage, which could significantly reduce the parameter searching effort. There are many options for implementing this process but here the contractive autoencoder was used.

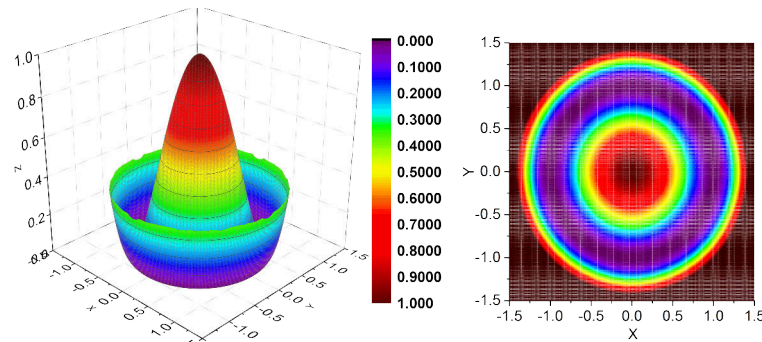


Figure 3.11.: The value of the example function in the xy parameter space (left). The data points with the lowest value form an approximately circular shape collection colored by dark purple (right).

3.4.1. Contractive autoencoder

According to the Kolmogorov–Arnold representation theorem [85], any multivariate continuous function (f) can be represented as a finite composition of continuous functions of a single variable and the binary operation of addition (Equation 3.12), in which $\phi_{q,p}$ are inner functions and Φ_q are outer functions.

$$f(x_1, \dots, x_n) = \sum_{q=0}^{2n} \Phi_q \left(\sum_{p=1}^n \phi_{q,p}(x_p) \right) \quad (3.12)$$

This provides a method to approach a complex function by multiple simple functions.

A neural network is an instantiation of the above, where the neurons and the activation functions play roles as the simple functions, thus it should have the ability to approximate any continuous function. An autoencoder is a special case of a neural

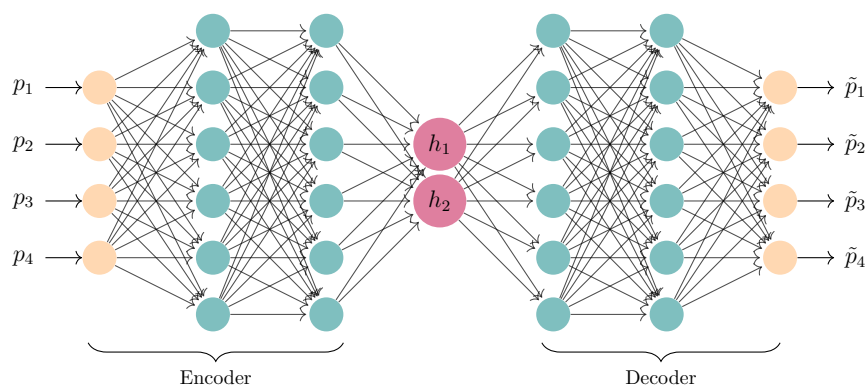


Figure 3.12.: A schematic of an autoencoder.

network with a bottleneck, which consists of the encoder layers, the code layer, and the decoder layers [86]. Here, the TENSORFLOW R2.6 package was used for building neural networks [87]. The encoder converts an input vector $\mathbf{p} = (p_1, \dots, p_m)$

(TensorFlow uses row vectors) to a code vector $\mathbf{h} = (h_1, \dots, h_n)$, where $n < m$. The decoder recovers the code to a output vector attempting to approach the input. Thus, an autoencoder tries to learn an identical operation for a given train set. The original parameter vectors with m components can be compressed into a code vector with n dimension. The vectors optimization in a code space can also be transformed back to the parameter space by the decoder's inverse operation.

Although the encoder converts the vectors from a high dimension to a low dimension, several inflated hidden layers are necessary. This is because the manifold consists of data points which may contain a complicated geometry structure, like knot. According to the weak Whitney embedding theorem, any two embeddings of an n -dimensional manifold into a \mathbb{R}^{2n+2} space are isotopic, which means two n -dimensional manifolds could be smoothly transformed into each other in a \mathbb{R}^{2n+2} space. Thus, a manifold with a knot structure could be unknotting in a high-dimensional space, then the encoding process could be done based on the unknotting manifold which is easier to handle.

Ideally, if two original vectors are close in the original space, then the expected code vectors should also be close in the code space, which requires the derivative of the code (\mathbf{h}) with respect to the original vectors (\mathbf{p}) should not be large. This guarantees the code will not drastically vary with a small change in the original vector. The same measure should also be implemented on the transformation process from a code to the recovered vector.

Such derivatives could be represent by two Jacobian matrices for the encoder ($\mathbf{J}^{(\text{en})}$) and the decoder ($\mathbf{J}_{(\text{de})}$), which are able be calculated based on the weights, bias, and the activation functions of the neural network.

For instance, an autoencoder have two hidden layers between the input (\mathbf{p}) and the code (\mathbf{h}), \mathbf{W}_1 and \mathbf{b}_1 are the weights and the bias of the first hidden layer respectively, and the original result \mathbf{Z}_1 are activated by the function ϕ and passed to the second layer. This processes were repeated multiple times until the code is given, and followed the recovered vector ($\tilde{\mathbf{p}}$).

$$\mathbf{Z}_1 = \mathbf{p}\mathbf{W}_1 + \mathbf{b}_1 \quad (3.13)$$

$$\mathbf{Z}_2 = \phi(\mathbf{Z}_1)\mathbf{W}_2 + \mathbf{b}_2 \quad (3.14)$$

$$\mathbf{h} = \phi(\mathbf{Z}_2)\mathbf{W}_3 + \mathbf{b}_3 \quad (3.15)$$

$$\mathbf{Z}_4 = \mathbf{h}\mathbf{W}_4 + \mathbf{b}_4 \quad (3.16)$$

$$\mathbf{Z}_5 = \phi(\mathbf{Z}_4)\mathbf{W}_5 + \mathbf{b}_5 \quad (3.17)$$

$$\tilde{\mathbf{p}} = \phi(\mathbf{Z}_5)\mathbf{W}_6 + \mathbf{b}_6 \quad (3.18)$$

Then, the Jacobian matrices of the encoder and the decoder can be obtained ac-

cording to the chain rule,

$$\mathbf{J}^{(\text{en})}(\mathbf{p}) = \frac{\partial \mathbf{h}}{\partial \mathbf{p}} = \frac{\partial \mathbf{Z}_2}{\partial \mathbf{p}} \frac{\partial \phi(\mathbf{Z}_2)}{\partial \mathbf{Z}_2} \mathbf{W}_3 = \mathbf{W}_1 \frac{\partial \phi(\mathbf{Z}_1)}{\partial \mathbf{Z}_1} \mathbf{W}_2 \frac{\partial \phi(\mathbf{Z}_2)}{\partial \mathbf{Z}_2} \mathbf{W}_3, \quad (3.19)$$

$$\mathbf{J}^{(\text{de})}(\mathbf{h}) = \frac{\partial \tilde{\mathbf{p}}}{\partial \mathbf{h}} = \frac{\partial \mathbf{Z}_5}{\partial \mathbf{h}} \frac{\partial \phi(\mathbf{Z}_5)}{\partial \mathbf{Z}_5} \mathbf{W}_6 = \mathbf{W}_4 \frac{\partial \phi(\mathbf{Z}_4)}{\partial \mathbf{Z}_4} \mathbf{W}_5 \frac{\partial \phi(\mathbf{Z}_5)}{\partial \mathbf{Z}_5} \mathbf{W}_6. \quad (3.20)$$

Finally, a scalar Jacobian term, the Frobenius norm of the Jacobian matrices, can be calculated by the sum over the square of the matrix elements,

$$\|\mathbf{J}^{(\text{en})}(\mathbf{p})\|_F^2 = \sum_{ij} \left(J_{ij}^{(\text{en})}(\mathbf{p}) \right)^2 = \sum_{ij} \left(\frac{\partial h_j(\mathbf{p})}{\partial p_i} \right)^2, \quad (3.21)$$

$$\|\mathbf{J}^{(\text{de})}(\mathbf{h})\|_F^2 = \sum_{i'j'} \left(J_{i'j'}^{(\text{de})}(\mathbf{h}) \right)^2 = \sum_{i'j'} \left(\frac{\partial \tilde{p}_{j'}(\mathbf{h})}{\partial h_{i'}} \right)^2. \quad (3.22)$$

In principle, the Jacobian term could be easily implemented for all differentiable (C^1) activation functions. But if the derivative of an activation function could be written into a finite polynomial form of the original function, calculation time could be saved, thus it is practical for rectified linear unit (ReLU), exponential linear unit (ELU), sigmoid, tanh functions,

$$\begin{aligned} \phi_{\text{ReLU}}(Z) &= \begin{cases} 0, & Z \leq 0 \\ Z, & Z > 0 \end{cases} \quad ; \quad \frac{\partial \phi_{\text{ReLU}}(Z)}{\partial Z} = \begin{cases} 0, & Z \leq 0 \\ 1, & Z > 0 \end{cases}, \\ \phi_{\text{ELU}}(Z) &= \begin{cases} e^Z - 1, & Z \leq 0 \\ Z, & Z > 0 \end{cases} \quad ; \quad \frac{\partial \phi_{\text{ELU}}(Z)}{\partial Z} = \begin{cases} \phi(Z) + 1, & Z \leq 0 \\ 1, & Z > 0 \end{cases}, \\ \phi_{\text{sigmoid}}(Z) &= \frac{1}{1 + e^{-Z}} \quad ; \quad \frac{\partial \phi_{\text{sigmoid}}(Z)}{\partial Z} = \phi(Z)(1 - \phi(Z)), \\ \phi_{\text{tanh}}(Z) &= \frac{e^Z - e^{-Z}}{e^Z + e^{-Z}} \quad ; \quad \frac{\partial \phi_{\text{tanh}}(Z)}{\partial Z} = 1 - \phi^2(Z). \end{aligned}$$

If a Jacobian term is added to the loss function with a used for optimizing the model, then such an autoencoder is called contractive autoencoder (CAE) [88]. It has a good property with resistance to noise from data.

$$\text{loss} = \|\mathbf{p} - \tilde{\mathbf{p}}\|^2 + \lambda \left(\|\mathbf{J}^{(\text{en})}(\mathbf{p})\|_F^2 + \|\mathbf{J}^{(\text{de})}(\mathbf{h})\|_F^2 \right) \quad (3.23)$$

To verify the effect of the Jacobian term, a test data set was made by an Archimedean spiral $\{(\rho, \theta) | \rho = \theta; \theta \in [0, 4\pi]\}$. The CAEs with the various Jacobian λ values are trained for twenty copies, with results shown in Figure 3.13. If the selected λ is too high (from 10^2 to 10^{-3}), the autoencoder lacks flexibility, and if it's too low (from 10^{-8} to 10^{-9}), then it is not able to constrain the weights of the model. By taking a suitable λ (from 10^{-4} to 10^{-7}), the Jacobian can improve the accuracy of the fitting.

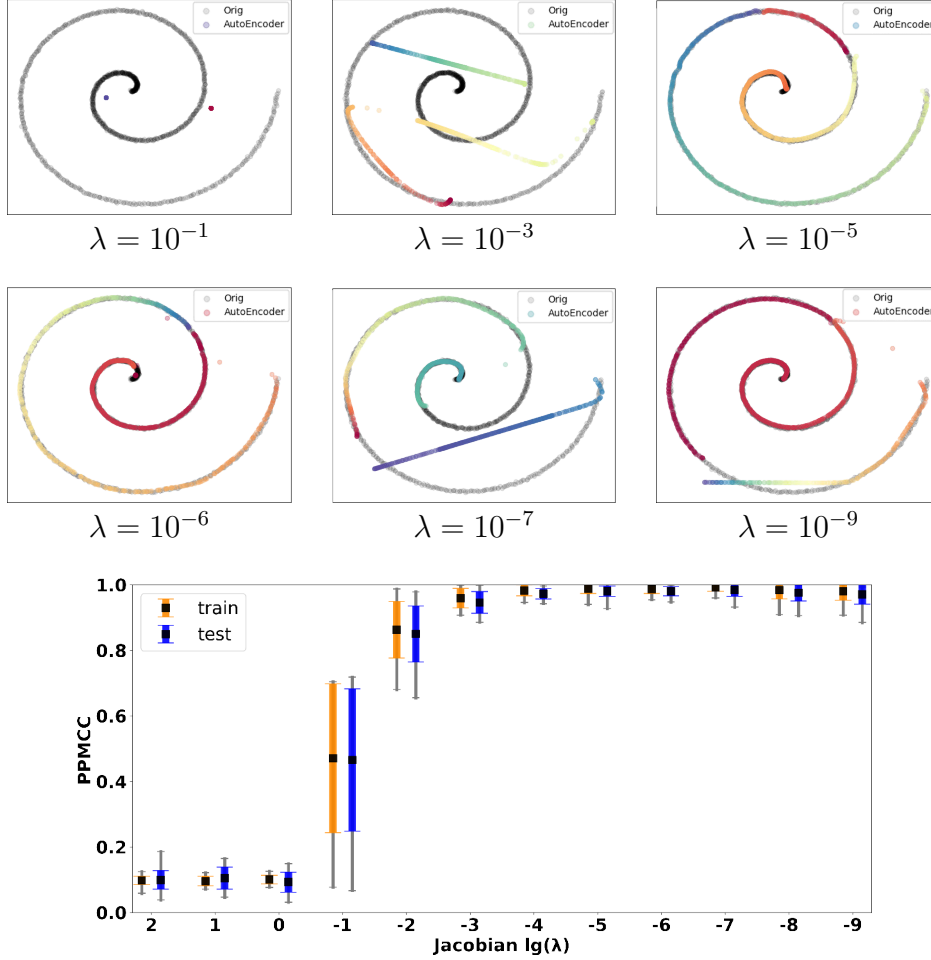


Figure 3.13.: The comparison between the actual data points (gray) and the fitting points colored by the code value based on the autoencoder. The λ of the Jacobian term is , 10^{-1} (top left), 10^{-3} (top center), 10^{-5} (top right) in the first row, 10^{-6} (middle left), 10^{-7} (middle center), 10^{-9} (middle right) in the second row. Twenty duplicates were calculated for each condition and the accuracy of the models evaluated by PPMCC are shown in the lower right corner part. The black square in the center represents the mean, the bar represents the standard deviation (bottom), and the thin grey line represents the maximum and minimum values.

3.4.2. Limitations

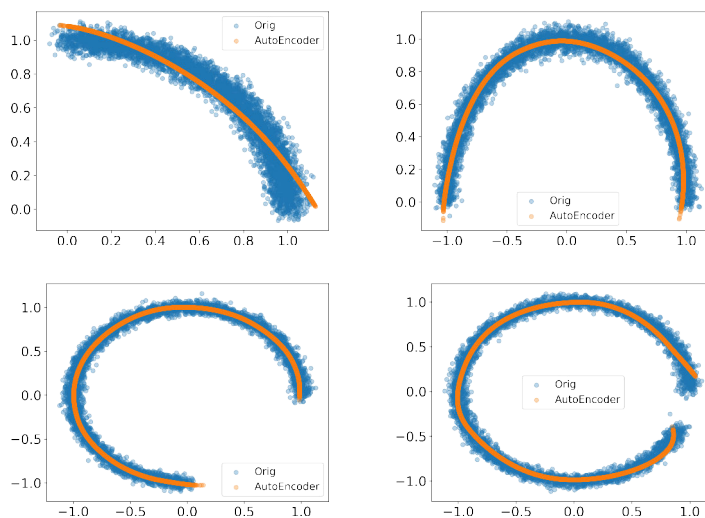


Figure 3.14.: The comparison between the actual data points (blue) and the fitting points by the autoencoder (orange) for arcs with 90 (top left), 180 (top right), 270 (bottom left), 337 (bottom right) degree's central angle.

The working mechanism of an autoencoder is relatively natural. For a data set with a simple, continuous, non-closed shape, like an arc of a circle, it could perform well (Figure 3.14). But for some complex shapes, it may encounter problems (Figure 3.15). The usually used activation function is continuous, thus, due to the natural of a neural network, it could only approach a continuous function. Therefore, the autoencoder tried to cover the two separate arcs with a continuous curve which leads to artefact points between the two arcs. It works similarly for a bifurcation shape: the autoencoder fitted one of the branches and drastically turned over to cover the rest. Of course, the situation here is mathematically different, because the shape could not be treated as a manifold and the dimension of the divergence point cannot be defined. Strictly speaking, it has a fractal structure, so the dimension is not an integer.

For a closed graph, like a circle, the start and end points are identical. On the one hand, the distance between the two points is zero, and they should have the same code. On the other hand, the two codes should be very different since the pathway between two points goes around a full loop. By introducing the periodicity into the encoder, such a problem could be partially solved. However, it introduces a new problem that such functions are not reversible, and could not be represented by the decoder. Such problems could also be solved by splitting the data set into two non-closed parts and trained by two autoencoders.

A common difficulty in high-dimensional spaces is, that it is hard to define a distance

between two points. The distance between two points on a manifold is actually the geodesic between them, rather than the Euclidean distance in the space of embeddings of the manifold. Normally, the distance between two places is the length of an arc on the Earth's sphere rather than a straight line through the Earth's crust. The Archimedean spiral is isomorphic to a line (\mathbb{R}), thus it should easily be encoded and decoded, however the results generated by an autoencoder are often not ideal. The main reason is that the loss function (*e.g.*, MSE) is defined by the Euclidean distance, so points that should be far apart in the code space are close together in the original space. It can confuse the model and make it difficult to train it effectively.

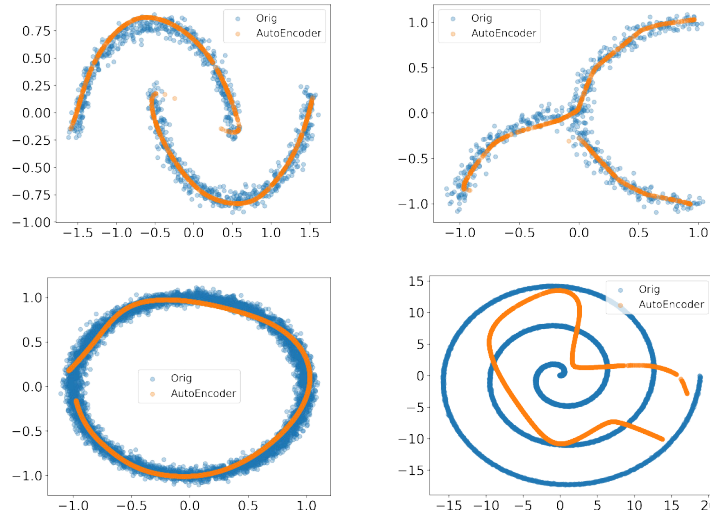


Figure 3.15.: The comparison between the actual data points (blue) and the fitting points by the autoencoder (orange) for the double arcs (top left), the bifurcation shape (top right), the full circle (bottom left), and the Archimedean spiral (bottom right).

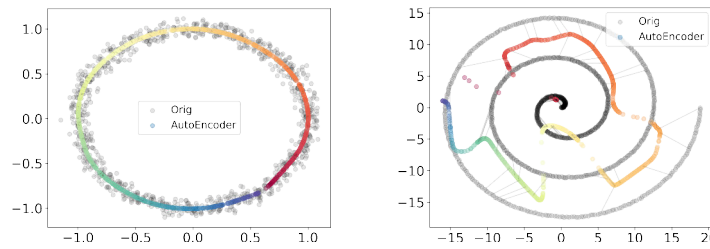


Figure 3.16.: The fitting points colored by the code value based on autoencoders for the full circle (left) and the the Archimedean spiral (right). The gray thin lines link the original sample points and the corresponding fitting points by the autoencoders.

3.4.3. Locally linear embedding (LLE)

The Euclidean distance is trivial to calculate, but the calculation of the geodesic requires the knowledge of the geometrical information of the manifold. However, in the neighborhood of a point, the geometry should be flat, thus the Euclidean distance could be used in a small area.

Locally linear embedding (LLE) is also a dimension reduction method [89], which seeks a projection of the data points to a lower-dimensional space preserving distances within their local neighborhoods. Thus, the distance between the points should remain the same before and after the transition. It could provide a relatively good initial guess for the code vector (\mathbf{h}).

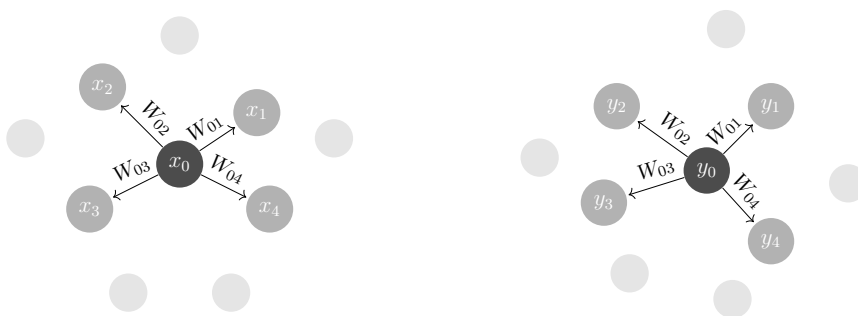


Figure 3.17.: A schematic of the local linear embedding method.

Since this method trying to preserve the pairwise distances in a local area, the selection of the number of the neighbors is crucial. If it is too small, a continuous manifold could be divided into disjoint sub-manifolds falsely, and some global geometrical information could be lost. If it is too large, a large number of the neighbors causes smoothing or elimination of small-scale structures in the manifold, the resulting manifold loses the nonlinear character, and LLE behaves like conventional PCA [90].

As verification, the LLE method with different number of neighbors were applied for the Archimedean spiral data set, and the resulting codes were used as initial guesses for the CAEs for training. As shown in Figure 3.18, if the chosen number of neighbors is low (*i.e.*, 4), the code values are not continuous along the spiral, which indicates the points in code space are disjoint. Consequently, the CAE gave a bad result. If the chosen number of neighbors is appropriate (*i.e.*, 8, 16, 32, 64), the code values are monotonic along the spiral, and the CAEs could improve the results to make the code values more evenly distributed on the spiral. If the chosen number of neighbors is too high (*i.e.*, 128), points that are not close to each other are forced to be together, resulting in similar code values, and the CAE partially improves the

result but did not completely correct the false of the initial guess. In short, CAE could improve results quantitatively, but it is not able to correct qualitative errors, so a qualitatively correct initial guess is essential.

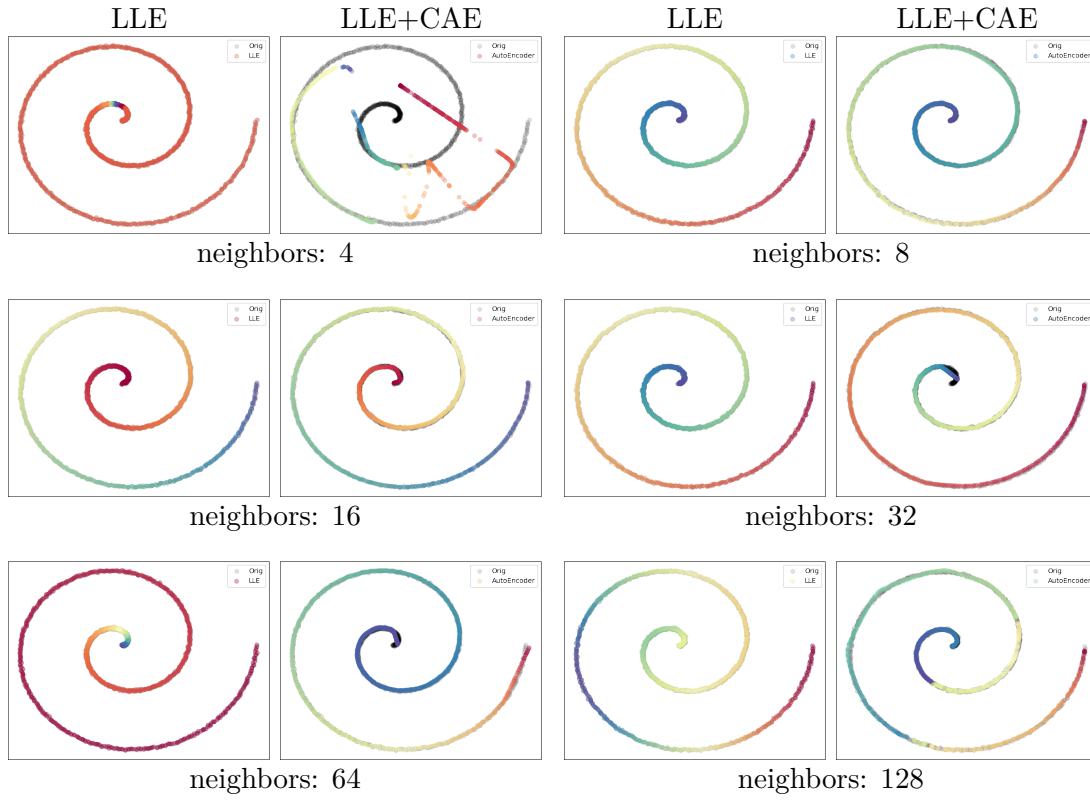


Figure 3.18.: The points colored by the code value based on the LLE method with different number of neighbors and the followed autoencoders for the Archimedean spiral.

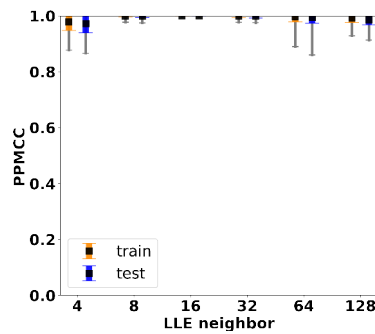


Figure 3.19.: For the Archimedean spiral, twenty duplicates were calculated under a various numbers of neighbors and the accuracy of the models evaluated by PPMCC. The black square in the center represents the mean, the bar represents the standard deviation and the thin grey line represents the maximum and minimum.

In order to verify this method in a real system, the sample set with 100000 data points of the C_{20} system was used for training of the CAE. The parameter vectors have 44 components, in the case of code vectors with 22, the encoder consists of the 11 hidden layers with the dimension 66, 99, 148, 176, 176, 176, 117, 78, 52, 34, 23, and the decoder is symmetric with the encoder.

Because the initial weights and biases of neural networks are randomly generated, they may converge to different local minima during the optimization process. Therefore, it is necessary to construct multiple copies for a same condition to test the reliability. As above, the initial code guesses were given by LLE, and the set number of the neighbors could affect the accuracy of the final trained CAE. In Figure 3.20, when the number of neighbors is not enough (*i.e.*, 10, 20), the accuracy and the deviations between the different CAE copies are unsatisfactory. As the set number of neighbors is higher than 40, both the two properties improve significantly, which means the initial code guesses are accepted by most of the copies. When the code dimension is above 35, the fidelity of the coding and decoding process is reliable, thus the parameter vectors contain redundant information that could be compressed. On the other hand, the CAEs trained without initial guesses showed more deviations between the copies, and it also reflects the effectiveness of LLE (Figure 3.21).

In principle, the manifold structure contained of the benign parameter vectors should be more clear by removing the other data points with higher score. Thus, the CAEs should show higher accuracy with lower upper boundary of score (smaller truncation ratio), which could be observed in the Figure 3.22. However, the smaller truncation ratio also reduces the sample data points, it will leads higher variance and uncertainty, thus the deviations and the inaccuracy of the test set are higher.

It's worth to note that not all components behave the same, for example, as shown in Figure B.10, the values of a component distribute in a relatively wide range. A wider sample distribution allows the CAE to learn more general situations, thus the deviations and accuracy of test are better. However, it also results in the CAE that does not have good predictability over all ranges of values. Such a sparse distribution may be due to the nature of the component itself, or to strong coupling with other components. In either case, more sampling for this component is required to increase the accuracy of the CAE.

For the concentrated distribution case in Figure B.11, values are clustered within a small range, thus the CAE performs well in that range. But it lacks predictive power for uncovered areas, as shown as a large deviation of the test set. The sampling for this type of components could be less because it showed signs of convergence.

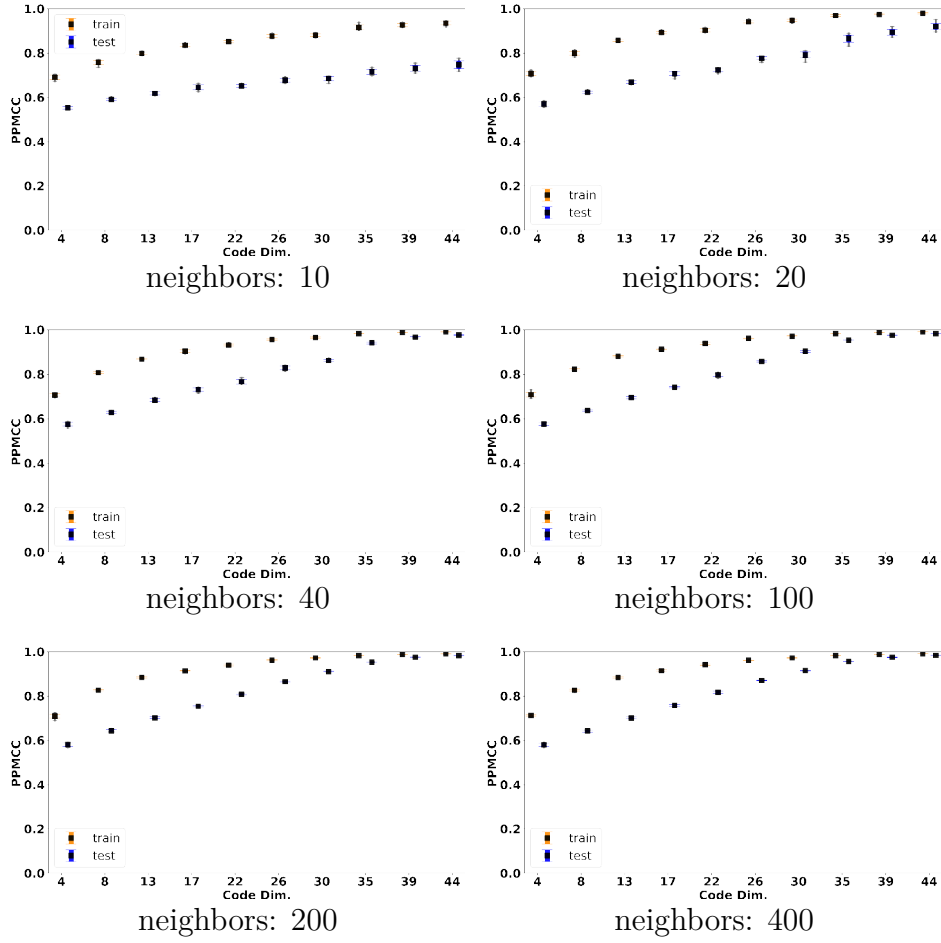


Figure 3.20.: For the C_{20} system, the accuracy of the CAEs with the different code dimensions evaluated by PPMCC were based on ten duplicates. The initial code vectors were generated by the LLE methods with the different neighbor number. The black square in the center represents the mean, the bar represents the standard deviation and the thin grey line represents the maximum and minimum values.

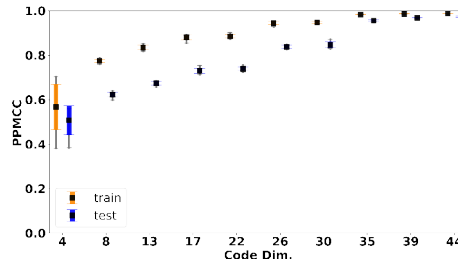


Figure 3.21.: For the C_{20} system, the accuracy of the CAEs with the different code dimensions evaluated by PPMCC were based on ten duplicates without initial code guesses. The black square in the center represents the mean, the bar represents the standard deviation and the thin grey line represents the maximum and minimum values.

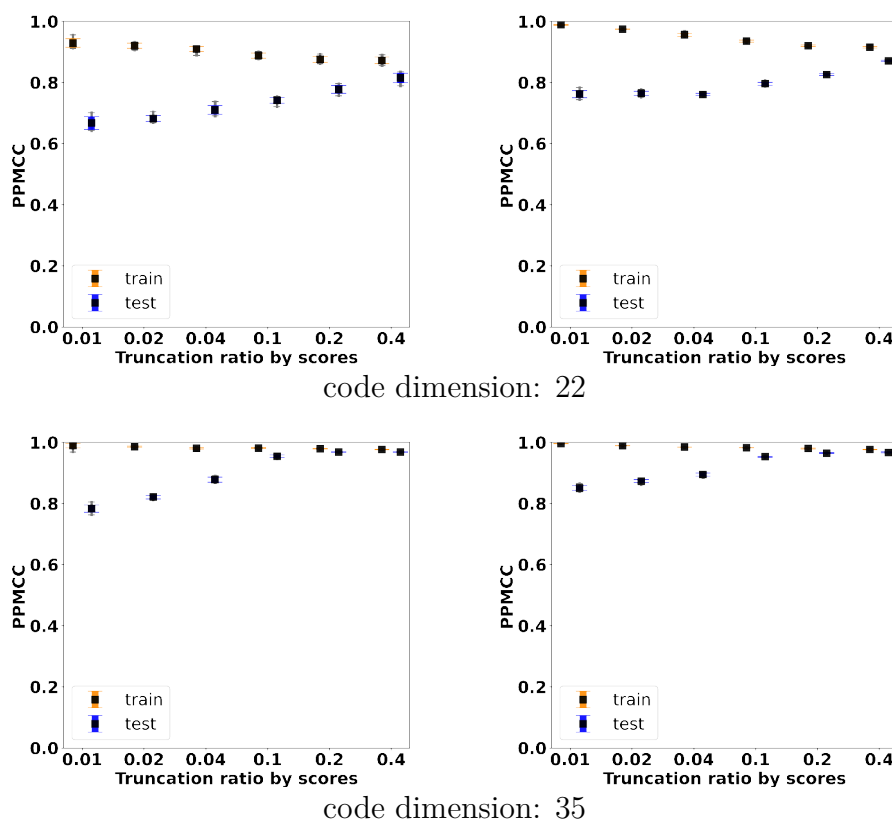


Figure 3.22.: For the C_{20} system, the accuracy of the CAEs evaluated by PPMCC were based on the ten duplicates without initial guesses (the left column) and with the initial code vectors given by the LLE methods (the right column). The sample data sets were truncated by scores with various ratios. The black square in the center represents the mean, the bar represents the standard deviation, and the thin grey line represents the maximum and minimum values.

3.5. Components segmentation

For the simple example above, the parameter vectors for the C_{20} system contains 44 components. For a complicated 4,4'-bis(thiol)benzil system which consists of C, H, S, O (Figure B.12), the number of components increases to 906. In principle, the above method is still valid, but it will be very inefficient to mutate and selected over all components. The components could be segmented into several groups with a suitable scheme and optimized by batches, where the components within a group should be optimized simultaneously. The `CorreComptSegOpt` module provides the functions for the segmenting.

First, we assume that the behavior of the score function of one component of \mathbf{p} is not qualitatively affected when other components are changed. Thus, the score along the component could be scanned. As shown in Figure 3.23, the score along

a single component has several behaviors. For an optimization process, if a component always behaves constant, linear, monotonic nonlinear, or convex, then the solution is trivial (the boundaries of the component). But that doesn't mean those components do not need to be optimized, as the behavior of the functions of these components may also change when the other components change a lot and deviate from the original point. Therefore, those values need to be checked when the other components are optimized. So far, only the components with at least one local minimum need to be considered. The components with jagged curves are special cases of the components with a local minimum, which the curve is oscillating within the scanned interval and is hard to be fitted by a polynomial. Such components need to be handled with care, thus they will be optimized individually.

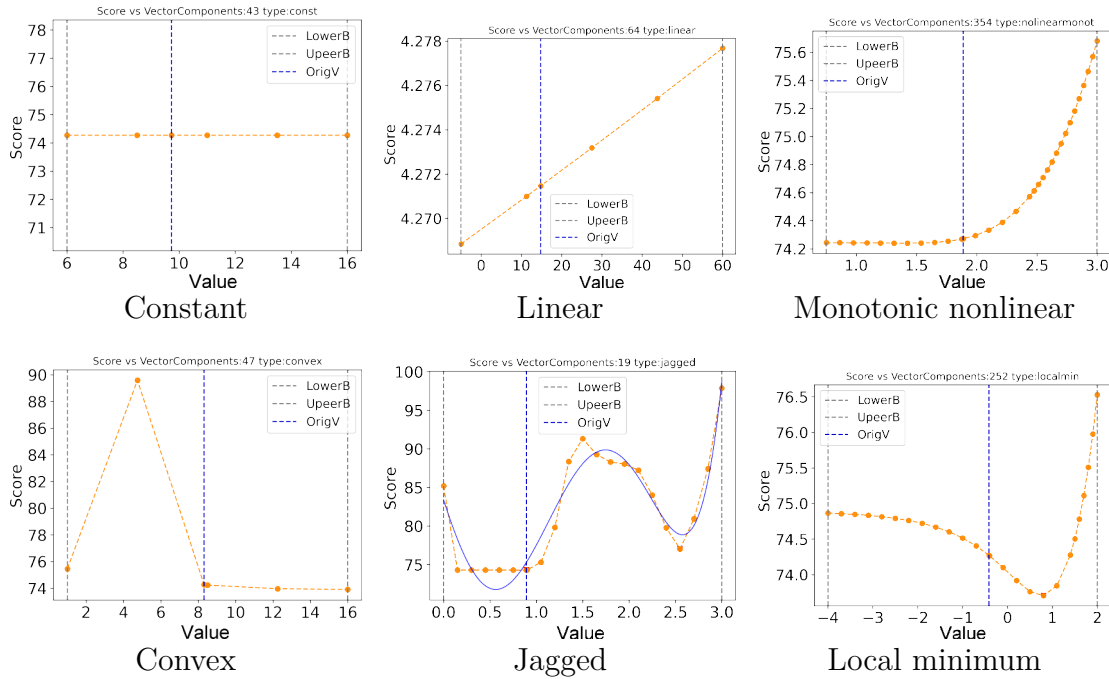


Figure 3.23.: Some possible curves of the score function S along a parameter vector component $\mathbf{p}^{(A)}$.

For those components with a local minimum, in principle, the correlation between any two of components needs to be checked. If two components are strongly coupled, then they need to be optimized simultaneously. As an example shown in Figure 3.24, when the component $\mathbf{p}^{(A)}$ changes a little in the vicinity of the original value, the corresponding changing of the score function with respect to the component $\mathbf{p}^{(B)}$ could be constant, mild or drastic. If the change is a constant, than obviously the change in $\mathbf{p}^{(A)}$ does not affect the score function behavior along the component $\mathbf{p}^{(B)}$. Otherwise, the difference of the two function, $\Delta S(\mathbf{p}^{(A)}; \mathbf{p}^{(B)}) = S(\mathbf{p}^{(A)} + \Delta \mathbf{p}^{(A)}; \mathbf{p}^{(B)}) - S(\mathbf{p}^{(A)} - \Delta \mathbf{p}^{(A)}; \mathbf{p}^{(B)})$, will be fitted by

a polynomial. If the amplitude of ΔS is larger than the set threshold and it could not be well fitted by a polynomial (as an example shown in Figure B.13), this means the component $\mathbf{p}^{(B)}$ is sensitive to the component $\mathbf{p}^{(A)}$. It should be noted that if $\mathbf{p}^{(B)}$ is sensitive to $\mathbf{p}^{(A)}$, $\mathbf{p}^{(A)}$ is not inevitably sensitive to $\mathbf{p}^{(B)}$, thus such relation has a direction.

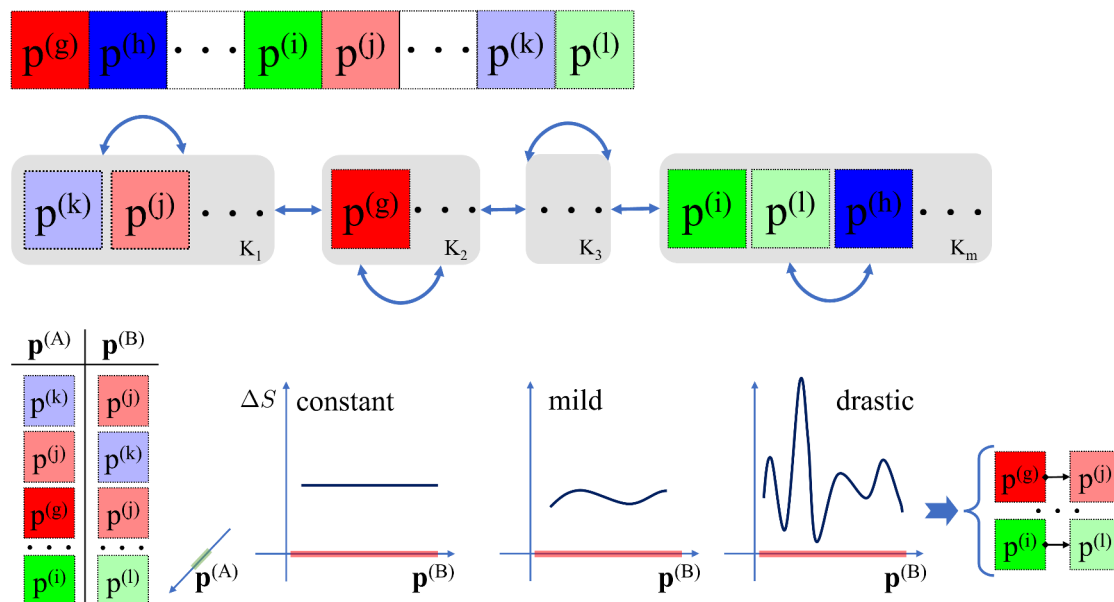


Figure 3.24.: Components with a local minimum are selected (top). These components are sorted and grouped (K) according to their influence on the score, and correlations between components will be only estimated within the same group or neighboring groups by a ΔS function (middle). $\Delta S(\mathbf{p}^{(A)}; \mathbf{p}^{(B)})$ is the differences of the score function along the component $\mathbf{p}^{(B)}$ when the component $\mathbf{p}^{(A)}$ is slightly changed. It could behave like a constant, mild, or drastic change (bottom). In a drastic changing case, the position of the local minimum of $\mathbf{p}^{(B)}$ could be changed, then $\mathbf{p}^{(B)}$ is sensitive to a tiny variation of $\mathbf{p}^{(A)}$, like $\mathbf{p}^{(j)}$ is sensitive to $\mathbf{p}^{(g)}$ and $\mathbf{p}^{(l)}$ is sensitive to $\mathbf{p}^{(i)}$. Moreover, such sensitivity (correlation) is directional, which forms a correlation pair (e.g., $\mathbf{p}^{(i)} \rightarrow \mathbf{p}^{(l)}$).

For a 4,4'-bis(thiol)benzil system, there are 91 components with a local minimum, then there will be 8281 pairs for checking, and for each pair at least 10 data points need to be calculated. The complexity of the task is proportional to the square of the number of components, and it must be reduced. Here, the components are assigned into several groups according to the scores' sensitivity, which is evaluated from the difference between the maximum and the minimum score values along a component with keeping the others fixed. The components are sorted according to their scores sensitivities, and segmented into the groups. The default setting is to have 32 elements per group. Only the intra-group components and the nearest

inter-group components will be checked (Figure 3.24, middle). Then, the complexity of the task is linear with the number of components. For the CHSO case, that will be 4665 pairs.

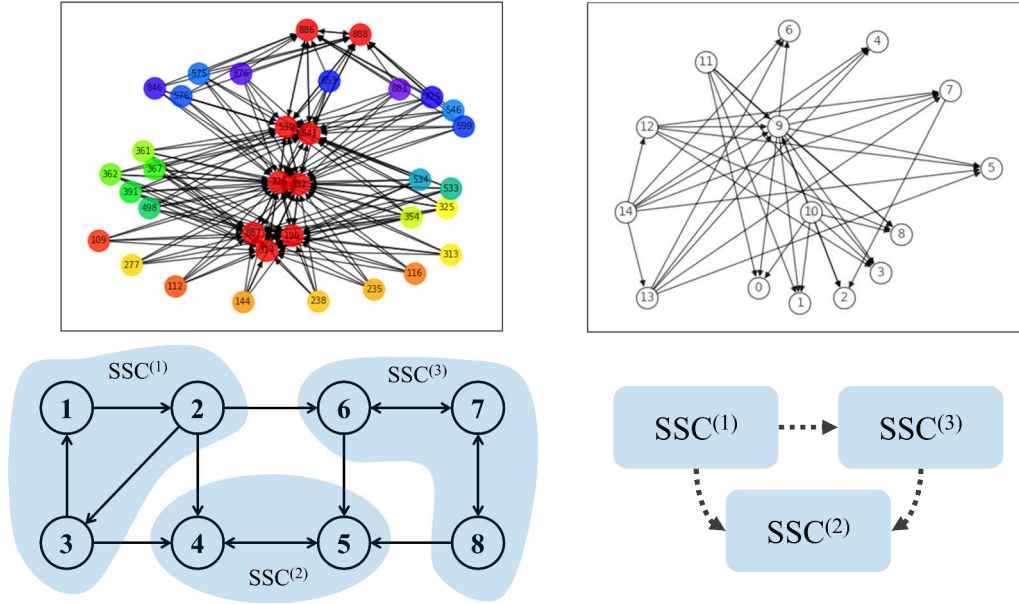


Figure 3.25.: According to the obtained set of the correlation pairs, a directed graph of components can be drawn (top left), where the vertices are colored by the affiliation of strongly connected component (SCC). The corresponding directed acyclic graph of the SCCs (top right). A schematic diagram of a directed graph (bottom left), the (SCCs) are highlighted in blue. The corresponding condensation of the graph (bottom right) is a directed acyclic graph, in which all nodes in the same SCC are represented by one node, and the connection between SCCs do not form a loop.

If the components with a local minimum as the vertices are linked by the arrows according to the sensitivity relation, a directed graph could be obtained. A directed graph is able to be decomposed into several subgraphs called strongly connected components (SCCs) (Figure 3.25). In an SCC, starting from any vertex one is able to end up on another vertex, and a path exists between any two points. In principle, the parameter components belonging to the same SCC need to be optimized simultaneously, because a tiny change in one component leads to a change in the behavior of the score functions along with the other component; they are strongly coupled. If the number of parameter components in the SCC is unacceptably large, then the SCC subgraphs could be converted to an undirected graph, and parts the new graph into two blocks using the bisection algorithm, like the Kernighan–Lin algorithm [91]. Then the optimization could be processed with a required number of components for each batch.

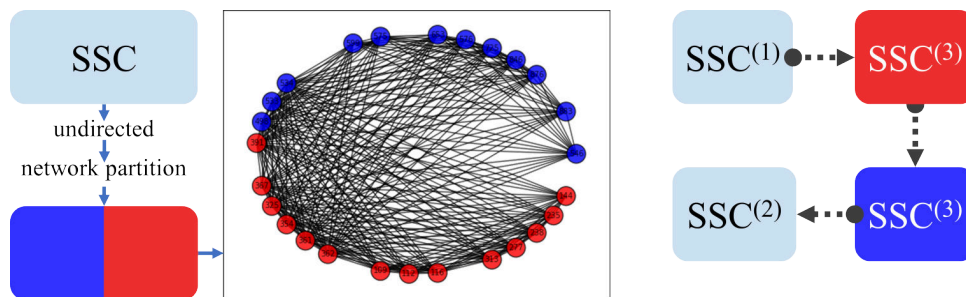


Figure 3.26.: If the number of components in a SCC exceeds the limit of a single batch for an optimization process. The subgraph of the SCC can be converted to an undirected graph, and then the resulting graph can be bisected (left). The sequence of batches for optimization can determined (right) according to the directed acyclic graph of SCCs.

In the process of the condensation of the original graph, each SCC is contracted to a single vertex (SCC node), and the resulting graph is a directed acyclic graph (DAG). In DAG, the possible path will never form a closed loop, thus a sequence for optimizing SCCs could be given. Generally, one of the source nodes could be assigned as the starting point and try to traverse other SCC nodes. When there are multiple branches, to determine the next node, the connection degree between the two SCCs in the original directed graph could be used as the weight in the DAG. More connection degrees means a possible higher correlation between inter-node parameter components. Then, the process is repeated by starting from another source node until all SCC nodes are included in the optimization sequence. Since the optimization sequence for each SCC is know, the sequence of the optimization batches for the parameter components with a local minimum are given.

After the optimization batches built above have been done, the jagged components could be optimized individually. The newly obtained vectors could deviate significantly from the original values at the beginning, so it is necessary to inspect the behavior of each component and the correlations between any two of them again, and making the process iterative until the parameter converge.

For the optimization process, the above machine-learning-assisted genetic algorithm can be used, or a gradient descent method. In particular, if the coupling between the components is not very strong, thus in any case the score function has only one local minimum along a component, then the function has a simple convex geometric structure in the space spanned by these components, and the gradient descent should be converged very fast.

It is worth noting that, if a complex system contains various subsystems, the above analysis needs to be carried out on each subsystem separately. Otherwise, if only

evaluated by the total score, then nearly all components will be coupled together. For example, for a subsystem describing the length of C-H bond, the parameter components for carbon and for hydrogen should be coupled. By a same reason, the components for oxygen and for hydrogen should be coupled by a subsystem consisting of the MD snapshots of a water molecule. If the score are generated by the two subsystems, the parameter components for carbon and oxygen will also be coupled.

3.6. Conclusion and outlook

In this chapter, we introduce the reparameterization tool for ReaxFF, REAXFF-FITTING. The module has an interface for generating and reading input and output files for molecular dynamics and quantum chemistry softwares. The scores of the given subsystem could be calculated for the different parameters, and could further be optimized.

The optimization process is executed by the machine-learning-assisted genetic algorithms, the parameters are generated and selected by the genetic algorithm, and the machine learning model tries to learn the score function with respect to the parameters, which could be used for the grid searching. Although the acceptance of the parameters predicted by the model is not ideal yet for the tested example C₂₀, such model learning and the grid searching processes only consume a short time, approximately one tenth of the actual data set calculation. With an improvement, the process could be achieved asynchronously. This method seems to be suitable to generate a small number of data points in each optimization cycle with many times of iterations. Even in the worst case, the genetic algorithm itself can guarantee the effectiveness of the optimization process. Thus, a good result were achieved on this small test system.

In addition, we have explored other methods of optimization. With the help of the initial code guesses by LLE, CAE had a more stable and accurate performance in terms of dimension reduction. For the C₂₀ system, the code with 35 dimension is able to represent the original 44 dimension parameter vector. For larger systems this value would be better due to more redundancy.

We also explored the method to segment the components according to their behavior on the score function and the correlations between any two of them. It should provide greater simplicity for complex systems. However, the efficiency and stability of the method needs more testing.

In summary, to segment the parameter components by a rational approach and

optimizing them in batches, to speed up the optimization process through machine learning is a promising solution for global optimization of a high-dimensional space. This needs to be achieved by further improving the accuracy of machine learning models especially for small data sets.

4. Theoretical insights into the interactions between nitroxide radicals and interfaces

4.1. TEMPO radicals on gold surfaces

4.1.1. Introduction

Electronic devices incorporating single molecules offer unique possibilities to implement new functionalities based on the spin degree of freedom. This approach represents a new paradigm to perform computations and offer a solution to the problem of heat dissipation in current electronic devices [92]. The unpaired electron on organic radical molecules provides a degree of freedom to register, store, and process information, which is an essential research part of spintronics [93–103]. As an example, the Scheer group posed single (2,2,6,6-tetramethylpiperidin-1-yl)oxidanyl-oligo-(p-phenyleneethynylene) (TEMPO–OPE)-based radical molecular junctions (Figure 4.1, right), which are fabricated with a mechanically controllable break junction (MCBJ) method [21]. The electron transport of the junctions was studied with a presence of magnetic fields. Positive magnetoresistances (MRs) of up to 287% were observed for a 4 T magnetic field, which is significantly large compared with junctions formed with the analogous pristine OPE (up to 4%). Such surprisingly large MRs were not expected by a conventional spin-dependent-transport calculation [35], since the frontier orbital of the TEMPO functional group is away from the Fermi level.

TEMPO–OPE molecules have intended bonding with gold electrodes through their thiol groups. A major challenge when engineering such devices is to ensure that the open-shell character of the molecule is preserved. However, the interactions between the radical groups with the surface are often neglected compared with other strong chemical bonding groups, which may delocalize spin on molecules [104]. In some recent reports [105–107], various experimental methods were used to verify the

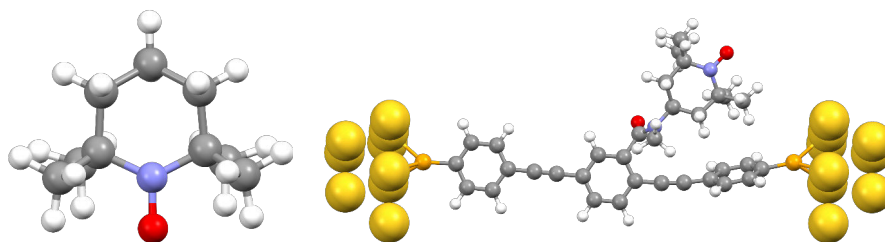


Figure 4.1.: The ball-and-stick models of the TEMPO molecule (left) and a TEMPO–OPE molecule anchoring on two gold electrodes by its thiol groups (right). The color mappings of atoms, carbon (gray); hydrogen (white); nitrogen (pale violet); oxygen (red); sulfur (orange); gold (yellow).

binding between gold nanoparticles (AuNPs) and nitroxyl radicals, but the results were in parts inconsistent.

As a representative of nitroxyl radicals, (2,2,6,6-tetramethylpiperidin-1-yl)oxidanyl (TEMPO) is one of the most commonly used in experiments (Figure 4.1, left). It could be used as a catalyst for the oxidation reaction in organic synthesis, as a structural probe for biological systems, *etc.* [108–111]. TEMPO is widely used in many studies, because it is easy to synthesize, provides a good thermal stability, and can be purified by a sublimation process. Further, it can be chemically modified and grafted onto other organic backbones to introduce free-radical characteristics.

Surface-suppressed electron resonance experiments made by the Freed group found that the noble metal surface was able to quench the EPR signal of nitroxyl radicals [104], including the TEMPO derivatives and di-*tert.*-butylaminyloxid (DTBN). As the paper suggested, for radicals directly contacting with the bare metal surface of the silver EPR cavity under high vacuum condition, the EPR signal from those deposited radicals was extremely broadened by the conduction electrons on the surface. The subsequent radicals were stacked on the previous layers and were well isolated from the surface, and then the EPR signals could be observed from the radicals away from the metal surface. Therefore, the EPR signals exhibited a hysteresis stage (covering bare metal surface) versus the dosage of radical, and the intensity-dosage relation was highly dependent on the molecular size. The N_{1s} X-ray photoelectron spectroscopy (XPS) data of the TEMPO derivative on a Ag surface found a shifted peak at 402.2 eV (original NO: 399.2 eV), which was assigned to the NO-Ag interaction [112]. The real-space topographic images of surface provided pictorial evidences. The coated gold nanoparticles (AuNPs) were well adsorbed on a gold surface only if the length of TEMPO chains is competitive with alkane chains. The AuNPs were co-coated by the anchoring thiol functionalized TEMPO chains and alkane chains on the single terminal, thus the interaction between AuNPs and

surface was limited to TEMPO–surface and alkane-surface. The surface IR spectrum found a peak at 280 cm^{-1} which was assigned to a Au-O-N vibration [113]. Some liquid phase experiments also proved the strong interaction between the TEMPO derivatives with AuNPs with the help of EPR and fluorescence spectroscopy [106].

TEM and calorimetry studies of citric acid stabilized AuNPs with the TEMPO derivatives suggested that the interaction between AuNPs and those radicals mainly arises from other groups (*e.g.*, carboxylate, amino) rather than the nitroxyl part [107]. But in both of the experiments, the competition between stabilizer and the derivatives cannot be avoided. It might be linked to the diverse stabilizers (*e.g.*, citric acid, polyamidoamine, *etc.*) which were used for coating and which compete with radicals, making the scenario of interaction complicated.

The interaction of radical groups with the interfaces is quite often disregarded in theoretical studies, this chapter aims to fill this gap. To understand the possible interaction between nitroxyl radicals with a metal surface, as the most commonly used combination of the metal substrate and the radical, the systems consisted of gold and TEMPO were built and explored by density functional theory (DFT). First of all, the reliability of the DFT functional was verified in the aspect of the bond strength. Then, TEMPO and the various anchoring groups were placed on different gold surfaces, and different binding scenarios were studied based on optimized structures. Finally, the clusters were cut out of the gold surfaces for the optimized molecule–surface systems, and wavefunction analysis was performed for each selected cluster. Due to fact that, as a functional group, TEMPO group is linked with many types of backbone molecule in many experiments, to mimic the electronic structure and the steric hindrance effect, in the following calculation an additional methyl group was added on the *para* position of the TEMPO molecule. So the actual molecule is (2,2,4,6,6-pentamethylpiperidin-1-yl)oxidanyl, and we still abbreviated it to TEMPO as convention.

4.1.2. Verifying the reliability of the exchange–correlation functional

A limitation of DFT, a certain exchange–correlation functional was optimized for a test set, the extensibility being unknown. For instance, the electrons near the Fermi level in metal systems do not feel too much attraction from the nucleus, and they behave like a free electron gas [114]. In this case, LDA and GGA (*e.g.*, PBE) functionals could be a good approximation. But for pure organic molecules or insulators, GGA frequently underestimates the HOMO–LUMO gap. A hybrid GGA (*e.g.*, B3LYP) could improve the description of the HOMO–LUMO gap by

introducing a part of Hartree–Fock exchange (exact-exchange) [115]. This works well for an isolated molecule, but to calculate the exact-exchange term is very expensive for a periodic system, thus usually GGA functionals remain as the only choice. Furthermore, a normal DFT functional cannot well describe the dispersion interaction. Besides others, Grimme’s group introduced empirical dispersion corrections (*e.g.*, DFT-D3), which enable the description of such interactions at a minimal computational cost [116].

Coupled-cluster (CC) theory is a successful electronic structure theory model for single-reference systems [117]. It is able to provide accurate results for energies and properties due to the inclusion of dynamical correlation. The commonly used CCSD(T) includes all single and double excitations, and the triples contribution is calculated non-iteratively using many-body perturbation theory. It is usually termed as the gold standard of quantum chemistry. We have to notice that single-reference CC methods fail in the presence of static or strong correlation due to the inadequacy of the reference [118]. For the studied systems, however, the vicinity near an equilibrium position of bonding is our main focus, which can be well described by a single reference.

Despite the vast improvements in modern algorithms and hardware, the computational cost of CCSD(T) is still considerable large. Here, we select three model molecules for the verification of DFT by comparing with CCSD(T), the dimethylnitroxide radical ($\text{Me}_2\text{NO}^\bullet$), the ethenethiol radical ($\text{C}_2\text{H}_3\text{S}^\bullet$), and methane molecule (CH_4), each with a gold atom (Figure 4.2).

The calculations were carried out using GAUSSIAN 16 [75], and def2-QZVPPD was used as a basis set [119, 120]. In the radical cases, an open-shell singlet state was set for the initial guess (antiferromagnetic coupling between radical and gold atom). Three complexes were optimized using the PBE functional with Grimme’s D3 dispersion [121]. The rigid-molecule bond length (Au-X) scans were applied for PBE-D3 level and CCSD(T) as the benchmark.

To evaluate the interaction strength between two molecular fragments, we need to calculate the energy difference before and after the complex is formed. E_{Binding} (Equation 4.2) requires relaxing other degrees of freedom during scanning a variable, however, structure optimizations are not feasible for CCSD(T). Here, $E_{\text{Complexing}}$ was used as defined by Equation 4.1, where all other degrees of freedom were fixed except the scanned variable.

$$E_{\text{Complexing}} = E_{A+B} - E_{A(\text{rigid})} - E_{B(\text{rigid})} \quad (4.1)$$

$$E_{\text{Binding}} = E_{A+B} - E_{A(\text{relaxed})} - E_{B(\text{relaxed})} \quad (4.2)$$

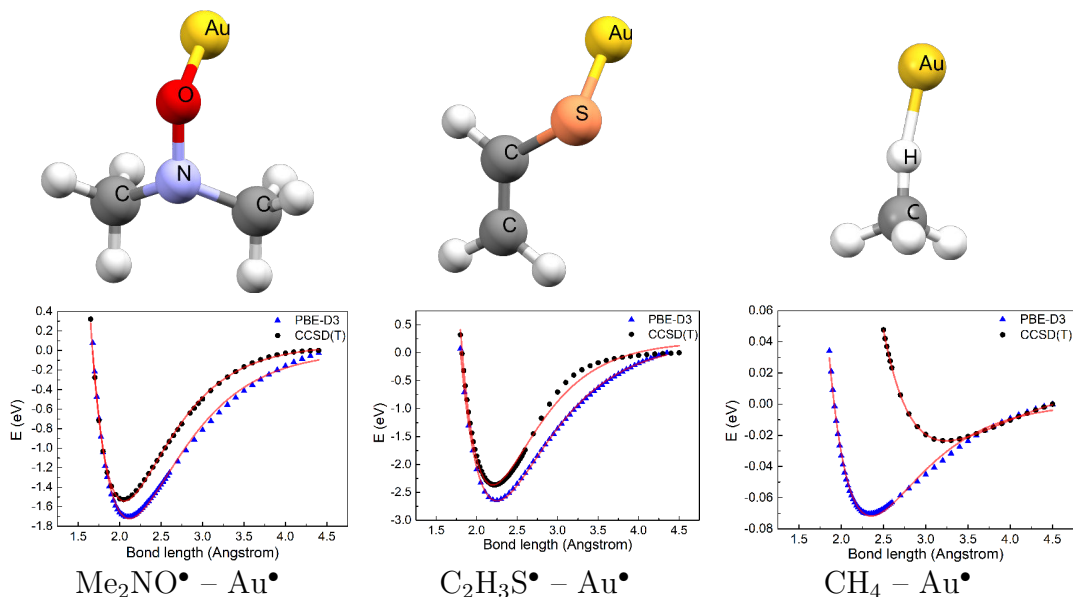


Figure 4.2.: In the first row, the ball-and-stick models of Me₂NOAu (left), C₂H₃SAu (middle), and CH₄Au (right). The color mappings of atoms, carbon (gray); hydrogen (white); nitrogen (pale violet); oxygen (red); sulfur (orange); gold (yellow). In the second row, the scanning $E_{\text{Complexing}}$ points of the corresponding system, where the blue triangles and the black circles represent data points based on PBE-D3 and CCSD(T) respectively, and the red curves were fitted by the Morse potential function.

Table 4.1.: The fitted parameters of the Morse potential for the PBE-D3 and CCSD(T) data points of Me₂NOAu, C₂H₃SAu, and CH₄Au.

	Me ₂ NO• – Au•		C ₂ H ₃ S• – Au•		CH ₄ – Au•	
	PBE-D3	CCSD(T)	PBE-D3	CCSD(T)	PBE-D3	CCSD(T)
D (eV)	1.72141	1.59895	2.85377	2.57585	0.07266	0.04034
a	1.55639	1.78887	1.50094	1.78888	1.57388	1.13650
r ₀ (Å)	2.11931	2.05613	2.25101	2.19818	2.35562	3.24336

The bond length scanning curves were fitting by Morse potentials, $E = -D + D(1 - e^{-a(r-r_0)})^2$, where D is the well depth, a represents the width of the potential, and r_0 is the equilibrium bond length. As suggested by results shown in Table 4.1, PBE-D3 could fairly well describe the radical–gold interactions. The well depth was

overestimated by 7.7% for Me_2NOAu , and 10.8% for $\text{C}_2\text{H}_3\text{SAu}$. The equilibrium bond length based on PBE-D3 in the above two cases is also closed to the CCSD(T) references, which means PBE-D3 is qualified for the further geometric optimization process. However, in the CH_4Au case, PBE-D3 overestimated the well depth by 80.1%, and the expected bond length was much shorter than the reference. Although, such interaction is much weaker than conventional chemical bonds, but for a organic molecule with abound hydrogen atoms, if trying to calculate the molecular structure on a gold surface based on PBE-D3, with an accumulation of many small errors, the molecule–gold distance may be underestimated.

4.1.3. The atomic structures of TEMPO on gold surfaces

Due to the chemical inertness, gold provides a clean chemical environment for studying the properties of adsorbed molecule. As the most commonly used cleavage plane for experiments, Au(111) has C_3 symmetry (viewed along the body diagonal of the cell) where the layers are alternated in the (ABCABC...) sequence. Therefore, it has several possible sites for adsorbed molecules, top (T), bridge (B), hollow-hcp (H) and hollow-fcc (F), as shown in Figure 4.3.

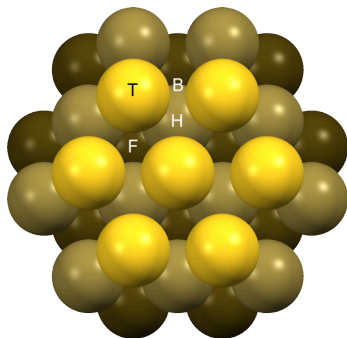


Figure 4.3.: The possible adsorption positions on the Au(111) surface. Here, bright yellow is used for the uppermost layer, light brown is used for the middle layer, and dark brown is used for the bottom layer.

The Au(111) surface used in the following was obtained from a slab of bulk gold ($a = 4.0786 \text{ \AA}$, with the Au-Au distance of 2.884 \AA). A hexagonal supercell was built with 4 gold layers and 20 \AA vacuum layer, which is enough to contain TEMPO or other small molecules, where the cell axes are $a = 17.3040 \text{ \AA}$, $c = 27.0643 \text{ \AA}$. The geometry optimizations and single-point energy were performed with the VASP 5.3.5 program package [74, 122–124], by using the PBE-D3 functional with dispersion correction and dipole moment correction along z axis. The GW type projector augmented wave (PAW) pseudopotentials were applied with the kinetic

energy cutoff set to 640 eV [125]. For the initial coarse optimization, the k -points mesh was set to Gamma point only, and improved to $2 \times 2 \times 1$ in the following steps. The threshold of maximum residual force was set to 0.01 eV/Å. The bottom two gold layers were fixed. To figure out the preference of TEMPO adsorption positions on Au(111), TEMPO molecules were docked on the surface with an appropriate Au-O distance (van der Waals radius can be used as a reference) and orientation of nitroxide's lone pair. Due to the symmetry, the lone pair can effectively overlap with different number of gold atoms for some scenarios, which were indicated by a number (*i.e.*, zero, one, two).

Table 4.2.: The binding energies (E_{Binding}) of the optimized TEMPO molecules on the different adsorbed positions of the Au(111) surface. The dispersion and the DFT contributions are represented by E_{D3} and E_{SCF} , respectively, where $E_{\text{Binding}} = E_{\text{D3}} + E_{\text{SCF}}$. The last column represents the net spin in a unit cell.

Initail	Final	E_{Binding} (kJ/mol)	E_{D3} (kJ/mol)	E_{SCF} (kJ/mol)	spin
Top	FCC-Top	-92.7740	-92.4918	-0.2822	0.6616
FCC(one)	FCC-Top	-93.6342	-93.0437	-0.5905	0.1778
FCC(two)	FCC-Top	-110.0266	-107.0900	-2.9366	0.5327
HCP(one)	HCP-Top	-96.9760	-107.9207	10.9447	0.0001
HCP(two)	Laydown	-112.0283	-115.3318	3.3035	0.4475
Bridge(zero)	FCC-Top	-110.0042	-106.9877	-3.0165	0.5424
Bridge(one)	FCC	-93.1197	-106.9800	13.8603	0.0000

From the results (Figure 4.4, Table 4.2), in most of the cases, TEMPO is retained in the standing mode except for the HCP(two) case, which converged to a laydown mode. The middle point between the top and the fcc hollow site is the preferential adsorption position of TEMPO on the Au(111) surface. The FCC(two) case lead to the most stable geometry. Further bonding analysis was also based on this optimized structure. The binding energy is around -110.0 kJ/mol, and the dispersion term contributed the majority (-107.1 kJ/mol).

The binding energy of a CH_4 molecule on the Au(111) surface is about -21.0 kJ/mol for the up-form (three hydrogen atoms pointing towards the surface) and -17.4 kJ/mol for the down-form (one hydrogen atom pointing towards the surface, molecule is inverted), which mainly captured by the dispersion term (Table C.3). For a free CH_4 molecule, there are two possible types of the adsorption configuration as above. Although, the up-form has a more stable configuration, but the methyl groups in TEMPO are limited by the steric hindrance, the down-form is more preferred, thus one hydrogen in a methyl group always points towards the closest surface gold atom to maximize the interaction. Here, the four methyl groups play crucial role, contributing about -70 kJ/mol binding energy.

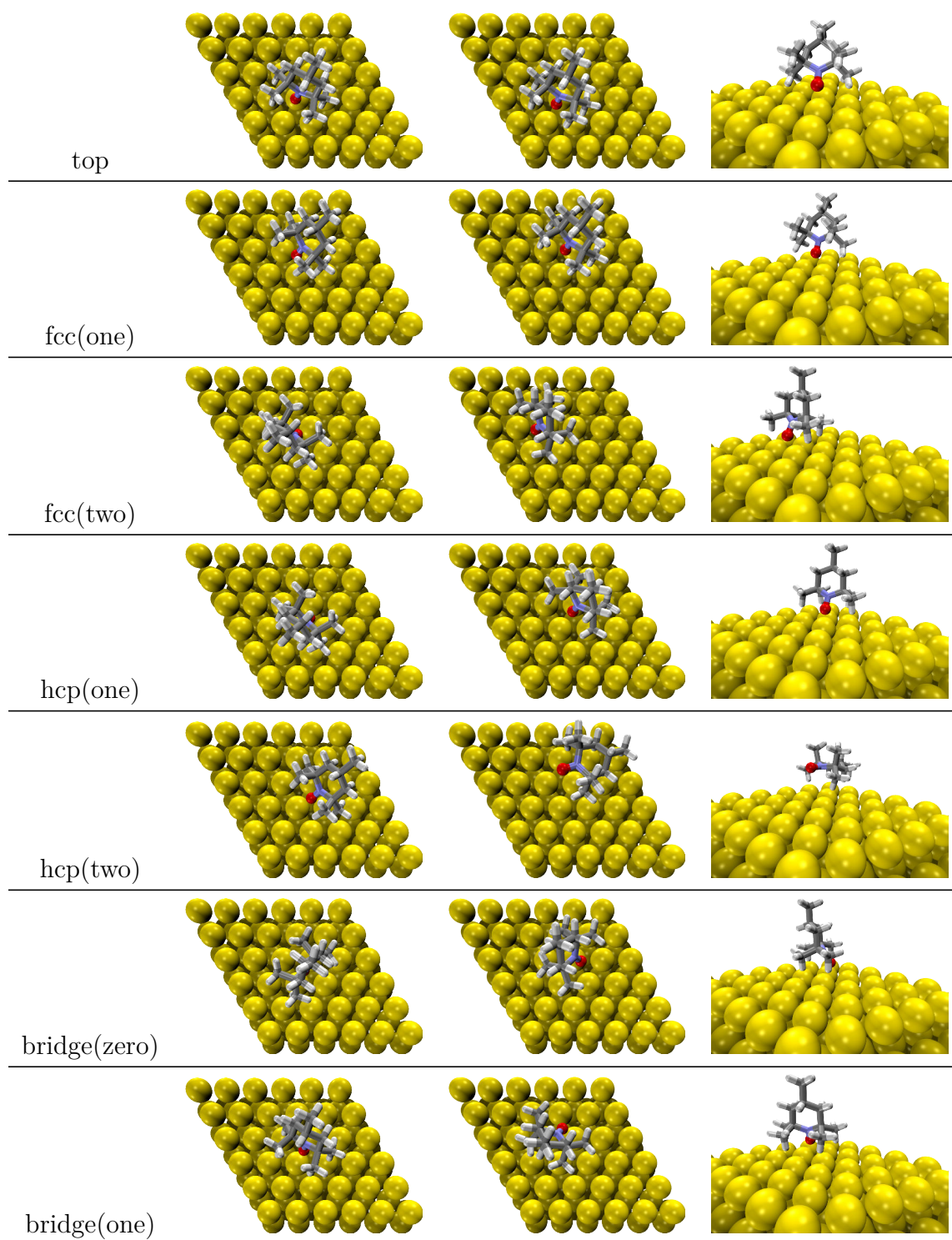


Figure 4.4.: The initial TEMPO structure on the Au(111) surface (the left column), the optimized structures from the top view (the middle column) and from the side view (the right column). The number of gold atoms that can effectively overlap with the lone pair of TEMPO is indicated in the bracket.

In order to approach the scenario in the experiments as closely as possible, the Au(100) surface, the Au(110) surface, and the Au(111) surfaces with defects were taken into account (Figure C.1, Figure C.2). As shown in Table C.1 and Table C.2, the preferential binding energies of TEMPO on those surfaces have not shown a significant difference compared with the Au(111) surface.

Interestingly, for the standing modes, TEMPO adsorbed on the clean Au(111) surface is based on the four methyl groups by the dispersion interaction, the nitroxyl radical is not able to overlap with the surface sufficiently due to the steric hindrance (with an Au-O distance of 2.5908 Å). In the Au(111+FCC) case, in which an additional gold atom is added to the fcc position of a Au(111) surface, the interaction between the TEMPO molecule and the additional gold atom is more like a chemical adsorption with a binding energy of -115.3 kJ/mol, where the binding nature could be captured by the DFT functional more significantly (-56.7 kJ/mol). The Au-O distance (2.16 Å) is also close to the equilibrium bond distance (2.12 Å) of Me_2NOAu predicted based on PBE-D3 KS-DFT. To remove the contribution from the methyl groups, the binding energy between the artificial molecule piperidinyloxy (methyl groups stripped from TEMPO) and the Au(111+FCC) surface was calculated as -89.9 kJ/mol, which is dominated by the E_{SCF} term (-62.0 kJ/mol), and the Au-O distance is 2.15 Å.

In short, the interaction between TEMPO and a gold surface is mainly made up of the NO group by the chemical-bonding-like interaction (around -60 kJ/mol) which could be captured by the PBE functional or the four methyl groups by the dispersion interaction (around -70 kJ/mol). However, due to the limitations of the geometry, on a perfect surface, it is difficult to achieve a maximum of the two interactions at the same time, therefore the binding energy on the Au(111) surface is around -110 kJ/mol. It is worth noting that the PBE-D3 could overestimate the interaction strength between CH_4 and the gold surface (Table 4.1), which means the interaction based on the NO group should have a even larger share in a real situation.

The binding energies between the model molecules with commonly used anchoring groups and the corresponding gold surfaces have also been calculated, including the thiophenol radical, the derivatives of cyclohexane (cyhex), and the derivatives of 2,2,6,6-tetramethylcyclohexane (tmch). As the optimized results shown in Figure C.10, Figure C.11, Table C.4, Table C.5, the additional methyl groups could increase the binding energy. In the Au(111) surface case, the structural analogs of TEMPO show relative close binding energies compared with TEMPO which are -147.2 kJ/mol for tmchSH (thiol), -107.1 kJ/mol for tmchOH (hydroxyl), and -140.5 kJ/mol for tmchNH₂ (amino). Therefore, the binding strength of the NO radical part in TEMPO is comparable with the undissociated thiol group, the hydroxyl group, and

the amino group. As the most commonly used strong anchoring group in various experiments, the binding energy of the thiophenol radical (PhS^\bullet) is -200.4 kJ/mol, which is around twice than the TEMPO on the surface. In short words, the interaction between TEMPO and gold is not negligible. Therefore, the TEMPO functional group could form a bond with the gold electrodes in the Scheer group’s TEMPO–OPE molecular junctions [21], and the passing electron through the TEMPO–gold bond could have a stronger spin polarization compared with the electron tunneling through the OPE backbone.

4.1.4. Chemical bonding analysis of the TEMPO–gold cluster complexes

To unveil the nature of bonding between TEMPO and gold surfaces, isolated complexes consisting of TEMPO and the gold clusters were built. The structures are cut from the optimized periodic cells. The metal clusters should be limited as small as possible for saving calculation time but with the following requirements: 1. the layer closest to the molecule should be large enough to represent possible interactions. 2. Keep the surface symmetry as possible, here is C_3 for the Au(111) surface. 3. The number of gold atoms should be even (correspond to the diamagnetic nature in bulk case), and easy to converge the SCF. Therefore, three molecule–gold cluster complexes were selected, TEMPO–Au₂₀ (the number of gold atoms in each layer: 10/6/4), PhS–Au₂₂ (12/6/4), and piperidinyloxy–Au₂₈ (1/12/10/5).

The atom-centered-orbital basis set calculations combined with post-processing software have great advantages with making a wavefunction analysis. Real functions are able to extract meaningful information from an abstract wavefunction and project it into a real space to visualize, which could help us for understanding the mechanism of an interaction. Without other special instructions, the single-point calculations were performed using GAUSSIAN 16 under PBE-D3/def2-TZVP level. Wavefunction analysis and the corresponding visualization were achieved by MULTIWFN 3.8 and VMD 1.9.3 [126, 127]. The values of isosurfaces were set to 0.02 a.u. for molecular orbitals and 0.005 a.u. for spin density unless otherwise specified.

4.1.4.1. The functional dependence of the complexing energy

The coordination number of gold atoms at edges and vertices is low, thus they can form very strong interactions with molecules. Such an artefact can lead to deviations from the original structure. However, only the radical–gold interactions were aimed at investigating, thus the geometries of the systems were not optimized,

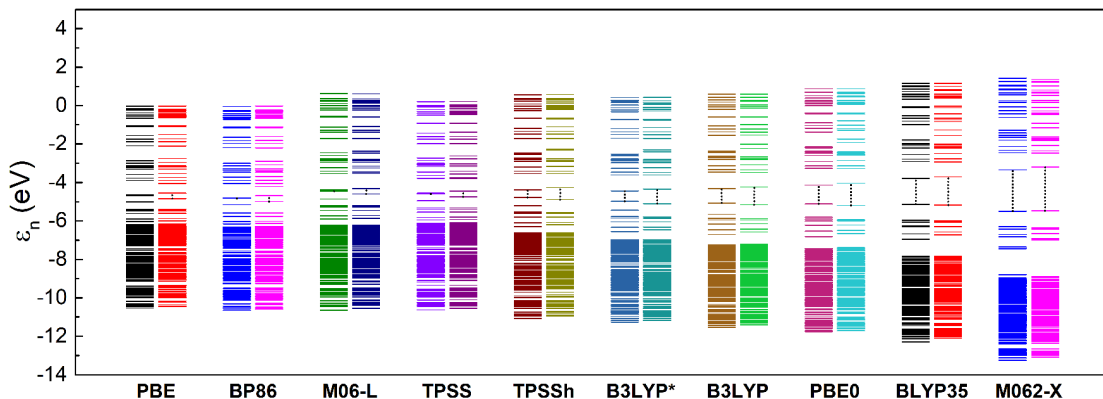


Figure 4.5.: Kohn-Sham orbital energy levels of the TEMPO-Au₂₀ complex calculated by different functionals, with the left side for α electrons, the right side for β electrons, and the black vertical dashes indicating HOMO-LUMO gaps.

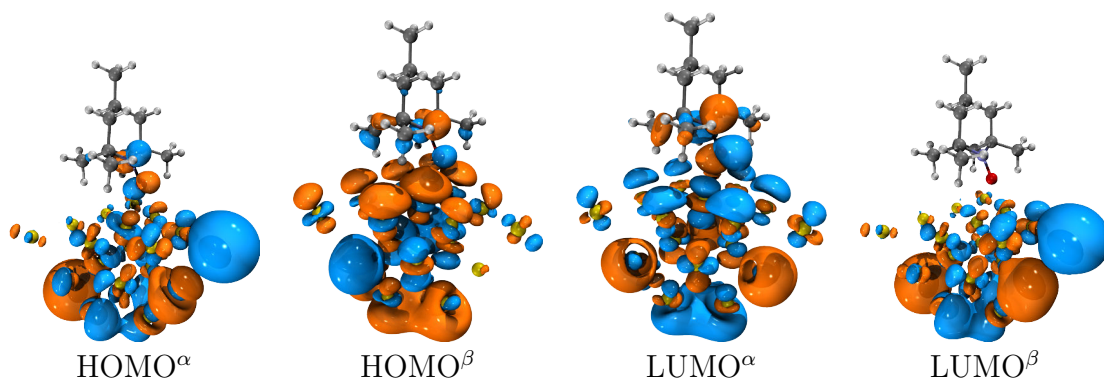


Figure 4.6.: The molecular orbital isosurfaces for the TEMPO-Au₂₀ complex based on PBE KS-DFT.

Table 4.3.: The complexing energies of TEMPO-Au₂₀ system based on different functionals.

Functional	$E_{\text{Complexing}}$ (kJ/mol)	E_{D3} (kJ/mol)	E_{DFT} (kJ/mol)
PBE	-93.1645	-66.7862	-26.3783
BP86	-129.8831	-115.9709	-13.9122
M06-L	-81.1699	-13.9171	-67.2528
TPSS	-103.4874	-88.2444	-15.2430
TPSSH	-93.5156	-87.6869	-5.8287
B3LYP*	10.7127	n.a.	10.7127
B3LYP	-86.3640	-105.2479	18.8839
PBE0	-76.3793	-69.6792	-6.7001
BLYP35	22.0955	n.a.	22.0955
M06-2X	-54.5744	-12.6875	-41.8869

and $E_{\text{Complexing}}$ is used. The single-point calculations of the single molecules, the gold clusters, and the complexes were performed based on the selected functionals.

As a representative of the gold clusters shown in Figure C.4, the frontier orbitals of the Au_{20} are delocalized, and the large value near the vertex in the LUMO should arise from a low coordination number. For TEMPO, the antibonding orbitals of NO (π_{NO}^*) dominate the frontier orbitals of TEMPO (Figure C.6), except the LUMO^α which is mainly constituted by the diffuse orbital from the hydrogen atoms on the methyl groups and the piperidine ring. It also can illustrate that the four methyl groups are essential to stabilize the TEMPO. The orbital energy of LUMO^α is quite higher than others, which means it does not likely participate in the bond with the gold cluster, especially since gold is not an obvious electronics donor.

There are many near-degenerate molecular orbitals just below the HOMO in both TEMPO and Au_{20} cases that could lead to complicated interactions (Figure C.3, Figure C.5). The frontier orbitals of the complex are not just a simply linear combination between the HOMOs of TEMPO and Au_{20} . This makes it difficult to draw a clear conclusion based on the fragments' MO analysis or other similar methods (*e.g.*, charge decomposition analysis).

To exclude a possible artifact, we check the complexing energies between TEMPO and Au_{20} under several common DFT functionals with their corresponding dispersion correction (Table 4.3). Due to lack of the dispersion correction parameters, the B3LYP* and BLYP35 failed to capture the interaction between the methyl groups and the gold cluster. Generally, the complexing energy decreases with a higher exact-exchange admixture. But using a functionals with an excessive exact-exchange component (M06-2X) does not help to describe a metal system [128]. Thus, the complexing energy of TEMPO and the Au_{20} cluster based on the most of the functionals are qualitatively consistent.

4.1.4.2. Partial density of states analysis

The density of states (DOS) is a fundamental concept of condensed matter physics, which describes the number of states in a unit energy interval. For a periodic system, the energy levels are continuous (*e.g.*, along a k -path), so DOS can be plotted as a curve. For an isolated system, the concept of DOS can be generalized. The discrete energy levels can be broadened artificially, therefore the DOS can be used as a valuable tool for analyzing the nature of molecular electronic structure. A Gaussian function with a 0.05 eV full width at half maximum (FWHM) is used for broadening the energy levels.

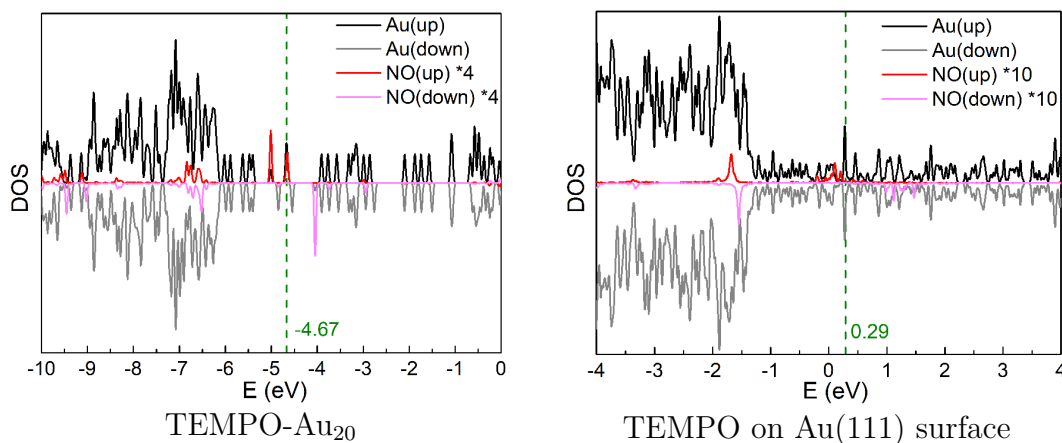


Figure 4.7.: The partial density of states (PDOS) of the TEMPO-Au₂₀ complexes (left) and the TEMPO molecule on the Au(111) surface (right) based on PBE KS-DFT. Black denotes the spin up electron of gold, gray denotes the spin down electron of gold. The PDOS curves of the NO group were enlarged by a factor of 4 on the left side and of 10 on the right side. The red and magenta represent the spin up and down of the NO group respectively. The green dash lines indicate the corresponding Fermi levels.

To account the contribution from a certain fragment, the partial density of states (PDOS) is frequently used, which decomposes the DOS into contribution from particular atoms or orbitals.

For instance, in the right part of Figure 4.7, the PDOS of gold shows a continuity below the Fermi level, and is quite broad in a large interval as typical metallic features, which means a sufficient overlap between the frontier orbitals of adjacent gold atom. As a comparison, the PDOS peaks of TEMPO are much sharper, due to the localized nature of typical molecular orbitals. However, the overlap between two PDOS areas cannot grant the nature of bonding or antibonding, because the phase information is missing.

For this reason, the overlap population density of state (OPDOS) was proposed [129]. The OPDOS is able to account for the orbital cross term between two fragments, which could determine bonding situations (a positive value for bonding, a negative value for antibonding). The OPDOS curves between the TEMPO's nitroxyl part (NO) and the Au₂₀ cluster were calculated for the two spin cases, and the significant peaks were labeled by the molecule orbital indices (Figure 4.8, Figure 4.9). The related MO isosurfaces can be found in Figure C.8.

The MOs with a bonding characteristic between NO and Au₂₀ (from 104 to 117) are quite below the Fermi level. The gold atom which is closest to the oxygen atom has a large contribution with *d* type symmetry. There are many negative peaks close to the

Fermi levels, making the bonding analysis quite difficult. The OPDOS method can only give a qualitative characterization of the bonding and anti-bonding character, but the energy contribution of each peak is absent. Due to this limitations, other approaches are investigated in the following.

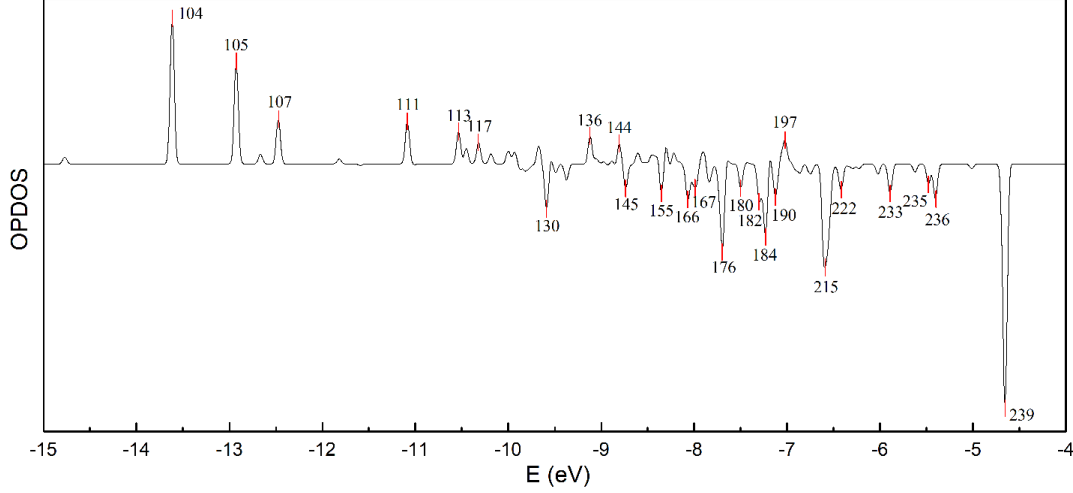


Figure 4.8.: The OPDOS between NO of TEMPO and Au_{20} for α electrons based on PBE KS-DFT. A positive value for bonding, a negative value for antibonding.

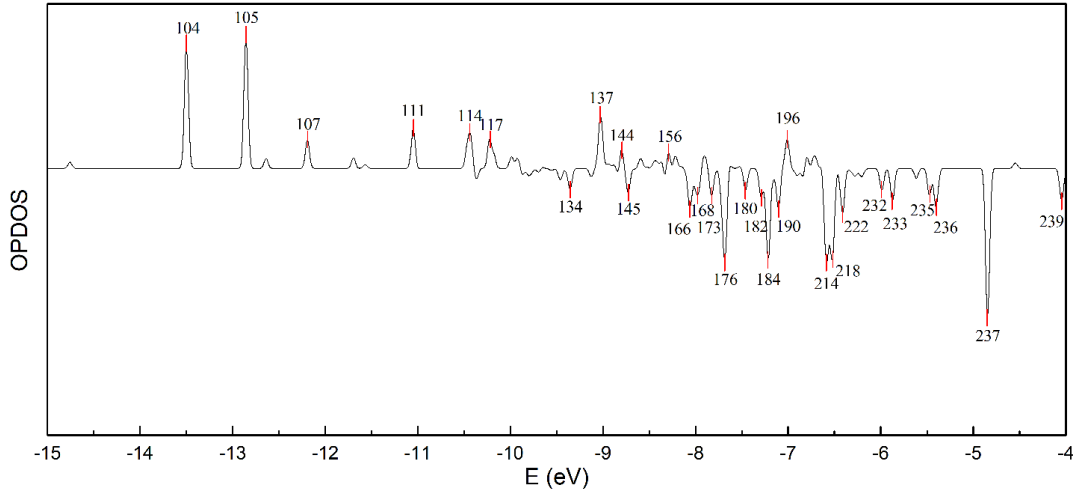


Figure 4.9.: The OPDOS between NO of TEMPO and Au_{20} for β electrons based on PBE KS-DFT. A positive value for bonding, a negative value for antibonding.

4.1.4.3. Extended transition state – natural orbitals for chemical valence

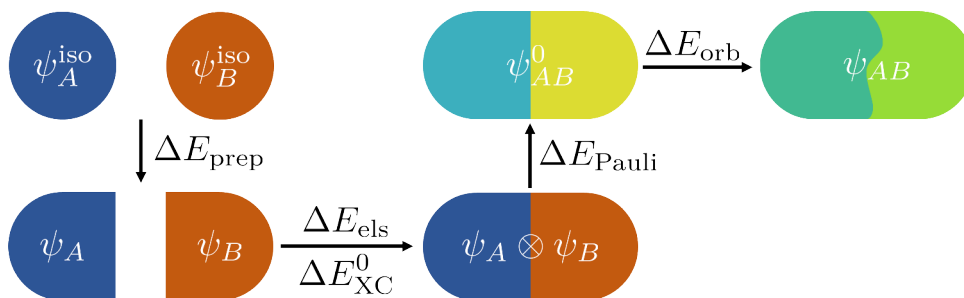


Figure 4.10.: The electronic structure variation during two fragments forming a complex. ψ is a state of a system. ΔE_{prep} is the energy change during the preparation. ΔE_{els} and ΔE_{XC}^0 are the change in classical Coulomb interaction energy and exchange–correlation energy, respectively. ΔE_{Pauli} represents the kinetic energy rising due to the Pauli exclusion principle. ΔE_{orb} stands for the energy change from the mixing of orbitals.

The Extended Transition State – Natural Orbitals for Chemical Valence (ETS-NOCV) method was proposed by Ziegler [130]. It has been widely used in exploring chemical bonds and weak interactions between fragments. It is based on the analysis of the variation of density matrix caused by the interaction. According to that, we are able to separate the complexing process into the following step. Such division is entirely artificial but useful [131].

Two fragments A and B are separated by infinity, with optimized isolated wavefunctions ψ_A^{iso} and ψ_B^{iso} , respectively. During the preparation stage, two fragments change the geometries of isolated states to the geometries in the complex, causing the energy change ΔE_{prep} . It is usually positive (also the difference between E_{Binding} and $E_{\text{Complexing}}$). In the next step, pulling two fragments together, the geometry is equivalent to the final complex. The electronic structure is still isolated. The inter-fragment electrostatic interaction may change the energy level of molecular orbital. But the wavefunction $\psi_A\psi_B$ is just the Hartree product of ψ_A and ψ_B , $\psi_A\psi_B = \psi_A \otimes \psi_B$, called a promolecular wavefunction. ΔE_{els} is evaluated as classical Coulomb interaction energy between original wavefunctions ψ_A and ψ_B . ΔE_{XC}^0 is the change in exchange–correlation (XC) energy during combination from ψ_A and ψ_B to $\psi_A\psi_B$ (*e.g.*, dispersion interaction). Due to the nature of a Fermion system, the wavefunction must be antisymmetrized (Pauli exclusion principle), $\psi_{AB}^0 = \psi_A \wedge \psi_B$. ψ_{AB}^0 is denoted as the frozen-state wavefunction, it corresponds to the Slater determinant constructed by all occupied orbitals of A and B . Further, Löwdin orthonormalization has been employed among these orbitals to make them orthonormal with each other. As the consequence from the orthonormalization, the electrons have to

use orbitals with higher (angular) momentum, which brings more kinetic energy, thus ΔE_{Pauli} should be a positive value. In the final step, the intra-fragment mix of occupied and unoccupied orbitals (polarization effect) and the inter-fragment mix of occupied and unoccupied orbitals (charge-transfer effect) turn the frozen-state into the actual complex wavefunction ψ_{AB} , which yielded after a normal self-consistent field (SCF) step. The energy variation caused by mixing is accounted for by the orbital interaction energy ΔE_{orb} .

$$\begin{aligned} E_A^{\text{iso}}[\psi_A^{\text{iso}}] + E_B^{\text{iso}}[\psi_B^{\text{iso}}] &\xrightarrow{\Delta E_{\text{prep}}} E_A[\psi_A] + E_B[\psi_B] \xrightarrow{\Delta E_{\text{els}} + \Delta E_{\text{XC}}^0} \\ E[\psi_A \psi_B] &\xrightarrow{\Delta E_{\text{Pauli}}} E[\psi_{AB}^0] \xrightarrow{\Delta E_{\text{orb}}} E[\psi_{AB}] \end{aligned}$$

NOCV orbitals are obtained from the diagonalization of the density matrix difference, $\Delta \mathbf{P}^{\text{orb}}$. It was defined to be the difference between the density matrices of actual complex state (ψ_{AB}) and the frozen-state (ψ_{AB}^0), where,

$$\begin{aligned} \Delta \mathbf{P}^{\text{orb}} \mathbf{C}^{\text{NOCV}} &= \mathbf{C}^{\text{NOCV}} \mathbf{v} \\ \Delta \mathbf{P}^{\text{orb}} &= \mathbf{P}[\psi_{AB}] - \mathbf{P}[\psi_{AB}^0] . \end{aligned}$$

It's easy to find that $\Delta \mathbf{P}^{\text{orb}}$ is traceless (conservation of probability), which means the eigenvalues come pairwise (opposite number). Thus, NOCV orbitals are also paired with a donor orbital (with a negative eigenvalue) and acceptor orbital (with a positive eigenvalue). Orbital interaction results in variation of electron density, which can be represented as “orbital deformation density” calculated from the NOCV orbitals and their eigenvalues,

$$\begin{aligned} \Delta \rho^{\text{orb}} &= \rho[\psi_{AB}] - \rho[\psi_{AB}^0] \\ \Delta \rho^{\text{orb}} &= \sum_{i=1}^N v_i \varphi_i^2 . \end{aligned}$$

A big advantage of ETS-NOCV is the ability to calculate the bonding energy contribution from all NOCV orbital pairs,

$$\Delta E_{\text{orb}} = \text{tr} (\Delta \mathbf{P}^{\text{orb}} \mathbf{F}^{\text{TS}}) = \sum_{\mu}^N \sum_{\nu}^N \Delta P_{\mu\nu}^{\text{orb}} F_{\mu\nu}^{\text{TS}} .$$

Here, μ and ν are indices of Löwdin-orthogonalized basis functions. \mathbf{F}^{TS} is the so-called extended transition state Fock matrix, which is constructed using average of ψ_{AB} and ψ_{AB}^0 . it refers to the artificial electronic structure at the midpoint between ψ_{AB} and ψ_{AB}^0 . For a practical reason, replacing it with the Fock matrix of the actual complex wavefunction usually does not lead to qualitative errors.

For the TEMPO-Au₂₀ complex, the density deformation during the forming the complex is mainly dominated by the orbital part (Figure 4.11). The deformation caused by the Pauli exclusion is relatively small. As shown in Table 4.4, the energy contributions of the 1st and the 647th NOCV orbital pairs are significantly larger than else, which are −12.9 and −16.7 kJ/mol respectively.

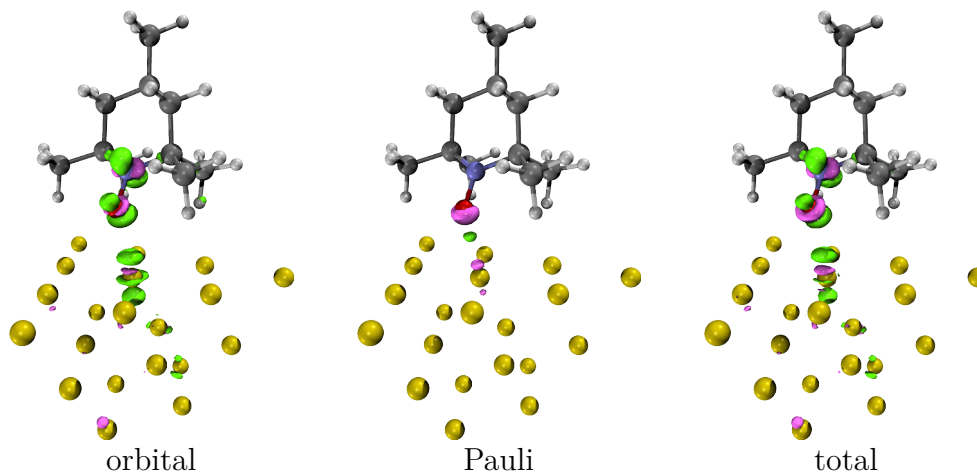


Figure 4.11.: The isosurfaces with the value of 0.0015 of the density deformation for the orbital part (left), the Pauli part (middle), and the total (right) of the TEMPO-Au₂₀ complex.

Table 4.4.: The significant NOCV orbital pairs of the TEMPO-Au₂₀ complex.

Alpha NOCV orbital pairs							
Pair	E (kJ/mol)	Orbital	Eigenvalue	E	Orbital	Eigenvalue	E
1	−12.9286	1	0.90876	−451.1607	1292	−0.90876	−436.8933
2	−6.9454	2	0.12166	−355.9329	1291	−0.12166	−298.9886
Beta NOCV orbital pairs							
Pair	E (kJ/mol)	Orbital	Eigenvalue	E	Orbital	Eigenvalue	E
647	−16.7360	1293	0.27931	−470.5326	2584	−0.27931	−410.5759
648	−3.6819	1294	0.10996	−531.7446	2583	−0.10996	−498.3981

From Figure 4.12, for the 1st pair, the probability density decreases in the donor orbital consisting of the anti-bonding molecular orbital between π_{NO}^* and the d orbital of the closest gold atom. The probability density increases in the acceptor orbital, which is mainly contributed by the gold atoms. The final net electron density change could be observed in the last column, where the electrons transfer from the TEMPO–gold interacting area to the edge of the gold cluster. For the 647th pair, the electrons transfer from the d orbital of the closest gold atom to π_{NO}^* , which is a backdonation.

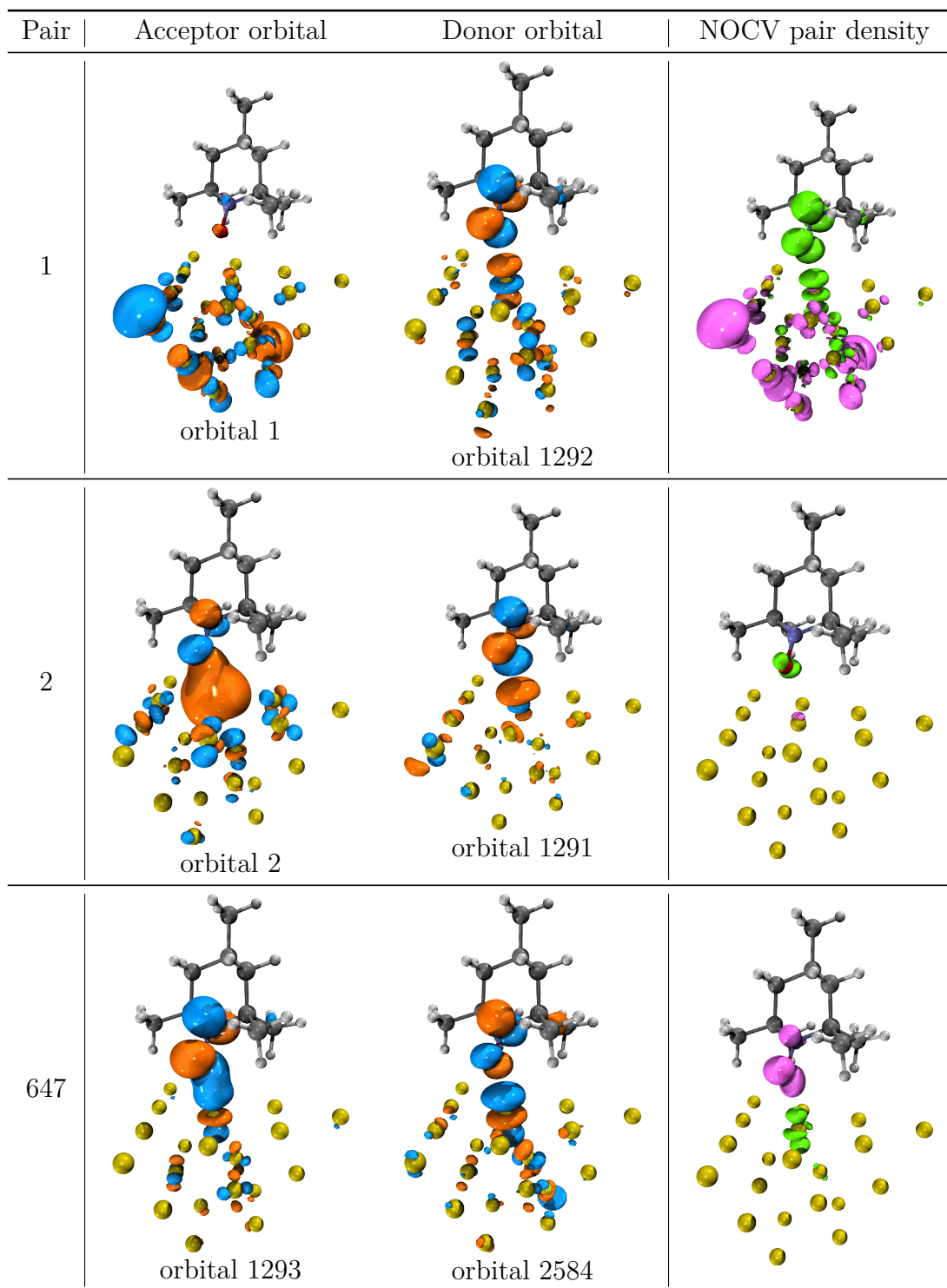


Figure 4.12.: The NOCV orbital pairs' isosurfaces with the value of 0.04 and the corresponding density isosurfaces with the value of 0.0015 for the TEMPO-Au₂₀ complex, where the green and the magenta indicate the decreasing and the increasing of the electronic density based on the contribution of the corresponding NOCV orbital pair.

In the piperidinyloxy-Au₂₈ case, the above two interactions could be observed even more clearly (Figure C.12, Table C.6). The 1st pair and the 700th pair indicate the electrons donation from the π_{NO}^* of piperidinyloxy to the cluster and the backdonation respectively. Due to the lack of the steric hindrance from the methyl group and the additional gold atom, the orbital overlapping between the NO group and the gold cluster is sufficient, leading to larger energy contributions of the NOCV pairs. They are -72.0 and -56.1 kJ/mol for the 1st and the 700th pairs.

Based on the above information, a TEMPO molecule would bind with a gold atom which has the shortest distance to the NO radical. The frontier orbital π_{NO}^* of TEMPO would mix with the d orbital of the gold atom. The resulting mixed orbitals could have electron donation and backdonation with the rest of the gold atoms, which result a chemical bond interaction between TEMPO and gold atoms.

4.1.4.4. Interaction region indicator

The reduced density gradient (RDG) is used to evaluate the deviation from a homogeneous electron distribution as a fundamental quantity in DFT. As the definition, $s = \frac{1}{2(3\pi^2)^{1/3}} \frac{|\nabla\rho(\mathbf{r})|}{\rho(\mathbf{r})^{4/3}}$, the 4/3 exponent makes sure RDG is dimensionless. It was re-discovered as a tool for revealing noncovalent interactions [132]. It can enhance our understanding of the weak chemical interactions during the preparatory stage of chemical reactions or other biomolecular organization pattern by visualization.

Recently, a revised version, interaction region indicator (IRI), has been proposed [133]. It overcomes some shortcomings of RDG, and is enable to visualize noncovalent interactions and conventional chemical bonds simultaneously.

$$\text{IRI}(\mathbf{r}) = \frac{|\nabla\rho(\mathbf{r})|}{[\rho(\mathbf{r})]^a} \quad a = 1.1 \quad (4.3)$$

Based on the atom in molecules a quantum theory (AIM), the electron density Hessian matrix, $\nabla^2\rho$, is a widely used tool to distinguish between the different types of interactions [134]. It can be decomposed into three eigenvalues λ_i ($\lambda_1 \leq \lambda_2 \leq \lambda_3$), where $\lambda_2(\mathbf{r})$ is the second largest eigenvalue of electron density Hessian matrix at \mathbf{r} . $\text{sign}(\lambda_2)\rho$ is mapped to IRI isosurface to visualize the nature of interactions. A large negative value of $\text{sign}(\lambda_2)\rho$ indicates an attractive interaction, a large positive value means the interaction is nonbonding, and a value near zero hints a weak noncovalent interaction.

As the result, the sigma bonds (C-H, C-C, C-N, C-S, N-O) and the metal bonds (Au-Au) were clearly indicated by the dark blue areas. The green parts indicated

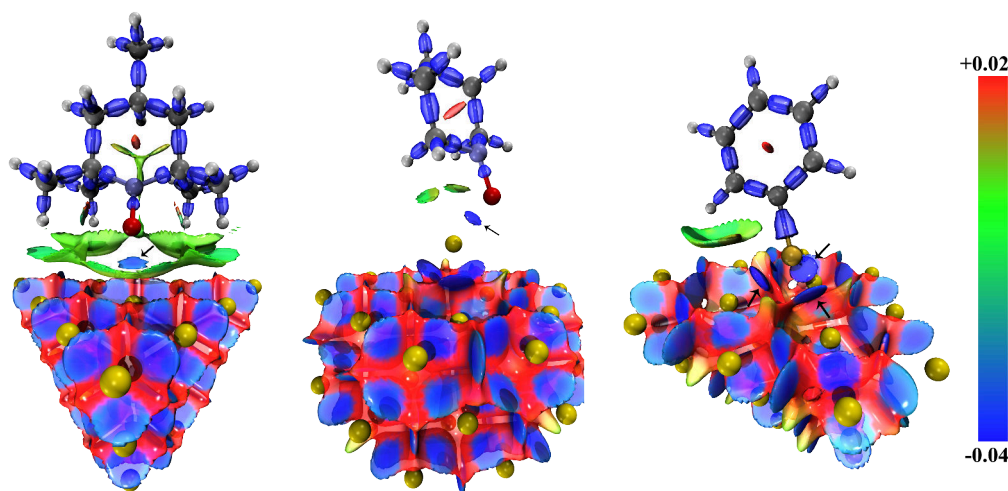


Figure 4.13.: The IRI isosurfaces of TEMPO-Au₂₀ (left), piperidinyloxy-Au₂₈ (middle), and PhS-Au₂₂ (right) colored by $\text{sign}(\lambda_2)\rho$ (with color bar). Blue indicates strong attractive interactions, green indicates noncovalent interaction, red indicates strong nonbonded overlap.

the van der Waals interactions between hydrogen and gold. In the TEMPO-Au₂₀ case (Figure 4.13 left), a distinct blue disc (marked with an arrow) can be observed between the oxygen atom and gold cluster surrounded by green parts, which means the interaction between nitroxide radical and the gold is much stronger than a typical noncovalent interaction as a conventional chemical bond. In the piperidinyloxy-Au₂₈ case, due to a shorter Au-O distance without the hindrance from methyl groups, the blue disc is much clear. In the PhS-Au₂₈ case, three blue discs could be observed between the sulfur atom and the three closest gold atoms.

4.2. TEMPO–OPE in double tunnel junctions

4.2.1. Introduction

As another attempt for molecule-based spintronics, double tunnel junctions (DTJs) based on organic molecules as quantum dots have been proposed [135–138]. In this regard, such a junction, molecules are embedded between two thin insulator layers, and an electron can tunnel from a semiconductor (*e.g.*, Si) to the molecules and further arrive at the reservoir (*e.g.*, gold electrode) (Figure 4.14). Thus, the transport can be tuned using the molecular orbitals, and the MO levels can be adjusted by modifying functional groups. In addition, this type of device has high stability to allow an operation at room temperature [139], even with other external stimulation (*e.g.*, electric field, magnetic field, light), which enables various types of experi-

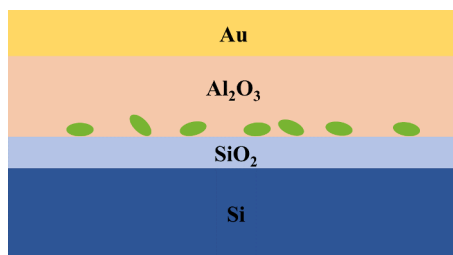


Figure 4.14.: A schematic diagram of the double tunnel junction. The guest molecules (green ellipses) are embedded between the insulated SiO_2 and Al_2O_3 layers.

ment. This method has a better compatibility with the existing complementary metal-oxide-semiconductor (CMOS) manufacturing technology. It is thus possible to overcome a main obstacle to achieve a large-scale integration of molecular devices.

In previous studies, the closed-shell molecules copper phthalocyanine (CuPc), diarylethene, and fullerene (C_{60}) were used for the embedded molecules [135–137]. Light and electric fields were employed for triggering molecular conductance switching.

In this case, our collaborator Dr. Ryoma Hayakawa used an open-shell molecule (2,2,6,6-tetramethylpiperidin-1-yl)oxidanyl-oligo(p-phenyleneethynylene) (TEMPO–OPE) as the quantum dot to explore magnetic-field-dependent conductivity properties. During the sample preparation stage, silicon substrates were cleaned by Shiraki’s method [140], followed by a treatment in 1% HF solution to remove a chemically grown SiO_2 layer. In an oxygen atmosphere, 1 nm-thick SiO_2 films were grown in a furnace by annealing at 500 °C. Then the organic radical molecule TEMPO–OPE was deposited on the surfaces in a vacuum chamber. Finally, the molecules were covered with Al_2O_3 thin films by atomic layer deposition (ALD) in a reactor chamber, which introduces trimethyl aluminum and water vapor alternately as precursors.

After that, the conductivity experiments can be performed for the prepared double tunnel junctions, in which the tunneling current is highly dependent on the electronic structure of the embedded TEMPO–OPE molecules. To simulate this system, exact knowledge of the structure is crucial, but not available from experiments. Thus, we rely on structures optimized employing DFT.

Due to the exact structure of the surface being unknown, we can not exclude that the formation of oxide layers could be over- or under-reacted. For an under-reacted case, the ratio between the oxygen and silicon atoms in an oxide layer is lower than two, while for an over-reacted case, the ratio is higher than two. Precursors

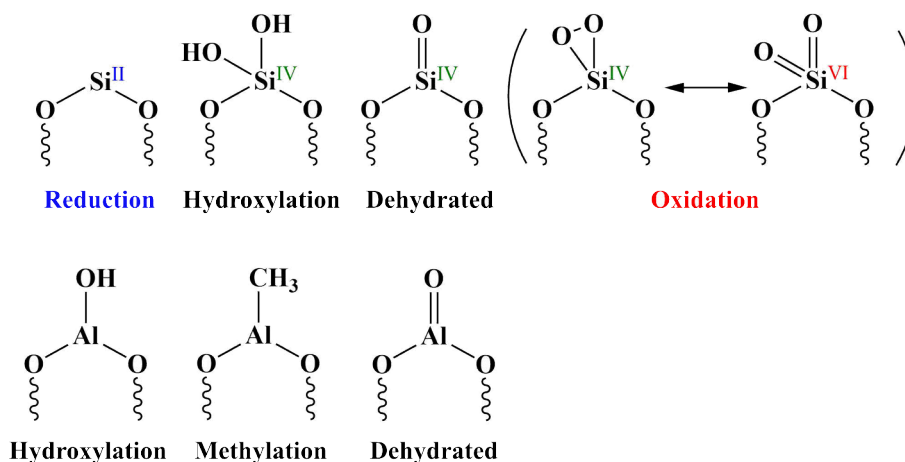


Figure 4.15.: The possible structures of the SiO_2 and Al_2O_3 surfaces.

may remain on the surface and form new structures. Therefore, the four kinds of SiO_2 (reduction, oxidation, hydroxylation, dehydrated types) and three kinds of Al_2O_3 (hydroxylation, dehydrated, methylation types) surface were taken into consideration as an initial guess. In addition, a reconstructed SiO_2 surface was included as the reference [141]. Its stacking density is slightly lower compared with quartz.

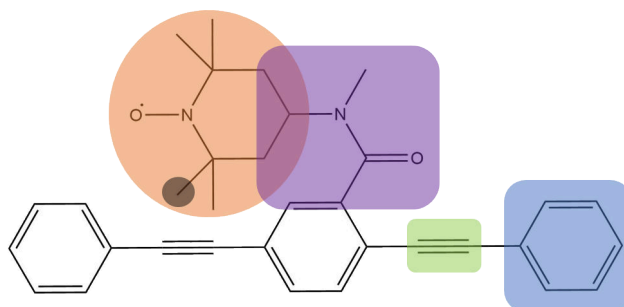


Figure 4.16.: The fragments of the TEMPO-OPE molecule, where the blue highlights benzene, the green highlights acetylene, the purple highlights iPrMeAc, the orange highlights TEMPO, and the gray highlights methane.

On the other hand, TEMPO-OPE contains multiple functional fragments: TEMPO, benzene, acetylene (C_2H_2), methane (CH_4), N-isopropyl-N-methylacetamide (iPrMeAc), as marked in Figure 4.16. In order to explore possible interactions between fragments and surfaces in detail, the geometry optimizations of the above fragments on different surfaces were also performed.

4.2.2. Methodology

The calculation follows the procedures outlined below. The α -Al₂O₃ (corundum) (001) surface and α -SiO₂ (α -quartz) (100) surface were cleaved and modified from the crystal structures [142], and the reconstructed SiO₂ surface was constructed according to the reference [141]. Surfaces were optimized with a fixed bottom layer. Then, molecules were docked on the relaxed surface and optimized under a single-Gamma-point k -mesh with the fixed substrate. Finally, the upper substrate layers were relaxed (keeping the bottom layer fixed) and the system was optimized with a residual force threshold of 0.02 eV/Å for TEMPO–OPE systems and 0.01 eV/Å for others. For the double-layered structures, an additional Al₂O₃ layer was placed on the TEMPO–OPE with an appropriate distance. The periodic boundary conditions (PBC) DFT calculations were performed with the VASP 5.4.4 package within the Perdew–Burke–Ernzerhof (PBE) exchange–correlation functional with Grimme’s D3 dispersion corrections (Becke–Johnson damping). PAW pseudopotentials and plane-wave basis sets with cutoff energies of 640 eV for wavefunctions were used. A $2 \times 2 \times 1$ Monkhorst-Pack k -mesh was employed for all systems. Visualization of the systems was achieved by VMD 1.9.3.

4.2.3. The adsorption energies on the surfaces

Table 4.5.: The binding energies of the optimized TEMPO–OPE molecules on the various SiO₂ and Al₂O₃ surfaces.

E_{Binding} (kJ/mol)	<i>cis</i> -TEMPO–OPE	<i>trans</i> -TEMPO–OPE
Reconstructed-SiO ₂	−123.7	−147.5
Hydro- α -SiO ₂ (100)	−156.2	−193.1
Dehydro- α -Al ₂ O ₃ (001)	−1135.0	−657.3
Hydro- α -Al ₂ O ₃ (001)	−172.8	−223.5
Methyl- α -Al ₂ O ₃ (001)	−102.0	−103.2

According to the results shown in Table 4.5 and Table C.8, the interaction between molecules and the reduced surfaces, the hydroxylated surfaces, and the methylated surfaces are mainly dominated by dispersion interactions. The molecules can form a strong chemical bond with the oxidized surfaces and the dehydrated surfaces. For example, the oxygen atom of the acyl group on the *cis*-TEMPO–OPE molecule is strongly binding with the undercoordinated Al atom on the Dehydro- α -Al₂O₃(001) surface. Such undercoordinated surface has a lot of electron vacancies provided by the empty p orbitals of the Al atoms, thus the surface has the characteristics of a strong Lewis acid.

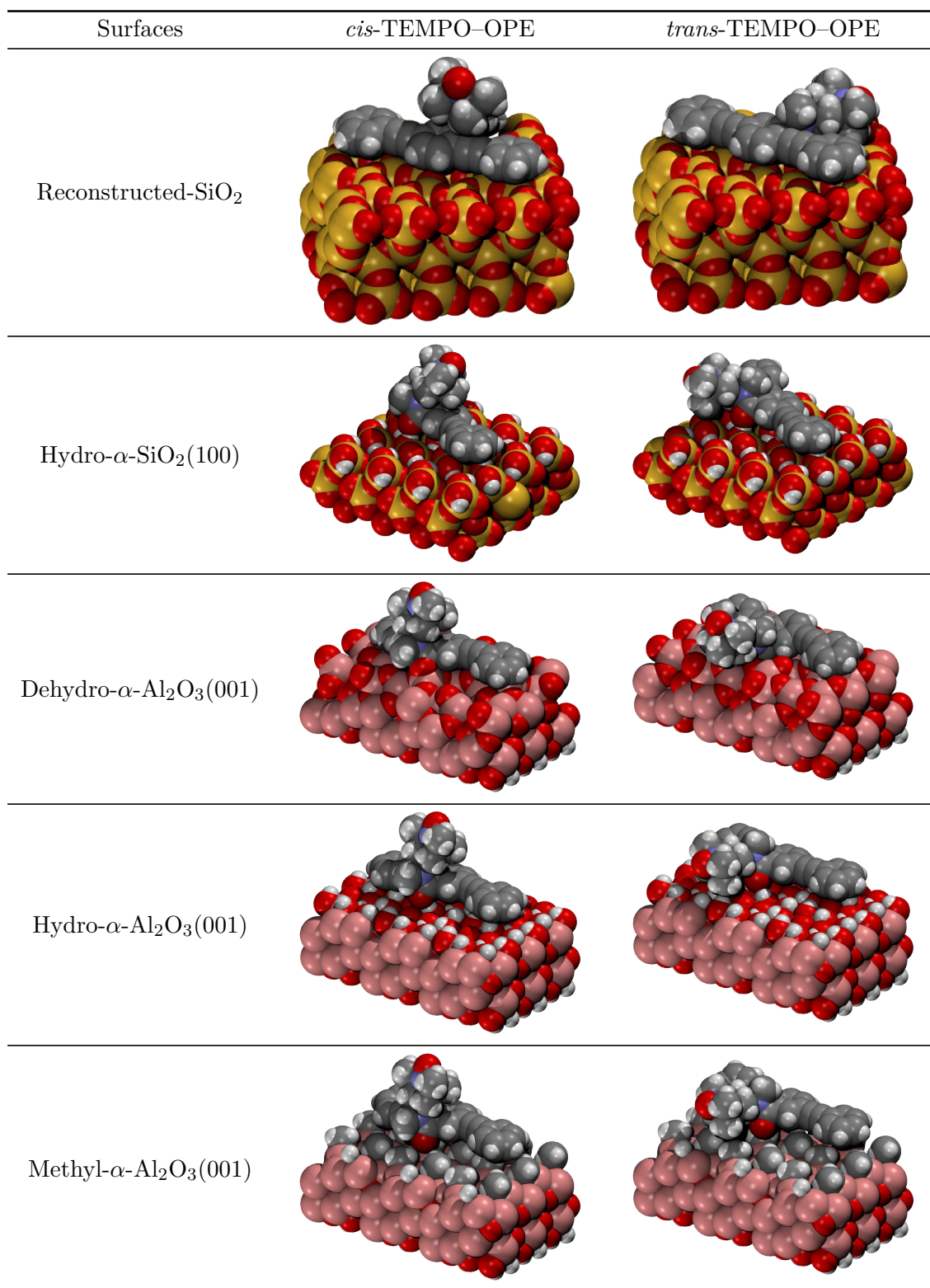


Figure 4.17.: The optimized structures of TEMPO-OPE on the various SiO₂ and Al₂O₃ surfaces.

In a vacuum, the *cis* configuration of TEMPO–OPE is slightly more stable than the *trans* configuration by 3.44 kJ/mol due to the intramolecular dispersion interaction. On the surfaces however, the *trans* configuration is more stable, which should be due to a larger contact area with the surface. Except for the two surfaces with high reactivity, the hydroxylated surfaces have higher binding energies with the TEMPO–OPE molecules. The hydrogen bonding sites provided by the hydrophilic groups could be the main reason (Table C.8). It is obvious for the acyl group (iPrMeAc) to form a hydrogen bond with hydroxyl groups. Furthermore, the TEMPO group can also form a hydrogen bond to the NO site. For a TEMPO on the hydro- α -SiO₂(100) surface, the standing type (−75.2 kJ/mol) is more stable than the laydown type (−40.1 kJ/mol), and the hydrogen atom of the closest hydroxyl group on the surface points to the NO site to achieve a lower energy. It is also supported by the IRI analysis of the hydrated TEMPO system (Figure C.7), in which a light blue disc existing between the NO site and the water molecule indicates a strong hydrogen bond.

4.2.4. The structure of the embedded TEMPO–OPE

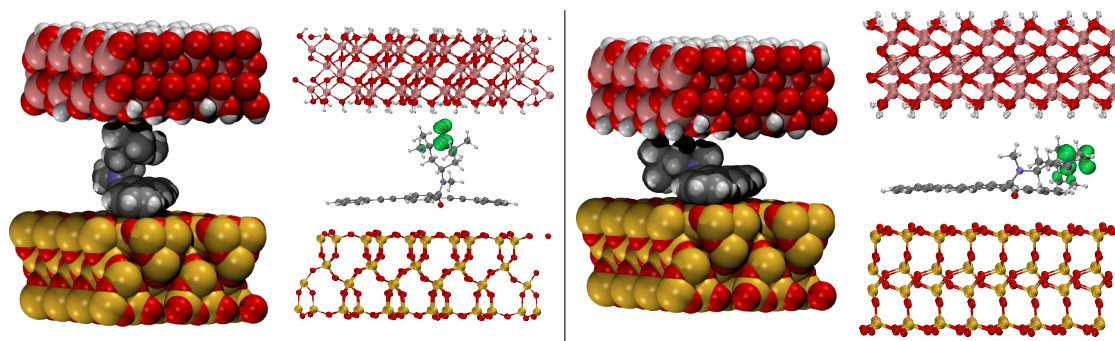


Figure 4.18.: The optimized structures and the spin density isosurfaces of *cis*-TEMPO–OPE (left) and *trans*-TEMPO–OPE (right) embedded between the reconstructed-SiO₂ and the hydro- α -Al₂O₃ layers.

To simulate the embedded TEMPO–OPE molecule in the double tunnel junction, the double-layered systems were built. Here, only the hydro- α -Al₂O₃(001) surface was used as the cover layer. During the ALD process, water vapor was introduced. Thus, highly reactive surfaces like the oxidized or the dehydrated types are not likely to form. The reconstructed-SiO₂ surface and the hydro- α -SiO₂(100) surface were used as the substrate layer. Both *cis* and *trans* TEMPO–OPE molecules were considered.

After the geometric structure optimizations, the results are shown in Figure 4.18

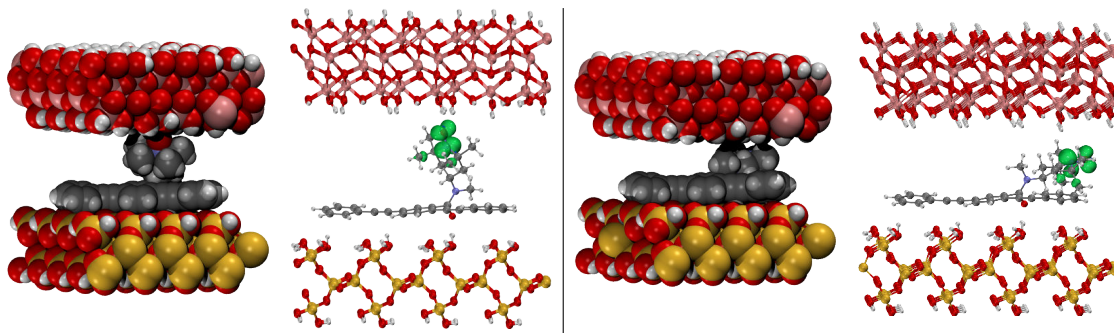


Figure 4.19.: The optimized structures and the spin density isosurfaces of *cis*-TEMPO-OPE (left) and *trans*-TEMPO-OPE (right) embedded between the hydro- α -SiO₂ and the hydro- α -Al₂O₃ layers.

and Figure 4.19. The OPE backbone on the reconstructed-SiO₂ surface has a slight arch shape, while it is flat and in close contact with the hydroxylation surface. This should be due to the stronger affinity of the fragments and the hydroxyl groups. The binding energies of benzene, C₂H₂, and iPrMeAc on the hydro- α -SiO₂(100) surface are higher than on the reconstructed-SiO₂ surface.

From the PDOS curves of TEMPO-OPE in the four systems, the frontier orbitals of the TEMPO-OPE molecules are located in the gap of the two insulator layers, which are well separated from the continuum of SiO₂ and Al₂O₃ (Figure C.17, Figure C.18, Figure C.19, Figure C.20). In those case, the spins are concentrated on the nitroxyl part without diffusion, which means the chemistry environment from the two insulator layers is able to preserve the open shell nature of TEMPO-OPE, and it also enhances the feasibility to making TEMPO-OPE-based spin devices.

4.3. Conclusion

In the first part of this chapter, an experimentally controversial topic was explored by theoretical approaches to whether the TEMPO radical can form a chemical bond with gold atoms. Based on the CCSD(T) reference, the selected PBE functional with Grimme's dispersion correction is able to describe the nitroxyl radical gold interaction well. As the result from the extended systems and the isolated systems, the interaction strength between the TEMPO radical and the gold surfaces is considerably strong (110 kJ/mol), which implies the binding energy is close to that of conventional anchoring groups (*e.g.*, amino, hydroxyl, carboxyl groups) calculated under the same condition, and it is approximately half of the binding energy between the strong anchoring thiophenol radical and gold.

The interaction mainly consists of the orbital interaction between the NO site and the closest gold atom, and the dispersion interaction between the four methyl groups and the gold surface. The two have a similar strength, but it is hard to achieve the maximum at the same time on a perfect surface due to the steric hindrance. On the defective surfaces however, the binding energy always maintain around the above value, and the two can complement each other. According to the bonding analysis by ETS-NOCV, the frontier orbital of TEMPO π_{NO}^* and the d orbital of the gold atom which has the shortest distance to the NO radical would mix and form a subsystem. The chemical bonding interaction between TEMPO and gold results from the electron donation and backdonation between the subsystem and the rest of the gold atoms.

In the second part, the structures of TEMPO–OPE embedded in double tunnel junctions with SiO_2 and Al_2O_3 layers are explored by geometry optimizations based on DFT. Due to experimental limitations, the actual structure information of the surfaces is unknown, but a few reasonable structures were built to represent the results under different reaction conditions. The molecules can form a strong chemical bond with the oxidized surfaces and the dehydrated surfaces, due to the strong Lewis base and acid nature of the surfaces. The hydroxylated surfaces can interact with the TEMPO–OPE molecules significantly, due to the hydrogen bonds between the hydroxyl groups on the surface and the hydrophilic groups on the TEMPO–OPE molecules. Meanwhile, the IRI analysis shows that the NO site of TEMPO could also form a hydrogen bond with hydroxyl groups. As a suggestion to the experiment, this demonstrates the necessity to use as less water vapor in the ALD reaction as possible. Otherwise, the excess surface hydroxyl groups may interact with TEMPO and thus broaden the energy level of the SOMO, and the vibrational modes of the hydrogen bonding hydroxyl group provide a thermal bath, which could accelerate the decoherence process [99]. The electronic structures of the TEMPO–OPE molecules between the double layers show that the frontier orbitals of TEMPO–OPE are isolated from the energy levels of the two insulator layers. Therefore, the radical characteristics can be preserved, which ensures the feasibility of making spin devices.

5. The conduction mechanism of switchable valence tautomer complexes

5.1. Background

As one of the most commonly used photochromic building blocks, diarylethene (DAE) is switchable between two isomers (open and closed-form) under a reversible photo-isomerization process induced by light of different wavelengths. This functional center is able to be chemically modified and further embedded into various materials [143–145].

For a transition metal coordination complex, the electrostatic interaction between ligand atoms and a metal ion is able to remove the degeneracy of d orbitals of transition metal ion. For example, in the most common octahedral coordination structure, the d orbitals of the transition metals split into e_g and t_{2g} . If the crystal field splitting energy is sufficiently large, the electrons tend to be distributed in lower-energy t_{2g} orbitals with pairings, then the complex is in a *low-spin* state. If on-site Coulomb repulsion (pairing energy) is comparable with the splitting energy, the electrons would occupy both e_g and t_{2g} orbitals, then the complex is in a *high-spin* state. By modifying ligands to regulate the crystal field splitting energy, it is possible to obtain a complex which is able to switch between a *low-spin* state and a *high-spin* state under certain external stimulation (*e.g.*, temperature, pressures). Such behavior is called spin crossover (SCO). As another candidate for molecular switcher, some specific coordination complexes are able to alter their molecular structures by SCO with the synergistic metal-ligand electron transfer induced by heat or light. The resulting valence tautomer (VT) exhibits different distributions of electrons.

Our collaborator Dr. Zhaoyang Li synthesized two materials composed of valence tautomeric building blocks (CoL_2) and photochromic diarylethene linkers 1,2-bis(2-methyl-5-(4-pyridyl)-3-thienyl)perfluorocyclopentene) (DAEpy) that exhibit reversible

structural isomerization upon light illumination, which are the open-form $(\text{CoL}_2\text{DAEpy})_2 \cdot (\text{MeCN})_6 \cdot (\text{H}_2\text{O})_1$ (**o-CoDAE**) and the closed-form $(\text{CoL}_2\text{DAEpy}) \cdot (\text{H}_2\text{O})_1$ (**c-CoDAE**). The pyridine groups on DAEpy are able to coordinate with cobalt ions. Thus, two blocks can be joined together to form a coordination polymer. The chelate ligand 3,5-di-*tert*-butyl-*o*-benzoquinone (L) has two very different electronic configurations depending on the oxidation state, which are the benzo-semiquinone form $\text{SQ}^{\bullet-}$ and the catecholate form Cat^{2-} (Figure 5.2).

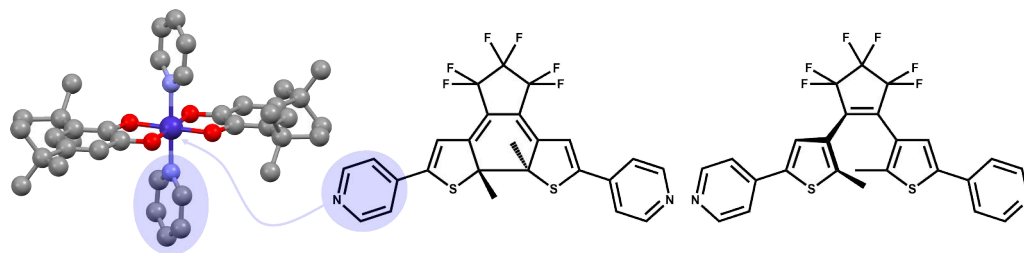


Figure 5.1.: The ball-and-stick model of the CoL_2 building block (left). The hydrogen atoms are omitted for clarity. The types of atoms are represented by colors: carbon (gray), nitrogen (pale violet), oxygen (red), cobalt (dark violet). The closed-form DAEpy (middle) and the open-form DAEpy (right). The pyridine groups on DAEpy coordinate with the cobalt centers.

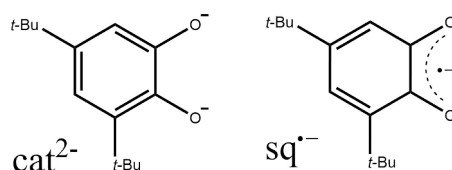


Figure 5.2.: The catecholate form Cat^{2-} (left) and the benzo-semiquinone form $\text{SQ}^{\bullet-}$ (right) of the chelate ligand 3,5-di-*tert*-butyl-*o*-benzoquinone.

Since both building blocks possess the behavior to transform their electronic and geometrical structures under certain illumination or thermal conditions, it is possible to design opto-electronic or thermo-electric spintronic devices based on these materials. Our main goal here is to explore their possible conductivity mechanisms. The experimental results were provided by the collaborator. The experimental data and the following calculations have not been published yet.

5.2. Geometrical Structure

The closed-form **c-CoDAE** crystallized in the $P2_1/n$ space group (monoclinic crystal system) with two crystallographically independent cobalt center coordination

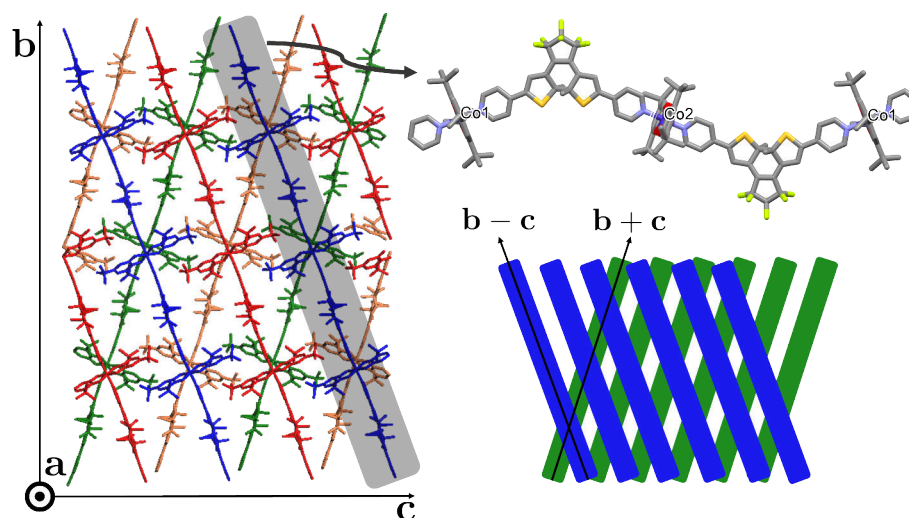


Figure 5.3.: Two types of CoL_2 units (Co1, Co2) are linked by a closed-form DAEpy ligand with forming a coordination polymer chain (right up). The 1D molecular chains (grey shade) along the $b \pm c$ direction are parallel arranged and form a 2D array, which are represented by the stick model. Two adjoint layers form a staggered stacking structure along the a direction (left). The simplified topological model for crystal stacking, each bar represents a molecular chain. Blue and green colored bars represent different stacking layers along the a direction. The blue bars grow along the $b - c$ direction, and the green bars grow along the $b + c$ direction (right down).

complexes CoL_2 (Co1, Co2), two DAEpy linker units, and water molecules of crystallization (Figure 5.3). The symmetric operation doubles the number of molecule in a unit cell. Thus, there are four copies of the CoL_2DAEpy complex. The crystallographic structures of the *low-spin* form (determined at 100 K) and the *high-spin* form (determined at 380 K) do not have an essential difference. The closed structure of the DAEpy linker provides a coplanar arrangement of the two pyridine groups. Thus, two pairs of the CoL_2DAEpy units are able to form a straight periodic chain along the $b + c$ direction (Figure 5.3). The parallel arranged molecular chains form an equidistant 2D array in the bc crystal planes. There are also two CoL_2DAEpy

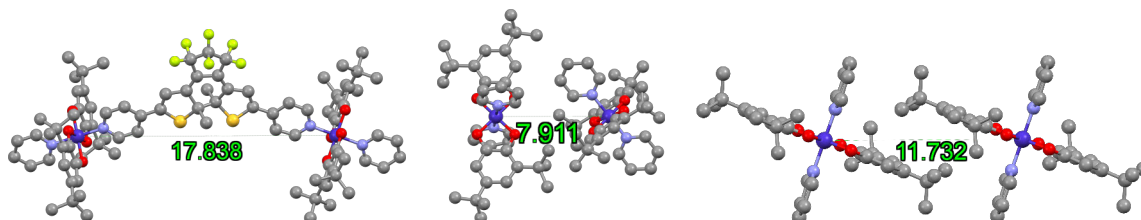


Figure 5.4.: For the closed-form **c-CoDAE** under 100 K, the pairs of CoL_2 linked by a DAEpy bridge (left), along the a axis (middle), along the b axis (right).

units form another straight chain but along the $b - c$ direction. Two adjoint 2D arrays form a staggered stacking structure along the a direction. Examining the surroundings of a CoL_2 unit (based on the *low-spin* structure) to find possible interactions, there are three types, Co1 and Co2 connected by a DAEpy linker in a chain with a 17.838 Å metal center distance, which is abbreviated to Co1–DAEpy–Co2, Co1 and Co2 stacking along the a axis with a 7.911 Å metal center distance, which is abbreviated to Co1–Co2, Co(1 or 2) and Co(1 or 2) stacking along the b axis with a 11.732 Å metal center distance which is abbreviated to Co1–Co1 or Co2–Co2 (Figure 5.4).

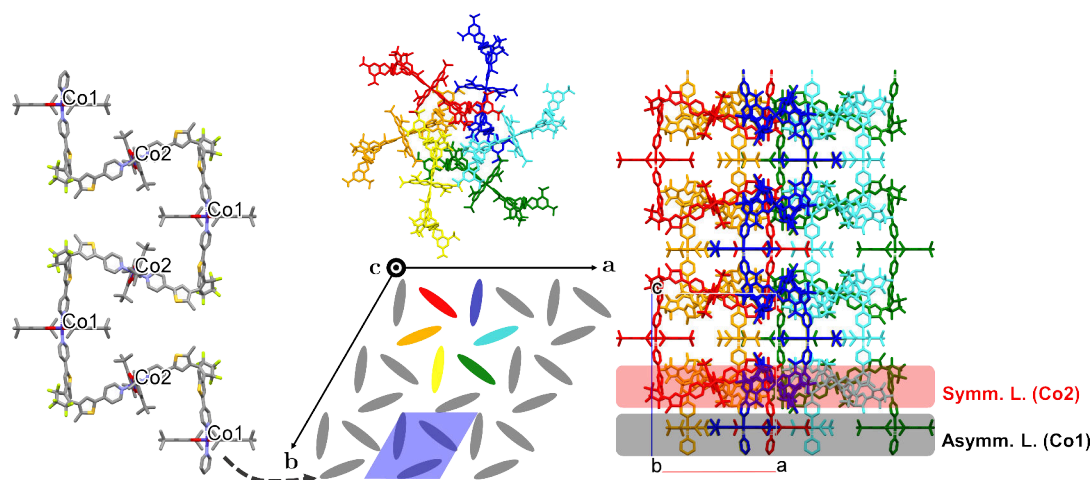


Figure 5.5.: For the open-form **o-CoDAE**, two types of CoL_2 units (Co1, Co2) are linked by an open-form DAEpy ligand with forming a zigzag coordination polymer chain (left). The simplified topological model for the crystal structure, each ellipse represents a chain from the view of the c direction, and the ellipses arrange in a hexagonal lattice in the ab plane. The unit cell is represented by the blue shade (middle down). Six coordination polymer chains form a hexamer, the views along the c direction (middle up) and along the b direction (right), where Co1 units form asymmetric layers (grey shade) and Co2 units form symmetric layers (red shade).

The open-form **o-CoDAE** crystallized in the $P6_3/m$ space group (hexagonal crystal system) also with two crystallographically independent cobalt center coordination complexes CoL_2 (Co1, Co2). But in this case, the open-form DAEpy linker has a 54 degree dihedral angle between the two pyridine groups, therefore four pairs of the CoL_2DAEpy units are needed to form a periodic zigzag chain along the c axis. An unit cell contains three molecular chains, and six aggregated zigzag chains form a closely packed hexamer (Figure 5.5). A periodic unit of the zigzag chain contains two asymmetric CoL_2 units (Co1) and two symmetric CoL_2 units (Co2). For the asymmetric CoL_2 unit (Co1), two ligands (L) are not crystallographically

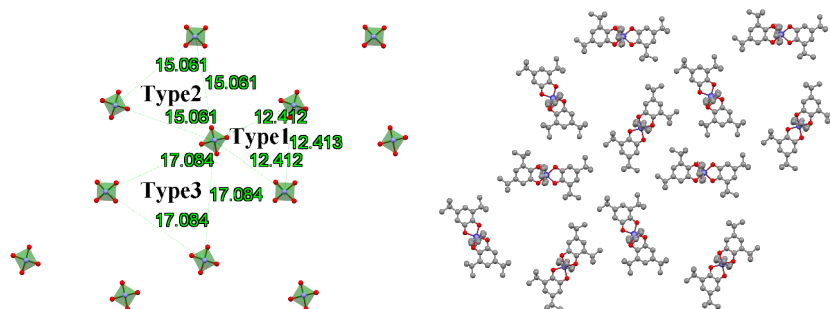


Figure 5.6.: For **o-CoDAE** under 100 K, the octahedral representation (left) and the ball-and-stick model (right) of the CoL₂ units in the asymmetric layer, and the three types of pairwise relations within the *ab* plane (asCo1–asCo1-t1/t2/t3).

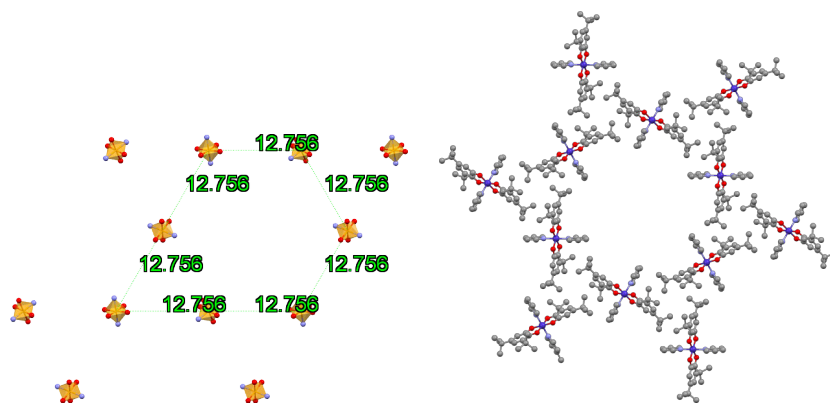


Figure 5.7.: For **o-CoDAE** under 100 K, the octahedral representation (left) and the ball-and-stick model (right) of the CoL₂ units in the symmetric layer, and the pairwise relation within the *ab* plane (sCo2–sCo2).

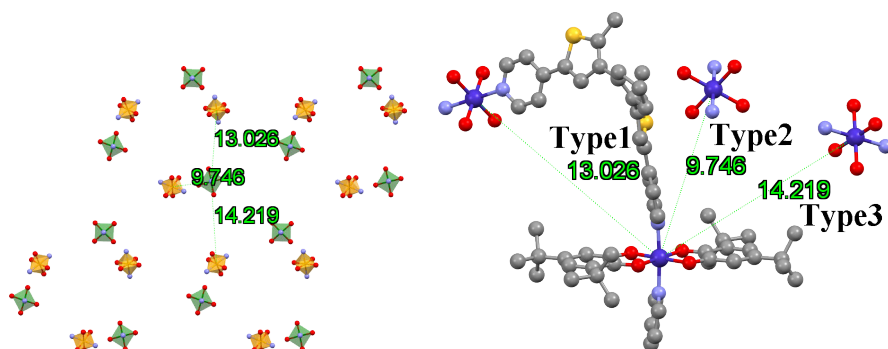


Figure 5.8.: For **o-CoDAE** under 100 K, the octahedral representation (left) and the ball-and-stick model (right) of the CoL₂ units in the symmetric and the asymmetric layers, and the three types of interlayer pairs of CoL₂ (asCo1–sCo2-t1/t2/t3).

equivalent. The symmetric CoL_2 unit (Co2) has a centrosymmetry, two ligands are equivalent. Each kind of CoL_2 unit forms a layer in the ab plane, resulting in the asymmetric layers and the symmetric layers. The asymmetric CoL_2 units are in a hexagonal lattice (three complexes as a lattice point), thus, there are three different types of pairwise relations around a CoL_2 with a distance of 12.412 Å (type 1), 15.061 Å (type 2), 17.084 Å (type 3) respectively (Figure 5.6) which are abbreviated to asCo1–asCo1-t1/t2/t3. The symmetric CoL_2 layer has a standard Kagome symmetry, therefore all CoL_2 units in this layer are equidistant with 12.756 Å (Figure 5.7), which is abbreviated to sCo2–sCo2. There are also three types of interlayer pairs of CoL_2 units between the asymmetric and the symmetric layers, with a distance of 13.026 Å (type 1), 9.746 Å (type 2), 14.219 Å (type 3) respectively (Figure 5.8), which are abbreviated to asCo1–sCo2-t1/t2/t3. It is worth noting that in the type 1, two CoL_2 units are linked by a open-form DAEpy.

For **o-CoDAE** and **c-CoDAE**, the bond lengths of Co–O and Co–N show around 4% deviation between the *low-spin* configuration and the *high-spin* one as their main geometric difference (Table D.1). Such a seemingly tiny difference has a large effect on their electronic structures, which will be discussed in the later sections.

5.3. Experimental results

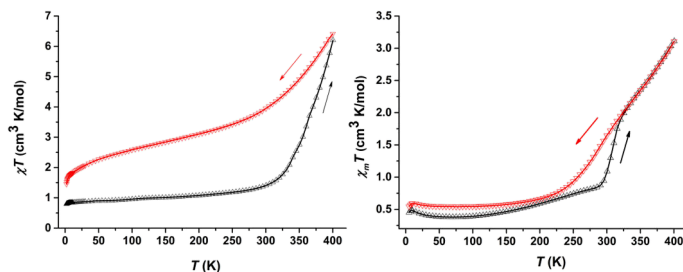


Figure 5.9.: The magnetic susceptibility curves for **c-CoDAE** (left) and **o-CoDAE** (right), where the black and the red curves represent the heating process and the cooling process respectively.

According to the magnetic susceptibility data, both **c-CoDAE** and **o-CoDAE** show a *low-spin* state at low temperature. During the heating process, **o-CoDAE** shows an abrupt transition at 300 K, while **c-CoDAE** has a moderate transition (Figure 5.9). The black curve representing the cooling process of **c-CoDAE** does not overlap well with the heating curve, which should result from the solvent water loss. The current–voltage characteristic shows a poor conductor behavior for **c-CoDAE**, while the conductivity of **o-CoDAE** is considerably higher than **c-CoDAE** (Fig-

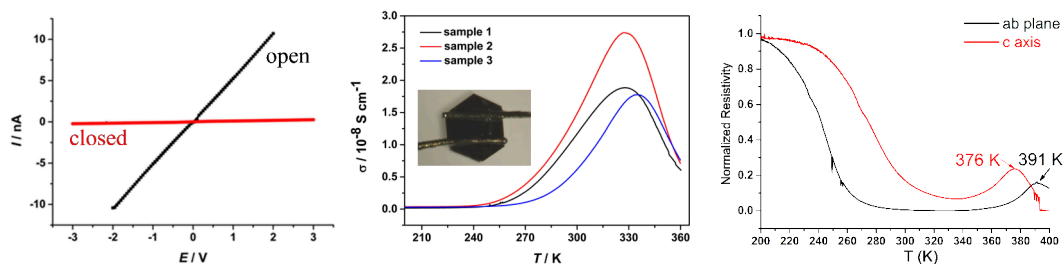


Figure 5.10.: The current–voltage characteristic for **c-CoDAE** (red) and **o-CoDAE** (black) at 300 K (left). The temperature-dependent electric conductivity of **o-CoDAE** shows a reproducible peak at 330 K for the three different single crystal samples (middle). The anisotropic conductive behaviors of **o-CoDAE** along the *ab* plane and the *c* axis (right).

ure 5.10). The temperature-dependent electric conductivity of **o-CoDAE** shows a strong anisotropic conductance: the conductivity along the *ab* plane is almost one order higher than along the *c* axis. The conductivity starts to decrease after the spin states transition happens. To unveil the possible mechanism of such a transition, the electronic structure of the crystal and the building blocks were studied by means of first-principles electronic structure methods.

5.4. Methodology

The system models were built from X-ray diffraction determined structures harvested for the closed-form (100 K, 380 K) and the open-form (100 K, 400K). The disorder information is removed manually by keeping the selected conformational isomer of a certain group. The isolated systems' calculations were performed by GAUSSIAN 16 [75], employing DFT and HF with the def2-TZVP basis set unless mention otherwise. A superfine integration grid was applied for numerical integrations and the tight convergence threshold (10^{-8} for the root mean square change in the density matrix) were used for the SCF procedure. Periodic boundary conditions (PBC) DFT calculations were performed with the VASP 5.4.4 package with the Perdew–Burke–Ernzerhof (PBE) exchange–correlation functional [74, 121–124]. Projector augmented wave (PAW) pseudopotentials and plane-wave basis sets with cutoff energies of 640 eV were used [125]. A Hubbard effective parameter $U_{\text{eff}} = 6.0$ eV is applied on the *d* electrons of the cobalt, where the determination of the value was described in the later section. For the self-consistent parts of band structure calculations, a $4 \times 4 \times 2$ Monkhorst-Pack *k*-points grid and a $2 \times 2 \times 2$ Gamma-centered grid were employed for the closed-form **c-CoDAE** and the open-form **o-CoDAE**,

respectively, with Gaussian smearing ($\sigma = 0.02$ eV). The spin orientation was initialized according to the electronic configuration of $ls\text{-Co}^{\text{III}}(\text{Cat}^{2-})(\text{SQ}^-)$, which is the *low spin* ground state of the CoL_2 unit at low temperature. Visualization of the molecule and isosurfaces was achieved by MULTIWFN 3.8 and VMD 1.9.3 [126, 127]. The values of isosurfaces were set to 0.02 a.u. for molecular orbitals and 0.005 a.u. for spin densities unless otherwise specified.

5.5. A photochromic bridging ligand (DAEpy)

MO	DAE(open)	DAEpy(open)	DAE(closed)	DAEpy(closed)
HOMO-1				
HOMO				
LUMO				
LUMO+1				

Figure 5.11.: The molecular orbital isosurfaces of DAE and DAEpy in the 100 K geometries based on B3LYP KS-DFT.

In this section, the electronic structure of the photochromic bridging ligand (DAEpy) is explored. The molecular structures were extracted from the crystal structures. The KS-DFT calculations were performed for the isolated systems of the DAEpy molecules.

The highest occupied molecular orbital (HOMO) and the lowest unoccupied molecular orbital (LUMO) of conventional organic ligands are usually well separated from the Fermi level of the resulting complexes due to a large gap which also leads to

their chemical stability. However, DAEpy is a large conjugation system, the HOMO–LUMO gap is relatively small, and the molecular orbitals may be mixed with the frontier orbitals of the other building blocks. Therefore, it is necessary to explore the molecular orbitals of DAEpy.

Comparing the the molecular orbitals of the two forms of DAEpy, the GGA functionals (*i.e.*, PBE) and the hybrid-GGA functionals (*e.g.*, B3LYP, M06-2X) predicted quite different HOMO and HOMO-1 (Figure D.3, Figure D.4). PBE also underestimates the HOMO–LUMO gap, which could cause unrealistic orbital mixing with the CoL₂ units (Table 5.1).

Table 5.1.: The HOMO–LUMO gap of DAEpy based on different exchange–correlation functionals KS-DFT.

Gap (eV)	Open(100K)	Closed(100K)
PBE	2.8221	1.2131
B3LYP	4.2126	2.3263
HSE06	3.8289	1.8983
PBE0	4.5789	2.5924
M06-2X	6.3881	4.1541

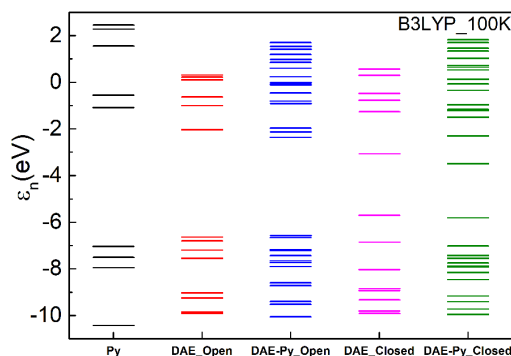


Figure 5.12.: Kohn-Sham orbital energy levels calculated by the B3LYP functional for pyridine, the open/closed-form DAE core and DAEpy based on the low-temperature crystal structure (100 K).

Based on the results obtained from B3LYP functional, due to the matching of orbitals' symmetry, the HOMO of the open-form DAE core mixes with the HOMO of the pyridine, resulting in the HOMO of the open-form DAEpy and the LUMO of the open-form DAEpy mainly consisting of the LUMO of the open-form DAE core, where,

$$\varphi_{\text{DAEpy(Open)}}^{\text{HOMO}} \propto \varphi_{\text{DAE(Open)}}^{\text{HOMO}} + c\varphi_{\text{py}}^{\text{HOMO}} \quad ; \quad \varphi_{\text{DAEpy(Open)}}^{\text{LUMO}} \approx \varphi_{\text{DAE(Open)}}^{\text{LUMO}} .$$

The HOMO of the closed-form DAEpy preserves the DAE core’s nature, but the LUMO mixes with the pyridine’s (Figure 5.12), where,

$$\varphi_{\text{DAEpy(Closed)}}^{\text{HOMO}} \approx \varphi_{\text{DAE(Closed)}}^{\text{HOMO}} \quad ; \quad \varphi_{\text{DAEpy(Closed)}}^{\text{LUMO}} \propto \varphi_{\text{DAE(Closed)}}^{\text{LUMO}} + c' \varphi_{\text{py}}^{\text{LUMO}} .$$

The HOMO–LUMO gap of the closed-form DAEpy is smaller than the open-form, which is originating from higher electron delocalization after the loop closure. The UV-vis spectrum predicted by TD-DFT based on CAM-B3LYP also indicates the closed DAEpy having lower-energy absorption bands (Figure D.5).

As a digression, the fluoride atoms on DAEpy are essential. If the six fluorine atoms on DAEpy(F6) are replaced by hydrogen atoms with a reasonable C-H bond length, the HOMO–LUMO gaps are not affected distinctly, but the energy levels do rise about 0.6~0.8 eV simultaneously, which is unneglectable to the further band structure calculations. It also suggests that the electron-withdrawing effect of fluorine atoms can stabilize this large conjugated system against oxidation by oxygen. So they should not be replaced by hydrogen atoms for a simplification of calculations (Table D.2).

$$U^{(v)} = \text{IP} - \text{EA} \quad ; \quad \text{IP} = E(n-1) - E(n) \quad ; \quad \text{EA} = E(n) - E(n+1) \quad (5.1)$$

In some strongly correlated systems, a strong on-site Coulomb interaction dominates the electronic structure, which is unable to be predicted by a mean-field method such as DFT. The values of the vacuum on-site Coulomb repulsion ($U^{(v)}$) of the DAEpy molecule could be estimated by the ionization potential (IP) and the electron affinity (EA) by Equation 5.1 [146]. Our results show the calculated $U^{(v)}$ is not strongly dependent on the exact-exchange admixture (Table D.3). The values of $U^{(v)}$ are 6.728 eV and 4.781 eV for the open and closed-form DAEpy respectively evaluated by the B3LYP functional.

5.6. The neutral monomer of the tautomeric building block (CoL₂)

In this section, the electronic structure of the tautomeric building block (CoL₂) is explored. The molecular structures were extracted from the crystal structures. The KS-DFT calculations were performed for the isolated systems of the neutral CoL₂ monomers.

Unlike conventional spin crossover complexes, the CoL₂ building block shows a valence-tautomeric interconversion, in which the transition between two spin states is cooperating with a metal-to-ligand charge transfer (MLCT) process, thus the

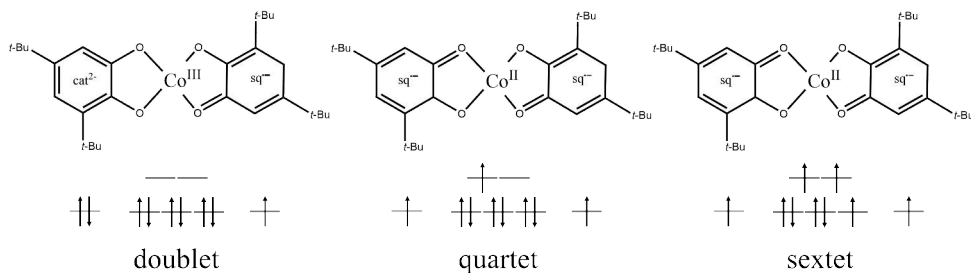


Figure 5.13.: The orbital diagrams of the doublet *low-spin* state (left), the quartet metastable state (middle), and the sextet *high-spin* state

oxidation number of the metal center is different after the transition: it shows the *low-spin* state $\text{Co}^{\text{III}}(\text{Cat}^{2-})(\text{SQ}^-)$ at low temperature and the *high-spin* state $\text{Co}^{\text{II}}(\text{SQ}^-)(\text{SQ}^-)$ at high temperature. Such transition could happen in one step or undergo two steps with a metastable intermediate state (Figure 5.13). Therefore, the selected method (exchange–correlation functional) for obtaining the electronic structure should fairly describe both cases, which should be able to correctly distinguish a preferential electronic configuration from the *low-spin* state and the *high-spin* state in the corresponding low/high-temperature molecular structure. The predicted energy difference between two states should be highly dependent on the ratio of the exact-exchange admixture. The multiple oxidation numbers and the spin multiplicity of the fragments combined with different magnetic coupled scenarios result in eight possible electron configurations as listed in Table 5.2.

Table 5.2.: Possible electron configuration initial guesses for the CoL_2 unit.

Guess	Co		L1	L2	Configuration
I(<i>ls</i>)	III	LS	0.00	FM	<i>ls</i> -Co ^{III} (Cat ²⁻)(SQ ⁻)
II	III	HS	0.00	FM	<i>hs</i> -Co ^{III} (Cat ²⁻)(SQ ⁻) _{FM}
III	III	HS	0.00	AFM	<i>hs</i> -Co ^{III} (Cat ²⁻)(SQ ⁻) _{AFM}
IV(metastable)	II	LS	FM	FM	<i>ls</i> -Co ^{II} (SQ ⁻) _{FM} (SQ ⁻) _{FM}
V	II	LS	AFM	FM	<i>ls</i> -Co ^{II} (SQ ⁻) _{FM} (SQ ⁻) _{AFM}
VI	II	LS	AFM	AFM	<i>ls</i> -Co ^{II} (SQ ⁻) _{AFM} (SQ ⁻) _{AFM}
VII(<i>hs</i>)	II	HS	FM	FM	<i>hs</i> -Co ^{II} (SQ ⁻) _{FM} (SQ ⁻) _{FM}
VIII	II	HS	AFM	FM	<i>hs</i> -Co ^{II} (SQ ⁻) _{AFM} (SQ ⁻) _{FM}
IX	II	HS	AFM	AFM	<i>hs</i> -Co ^{II} (SQ ⁻) _{AFM} (SQ ⁻) _{AFM}

The single-point KS-DFT energies were calculated with the selected functionals for both low (100 K) and high (380 K) temperature structures of the CoL_2 (Co_2) unit from **o-CoDAE**. The listed configurations were used as the initial guesses, by symmetry-breaking DFT: first, the wavefunctions of the cobalt ion and the two ligands are calculated respectively according to the charge and the spin multiplicity. Then the initial guess wavefunction of CoL_2 are generated by the wavefunctions of

three fragments. The converged Kohn-Sham wavefunctions were checked by second order perturbation to remove a possible instability, because self-consistent optimization process can only guarantee that a wavefunction converges on a stationary point, which could also be a saddle point. The spin density isosurfaces based on the resulting show the system is easy to converge to the initial guess assigned for the high temperature molecular structure, while the wavefunctions based on the low temperature molecular structure would converge to another configuration which is different than the setting one in some initial guesses (Figure D.11). According to the results, the exact-exchange admixture is able to stabilize the *high-spin* state (VII) as well as the metastable state (IV), but as a metastable state, the energy should be slightly higher than the *low-spin* state and the *high-spin* state, thus B3LYP with 20% exact-exchange admixture is suitable for the CoL₂ system (Table D.4 – D.11).

The CoL₂ units have two different structures with a tiny deviation in both **c-CoDAE** and **o-CoDAE**. The CoL₂ units in **c-CoDAE** have centrosymmetry, and one of the units in **o-CoDAE** is asymmetric. For a centrosymmetric CoL₂ unit, two ligands are identical, therefore the charge and spin are delocalized on the two ligands, and the semiquinonate and catecholate forms are indistinguishable. However, the spin density of the asymmetric CoL₂ unit is mainly localized on the semiquinonate ligand (Figure D.12).

The B3LYP KS-DFT results suggest that the HOMO and LUMO of the *low-spin* CoL₂ unit mainly consist of a linear combination of the frontier molecular orbitals of the ligands (Figure 5.14), where,

$$\begin{aligned} \text{HOMO}^\beta : \varphi_{\text{CoL}_2}^{\text{HOMO}} &\propto \varphi_{\text{L}_a^{2-}}^{\text{HOMO}} + \varphi_{\text{L}_b^{2-}}^{\text{HOMO}} \\ \text{HOMO}^\alpha, \text{LUMO}^\beta : \varphi_{\text{CoL}_2}^{\text{SOMO}} &\propto \varphi_{\text{L}_a^{2-}}^{\text{HOMO}} - \varphi_{\text{L}_b^{2-}}^{\text{HOMO}} \\ \text{LUMO}^\alpha : \varphi_{\text{CoL}_2}^{\text{LUMO}} &\propto \varphi_{\text{py}_a}^{\text{LUMO}} + \varphi_{\text{py}_b}^{\text{LUMO}} . \end{aligned}$$

We also notice that the *t*-Bu groups' orbitals largely participate in the LUMO of the catecholate ligands (Cat²⁻). Therefore, this groups could not be removed for simplification (Figure D.6), otherwise potentially leading to a wrong energy ranking of different spin states.

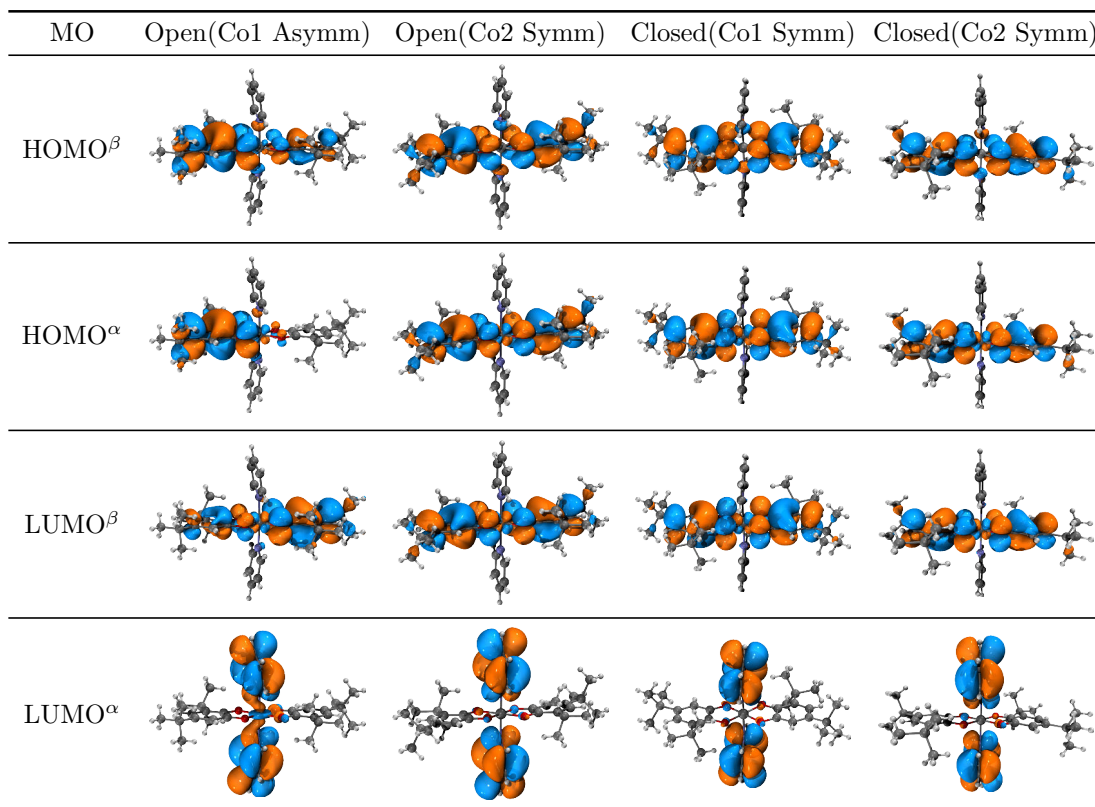


Figure 5.14.: The molecular orbital isosurfaces of $ls\text{-Co}^{\text{III}}(\text{Cat}^{2-})(\text{SQ}^-)$ in the 100 K molecular structures based on B3LYP KS-DFT.

5.7. The charged monomer of the tautomeric building block ($\text{CoL}_2^+ / \text{CoL}_2^-$)

According to the conductivity measurement, the transport should be dominated by a hopping mechanism. In this case, a charge could be localized on a site for a moment which allows the local system (*i.e.*, CoL_2 , DAepy) to relax to a new electron configuration with lower energy. For the bridging ligand DAepy, the charged configurations are trivial: an electron would be removed from the HOMO or added to the LUMO, but for the CoL_2 unit, there are more possible configurations due to the multiple redox centers with various magnetic couplings as listed in Table 5.3. Based on the molecular structures of the CoL_2 unit under low (100 K) and high (380 K) temperature extracted from **o-CoDAE**, the Kohn-Sham wavefunctions starting with the listed initial guesses were calculated with the selected DFT functionals by the SCF procedure. The corresponding spin density isosurfaces based on the results are shown in Figure D.14 and Figure D.15. The single-point energies of the configurations based on the functionals are shown in Table D.12 – Table D.15, and

summarized in Figure 5.15.

Table 5.3.: Possible electron configuration initial guesses for the singly positively or singly negatively charged CoL_2 .

CoL_2^+		CoL_2^-	
I ⁺	$ls\text{-Co}^{\text{III}}(\text{SQ}^-)(\text{SQ}^-)_{\text{FM}}$	I ⁻	$ls\text{-Co}^{\text{III}}(\text{Cat}^{2-})(\text{Cat}^{2-})$
II ⁺	$ls\text{-Co}^{\text{III}}(\text{SQ}^-)(\text{SQ}^-)_{\text{AFM}}$	II ⁻	$hs\text{-Co}^{\text{III}}(\text{Cat}^{2-})(\text{Cat}^{2-})$
III ⁺	$hs\text{-Co}^{\text{III}}(\text{SQ}^-)_{\text{FM}}(\text{SQ}^-)_{\text{FM}}$	III ⁻	$ls\text{-Co}^{\text{II}}(\text{Cat}^{2-})(\text{SQ}^-)_{\text{FM}}$
IV ⁺	$hs\text{-Co}^{\text{III}}(\text{SQ}^-)_{\text{FM}}(\text{SQ}^-)_{\text{AFM}}$	IV ⁻	$ls\text{-Co}^{\text{II}}(\text{Cat}^{2-})(\text{SQ}^-)_{\text{AFM}}$
V ⁺	$hs\text{-Co}^{\text{III}}(\text{SQ}^-)_{\text{AFM}}(\text{SQ}^-)_{\text{AFM}}$	V ⁻	$hs\text{-Co}^{\text{II}}(\text{Cat}^{2-})(\text{SQ}^-)_{\text{FM}}$
VI ⁺	$hs\text{-Co}^{\text{II}}(\text{L}^0)(\text{SQ}^-)_{\text{FM}}$	VI ⁻	$hs\text{-Co}^{\text{II}}(\text{Cat}^{2-})(\text{SQ}^-)_{\text{AFM}}$
VII ⁺	$hs\text{-Co}^{\text{II}}(\text{L}^0)(\text{SQ}^-)_{\text{AFM}}$		

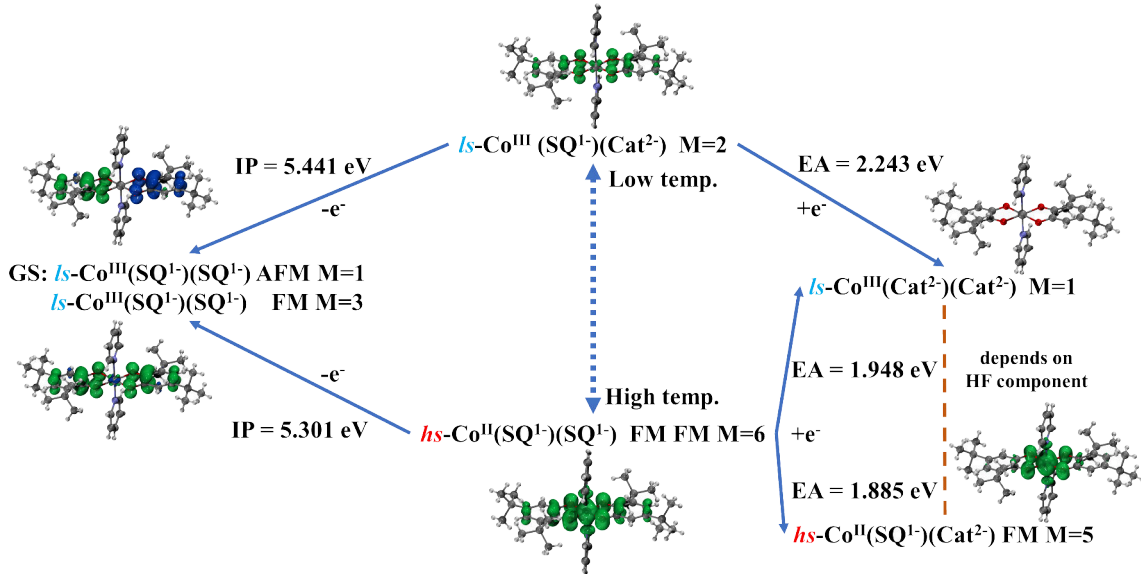


Figure 5.15.: The stable electronic configurations with the corresponding spin density isosurfaces of the differently charged CoL_2 unit form **c-CoDAE** under low (100 K) and high (380 K) temperature based on B3LYP KS-DFT.

In the positively charged case $[\text{CoL}_2]^+$, the system always converged to the II⁺ configuration as the ground state with a closed-shell $ls\text{-Co}^{\text{III}}$ center and a pair of AFM coupled semiquinonate radicals. The two semiquinonate ligands could also be FM coupled with a slightly higher energy. Based on the B3LYP KS-DFT results, the differences are 0.0158 eV and 0.0052 eV for the low and high temperature molecular structures, respectively. In the negatively charged case $[\text{CoL}_2]^-$, the system with a low temperature molecular structures likely converged to the I⁻ configuration with a closed shell. However, the results are divided for a high temperature molecular structures, which depends on the ratio of exact-exchange. The system may con-

verge to the V^- configuration with a $hs\text{-Co}^{\text{II}}$ center and a FM coupled semiquinonate ligand. Here, PBE, TPSSh, and B3LYP predicted the I^- configuration. PBE0 with more exact-exchange admixture predicted the V^- one.

5.8. Determining a suitable U for the systems

As in the method used to determine the values of vacuum on-site Coulomb repulsion ($U^{(v)}$) for the DAEpy linker, the $U^{(v)}$ of the CoL_2 units could also be calculated as long as knowing the most stable configuration of the charged states, which has been done above. The estimated $U^{(v)}$ values are from 3.146 eV to 3.380 eV based on B3LYP KS-DFT (Table 5.4), the values are close for the different CoL_2 units. However, as forming a crystal structure, the environment becomes polarizable, and the charged molecule is able to be stabilized by the shielding effect of surrounding molecules, which reduces the effective on-site Coulomb repulsion (U). As another approach, the intra Coulomb integral of the singly occupied molecular orbital (SOMO) of CoL_2 shows a significantly large value (more than 2.6 eV in average). Because in such a case, the gain and loss of an electron only happen in the SOMO, the entire electronic structure does not relax.

Table 5.4.: The vacuum on-site Coulomb repulsion ($U^{(v)}$) estimated by the IP and EA (Equation 5.1), and the Coulomb integral of the SOMO of CoL_2 with the low temperature molecular structure, $\langle \varphi^{\text{SOMO}} \varphi^{\text{SOMO}} | \frac{1}{\|\mathbf{r}\|} | \varphi^{\text{SOMO}} \varphi^{\text{SOMO}} \rangle$, where φ^{SOMO} is the spatial part of the SOMO single-particle Kohn-Sham wavefunction and $\|\mathbf{r}\|$ represents the distance between two electrons in the SOMO.

$\text{CoL}_2(100K)$	$U^{(v)} = \text{IP-EA (eV)}$	Coulomb integral
Closed(Co1)	3.198	5.628
Open(Co1;Asymm)	3.380	6.483
Open(Co2;Symm)	3.146	5.457

As we found above, GGA functionals are not able to correctly describe the system. The computational complexity of the exact-exchange term in a PBC system limits applying a hybrid-GGA functional (*e.g.*, B3LYP, PBE0) to such large systems.

As a possible solution, the GGA+ U method adds an artificial effective on-site Coulomb repulsion term U_{eff} to describe systems with localized d and f -electrons [147]. It successfully predicted an insulator behavior of the NiO system rather than metal by pure GGA [148]. U_{eff} plays a role to open a bandgap turning partial filled bands into two sets of fully filled bands with an energy separation.

For CoL_2 , to determine a suitable U_{eff} , it requires a fair description of the *low-spin* and the *high-spin* states as above. The CoL_2 units with the low and high temperature molecular structures are placed in a cell ($20\text{\AA} \times 24\text{\AA} \times 20\text{\AA}$) which is able to separate two adjacent fragments apart without overlapping. Unlike an isolated system, only the initial magnetic moment for each atom could be assigned as the initial guess for a DFT calculation with PBC, due to the limitation of the software. Thus, the various combinations of the initial magnetic moment were used for the CoL_2 units with the low and high temperature molecular structures. The PBE functional was used with a U_{eff} ranging from 0 to 20 eV applied on the d electrons in the cobalt. The final electron configurations and the corresponding spin density isosurfaces are listed in Table 5.5 and Figure D.16. Here, the \mathbf{V} configuration and the \mathbf{I} correspond to the *low-spin* state $ls\text{-Co}^{\text{III}}(\text{Cat}^{2-})(\text{SQ}^-)$ and the *high-spin* state $hs\text{-Co}^{\text{II}}(\text{SQ}^-)_{\text{FM}}(\text{SQ}^-)_{\text{FM}}$ respectively.

As a requirement, the *low-spin* state should have a lowest energy in the low temperature molecular structure, and it requires an analogous condition for the *high-spin* state, thus when $6\text{ eV} \leq U_{\text{eff}} \leq 10\text{ eV}$, the conditions are satisfied (Figure 5.16). To avoid other metastable states possibly having a lower energy than the *low-spin* state, the lowest possible $U_{\text{eff}} = 6\text{ eV}$ was selected.

Table 5.5.: The possible electronic configurations of CoL_2 for PBC calculations. The converged spin values by summing over the atomic Mulliken spin of the fragments based on the PBE functional KS-DFT with the effective on-site Coulomb repulsion U_{eff} applied on the d electrons in the cobalt. The possible setting of U_{eff} and the molecular structures to converge the wavefunction to the desired configuration.

Configuration					Spin			U_{eff} (eV)	geom.
	Co	L1	L2		Co	L1	L2		
I	II	<i>hs</i>	FM	FM	2.87	0.69	0.69	$0 \sim 20$	<i>hs, ls</i>
II	II	<i>hs</i>	AFM	FM	2.80	-0.49	0.61	$2 \sim 20$	<i>hs</i>
III	II	<i>hs</i>	AFM	FM	2.86	0.05	0.05	$1 \sim 20$	<i>hs</i>
IV	II	<i>hs</i>	AFM	AFM	2.67	-0.56	-0.56	$4 \sim 20$	<i>hs</i>
V	III	<i>ls</i>	0	FM	0.00	0.33	0.33	$0 \sim 20$	<i>hs, ls</i>
VI	III	<i>ls</i>	AFM	FM	0.00	0.28	-0.28	$1 \sim 20$	<i>hs, ls</i>
VII		0	0	0	0.00	0.00	0.00	$0 \sim 20$	<i>hs, ls</i>
VIII	II	<i>ls</i>	F	FM	1.13	0.64	0.64	$4 \sim 20$	<i>hs</i>
IX	II	<i>ls</i>	AFM	FM	1.23	-0.06	-0.06	$4 \sim 20$	<i>hs</i>
X					1.57	0.03	0.03	$5 \sim 6$	<i>hs</i>
XI	III	<i>hs</i>	0	FM	1.89	0.33	0.33	$3 \sim 14$	<i>ls</i>

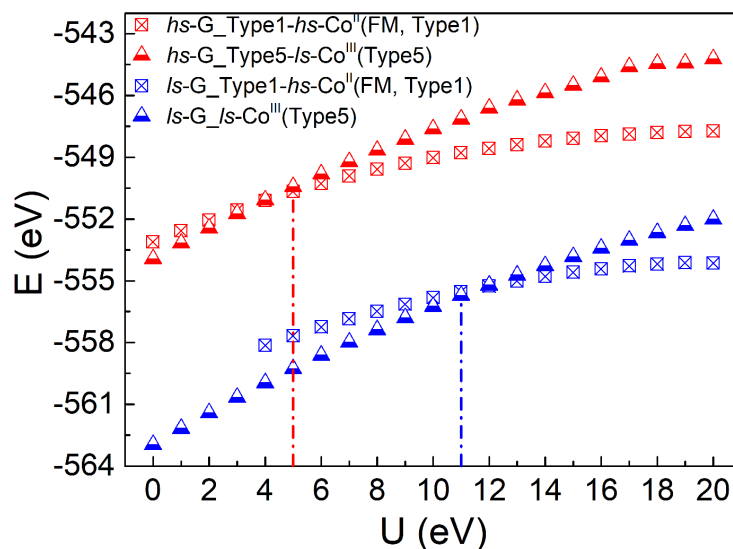


Figure 5.16.: The energies of the *low-spin* and the *high-spin* configured CoL_2 in the low and high temperature molecular structures versus U_{eff} applied on the d electrons of cobalt.

5.9. The complex of tautomeric building block and photochromic bridging ligand

For the CoL_2 units linked by DAEpy bridging ligands, the crystal systems are not able to be treated like a pile of stacking individual molecules, since the orbitals could be mixed significantly. Thus, the frontier molecular orbitals of the complex CoL_2DAEpy may be the mixtures of the frontier orbitals of the fragments (*i.e.*, CoL_2 , DAEpy).

Here, the frontier molecular orbitals were calculated based on B3LYP KS-DFT for the *low-spin* configuration in low temperature molecular structure. As shown in Figure D.22, the LUMO of the open DAEpy is slightly lower than the α -spin LUMO of the CoL_2 unit, and the LUMO of the closed DAEpy is lower than the both α and β -spin LUMO of the CoL_2 unit. But the HOMOs of the two forms of DAEpy are lower than the HOMO of the CoL_2 unit. Thus, the complexes' HOMOs of both spin components are nearly identical with the corresponding CoL_2 units', the LUMOs of the closed-form complex are nearly the same as the LUMO of the closed DAEpy linker. The β component LUMOs of the open-form complexes are still located on the CoL_2 units, but the α component LUMOs of the open-form complexes consist of the LUMO of the open-form DAEpy core and the LUMO of the pyridine (Figure 5.17). The above conclusions are valid for the results based on PBE as well (Figure 5.17).

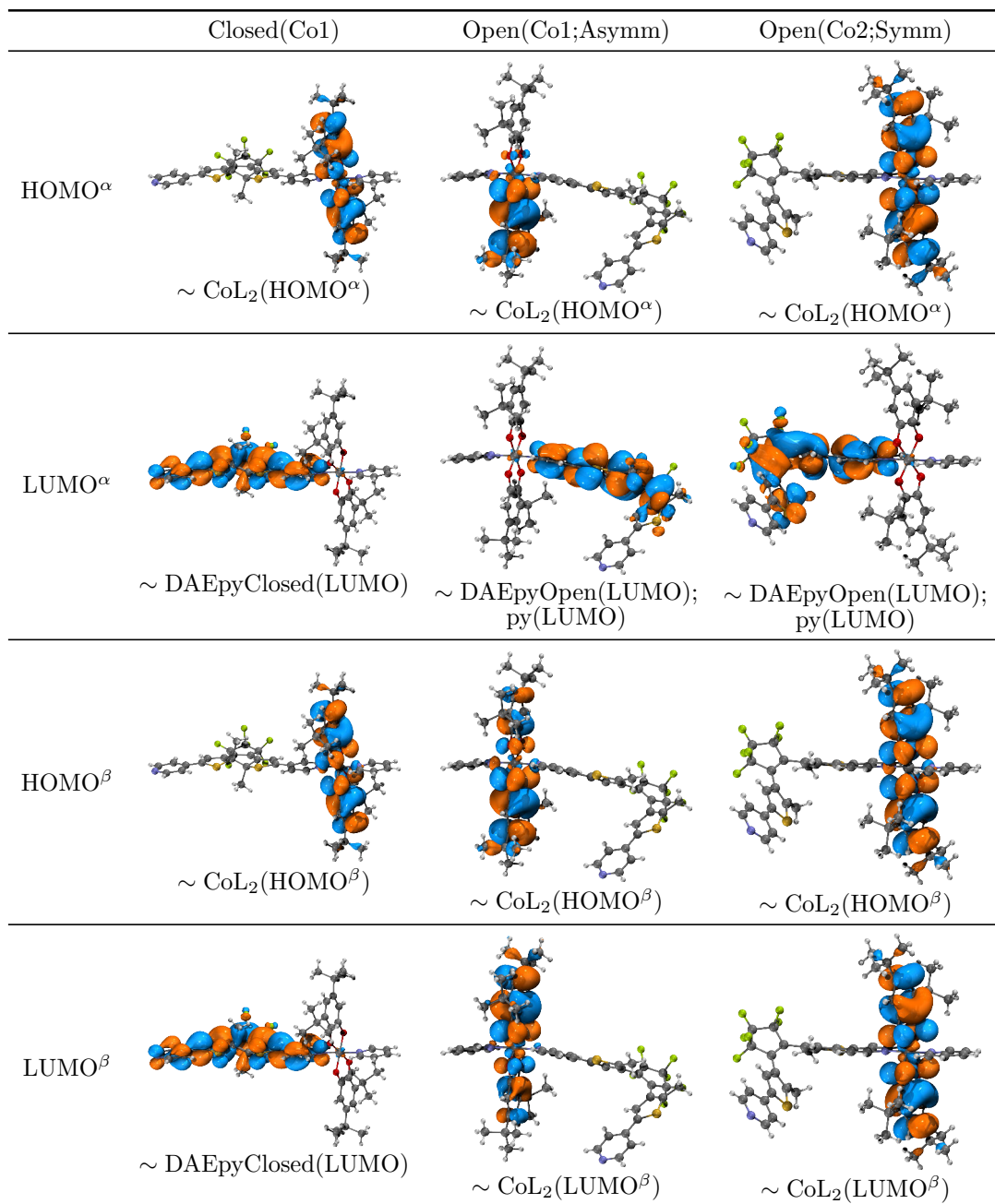


Figure 5.17.: The molecular orbital isosurfaces of the *low-spin* CoL₂DAEpy complexes in low temperature molecular structures (100 K) based on B3LYP KS-DFT.

To clarify possible photon-induced charge transfer processes, the low-lying excited states of the CoL₂DAEpy complexes are calculated by the CAM-B3LYP TD-DFT method. The corresponding simulated UV-vis spectra and the orbital contributions for each excitation represented by the hole-electron distributions are shown in Figure D.23 – D.28. All excitations with a large amplitudes are mainly localized on a fragment, the DAEpy core or the CoL₂ unit, but not between DAEpy and CoL₂. This means the charge transfer processes should happen between CoL₂ units or

between DAEpy cores.

Due to the frontier orbitals of the CoL_2DAEpy complexes having contributions from the DAEpy linker, the additional charge could also be localized on the linker. Thus, it is necessary to determine the stabilize charged states. Because the *low-spin* configuration dominates at low temperature, only the *low-spin* configurations with low temperature molecular structures were explored as shown in Table 5.6. The single-point energies and the corresponding IP or EA were calculated based on B3LYP KS-DFT (Table D.18 – D.18).

Table 5.6.: Possible singly positively charged or singly negatively charged configurations of the CoL_2DAEpy complexes.

$[\text{CoL}_2\text{DAEpy}]^+$			$[\text{CoL}_2\text{DAEpy}]^-$		
1^P	$ls\text{-Co}^{\text{III}}(\text{SQ}^-)(\text{SQ}^-)_{\text{AFM}}(\text{DAEpy}^0)$		4ⁿ	$ls\text{-Co}^{\text{III}}(\text{Cat}^{2-})(\text{Cat}^{2-})(\text{DAEpy}^0)$	
2^P	$ls\text{-Co}^{\text{III}}(\text{Cat}^{2-})(\text{SQ}^-)(\text{DAEpy}^+)_{\text{FM}}$		5ⁿ	$ls\text{-Co}^{\text{III}}(\text{Cat}^{2-})(\text{SQ}^-)(\text{DAEpy}^-)_{\text{FM}}$	
3^P	$ls\text{-Co}^{\text{III}}(\text{Cat}^{2-})(\text{SQ}^-)(\text{DAEpy}^+)_{\text{AFM}}$		6ⁿ	$ls\text{-Co}^{\text{III}}(\text{Cat}^{2-})(\text{SQ}^-)(\text{DAEpy}^-)_{\text{AFM}}$	

In the singly positively charged case $[\text{CoL}_2\text{DAEpy}]^+$, all calculation consistently predicted the **1^P** ground state regardless of the initial guess, where the oxidation happens on the CoL_2 unit keeping the DAEpy linker in a charge neutral state. The resulting two semiquinonate ligands are AFM coupled. In the singly negatively charged case $[\text{CoL}_2\text{DAEpy}]^-$, the energy difference between the closed-shell **4ⁿ** configuration and the diradical configuration **6ⁿ** is quite small (Figure D.29). For the **6ⁿ** configuration, there are an unpaired electron on both SQ^- and DAEpy^- which are AFM coupled. The diradical configurations are 0.01 eV, 0.004 eV, 0.087 eV more stable than the closed-shell configurations of the open-form asymmetric complex (Co1), the open-form symmetric complex (Co2), and the closed-form complex (Co1) respectively. Here the closed-form complex prefers the diradical configuration due to a lower LUMO of the closed DAEpy.

5.10. The dimer of the tautomeric building block ($[\text{CoL}_2]_2$)

To understand the details of the electronic structure, it is essential to figure out the magnetic coupling between the CoL_2 units in the low temperature molecular structures. The energy difference between the pairs of CoL_2 units which are adjacent in space or connected by the DAEpy linker were calculated based on the selected exchange–correlation functionals (Table D.21). The *low-spin* electronic configuration $ls\text{-Co}^{\text{III}}(\text{Cat}^{2-})(\text{SQ}^-)$ was selected for each monomer. In the **o-CoDAE** case,

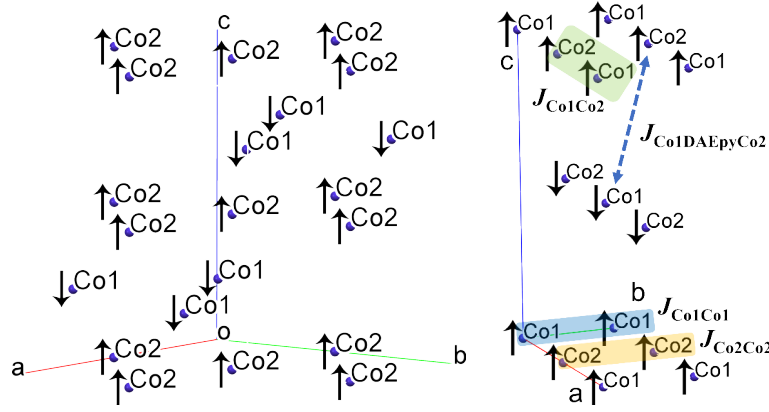


Figure 5.18.: The magnetic coupling between any two CoL_2 units is almost negligible in both crystals, for the open-form (left) and the closed-form (right). But the interlayer AFM phase is slightly more stable compared with others.

the adjacent pair of CoL_2 units in the symmetric layers are weakly FM coupled, same as the units in the asymmetric layer based on the B3LYP data, but the interlayer couplings are negligible small. However, the GGA functionals (*e.g.*, PBE, TPSS) get a weak AFM coupled result between the symmetric and the asymmetric layer. Thus, **o-CoDAE** forms interlayer-AFM-coupled layers, where CoL_2 units in a same layer are FM coupled (Figure 5.18, left). In the **c-CoDAE** case, the adjacent pair of CoL_2 units are weakly FM coupled along the *a* and *b* axes. The units linked by the closed-form DAEpy are weakly AFM coupled based on the B3LYP data. The above couplings result in two kinds of CoL_2 chains located at the edge and the center of the unit cell, which are intrachain FM coupled and interchain AFM coupled (Figure 5.18, right). For VASP PBC calculations, the magnetic coupling between two CoL_2 units for this system is not sensitive to the computational parameters (*e.g.*, kinetic energy cutoff, cell size, U_{eff} value) according to the result from the Co1-Co2 dimer in **c-CoDAE** (Table D.22). It has to be mentioned that the couplings are quite weak, on the order of 10^{-2} cm^{-1} , even smaller than the thermal fluctuations at liquid-helium temperature, thus the two systems should be in paramagnetic states under the experimental conditions.

5.11. Band structures of **c-CoDAE** and **o-CoDAE**

To get the electronic structures of **o-CoDAE** and **c-CoDAE**, the band structures and the corresponding DOS are calculated by PBE KS-DFT with applying an effective on-site Coulomb repulsion of $U_{\text{eff}} = 6 \text{ eV}$ on the *d* electrons of the cobalt atoms. Although the magnetic couplings are small in both cases, the initial mag-

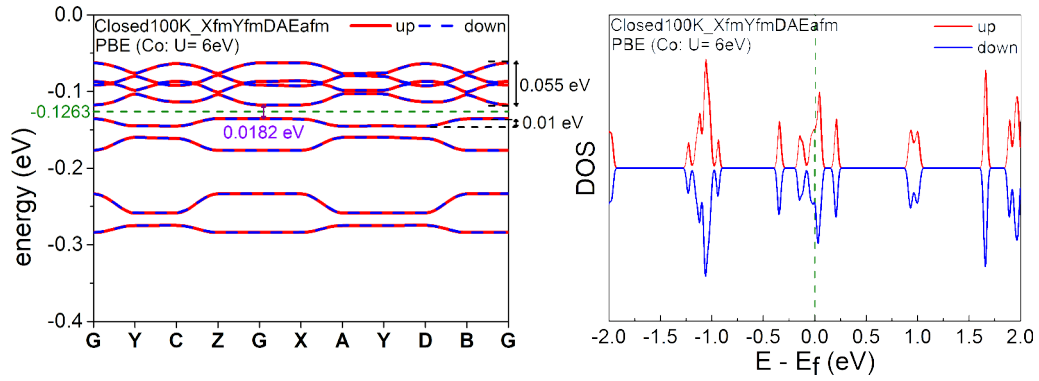


Figure 5.19.: The PBE+U band structure (left) and DOS (right) of the *low-spin c-CoDAE* in the low temperature (100 K) crystal structure, where $U_{\text{eff}} = 6$ eV. In the left part, the red lines and the blue dash lines represent the spin-up (α) and spin-down (β), respectively. The green dash line represents the Fermi level. G(0.0,0.0,0.0); X(0.5,0.0,0.0); Y(0.0,0.5,0.0); Z(0.0,0.0,0.5); A(0.5,0.5,0.0); B(0.5,0.0,-0.5); C(0.0,0.5,0.5); D(0.5,0.5,-0.5).

netic moment were configured according to the CoL_2 dimer calculations, with the AFM interlayer magnetic ordering for **o-CoDAE** and AFM interchain magnetic ordering for **c-CoDAE**.

According to the band structure of **c-CoDAE** and the energy levels of the isolated CoL_2DAEpy complex, the topmost four valence bands consist of the HOMOs of the four CoL_2 units, and the bottommost four conduction bands consist of the LUMOs of the four closed-form DAEpy linkers. The topmost valence band and the bottommost four conduction bands have a 0.01 eV and a 0.055 eV bandwidth, respectively. From the band structure of **o-CoDAE**, the α component has flat bands at 0.51 eV, which are just below the Fermi level, consisting of the linear combinations of the HOMOs^α of the CoL_2 in the asymmetric layer. The bandwidth is 2.7×10^{-3} eV, and the bandwidth of the corresponding β flat bands is 1.7×10^{-3} eV. The lower α component flat bands represent the components from the HOMOs^α of the CoL_2 in the symmetric layer. The bottommost six conduction bands with α spin consist of the LUMOs of the open-form DAEpy, and the corresponding bandwidth is 2.9×10^{-3} eV. The bottommost six conduction bands with β spin consist of the LUMOs^β of the CoL_2 units, and the corresponding bandwidth is 2.9×10^{-3} eV.

From the band structures, both cases show the characteristics of a semiconductor. The band gap of **c-CoDAE** (0.0182 eV) is one order smaller than **o-CoDAE** (0.2141 eV). Both of them should have a high conductivity, but this is not consistent with the experimental results.

One possible explanation is that due to the bulky *t*-Bu groups, the effective overlap

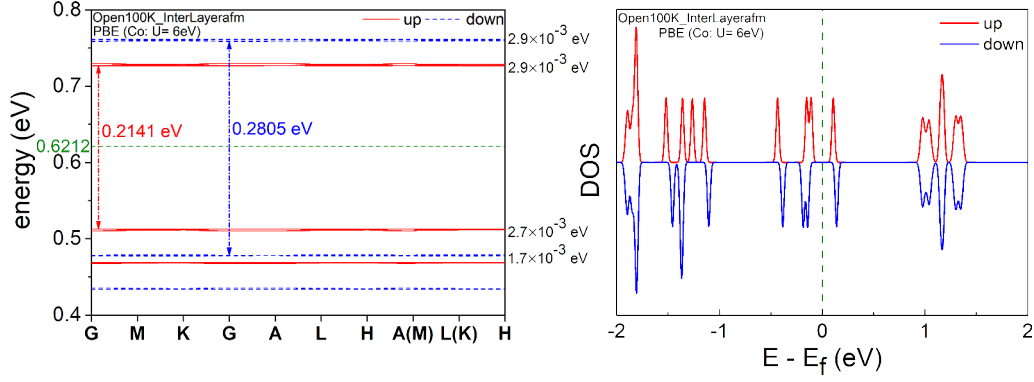


Figure 5.20.: The PBE+U band structure (left) and DOS (right) of the *low-spin o-CoDAE* in the low temperature (100 K) crystal structure, where $U_{\text{eff}} = 6$ eV. In the left part, the red lines and the blue dash lines represent the spin-up (α) and spin-down (β), respectively. The green dash line represents the Fermi level. G(0.0,0.0,0.0); A(0.0,0.0,0.5); L(0.5,0.0,0.5); M(0.5,0.0,0.0); K(1/3,1/3,0.0); H(1/3,1/3,0.5).

between two CoL₂ units' frontier orbitals is not sufficient, leading such small bandwidths ($10^{-3} - 0.05$ eV), and the effective on-site Coulomb repulsion is comparable huge. The values of the vacuum on-site Coulomb repulsion $U^{(v)}$ are 3.146 – 3.380 eV for the CoL₂ units, 4.781 eV for the closed-form DAEpy, and 6.728 eV for the open-form DAEpy based on B3LYP. The shielding effect could reduce the final effective repulsion, but the values should at least be an order larger than the bandwidths. Thus, the electrons should be localized on the fragments, leading the system into a hopping conductive region, which is not able to be captured by the PBE+U band structure.

5.12. Electron transfer matrix elements between CoL₂ units

To unveil the mechanism of electronic conductivity and the peak of conductivity for **o-CoDAE** (Figure 5.10, middle), the electron transfer rate (k_{ET}) defined by Marcus' theory is an alternative for explaining. It is depended on the electron transfer matrix element (\mathbf{V}_{ab}) between the reactant state ($|\psi_a\rangle$: $A^{+/-} + B$, a charge localized on A) and the product state ($|\psi_b\rangle$: $A + B^{+/-}$, a charge localized on B), the nuclear reorganization energy (λ), and the temperature (T) (Equation 5.2) [149]. The electron transfer matrix element (also called the electronic coupling energy) could be calculated by the corresponding matrix elements of the Hamiltonian (\mathbf{H}_{aa} ,

\mathbf{H}_{bb} , \mathbf{H}_{ab}) and the overlap integral (\mathbf{S}_{ab}), which implemented in Northwest Computational Chemistry Package (NWChem 6.8) (Equation 5.3) [150]. The basis set 6-31G** and 6-311G** were used for the cobalt atom and the other atoms respectively. The range separated hybrid functional rCAM-B3LYP was used for stabilizing the charge on a site.

$$k_{\text{ET}} = \frac{2\pi}{\hbar} \mathbf{V}_{ab}^2 \frac{1}{\sqrt{4\pi\lambda k_B T}} \exp\left(\frac{-\Delta G^*}{k_B T}\right) \quad (5.2)$$

$$\mathbf{V}_{ab} = \frac{\mathbf{H}_{ab} - \mathbf{S}_{ab}(\mathbf{H}_{aa} + \mathbf{H}_{bb})/2}{1 - \mathbf{S}_{ab}^2} \quad (5.3)$$

$$\begin{aligned} \mathbf{H}_{aa} &= \langle \psi_a | \hat{H} | \psi_a \rangle & \mathbf{H}_{bb} &= \langle \psi_b | \hat{H} | \psi_b \rangle & \mathbf{H}_{ab} &= \langle \psi_a | \hat{H} | \psi_b \rangle \\ \mathbf{S}_{ab} &= \langle \psi_a | \psi_b \rangle \end{aligned}$$

The *high-spin* CoL₂ units are the majority at high temperature, *low-spin* states at low temperature. At certain temperature, the neutral CoL₂ units with the corresponding spin-state are the majority species in the crystal lattice as the background environment. Due to the nature of semiconductors, only a very small number of CoL₂ units are thermally excited to charged states. The charged CoL₂ units are embedded in the background. Here, only the singly charged cases were considered. The singly positively and the singly negatively charged CoL₂ units with various electronic configurations need to be taken into account as the charge carrier could either be hole or electron. The possible configurations of the charge transfer pairs are listed in Table 5.7. Here, the electron transfer matrix elements between two adjacent or DAEpy-connected CoL₂ units with the above configurations were calculated as shown in Table 5.8. There are a few observations.

When the neutral unit is in the *high-spin* state, the only possible configuration is **6**, the carrier is an electron, which also indicates the matrix element is zero if the spin states of two cobalt centers are different.

In **c-CoDAE**, the charge transfer events likely happen along the *b* axis (the CoL₂ pairs of Co1–Co1 and Co2–Co2), and it is higher than **o-CoDAE**, but the matrix elements along the *a* (Co1–Co2) or *c* (can be ignored as two CoL₂ units are far apart) axis are much lower than along the *b* axis or even compared with **o-CoDAE**.

In **o-CoDAE**, for the *low-spin* neutral unit, the matrix element of the units in the symmetric layer (sCo2–sCo2) is larger than the units in the asymmetric layer (asCo1–asCo1-t1/t2/t3) or the units in two different layers (asCo1–sCo2-t1/t2/t3). For the *high-spin* neutral unit, the asCo1–asCo1-t3 pairs of the CoL₂ also show a comparably high value, but they can only form a local triangle, so the rate should be limited by the electron transfer rate between the asCo1–asCo1-t2 pairs (Figure

D.30). This means the charge hopping events mainly happen in the symmetric CoL₂ layer, and **o-CoDAE** behaves as a 2D semiconductor.

Table 5.7.: The possible electronic configurations of a CoL₂ pair during the charge transfer process.

Config.	Neutral unit	Charged unit	Intermolecular coupling	Charge
1	<i>hs</i> -Co ^{II} (SQ ⁻) _{FM} (SQ ⁻) _{FM}	<i>ls</i> -Co ^{III} (SQ ⁻)(SQ ⁻) _{AFM}	AFM	1
2		<i>ls</i> -Co ^{III} (SQ ⁻)(SQ ⁻) _{AFM}	FM	1
3		<i>ls</i> -Co ^{III} (SQ ⁻)(SQ ⁻) _{FM}	AFM	1
4		<i>ls</i> -Co ^{III} (SQ ⁻)(SQ ⁻) _{FM}	FM	1
5		<i>hs</i> -Co ^{II} (Cat ²⁻)(SQ ⁻) _{FM}	AFM	-1
6		<i>hs</i> -Co ^{II} (Cat ²⁻)(SQ ⁻) _{FM}	FM	-1
7		<i>ls</i> -Co ^{III} (Cat ²⁻)(Cat ²⁻)		-1
8	<i>ls</i> -Co ^{III} (Cat ²⁻)(SQ ⁻)	<i>ls</i> -Co ^{III} (SQ ⁻)(SQ ⁻) _{AFM}	AFM	1
9		<i>ls</i> -Co ^{III} (SQ ⁻)(SQ ⁻) _{AFM}	FM	1
10		<i>ls</i> -Co ^{III} (SQ ⁻)(SQ ⁻) _{FM}	AFM	1
11		<i>ls</i> -Co ^{III} (SQ ⁻)(SQ ⁻) _{FM}	FM	1
12		<i>ls</i> -Co ^{III} (Cat ²⁻)(Cat ²⁻)		-1

Table 5.8.: The electron transfer elements (Equation 5.3) in the different electronic configurations for the adjacent pairs.

High temperature configuration ET elements (eV)							
CoL ₂ pair	1 (hole)	2 (hole)	3 (hole)	4 (hole)	5 (elec)	6 (elec)	7 (elec)
Closed(Co1-Co2)	0.0000	0.0000	0.0000	0.0000	0.0000	0.0157	0.0000
Closed(Co1-Co1)	0.0000	0.0000	0.0000	0.0000	0.0000	1.5926	0.0000
Closed(Co2-Co2)	0.0000	0.0000	0.0000	0.0000	0.0000	0.0338	0.0000
Open(asCo1-asCo1-t1)	0.0000	0.0000	0.0000	0.0000	0.0000	0.0001	0.0000
Open(asCo1-asCo1-t2)	0.0000	0.0000	0.0000	0.0000	0.0000	0.0725	0.0000
Open(asCo1-asCo1-t3)	0.0000	0.0000	0.0000	0.0000	0.0000	0.2044	0.0000
Open(asCo1-sCo2-t1)	0.0000	0.0000	0.0000	0.0000	0.0000	0.0001	0.0000
Open(asCo1-sCo2-t2)	0.0000	0.0000	0.0000	0.0000	0.0000	0.0001	0.0000
Open(asCo1-sCo2-t3)	0.0000	0.0000	0.0000	0.0000	0.0000	0.0105	0.0000
Open(sCo2-sCo2)	0.0000	0.0000	0.0000	0.0000	0.0000	0.1515	0.0000
Low temperature configuration ET elements (eV)							
CoL ₂ pair	8 (hole)	9 (hole)	10 (hole)	11 (hole)	12 (elec)		
Closed(Co1-Co2)	0.5057	0.2812	0.0000	0.1495	0.1321		
Closed(Co1-Co1)	0.0108	2.1622	0.0000	4.8475	5.2183		
Closed(Co2-Co2)	1.1068	0.0068	0.0000	2.6516	2.5855		
Open(asCo1-asCo1-t1)	0.0004	0.0004	0.0000	0.1642	0.0125		
Open(asCo1-asCo1-t2)	0.0001	0.0000	0.0000	0.0000	0.0321		
Open(asCo1-asCo1-t3)	0.0006	0.0000	0.0000	0.0001	0.0069		
Open(asCo1-sCo2-t1)	0.1322	0.0000	0.0000	0.0000	0.0146		
Open(asCo1-sCo2-t2)	0.0109	0.0641	0.0000	0.0000	0.6780		
Open(asCo1-sCo2-t3)	0.0018	0.0000	0.0000	0.0068	0.0567		
Open(sCo2-sCo2)	1.5395	0.1161	0.0000	0.2702	0.9400		

5.13. Discussion

The hybrid compounds **o-CoDAE** and **c-CoDAE** were synthesized from the photochromic linker DAEpy and the valence tautomer building block CoL₂. To unveil the corresponding conductive mechanism, the related electronic structures are studied.

According to the results, the B3LYP functional is able to fairly describe the different spin states of the low and the high temperature structures. At low temperature, the CoL₂ units are in the *low-spin* state $ls\text{-Co}^{\text{III}}(\text{Cat}^{2-})(\text{SQ}^-)$, while at high temperature, the CoL₂ units are in the *high-spin* state $hs\text{-Co}^{\text{II}}(\text{SQ}^-)_{\text{FM}}(\text{SQ}^-)_{\text{FM}}$.

The PBE+U band structures show the two systems should show high conductivity due to small band gaps, but this contradicts the experimental results. Here, the effective on-site Coulomb repulsion was only added on the *d* electrons of cobalt atoms, but the bands close to the Fermi level mainly consist of the frontier orbitals of the organic ligands. In principle, by using a hybrid functional (*e.g.*, B3LYP, PBE0), it is possible to solve the overdelocalization problem to predict a more accurate band gap, but it requires to calculate the exact-exchange term which is expensive for PBC, such that for such a large system, it is nearly unaffordable. According to the band structures and the calculations for the isolated systems, the vacuum on-site Coulomb repulsion is much larger than the bandwidths. This means the two system are likely in a spin-localized state as a Mott insulator. Furthermore, a band structure can only reflect a conductivity pathway in which the electrons are added or removed from the bands in the vicinity of the Fermi level without electron configuration relaxation and without lattice relaxation. For the **o-CoDAE** and **c-CoDAE** cases, the hopping mechanism should dominate the conductivity, thus the charged CoL₂ units could be relaxed into a new configuration with a lower energy. For the positively charged CoL₂ units, the $ls\text{-Co}^{\text{III}}(\text{SQ}^-)(\text{SQ}^-)_{\text{AFM}}$ configuration is the ground state, which means even at high temperature, the spin state of cobalt should convert from $hs\text{-Co}^{\text{II}}$ to $ls\text{-Co}^{\text{III}}$. For the negatively charged CoL₂ units, the closed-shell $ls\text{-Co}^{\text{III}}(\text{Cat}^{2-})(\text{Cat}^{2-})$ and the open-shell $hs\text{-Co}^{\text{II}}(\text{Cat}^{2-})(\text{SQ}^-)_{\text{FM}}$ configurations have close energies. The electron transfer matrix elements were calculated based on the above electronic configurations and the pairwise relations of the CoL₂ units in the two crystals. As results, **o-CoDAE** shows the properties of a 2D semiconductor in the *ab* plane, while the symmetric CoL₂ layers play the main role for conductivity. This is consistent with the anisotropic conductivity experimental result (Figure 5.10, right). **c-CoDAE** shows a high conductivity along the *b* axis, but the matrix elements are much lower along the other two axes, thus it behaves like a 1D semiconductor. This result could also be used to explain the

contradiction with the experiment: needle-shaped crystals are common forms for a unit cell with low symmetries (*e.g.*, monoclinic), for which is not easy to determine the orientations of the cell axes by face indexing, thus the measurement could be made along the other two axes with low conductivity. For the powder sample, due to the 1D conductor having the main contribution from one direction, the percolation possibility should be much lower than for the 2D or 3D conductor, and the transfer of electrons on one microcrystal could be blocked by the other microcrystal, if their orientations are different. At low temperature, the charge carriers could be electrons and holes, but at high temperature, it only could be electrons, because the electron transfer matrix elements between different spin states of cobalt are zero. Therefore, at high temperature, the possible conductive pathways and the amplitudes are much less compared with at low temperature.

For **o-CoDAE**, as the temperature increases, the density of the carrier increases due to thermal excitation, which is normal for a semiconductor, thus the conductivity increases. At around 300 K, the spin states of the CoL_2 units start to convert from *low-spin* to *high-spin*, thus a CoL_2 unit could be surrounded by other units with different spin states. Then the electron transfer rate decreases to zero as above, which leads to the conductivity to drop, which could explain why the peak of the conductivity was observed.

6. The conduction behavior of layered single-molecule-magnet organic-conductor hybrid compound

6.1. Background

In 1911, the superconductivity phenomenon was discovered in solid mercury under at liquid-helium temperature [151]. The material shows zero electronic resistance and the iconic Meissner effect [152]. Later in 1957, the Bardeen–Cooper–Schrieffer (BCS) theory was proposed [153, 154]. This theory explains superconductivity as caused by a condensation of Cooper pairs, a pair of electrons bound together by phonons (the vibrating crystal lattice). Such materials were classified as type-I superconductors (*e.g.*, pure metal systems, alloys, *etc.*). However, with the discovery of more types of superconductors, for some of them, the critical temperature is far beyond the prediction by BCS theory. These are so-called type-II superconductors (*e.g.*, the YBCO family, iron-based superconductors, MgB_2 , organic superconductors, *etc.*). Unlike the type-I superconductors, the type-II superconductors allow some magnetic flux to penetrate the material and form a mixed state above a certain critical magnetic field strength H_{c1} . But the superconductive property still breaks down if the magnetic field strength is larger than the high critical point H_{c2} .

As a significant extension, the discovery of unconventional organic superconductors (fulvalenes, doped fullerenes) enables a new path to tune material properties by using synthetic chemistry. It provides more possibilities and exploration directions for revealing the mechanism of superconductivity. In 1979, the first organic superconductor $(\text{TMTSF})_2\text{PF}_6$ was synthesized by the Bechgaard group [155]. Here, $(\text{TMTSF})_2\text{PF}_6$ is the abbreviation of di-(tetramethyltetraselenafulvalene)-hexafluorophosphate. Later an organosulfur compound tetrathiafulvalene (TTF) with a similar structure also inspired many studies [156]. Due to the na-

ture of fulvalene derivatives, the various types of inter-molecular interaction lead to a polymorphism of the TTF packing pattern (Figure 6.1). For the β , β' , κ , and λ phases, the TTF molecules are strongly dimerized, a pair of TTF molecules stacks closer than others, could be treated as a hopping site, where the intra-site Coulomb repulsion could be neglected. For the α , β'' , and θ phases, the dimerization is weak or absent, the arrangement is more even. The electronic structures of the TTF complexes are sensitive to a tiny change of the structure which is even caused by temperature, hydrostatic and chemical pressure. The various packing patterns could tune the possible pathway of the electron hopping and the effective Coulomb repulsion, leading to enriched properties of this class of compounds.

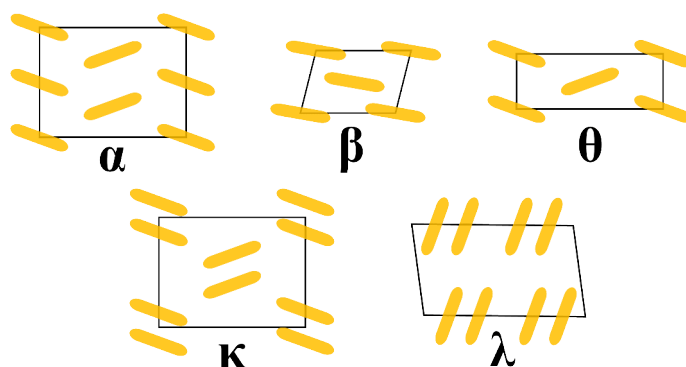


Figure 6.1.: TTF molecules (yellow ellipses) are able to form various 2D stacking modes with certain periodicities (black box) in different crystal phases.

As another leading actor in materials science, single-molecule magnets (SMMs) have aroused a large amount of attention since the discovery of Mn_{12} [157]. Due to the magnetic bistability of SMMs, they have been regarded as versatile candidates for use in various fields, such as qubits, spintronics and other quantum devices [9, 158]. The mismatch between the short coherence time of SMMs and the long duration time of quantum gates' operation is the main issue for spin manipulation [159–161]. A high energy barrier between ground state and excited states is a necessary condition to guarantee to prolong the coherence time. In such cases, the ground state with large angular momentum will be well separated from other energy levels, which means the ground eigenstate is not easy to be contaminated by others. A common strategy is to take advantage of a transition metal's diffuse d orbitals, by linking multiple ion centers through bridging ligands. A strong ferromagnetic exchange coupling binding two neighbor large-spin-state ions can create a stable ground state with high spin number. But for such multicenter SMMs, even though they exhibit a high energy barrier, the coherence time will not be ideal because the ground state could be broadened by phonons and spin flip-flop. In such a case, multiple bridging ligands are required to bind those metal centers together. The

extra atoms bring the additional degrees of freedom of lattice vibration (phonon) and the nuclear spin (*e.g.*, ^1H , ^{13}C), which play a role as a source of perturbation that is able to mix the electronic angular momentum eigenstates by electron–phonon coupling and hyperfine interaction respectively [162]. Those processes could also accelerate decoherent. As an alternative, it has been shown that a ligand field with $C_{\infty v}$, $D_{\infty h}$, S_8 , D_{4d} , D_{5h} , or D_{6d} symmetry can remarkably diminish the off-diagonal terms of the Hamiltonian represented by the total angular momentum base (*e.g.*, for d or f electrons) as under such ligand field, the off-diagonal terms are able to mix Stark sublevels [163, 164]. Altering the symmetry and the hardness-softness of coordinated atoms is also a promising method to give a single metal center based SMM with a high barrier [165].

The incompatibility between the magnetic nature and superconductivity as a former dogma has been broken by the discovery of iron-based superconductors [166, 167]. It encourages us to look at novel superconductors and to unveil the underlying mechanism. Among these, a material coexisting single-molecule magnetism and superconductivity is always a popular direction of exploration. It is possible to achieve a long coherence time of the magnetic ground state with the help of the Meissner effect, which is able to shield fluctuations of external magnetic fields but also lead to a novel conductive behavior. So far, depositing SMM molecules on superconducting surfaces or detecting the magnetism of a single SMM molecule by a Josephson junction (nano-superconducting quantum interference devices, nano-SQUIDS) are active areas of research [168, 169], but a coordination complex with the two properties has not been found yet.

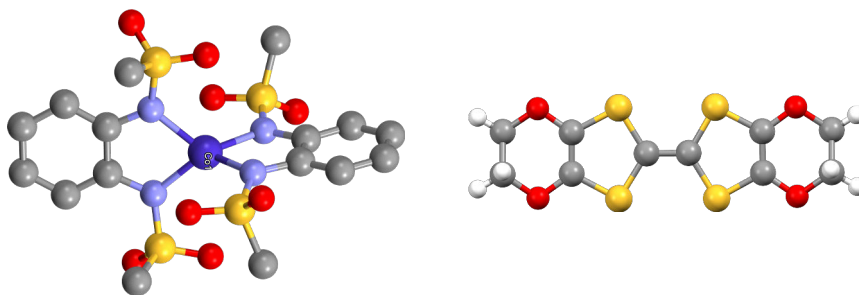


Figure 6.2.: Ball-and-stick models of $\text{Co}(\text{pdms})_2$ (left) and BO (right). The correspondence between atoms and colors, carbon (gray); hydrogen (white); nitrogen (pale violet); oxygen (red); sulfur (yellow); cobalt (dark violet).

As an attempt to combine the above two properties, a layered molecule-based compound, $\beta''\text{-(BO)}_4[\text{Co}(\text{pdms})_2]\cdot 3\text{H}_2\text{O}$ (CoBO_4) was synthesized by using an electrochemical crystallization method by our collaborator Dr. Yongbing Shen. As a well studied TTF derivative, bis(ethylenedioxy)tetrathiafulvalene (BO) is a typical

organic molecular conductor which is easy to be partially oxidized and form a conducting layer. The selected counterion, the single-molecule anion $\text{Co}(\text{pdms})_2$ was discovered by the van Slageren group [170], here pdms represents the deprotonated 1,2-bis(methane sulfonamido)-benzene (Figure 6.2). The content of this chapter has been published [44].

6.2. Geometrical structure

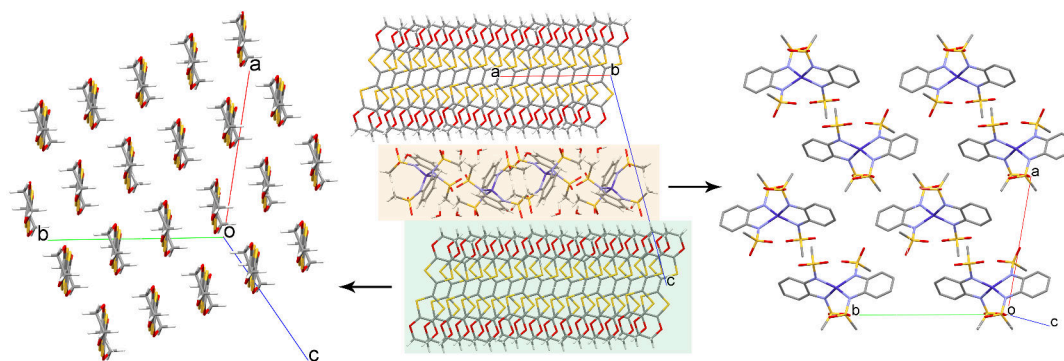


Figure 6.3.: Stick models for the BO layer (left), the packing structure (middle), and the $\text{Co}(\text{pdms})_2$ layer (right) based on the 120 K crystal data.

In general, CoBO_4 crystallizes in the $P\bar{1}$ space group. There are four crystallographically independent BO molecules and one $\text{Co}(\text{pdms})_2$ unit in a unit cell. The centrosymmetric operation doubles the numbers. The BO molecules and the $\text{Co}(\text{pdms})_2$ units form two layers which are stacked alternately. A strong electrostatic interaction exists between the two layers. Due to the nature of the BO molecule, which easily losses an electron, the formal charge of each BO is $+0.5$ on average. $\text{Co}(\text{pdms})_2$ has a formal charge of -2 which could compensate the charge of BO, and the relatively high symmetry of quasi- T_{4d} combined with a cobalt(II) ion with unquenched orbital angular momentum guarantees a relatively high energy barrier to flip the magnetic moment as discussed in the previous report [170]. The nearly homogeneous packing of BO prevents charge localization, leading to a high conductivity.

Due to the symmetry of the $P\bar{1}$ space group, there are eight BO molecules connected by centrosymmetry in a quite large unit cell. To simplify it for further calculations, and a reduced lattice was extracted, a mean structure by averaging the structures of the eight BO molecules was used. All the eight BO molecules can be placed in a same ab plane by translating some BO molecules (along the c vector), then average the Cartesian coordinates of each set of translationally equivalent atoms on the eight BO molecules to give the mean structure (making sure the sequence of the atoms in

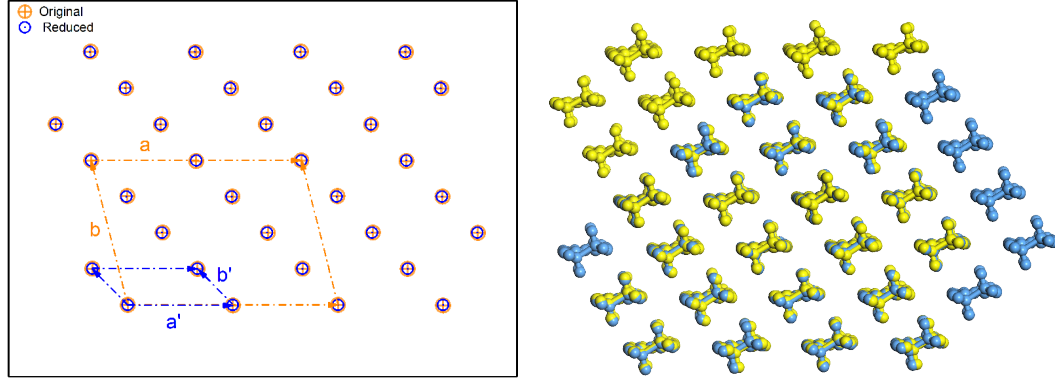


Figure 6.4.: The original BO lattice and the reduced one as employed in the calculations (left). The overlap of original lattice (yellow) and the reduced lattice (blue) (right).

each BO molecule is same). The new lattice axes were defined as, $a' = \frac{a}{2}$, $b' = \frac{b}{4} - \frac{a}{8}$, $c' = c$. The reduced structure is shown in Table E.1. According to the comparison between the original lattice and the reduced lattice, the deviation is small (Figure 6.4).

6.3. Experimental results

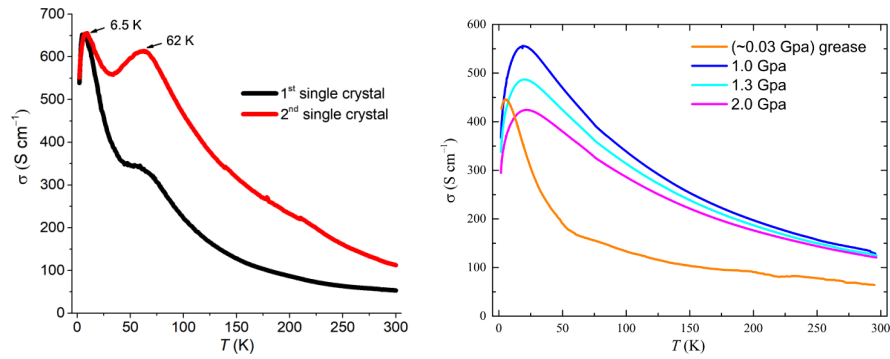


Figure 6.5.: The temperature-dependent electrical conductivity of CoBO_4 based on two different samples at ambient pressure (left) and under high pressures (right) [44].

According to the experimental data, at an ambient pressure, the electrical conductivity of CoBO_4 increases with decreasing temperature as in normal metal conductivity. From 62 K to 32 K, the conductivity decreases or increases more slowly depending on sample, then increases again up to 6.5 K, and finally drastically decreases to 2 K (Figure 6.5, left). It is worth noting that the transition point at

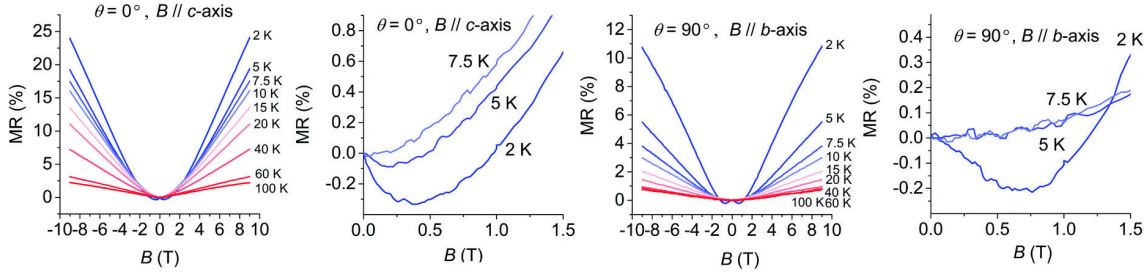


Figure 6.6.: The magnetoresistance of the CoBO_4 single crystal sample at different temperatures, with the magnetic field along the c axis (perpendicular to the BO layer; left, middle left) and along the b axis (nearly parallel with the magnetic easy axis of the SMM layer; middle right, right) [44].

higher temperature seems to have a sample dependence, which is more clear for the second single crystal sample compared with the first sample. The reasons may be various, like disorder-caused charge localization reducing the conductivity, due to which the BO or the SMM molecules may have some random deviation from their ideal lattice positions and generating a random local potential trapping electrons. Magnetoresistance (MR) is the behaviour of a material that changes its resistance in an externally applied magnetic field. This is essential for making magnetic storage devices. Here, the value of MR is defined by: $\text{MR}(B, T) = [\rho(B, T)/\rho(0, T)] - 1$, where ρ is the resistivity. CoBO_4 shows the MR effect in the temperature range of 2 to 100 K. The MR effect was maximized up to 24% where the magnetic field is along the c axis (perpendicular to the BO layer) with 9 T at 2 K. It shows a negative MR effect below 5 K in the c and b directions (Figure 6.6). Magnetic hysteresis behavior could be observed under 5 K as an iconic feature of SMM (Figure E.2, middle). Furthermore the slow magnetic relation showed as a peak in the out-of-phase alternating current (AC) magnetic susceptibility (χ'') curve up to 11 K (Figure E.3, right). In order to reveal the mechanism of conduction and the reason for the drop of the conductivity at 6.5 K, the electronic structure of the crystal and the important piece of fragments were studied.

6.4. Methodology

The system models were built from X-ray diffraction-determined structures harvested at 120 K. The isolated systems' calculations were performed by GAUSSIAN 16 [75], employing DFT and HF (def2-TZVP). A superfine integration grid was applied for numerical integrations and the tight convergence threshold (10^{-8} for the root mean square change in the density matrix) were used for the SCF pro-

cedure. Periodic boundary conditions (PBC) DFT calculations were performed with the VASP 5.4.4 package with the Perdew–Burke–Ernzerhof (PBE) exchange–correlation functional [74, 121–124]. Projector augmented wave (PAW) pseudopotentials and plane-wave basis sets with cutoff energies of 800 eV were used [125]. A $4 \times 4 \times 2$ and a $4 \times 4 \times 1$ Monkhorst-Pack k -mesh were employed for CoBO_4 and for the organic conductor layer $[\text{BO}_8]^{4-}$, respectively. The magnetic anisotropic energies were calculated taking in account the spin-orbital coupling (SOC) employing the zeroth order regular approximation (ZORA) as implemented in VASP [171]. Visualization of the molecule and isosurfaces was achieved by MULTIWFN 3.8 and VMD 1.9.3 [126, 127]. The values of isosurfaces were set to 0.02 a.u. for molecular orbitals and 0.005 a.u. for spin densities unless otherwise specified.

6.5. The monomer of the organic conductor (BO)

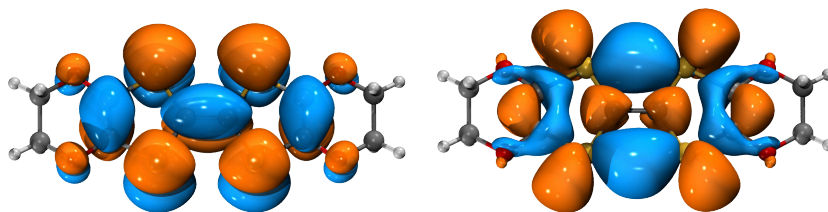


Figure 6.7.: The highest occupied molecular orbital (HOMO, left) and the lowest unoccupied molecular orbital (LUMO, right) isosurfaces for the neutral BO monomer based on B3LYP KS-DFT.

To compare the influence of the approximate exchange–correlation functional and to avoid possible artifacts, a few of the most commonly used functionals are selected to calculate the electronic structures. According to the results, the HOMOs and LUMOs of a neutral BO molecule based on the various functionals do not show qualitative differences. The frontier orbitals of BO are mainly formed by the π orbitals and show a delocalized nature which is important to explain the conductivity behavior later (Figure 6.7). However, the HOMO–LUMO gaps for the different functionals have a large discrepancy. The gap increases with the exact-exchange weight in a DFT functional as in many other cases (Figure E.4 , Table 6.1) [115]. Fortunately, as a partially oxidized molecule, the bands near the Fermi level of a formed stack layer should mainly keep the nature of the HOMO, while the LUMO should not be largely mixed into these bands. So it should not have a qualitative effect on explaining the conductive behavior.

Table 6.1.: The HOMO–LUMO gaps of the neutral BO monomer evaluated with different exchange–correlation functionals ordered according to increasing exact-exchange admixture.

Functional	PBE	BP86	TPSS	M06-L		
HOMO–LUMO Gap (eV)	1.450	1.455	1.621	1.788		
Functional	TPSSh	B3LYP	HSE06	PBE0	M06-2X	HF
HOMO–LUMO Gap (eV)	2.345	2.970	2.544	3.300	5.159	9.116

6.6. The dimer of the organic conductor (BO)

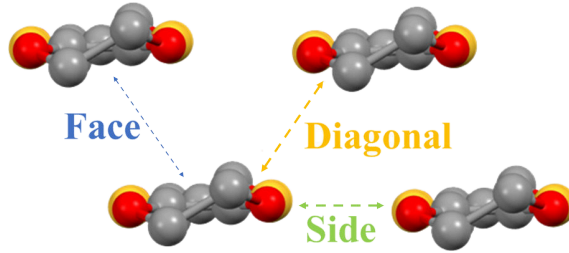


Figure 6.8.: The three different short contacts between adjacent BO units.

To reveal the mechanism of conduction, we need to examine possible interactions between molecule units. According to the crystal structure, there are three types stacking relation between two BO molecules (face, diagonal, side). Two neutral BO molecules do not seem to have a strong interaction, as supported by the calculation results (Figure E.5). Therefore, a neutral BO dimer's ($[\text{BO}_2]^0$) HOMO and HOMO-1 are the linear combination of two BO monomer's HOMO (Equation 6.1, Equation 6.2). The same hold for LUMO and LUMO+1 (Equation 6.3, Equation 6.4). where a, b represent two adjacent BO units, $S_h = \langle \varphi_{\text{BO}_a}^{\text{HOMO}} | \varphi_{\text{BO}_b}^{\text{HOMO}} \rangle$, $S_l = \langle \varphi_{\text{BO}_a}^{\text{LUMO}} | \varphi_{\text{BO}_b}^{\text{LUMO}} \rangle$ are the overlap integrals between the HOMOs and the LUMOs respectively. In the neutral case, the bonding orbital $\varphi_{\text{Dimer}}^{\text{HOMO}-1}$ and the antibonding orbital $\varphi_{\text{Dimer}}^{\text{HOMO}}$ are doubly occupied, thus it does not exhibit the characteristics of a bonding. However, if an electron is removed from the antibonding orbital, the interaction between two BO units could there be enhanced.

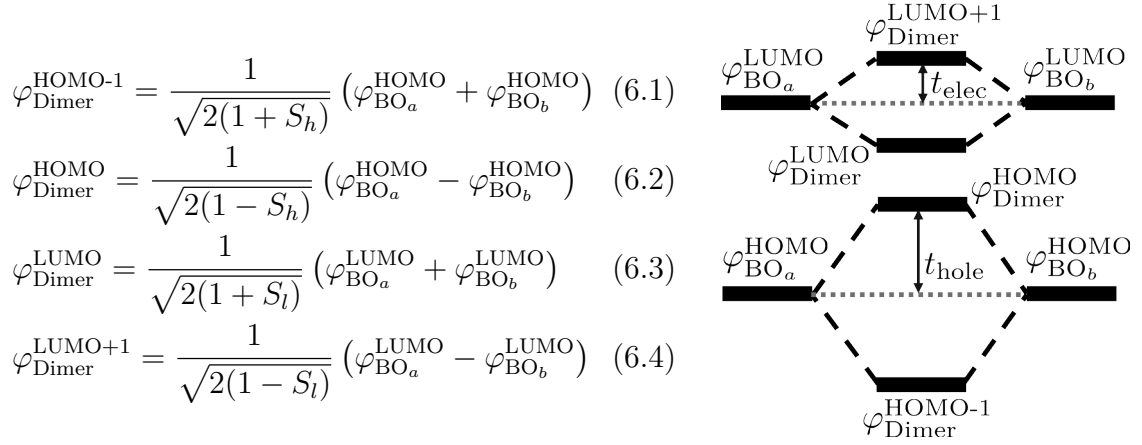


Figure 6.9.: The frontier MO levels of a BO dimer based on the linear combination of two BO monomers.

To explain the conductive behavior, the tight-binding Hamiltonian is commonly used as the most concise and effective model, $H = -t \sum_{i,j,\sigma} (c_{i\sigma}^\dagger c_{j\sigma} + H.c.)$, where i, j are the label of sites, σ is normally reserved for the spin label (*i.e.*, α, β), $c_{i\sigma}^\dagger$ ($c_{j\sigma}$) is the creation (annihilation) operator on the site i (j), t is the electronic coupling matrix elements as a crucial parameter representing the possibility of charge transfer happening between two sites. The electronic couplings (t) between two BO units were estimated by energy splitting in dimer (ESID) method [172]. The electronic coupling is qualitatively dependent on the overlap between the frontier orbitals of molecules, which also highly affect the energy level splitting. Thus, the electronic couplings for the hole transport and the electron transport could be estimated as following, $t_{\text{hole}} = (\varepsilon_{\text{HOMO}} - \varepsilon_{\text{HOMO-1}})/2$, $t_{\text{electron}} = (\varepsilon_{\text{LUMO+1}} - \varepsilon_{\text{LUMO}})/2$, where ε_i represents the energy level of $[\text{BO}_2]^0$. Due to the interactions between the frontier orbitals of two BO monomers, in an ideal case (neglecting the overlap integrals), the HOMO of the dimer is raised up by t_{hole} , and the LUMO is lower down by t_{electron} . Thus, the HOMO–LUMO gap of the BO dimers should be smaller than the gap of the BO monomer. While the HOMO–LUMO gap varies by different functionals quite a lot, the electronic coupling is much more consistent based on those functionals (Table 6.2). This means the band structure of BO layers evaluated from those functionals just under the Fermi energy should be similar. The couplings for the side-type and the diagonal-type directions are much stronger than the face-type. The hole coupling is much larger than the electron one (Table 6.3). Thus, the conductive behavior is dominated by the hole formed by the oxidation. According to the coupling matrix elements, it is possible to roughly estimate the bandwidth (W) of the formed crystal structure, where the bandwidth represents the range of the energies of the band dispersion. In an ideal case of a 1D molecular chain,

if the electronic coupling between the adjacent is t , then the bandwidth could be estimated as $W = 4t$ [173]. Here, the face-type coupling is neglected, we have $W = 4(t_{\text{side}} + t_{\text{diagonal}})$, it was estimated as 1.033 eV based on the B3LYP results. It should be mentioned the method to calculate charge transfer integrals implemented in NWCHEM is not feasible for BO molecules, due to the two BO molecules being geometrically identical and closely stacked, such that even the HF method is not able to give a charge localized state. For example, in the case of the hole transport, The delocalized state $[\text{BO}^{0.5+} - \text{BO}^{0.5+}]$ will give almost the same wave functions of the reactant (an ideal charge localized state before the transfer process, $[\text{BO}^+ - \text{BO}^0]$) and the product (an ideal charge localized state after the process, $[\text{BO}^0 - \text{BO}^+]$) and lead to an infinitely large transfer integral.

Table 6.2.: The HOMO–LUMO gap and electronic coupling of a neutral diagonal-type BO dimer ($[\text{BO}_2]_{\text{diagonal}}^0$) calculated by different functionals.

	PBE	BP86	TPSS	M06-L		
HOMO–LUMO gap (eV)	1.3021	1.3042	1.4672	1.6199		
t(hole) (eV)	0.1199	0.1205	0.1211	0.1233		
t(electron) (eV)	0.0024	0.0041	0.0052	0.0105		
	TPSSh	B3LYP	HSE06	PBE0	M06-2X	HF
HOMO–LUMO gap (eV)	2.1813	2.8047	2.3723	3.1263	4.9525	8.8276
t(hole) (eV)	0.1261	0.1280	0.1313	0.1324	0.1395	0.1536
t(electron) (eV)	0.0053	0.0011	0.0033	0.0031	0.0027	0.0388

Table 6.3.: The HOMO–LUMO gap and electronic coupling of the three dimers ($[\text{BO}_2]^0$) calculated by B3LYP.

	Face	Side	Diagonal
HOMO–LUMO gap (eV)	2.8844	2.8455	2.8047
t(hole) (eV)	0.0457	0.1302	0.1280
t(electron) (eV)	0.0333	0.0030	0.0011

For some strongly correlated systems which show a strong on-site Coulomb interaction, mean-field methods (*e.g.*, DFT, HF) are normally inadequate to describe the electronic structures. In many cases, the system is actually in a semiconductor state, but mean-field methods give a metallic prediction, because the strong Coulomb interaction is able to open the band gap, leading to a transition from metal to semiconductor (or insulator). To overcome such shortcomings, the on-site Coulomb repulsion term, $U \sum_{i=1}^N n_{i,\alpha} n_{i,\beta}$, is commonly added into a Hamiltonian, here n is the number operator and U is the on-site interaction that represents the electron repulsion [147]. In general, it is not trivial to calculate the effective Coulomb

interaction (the Hubbard U) in molecular solids due to the polarization effect. The system has a tendency to shielding a charge by the rearranged the charge distribution of the surrounding, as a result, the charge is stabilized by the redistribution or so-called the polarization effect. It could be written as $U = U^{(v)} - \Delta U^{(p)}$, where $U^{(v)}$ is the bare Coulomb interaction in vacuum and $\Delta U^{(p)}$ is the result of shielding effect from the polarizable crystalline environment [174].

The bare term $U^{(v)}$ could be effortlessly obtained by the normal DFT calculations. In the BO case, it is equal to the difference between the second ionization potential energy (IP_2) and the first ionization potential energy (IP_1), $U^{(v)} = IP_2 - IP_1 = E(\text{BO}^{2+}) + E(\text{BO}) - 2E(\text{BO}^+)$, which can be explained as the energy cost of the charge disproportionation reaction $2(\text{BO}^+) \rightarrow \text{BO} + \text{BO}^{2+}$ for infinitely separated BO molecules. Despite the difference between various exchange–correlation functionals, the resulting $U^{(v)}$ values are quite consistent around 4.5 eV (Table 6.4).

There is another approximate way to get the Hubbard U by accounting for the Coulomb repulsion between two electrons in the HOMO, the Coulomb integral $\langle \varphi^{\text{HOMO}} \varphi^{\text{HOMO}} | \frac{1}{\|\mathbf{r}\|} | \varphi^{\text{HOMO}} \varphi^{\text{HOMO}} \rangle$, where $\|\mathbf{r}\|$ represents the distance between two electrons in the HOMO. However in this treatment, other electrons are frozen during the ionization process, thus the estimated value should be larger than $U^{(v)}$, due to lack of electron relaxation in the molecule [175]. These data can be found in Table 6.4 and show that the Coulomb integral is almost 1.1 eV large than the calculated $U^{(v)}$.

But the hard part is to calculate $\Delta U^{(p)}$. In principle, the dielectric constant (ε) of the crystal is required to reproduce the polarization behavior of the surrounding environment after one BO molecule is charged or discharged. However, ε requires high level methods, *e.g.*, constrained random-phase approximation (cRPA), GW approximation, to capture the dynamical correlation, which are not feasible for this large system. Furthermore, the stacking distance between BO molecules is comparable with the molecular size, the symmetry of the BO molecule is low, and the electronic structure of the anion is also not as simple as normal halide ions, which means this crystal system is not able to be simplified as a lattice of dipoles.

As an alternative, the single-point energies were calculated in a polarizable continuum model (PCM). It is irrefutable that the implicit solvation treatment is not comparable with the true crystal environment, but it is possible to give a tendency of the $\Delta U^{(p)}$ dependence on ε of the selected model solvent. As a result, the U predicted by HF with a PCM model for tetrahydrofuran (thf, $\varepsilon = 7.43$) drastically decreases by near 3 eV to $U = 1.95$ eV, which means the PCM condition is able to stabilize the charged states. With modifying the model by a higher dielectric

constant solvent, water ($\varepsilon = 78.36$), the U decreases to 1.49 eV. According to an empirical model which simplifies the molecule as a charged conducting ellipsoid, the shielding effect could be estimated by $\Delta U^{(p)} = 3.993 \left(\frac{\varepsilon-1}{\varepsilon} \right)$ eV by assuming the model for bis(ethylenedithio)tetrathiafulvalene also works for the isostructural BO molecule [146]. The Hubbard U values are estimated as 1.49 eV and 1.00 eV for thf and water respectively from the HF result. The lowest U value would be 0.3719 eV based on the PBE results with an infinitely high ε . Going one step further, to mimic the crystal environment, the U of one BO molecule surrounded by the other eight BO molecules ($\text{BO}@\text{[BO}_8^{4+}]$) was predicted to be 0.1707 eV by the HF method associated with PCM (water). Due to the symmetry, the charge tends to be delocalized on other BO molecules, therefore the value could be underestimated.

Above all, the Hubbard U for the BO could be estimated as 0.37 eV to 1.95 eV depending on the methods. Compare with the 1 eV bandwidth W , this crystal system seems not to be dominated by the Coulomb repulsion. Thus, normal DFT methods should be able to describe the electronic structure.

Table 6.4.: The ionization energies, the bare Coulomb interaction ($U^{(v)}$), and the Coulomb integrals of the HOMO electrons for the BO molecule based on different exchange–correlation functionals.

Functional	IP ₁ (eV)	IP ₂ (eV)	$U^{(v)}$ (eV)	Coulomb integral (eV)
PBE	5.39	9.76	4.36	5.54
BP86	5.49	9.85	4.36	5.55
TPSS	5.39	9.78	4.39	5.54
M06-L	5.38	9.74	4.36	
TPSSh	5.51	9.94	4.43	
B3LYP	5.65	10.11	4.45	5.60
HSE06	5.66	10.14	4.48	5.59
PBE0	5.68	10.17	4.49	5.59
M06-2X	5.98	10.47	4.49	5.64
HF	5.40	10.35	4.94	5.71
HF(PCM THF)	4.20	6.15	1.95	
HF(PCM H ₂ O)	4.05	5.54	1.49	
HF(PCM H ₂ O; $\text{BO}@\text{[BO}_8^{4+}]$)	2.76	2.93	0.17	

To verify the above result about the electronic couplings in the periodic system, a supercell of the face-type BO dimer $[\text{BO}_2]_{\text{face}}^{1+}$ was built base on the reduced BO lattice with one electron removed from the unit cell. As shown in Figure 6.10, the band structure predicted by HSE06 and PBE almost only differs in the band gap, but with similar band dispersion. The hybrid functional HSE06 evaluated a larger gap. The band dispersion along the G-X direction (side-type) is larger than along the G-Y direction (face-type), and the valence bandwidth is larger than the conduction bands', which is consistent with the above discussion. Due to an electron being removed from the system, the Fermi level sits within the bands consisting of

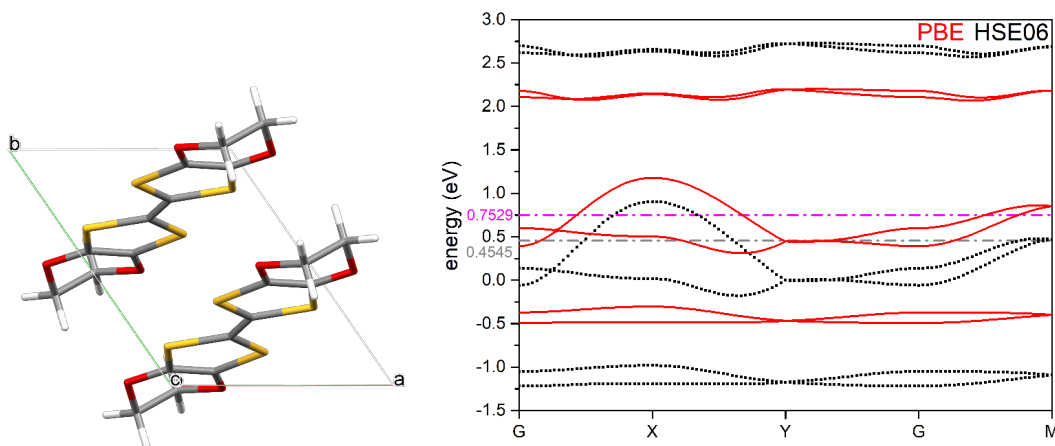


Figure 6.10.: The supercell of the singly positively charged face-type BO dimer ($[\text{BO}_2]_{\text{face}}^{1+}$, left). The band structure of the supercell calculated by PBE and HSE06 (right), the corresponding Fermi levels are represented by the magenta (PBE) and the gray (HSE06) dash-dot lines. G (0, 0, 0); X (0.5, 0, -1.0); Y (0, 0.5, 0); M (-0.5, 0.5, 0).

the HOMO of BO, which makes the difference between HSE and PBE negligible. In short, PBE is practicable to describe the BO layer with a fractional occupation number.

In general, if the electronic couplings between BO molecules are strong enough to neglect the on-site Coulomb repulsion, then the system should form a band structure with a closed shell with no net spin density remaining in the crystal. In the worst case, the Hubbard U is able to create spin localized states, thus the spin-polarized configuration should also be considered. In order to qualitatively understand the magnetic coupling between the BO molecules, one electron was removed from a BO molecule to artificially create a spin on the molecule. The magnetic coupling constant between two BO^+ cations ($J_{\text{BO-BO}}$) could be calculated by a Heisenberg model Hamiltonian $H = -2J_{AB}\mathbf{S}_A\mathbf{S}_B$ ($J < 0$ for AFM; $J > 0$ for FM) [176] based on the results of broken-symmetry DFT for the AFM and the FM configurations of a pair of BO^+ . The single-point energies were calculated by various exchange–correlation functionals. Despite the energy varying largely with the functional (Table 6.5), all have an AFM ground state, and the magnetic coupling of the face-type is one order magnitude smaller than the other two.

This means the AFM configuration is the ground state for an unperturbed $[(\text{BO})_8]^{4+}$ layer, with AFM along the side and the diagonal directions. Therefore the face direction is forced to be FM ordered (Figure 6.11). The PBC calculations for the reduced side-type BO dimer ($[\text{BO}_2]_{\text{side}}^{1+}$) with the hybrid exchange–correlation functional PBE0 also suggest the AFM configuration is the ground state, which is 22.14

meV and 22.99 meV lower than the FM and the closed-shell configurations respectively.

Table 6.5.: The isotropic magnetic coupling constant $J_{\text{BO-BO}}$ calculated from the doubly positively charged dimers ($[\text{BO}_2]^{2+}$) based on Noodleman broken-symmetry approach.

$(\text{BO}^{1+})_2$	$J_{\text{BO-BO}} \text{ (cm}^{-1}\text{)}$		
	Face	Diagonal	Side
PBE	-113.60	-703.87	-689.70
BP86	-123.44	-723.06	-697.69
TPSS	-99.21	-571.93	-524.79
M06-L	-142.30	-646.01	-504.52
TPSSh	-57.11	-337.50	-300.13
B3LYP	-40.23	-261.73	-255.91
HSE06	-38.85	-266.81	-251.14
PBE0	-32.23	-228.39	-211.40
M06-2X	-20.39	-178.99	-163.42
HF	-0.47	-56.48	-84.13

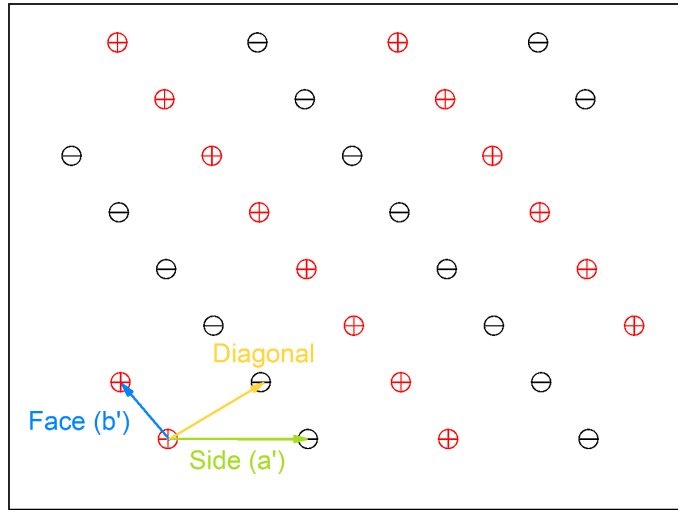


Figure 6.11.: The spin density oscillates along the $a' + b'$ direction in the BO layer and forms a 1D strip spin pattern, in which the side and diagonal BO pairs are AFM coupled and the face pairs are FM coupled.

6.7. The single-molecule magnet ($[\text{Co}(\text{pdms})_2]^{2-}$)

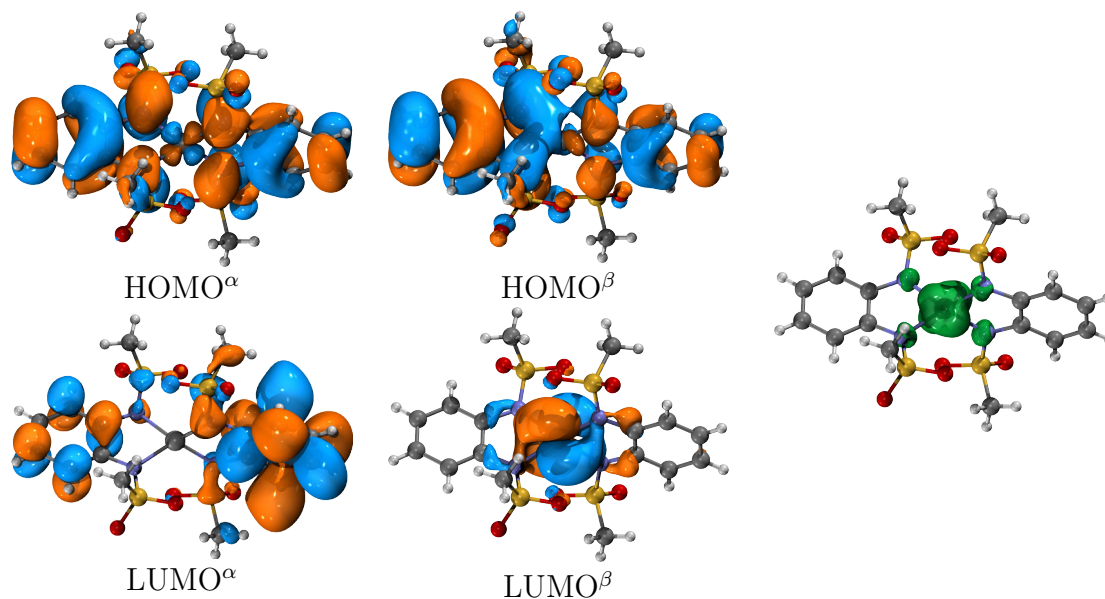


Figure 6.12.: Molecular orbitals (left) and the spin density (right) of $[\text{Co}(\text{pdms})_2]^{2-}$ based on B3LYP KS-DFT.

The single-point calculations of the single-molecule magnet part ($[\text{Co}(\text{pdms})_2]^{2-}$) by using varied functionals gave consistent frontier orbitals suggesting the HOMO energy levels calculated by PBE is qualitatively correct (Figure E.8). Also PBE made the correct prediction that $S = 3/2$ is the ground state of $[\text{Co}(\text{pdms})_2]^{2-}$ as the experimental result [44, 170], which is 0.49 eV and 3.63 eV lower than the $S = 1/2$ state and the unconverged $S = 5/2$ state. The delocalized HOMO of $[\text{Co}(\text{pdms})_2]^{2-}$ mainly consists of the HOMOs of the ligands (pdms^-) and the d orbitals of Co^{2+} . The spin is almost concentrated fully on the Co^{2+} center, slight by delocalizing to the four coordinated nitrogen atoms. As a digression, the TD-DFT calculations suggest that the solid-state UV-Vis-NIR absorption peaks of $(\text{HNEt}_3)_2[\text{Co}(\text{pdms})_2]$ mainly result from the $d-d$ transitions on the Co^{2+} center (Figure E.9, Figure E.10).

For isolated systems, the Fermi energy of $[\text{Co}(\text{pdms})_2]^{2-}$ is much higher than $[\text{BO}_2]^+$ (Figure E.8, Figure E.7). Thus, in the bulk state, we are not able to assume the formal charge of the $[\text{Co}(\text{pdms})_2]^{2-}$ unit is exactly equal to -2 , which could be less by orbital mixing with the BO layer. As an extreme case, $[\text{Co}(\text{pdms})_2]^-$ was also taken into account here. All functionals suggest that an electron is removed from the pdms ligands and the cobalt center preserves the $+2$ valence. Due to the symmetry, the hole is delocalized on the two ligands. The unpaired electron on the ligands is also able to magnetic couple with the cobalt center leading to two possible configurations (FM and AFM) for $[\text{Co}(\text{pdms})_2]^-$ (Figure 6.13). According to the

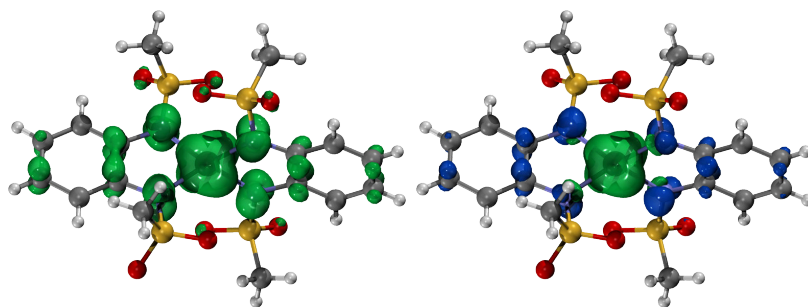


Figure 6.13.: The spin density of $[\text{Co}(\text{pdms})_2]^{1-}$ with the FM (left) and the AFM (right) magnetic couplings between the Co center and the ligands calculated by B3LYP.

single-point energies of the two configurations based on those functionals, the Co^{2+} center should be AFM coupled with the two ligands (Table E.2).

In order to know the preferential magnetic coupling between the BO molecules and the $[\text{Co}(\text{pdms})_2]^{2-}$ unit, broken-symmetry DFT calculations were performed by taking the initial guesses of the FM and AFM the coupled $[\text{BO}]^+ - [\text{Co}(\text{pdms})_2]^{2-}$. The wavefunctions of the fragments (*i.e.*, $[\text{BO}]^+$, $[\text{Co}(\text{pdms})_2]^{2-}$) were calculated based on the magnetic couplings (*i.e.*, FM, AFM), and then the initial guesses of the molecule wavefunctions were obtained by the wedge products of the fragments' wavefunctions. However, the Fermi level of the $[\text{BO}]^+$ unit is lower than that of $[\text{Co}(\text{pdms})_2]^{2-}$, such that all results converged into a $[\text{Co}(\text{pdms})_2]^-$ configuration with a neutral BO unit, which degenerated to the above case. Thus, the AFM configuration is more stable. This means that in the BO layer, if there is an itinerant electron tending to be localized in the vicinity of the $[\text{Co}(\text{pdms})_2]^{2-}$ unit, then the spin of the electron prefers the antiparallel alignment with the cobalt center. The above process behaves like a magnetic shielding effect that cancels the local magnetic moments from the metal center.

As before, the chemical environment surrounding a $[\text{Co}(\text{pdms})_2]^{2-}$ unit was evaluated. There are four short contacts (A B C D) between two adjacent units (Figure 6.14). The magnetic couplings between two units were calculated by comparing the energy difference between the AFM and the FM configurations of a pair of units.

In the fully charged case ($[\text{Co}(\text{pdms})_2]^{2-} - [\text{Co}(\text{pdms})_2]^{2-}$), the magnetic couplings between two units are negligible (around 10^{-7} eV). However, in the partially charged case ($[\text{Co}(\text{pdms})_2]^{2-} - [\text{Co}(\text{pdms})_2]^-$), here taking the AFM configuration for the $[\text{Co}(\text{pdms})_2]^-$ unit, all functionals predicted a FM coupling between two units, which is consistent with a PBC calculation with the PBE functional (Table 6.6). The spin density of the AFM-configured partially charged case shown in Figure E.13 shows

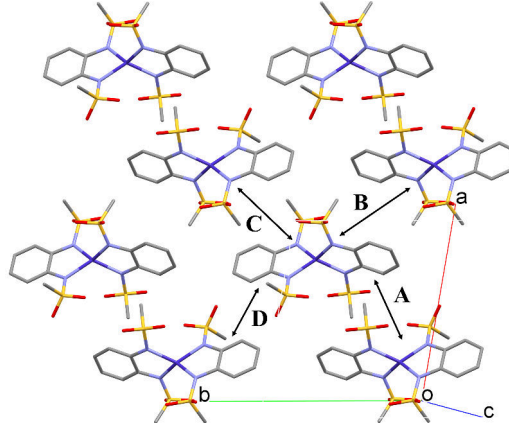


Figure 6.14.: The four different short contacts between adjacent $[\text{Co}(\text{pdms})_2]^{2-}$ units.

that in one of the $[\text{Co}(\text{pdms})_2]$ monomer, the spin alignments on the pdms ligand and the cobalt center are forced to be the same. This suggests that electrons could be delocalized on two pdms ligands belong different $[\text{Co}(\text{pdms})_2]$ monomers, and the magnetic exchange is caused by the overlap between two ligands, which is even stronger than the intramolecular coupling between the ligands and the cobalt center.

Table 6.6.: The energy difference between FM and AFM electronic configurations of $[\text{Co}(\text{pdms})_2]^{2-} - [\text{Co}(\text{pdms})_2]^-$ dimers, in which the pdms ligands are AFM coupled with the cobalt center in the $[\text{Co}(\text{pdms})_2]^-$ unit.

	$E_{\text{FM}} - E_{\text{AFM}}$ (eV)			
	A	B	C	D
TPSSh	-0.2889	-0.1232	-0.1086	-0.1134
B3LYP	-0.2426	-0.0983	-0.0841	-0.0874
HSE06	-0.2449	-0.0812	-0.0750	-0.5161
PBE0	-0.2407	-0.0865	-0.0710	-0.0738

6.8. The electronic structure in bulk CoBO_4

Based on the exploration of the isolated systems mentioned above, just like other GGA functionals, PBE would overestimate the delocalized nature of a system. However, it is still qualified to describe this semi-metallic system, since the Hubbard U should be in the same order as the bandwidth.

The band structure of the $[\text{BO}_8]^{4+}$ layer in CoBO_4 (the left part of Figure 6.3, the left side of Figure 6.15) clearly shows that the bands close to the Fermi level consist of eight HOMOs of BO units with a 0.8823 eV bandwidth, which is very close

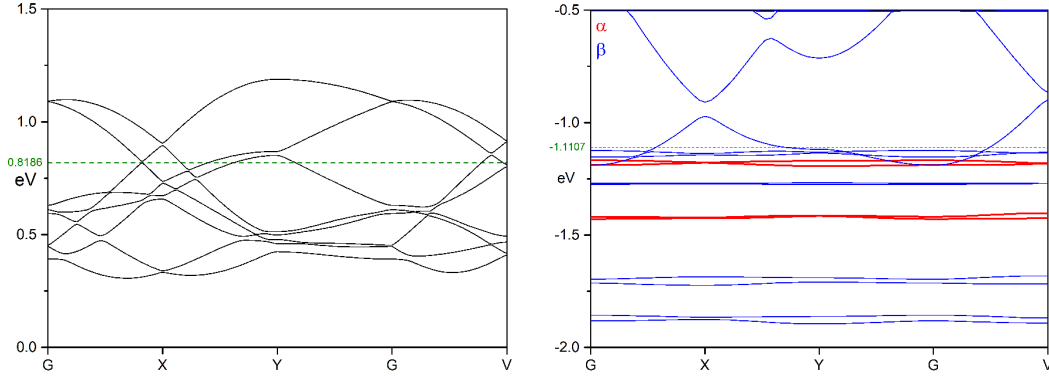


Figure 6.15.: The band structures of the $[\text{BO}_8]^{4+}$ layer (left) and the $[\text{Co}(\text{pdms})_2]^{4-}$ layer (right) in CoBO_4 calculated by PBE. The red and blue lines in the right part represent the spin-up (α) and spin-down (β) bands respectively. G(0, 0, 0), X(0.5, 0, 0), Y(0, 0.5, 0), V(0.5, -0.5, 0).

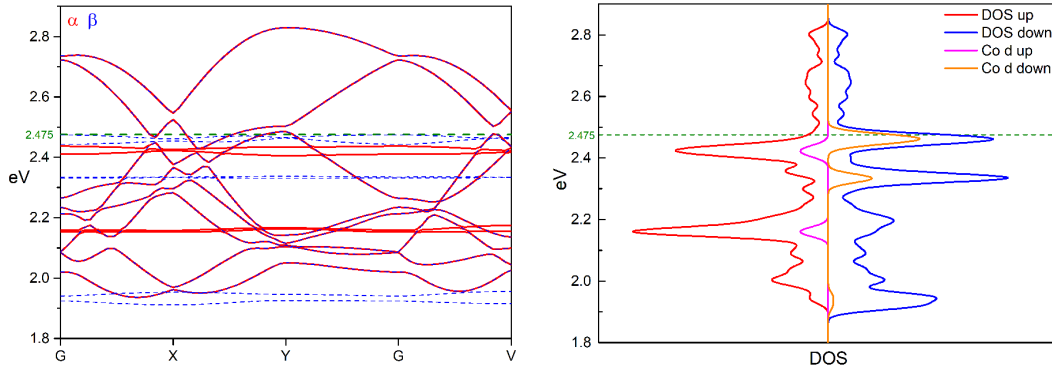


Figure 6.16.: The PBE band structure (left) and DOS (right) of CoBO_4 . In the left part, the red lines and the blue dash lines represent the spin-up (α) and spin-down (β).

to the estimation based on the electron coupling matrix elements (1.033 eV). The system shows metallic character, because the Fermi level crosses through the middle of the valance bands. Near the Fermi level, the electron could be easily promoted and gain a high mobility. The large dispersion in all directions also suggests that the conductance does not have a dominating preferential direction in the 2D layer. This is consistent with the above conclusion that BO units have a large electronic coupling between a side-type pair and a diagonal-type pair.

For the $[\text{Co}(\text{pdms})_2]^{4-}$ layer in CoBO_4 (the right part of Figure 6.3, the right side of Figure 6.15), the FM-configuration between two $[\text{Co}(\text{pdms})_2]^{2-}$ was used as the initial guess for the SCF algorithm, due to the energy being lower than the AFM-configuration by 0.2485 eV and also due to the support from the magnetic coupling of the $[\text{Co}(\text{pdms})_2]$ dimer. In contrast with the above organic layer, the bands of

the SMMs layer are relatively flat, based on the fact that the intermolecular overlap is not as significant as for BO (Figure 6.15, right).

The band structure of **CoBO**₄ looks like the superposition of the above two figures (Figure 6.15), but there are many avoided crossing points between the $[\text{BO}_8]^{4+}$ bands and the $[\text{Co}(\text{pdms})_2]_2^{4-}$ bands, which indicates at some points the orbitals of the two layers are symmetry matched and would be mixed. The conduction electrons could also have a large contribution from the cobalt's *d* electrons since the flat bands from $[\text{Co}(\text{pdms})_2]_2^{4-}$ are just below the Fermi level and (Figure 6.16). Like the organic layer case, **CoBO**₄ shows a large dispersion along two axes, while being nearly flat on the remaining one, consistent with the features of a 2D conductor (Figure E.17).

For the isolated molecules in a vacuum, the HOMO level of $[\text{Co}(\text{pdms})_2]_2^{2-}$ is much higher than the LUMO of $[\text{BO}_2]^+$. This seems to imply that the electrons are readily transferred from $[\text{Co}(\text{pdms})_2]_2^{2-}$ to $[\text{BO}_2]^+$. But in the condensed phase, the Fermi levels of the $[\text{BO}_8]^{4+}$ layer and **CoBO**₄ are relatively unchanged compared with the eight BO HOMO bands. This means the formal charge of the BO layer still remains at 4+ according to the band structure. During the cooling process of conductivity measurements, the amplitude of the vibrations of the molecules decreases due to the reduction of the phonon population, which can be manifested as a reduction in crystal volume. To explore the effect of this process on the electronic structure, the Fermi levels of the $[\text{BO}_8]^{4+}$ layer and the $[\text{Co}(\text{pdms})_2]_2^{2-}$ layer were calculated. Due to the fact that the overlap integral between the BO units is larger than for $[\text{Co}(\text{pdms})_2]_2^{2-}$, the Fermi energy of the BO layer increases more drastically with the lattice shrinking compared with the $[\text{Co}(\text{pdms})_2]_2^{2-}$ layer, because of the Coulomb repulsion between electrons at occupied orbitals (Figure E.23). In simple terms, during the crystal formation, BO units could adjust their Fermi level by tuning their intermolecular distance to adapt the Fermi level of the $[\text{Co}(\text{pdms})_2]_2^{2-}$ layer. A relatively close distance between BO molecules is able to raise the Fermi level quickly compared with the $[\text{Co}(\text{pdms})_2]_2^{2-}$ layer's. At a certain point, both levels will be equal, then the electron number in each layer will just as the formal charge.

From the 2D band structure, it is easier to see the shape of the bands in the reciprocal space close to the Fermi level (Figure E.18). The hole band and the electron band are intercepted by the Fermi level. In Figure 6.17, the resulting cross-sections (1D contours) are shown by the color-filled blocks. These cross-sections are the profile of the Fermi surface on the a^*b^* plane ($k_z = 0$). Due to the dispersion along the c^* axis being negligible, the shapes of cross-sections are identical in all c^* values. 1D contours form 2D tube-like surfaces, thus the corresponding Fermi surface consists of two hole tubes and one electron tube.

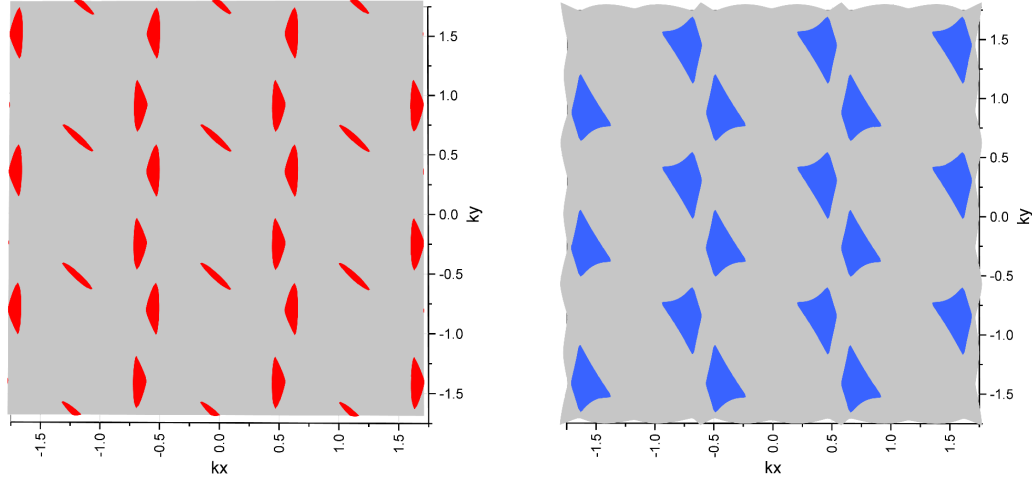


Figure 6.17.: The cross-section of the hole band (left, red) and electron band (right, blue) with the Fermi surface of CoBO_4 respectively.

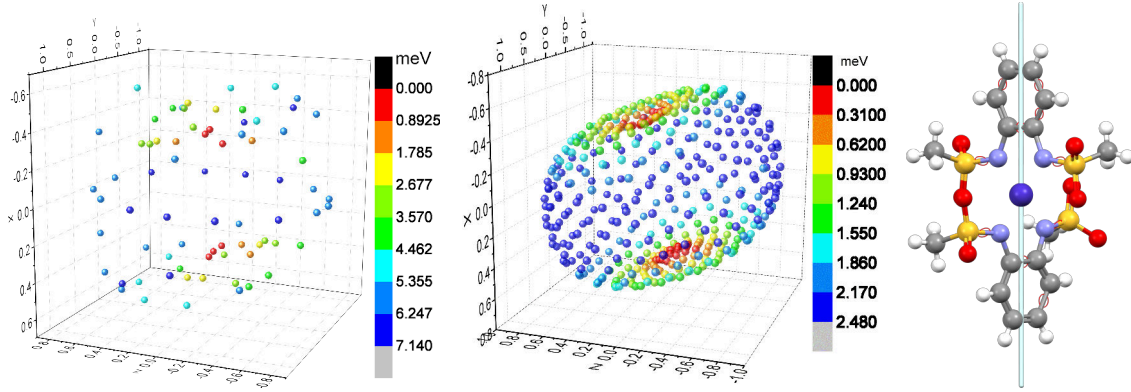


Figure 6.18.: The magnetic anisotropy energy of CoBO_4 (left) and $[\text{Co}(\text{pdms})_2]^{2-}$ (middle), the anisotropy energies were represented by the radius and the colors of dots for clear along the selected direction. The easy axis of $[\text{Co}(\text{pdms})_2]^{2-}$ (right).

The magnetic anisotropy energies were calculated by non-self-consistent SOC calculations with the PBE exchange–correlation functional on a Lebedev grid, with 434 points for the $[\text{Co}(\text{pdms})_2]^{2-}$ unit and 74 points for CoBO_4 . As a result, the easy axis of an isolated $[\text{Co}(\text{pdms})_2]^{2-}$ in a supercell is along the $(-0.0992, 0.9372, -0.3344)$ direction in Cartesian coordinates with an anisotropic energy of 2.48 meV (Figure 6.18, left). It almost overlaps with the principal axis of the molecule and also agrees with the previous report [170]. The easy axis of the CoBO_4 crystal system is along the $(0.0000, 0.9472, -0.3208)$ direction in Cartesian coordinates with an anisotropic energy of 7.14 meV (Figure 6.18, right), which means the complex preserves the anisotropic nature of the isolated $[\text{Co}(\text{pdms})_2]^{2-}$ unit in the crystal.

6.9. Discussion

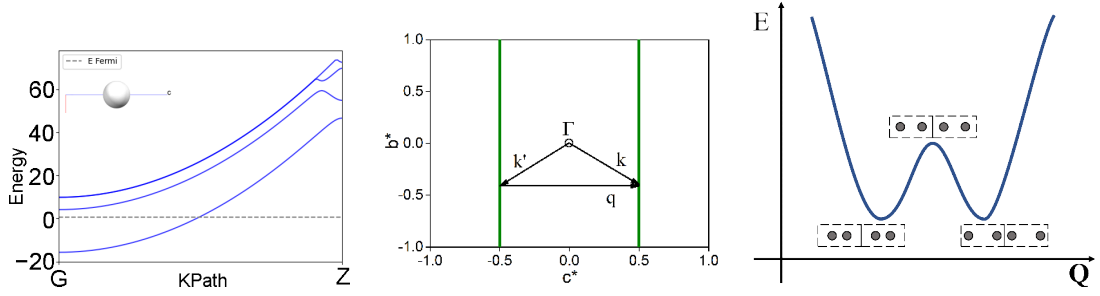


Figure 6.19.: The PBE band structure of 1D hydrogen atoms chain with an equal distance 0.75 \AA (left). The Fermi surface of the 1D hydrogen atoms chain is represented by two green lines, which could be nested by a vector \mathbf{q} (middle). Bistable symmetry-broken ground states along the general coordinate \mathbf{Q} (in the 1D hydrogen atoms chain case, it is the interatomic distance), which represents an intercell dimerization and an intracell dimerization. The two are equivalent if the cell repeats infinite times. The high symmetry state in the center has a higher energy (right).

In low-dimensional metallic systems with partially filled band(s), there is a commonly existing electronic instability: when a part of a Fermi surface can be translated by a vector \mathbf{q} and superimposed on another part of the Fermi surface, then the Fermi surface is nested by the vector \mathbf{q} [177].

In the left side of Figure 6.19, an infinite 1D hydrogen atoms chain should show a metallic conductivity due to the half-filled band. When the interchain interactions are neglected, the band dispersions along the a^* and b^* axes are zero, thus the Fermi surface of the system consists of two parallel planes at $k_z = \pm \frac{c^*}{2}$. The profile in the b^*c^* plane are two parallel lines. It is easy to see there are an infinite number of possibilities to nest the Fermi surface by \mathbf{q} vectors as long as $k_z = 2k_f$ (Figure 6.19, middle). The above discussion is based on the case of 0 K temperature, where all electrons are settled just below the Fermi level. If the temperature is non-zero and the Fermi surface is smeared according to the Fermi–Dirac distribution, the nesting process is not expected to be sufficient. This is also a reason why Fermi surface nesting normally happens at low temperatures.

It must be pointed out that the existence of a nesting vector \mathbf{q} just means the existence of a possible instability. The system will still remain it is unless a perturbation is appearing.

For instance, the crystal orbitals $\phi(\mathbf{k})$ and $\phi(\mathbf{k}')$ are two eigenfunctions of the unperturbed Hamiltonian H^0 . By introducing a perturbation H^1 , the above two functions shall mix and give two new eigenfunctions ($\varphi(\mathbf{k})$, $\varphi(\mathbf{k}')$) of the modified Hamilto-

nian $H^0 + H^1$. For a Fermi surface nesting case, the wavevector is equal to a Fermi wavevector (or located at the vicinity) $\mathbf{k} = -\mathbf{k}' = \mathbf{k}_f$, thus the original degeneration is removed by the perturbation, which leads to an energy difference between the two new states $(\varphi(\mathbf{k}), \varphi(\mathbf{k}'))$, then a gap is opened, and the Fermi surface vanishes. This transformation usually results in a metal–insulator transition (MIT), due to the presence of a gap, the carriers can only be generated by thermal population, which drastically decreases the number of charge carriers.

For a different type of perturbation, the transformation can vary. As the most common perturbation in crystal systems, lattice vibrations are able to mix the two states by electron–phonon coupling, which results in a Peierls distortion and charge density wave (CDW). For instance, if the positions of hydrogen atoms in a 1D chain are altered, in which two structural units (hydrogen atoms) tend to dimerize, the bandgap is gradually opened with the dimerization. Such a process stabilizes the system where the Fermi level also decreases (Figure E.24). The resulting system is still with a closed shell, then obviously, the electron density is oscillation along the c axis, which is the CDW. The instability is able to lead the system to form a low-symmetry state for lowering the energy (Figure 6.19, right). As another common source of perturbation, the on-site Coulomb repulsion, Hubbard U , is also possible to open a gap, resulting in a Mott insulator. However, in this case the geometrical difference should be small, and it will lead to a spin density wave (SDW).

In a special case, the matrix elements $\langle \phi(\mathbf{k}') | H^1 | \phi(\mathbf{k}) \rangle$ which are responsible for the CDW or SDW transition do not dominate the perturbation comparing with the two-body interaction term $\langle \phi(\mathbf{k}') \phi(-\mathbf{k}') | H^1 | \phi(\mathbf{k}) \phi(-\mathbf{k}) \rangle$, which represents the electron–phonon interaction between two pairs of electrons (called Cooper pairs) having opposite momenta. Such a system is likely to undergo a metal–superconductor transition. The perturbation H^1 opens a superconducting energy gap preventing Cooper pairs from breaking up.

To investigate the above electronic instability, the Fermi surfaces of **CoBO₄** and the original $[\text{BO}_8]^{4+}$ layer are calculated as shown in Figure 6.17 and Figure E.19. Due to the two large supercells containing multiple molecules, the band structures are folded multiple times, which causes a complex Fermi surface. For this reason, the system of the charged side-type BO dimer based on the reduced structure $[\text{BO}_2]_{\text{side}}^{1+}$ was selected to unfold the bands (the left part of Figure 6.20; the Fermi faces of the tetramer and the octamer are shown in Figure E.21 and Figure E.20). The Fermi surface of the charged side-type BO dimer consists of contacting ellipses along the a^* direction. The shown Fermi surfaces, which calculated based on the 120 K crystal structure with the PBE exchange–correlation functional, are not able to be fully nested. But the approximate 1D Fermi surface (the green lines in the right side

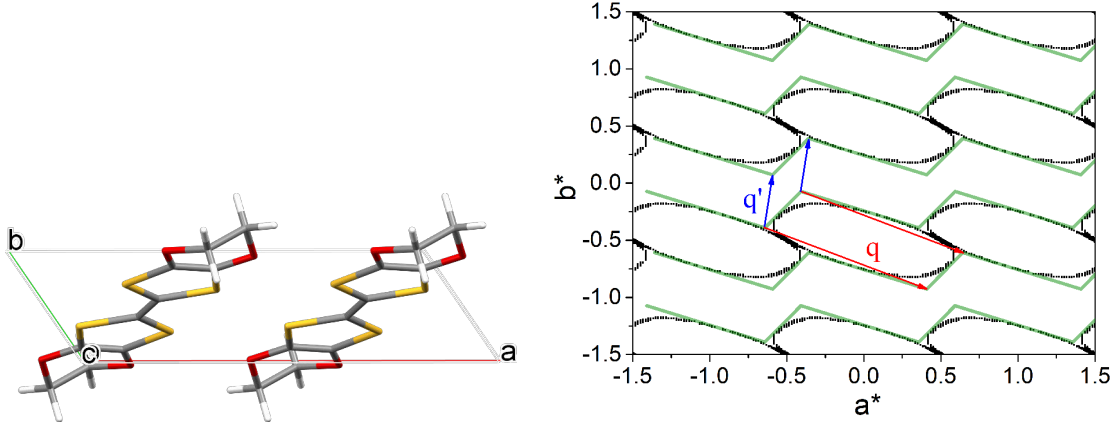


Figure 6.20.: The supercell of charged side-type BO dimer based on the reduced structure ($[\text{BO}_2]_{\text{side}}^{1+}$, left). The Fermi surface profile in the a^*b^* plane with $k_z = 0$ based on PBE results (right), where the black points and the green lines represent the data points and the approximate 1D Fermi surface respectively. The approximate 1D Fermi surface could be nested by the vector $\mathbf{q} \approx (1.05a^*, -0.54b^*, c^*)$ or the vector $\mathbf{q}' \approx (0.05a^*, 0.46b^*, c^*)$.

of Figure 6.20) is able to be nested by the wavevector $\mathbf{q} \approx (1.05a^*, -0.54b^*, c^*)$ or $\mathbf{q}' \approx (0.05a^*, 0.46b^*, c^*)$. This indicates some pieces of the Fermi surface are able to nest by \mathbf{q} or \mathbf{q}' , which is also able to decrease the charge carrier density, not to mention that the geometrical structure could be altered in a particular way to satisfy the condition of full Fermi surface nesting at low temperatures if there are appropriate electron–phonon couplings.

In case of the electron–phonon coupling dominating the perturbation, a dimerization could happen between the diagonal pairs by the wavevector \mathbf{q} or between the face pairs by the wavevector \mathbf{q}' with a corresponding CDW along the dimerization direction. The preferential dimerization needs to give an optimum energy lowering by balancing the electronic energy and the lattice vibrations. The X-ray diffraction under such temperature could possibly prove the type of distortion of the BO lattice. By the diffuse scattering, the superlattice spots between the Bragg’s peaks of the corresponding direction should be observed. Due to all electrons being paired, the radical EPR signal from $[\text{BO}]^{0.5+}$ is expected to vanish under liquid helium-temperature.

In the other case, if the estimated Hubbard U of the BO molecule is comparable with the bandwidth W , the BO layer is also able to transform into a Mott insulator. According to the AFM magnetic coupling between the side- and diagonal-type BO pairs, if the Hubbard U is strong enough, the BO layer tend to form a SDW state as shown in Figure 6.11. The resulting AFM magnetic order pattern does not match

with the original lattice, such that it will form a magnetic lattice placed in a $1 \times 2 \times 1$ supercell. Thus, if we are able to use neutron diffraction, it is expected to observe new magnetic lattice diffraction peaks between the Bragg's peaks ($\frac{b^*}{2}$).

Because some solid evidence are still missing, here we provide a possible explanation combined with the above calculation results. The external-hydraulic-pressure-dependent conductivity gives a hint that the **CoBO**₄ system undergoes a CDW phase transition (Figure 6.5, right). As a consequence of the compression from the external pressure, the bandwidth W should be increased resulting from a more effective intermolecular overlap by a shorter distance. The permittivity (ϵ) should be positively correlated with external pressure as for other reported TTF systems [178, 179]. Then the Hubbard U should be decreased due to a higher permittivity being able to stabilize the charged states. If the system converts into a SDW state, a higher external pressure is able to reduce the U/W ratio and leads the system to reentry into a metallic or even superconductive state. But in this case, the highest conductivity peak in the whole temperature range decreases as the external pressure increases, and the transition happens at a higher temperature under a higher pressure. From one aspect, a high pressure increases the spring constants of vibration modes resulting from steeper potential wells, which diminishes the populated phonon number and the amplitude. Therefore, the system becomes harder to overcome the barrier between the different dimer configurations (Figure 6.19, right) and eventually is trapped in a certain dimer configuration with a lower symmetry. From another point of view, the external pressure can also raise the Fermi level of the $[\text{BO}_8]^{4+}$ layer by forcing to decrease the BO intermolecular distance, which leads to the decoupling between the SMM layer and the Peierls transition occurring at a higher temperature.

All in all, at high temperature, due to the vibrations smearing the configuration difference (Figure 6.19, right), the BO layer is in a high-symmetry regular form with an equal distance. The Fermi level is close to the top of the hole band, thus electrons on the hole band (the SMM layer) could thermally populate the electron band (the BO layer). Thus, some holes are created in the SMM layer. According to the magnetic coupling results for the $[\text{Co}(\text{pdms})_2]$ dimer, $[\text{Co}(\text{pdms})_2]^{2-}$ units are likely FM coupled. The system shows a metallic conductivity during this stage from 300 K to 62 K as predicted from the band structure and the experiment, thus the BO layer is in a metallic state with Pauli paramagnetism.

While the temperature is decreasing, the amplitude of vibrational modes starts to diminish with the shrinking of the average distance between BO units. The Fermi level of the $[\text{BO}_8]^{4+}$ layer rises, and as a consequence, the electrons become harder to transfer from the SMM layer to the BO layer. Approaching 6.5 K, the electrons

almost settle under the Fermi level. A Fermi surface nesting is likely to happen, forming a charge ordered state. For the BO layer, the vibrations are not enough to avoid the tendency to form a dimer configuration, in which two nearest BO units along the face or the diagonal directions form a closer stacking dimer. A band gap opens, new valence and conduction bands form by the electron–phonon interaction, and a CDW should be observed below 6.5K after the metal–insulator transition (MIT).

Meanwhile, the SMM layer transforms into a super-paramagnetic state (Figure E.2, Figure E.3), The randomly orientated local magnetic moments from the cobalt centers could also make a contribution to reducing the conductivity by magnetic scattering. A low magnetic field would assign a preferenced magnetic orientation to the SMM layer, then such scattering could partially be suppressed. This could be an explication for the negative magnetoresistance observed in the experiment.

7. Conclusion and outlook

To simulate the properties of spintronic devices, dynamic information is often required. Due to a large number of atoms in a device system, classical molecular dynamics (MD) simulations are almost the only option for capturing these dynamics. This requires an appropriate force field for the system. In Chapter 3, a reparameterization tool for reactive force fields (ReaxFF), REAXFFFITTING, was introduced. The score function is proposed to measure the performance of each parameter in the test systems. New parameters are generated by mutation and exchange processes as in a conventional genetic algorithm, and then the score for each parameter is calculated by MD simulations. A first method uses random forest regressor models to learn the score function in the parameter space, followed by grid searching processes to obtain optimized parameters by using the trained models. For the small tested system C_{20} , the accuracy of the predictions was not ideal yet, which mainly results from the fact that the number of data points is still too sparse relative to the high-dimensional parameter space. The duration of the model training and the searching process is one order of magnitude lower than the data preparation, and the validity of the optimizations is guaranteed by genetic algorithms even in the worst case (in which all predictions by the models fail). By tuning hyperparameters of machine-learning models, it is expected to achieve higher accuracy. Therefore, this is a feasible way to accelerate the optimization process. A second method uses contractive autoencoder (CAE) and locally linear embedding (LLE) to learn the distribution of the parameters with good performance, which enables dimension reduction. CAE has a more stable and accurate performance than a conventional autoencoder with a suitable setting of the Jacobian term. For the tested C_{20} system, the original 44-dimensional parameter vector can be reduced to 35 dimensions. This reduction should work better for a more complicated force field (with higher dimensions) due to more redundancy in the parameter for a certain subsystem. For example, a subsystem only needs a certain part of the parameter components to describe its dynamics. Then the rest of the components are redundant for this subsystem. A third method tries to segment the components of the parameter vector based on the correlations between any two components. The correlations can be represented by a diagram, which can then be partitioned into smaller subdiagrams

by means of graph theory. It could provide great simplification for complex systems. Parameter components could be segmented into small portions, and then the optimization process could be done on those portions sequentially. The desired one-click optimization is not yet available, but it offers a promising path to optimize parameters in high-dimensional spaces.

Computational chemistry methods can also be used to obtain reasonable geometrical information and to unveil possible interactions between molecular fragments or between molecules and surfaces. The nitroxyl radical TEMPO is commonly used for spintronic devices based on mechanically controlled break junctions (MCBJs) and double tunnel junctions (DTJs). Gold is a common electrode material for MCBJ. The interaction between TEMPO and gold could play an important role in addition to the binding of molecular bridges via the anchoring groups if the structure of the molecular bridge allows for it. In the first part of Chapter 4, we found that the interaction between TEMPO and gold is as strong as for some conventional anchoring groups (*e.g.*, amino, hydroxyl, carboxyl). The validity of the selected PBE functional with Grimme’s dispersion correction (PBE-D3) was verified by a CCSD(T) reference. The interaction mainly consists of the orbital interaction between the NO site and the closest gold atom, and the dispersion interaction between the four methyl groups and the gold surface. They are competitive and complementary, which results in similar adsorption energies on the various types of gold surfaces. Based on the extended transition state–natural orbitals for chemical valence (ETS-NOCV) analysis, the frontier orbital of TEMPO, π_{NO}^* , and the d orbitals of the nearest gold atom are mixed. The electron donation and backdonation between the mixed orbitals and the orbitals of the rest gold atoms contributes most of the orbital interaction. In the second part, for the DTJ, the structures of TEMPO–OPE molecules embedded between SiO_2 and Al_2O_3 layers are explored. The molecules can form a strong chemical bond if the surfaces show the nature of a strong Lewis base or Lewis acid. Because the TEMPO group and the amide group in TEMPO–OPE can form hydrogen bonds between hydroxyl groups, TEMPO–OPE can interact with a hydroxylated surface significantly. Meanwhile, the excess surface hydroxyl groups may broaden the SOMO energy level of TEMPO. If the SOMO is used to store information as a register by an electron paramagnetic resonance (EPR) method, such an interaction could accelerate the decoherence process. The vibrational modes of the hydrogen bonding hydroxyl group provide a thermal bath for the electronic state of TEMPO. The coherence of the TEMPO ensemble prepared by an EPR pulse sequence could be destroyed by the noise from the thermal bath through the electron–phonon couplings. From a theoretical point of view, it is thus important to avoid excessive water vapor during the preparation. Based on the calculations of the

TEMPO–OPE molecules between the double layers, the spin is mainly preserved on the TEMPO group, which ensures the feasibility of making a spin devices.

As a routine characterizing method, spintronics experiments often focus on the measurement of conductivity. For crystalline materials, the conductivity mechanisms can be derived from band structure calculations or by analyzing the possible interactions between neighboring molecules. In Chapter 5, two hybrid compounds consisting of a photochromic linker and a valence tautomer unit show spin crossover (SCO) behavior. Furthermore, the open-form **o-CoDAE** shows an abnormal conductivity change at the same transition temperature as the SCO. The PBE+U band structures suggest a high conductivity in both cases, which is contradictory to the experimental results. This likely results from the on-site Coulomb repulsion of the frontier orbitals located on the ligands, which makes the mean-field method inapplicable in this system. The conductivity is more likely dominated by the hopping mechanism. Thus, the electron transfer matrix elements between the various combinations of the differently charged units were determined. As a result, the closed-form **c-CoDAE** behaves like a 1D semiconductor with high conductivity along the *b* axis. **o-CoDAE** behaves like a 2D semiconductor in the *ab* plane, and the symmetric CoL₂ layers play the main part in conductivity. The abnormal conductivity at around 330 K is due to the zero electron transfer matrix elements between the *low-spin* and the *high-spin* units, which leads to the conductivity dropping when the spin crossover occurs.

In Chapter 6, **CoBO**₄ shows metallic conductivity, but with an abnormal drop at 6.5 K. The PBE band structure based on the crystal structure shows Fermi surfaces, which means the system is metallic just as the experiment suggests. However, due to the lack of structural data at low temperatures, the mechanism of the drop cannot be rationalized in the same manner. Thus, the on-site Coulomb repulsion, the inter-fragment electronic couplings, and the possible electron–phonon couplings were explored. As a result, at low temperature, the system has a metal–insulator transition and converts into a charge density wave (CDW) by electron–phonon coupling, which causes the drop in conductivity.

To sum up the above, we have discussed some example applications of computational chemistry in spintronics along with steps towards improving simulation methods. As the modeled objects have different scales in time and space, it is necessary to establish an effective model by simplifying the system with suitable approximations. For the time dimension, it is necessary to properly average out the degrees of freedom with rapid fluctuations. The motion of electrons is thousands of times faster than atoms, thus, for MD simulations, the consequence of the motion can be effectively represented by a force field since the details of electron motion are not important.

For the space dimensions, some structural details could also be simplified if a set of particles can be considered as a whole. Such coarse-grained methods could largely reduce the degrees of freedom. Such a multiscale model is a valuable goal for future simulations of nanoscale spintronics systems and beyond.

A. Supporting information for theoretical background

A.1. Creation and annihilation operators

In addition to the Slater determinant, we also can use second quantization to construct the antisymmetric vectors. Here we define the annihilation operators X and the creation operators X^\dagger for the Fermion system. The annihilation operator X_p annihilates a particle in the p state. If the state is already unoccupied, it yields a zero. On the other hand, the creation operator X_p^\dagger create a particle in the p state. If the creation operator is applied to a already occupied state, it also returns zero. This violates the Pauli exclusion principle.

$$X_p |\cdots n_p \cdots\rangle = (-1)^m n_p |\cdots (n_p - 1) \cdots\rangle \quad ; \quad m = \sum_{k=1}^{p-1} n_k$$

$$X_p |\cdots n_p \cdots\rangle = \begin{cases} (-1)^m |\cdots 0 \cdots\rangle & ; \quad n_p = 1 \\ 0 & ; \quad n_p = 0 \end{cases}$$

$$X_p^\dagger |\cdots n_p \cdots\rangle = (-1)^m (1 - n_p) |\cdots (1 - n_p) \cdots\rangle \quad ; \quad m = \sum_{k=1}^{p-1} n_k$$

$$X_p^\dagger |\cdots n_p \cdots\rangle = \begin{cases} 0 & ; \quad n_p = 1 \\ (-1)^m |\cdots 1 \cdots\rangle & ; \quad n_p = 0 \end{cases}$$

The two operators obey the canonical anticommutation relations. The swap between any two annihilation operators or any two creation operators will change the sign. The change of the sign of swapping an annihilation with a creation operator depends on the state they are applied to.

$$\{X_p^\dagger, X_q\} = \delta_{pq} \quad , \quad \{X_p, X_q\} = 0 \quad , \quad \{X_p^\dagger, X_q^\dagger\} = 0$$

Thus, for a state vector, if $\{p_n\}$ is ordered, *i.e.*, $p_1 < \cdots < p_N$, it could be written as $|\Phi_{p_1 \cdots p_N}\rangle = X_{p_1}^\dagger \cdots X_{p_N}^\dagger |0\rangle$.

A.2. Operators in second quantization

In the most general form of an operator, it can be written as a sum over all k -body operators, $\hat{O} = \sum_{k=0}^N \hat{O}_k$. Here, \hat{O}_k describing the interaction based on all possible combinations of k -particles over N , $\hat{O}_k = \sum_{1=i_1 < \dots < i_k}^N \hat{o}_k(\mathbf{x}_{i_1} \dots \mathbf{x}_{i_k})$. An operator should be symmetric with respect to a permutation operation, $[\hat{O}, \pi] = 0$, $\forall \pi \in S_N$. Thus under a permutation, the states are antisymmetric, and the operators are symmetric, which leading antisymmetric expectation values.

$$\begin{aligned}
 & \hat{O}_1 \Phi_{p_1 \dots p_N}(\mathbf{x}_1 \dots \mathbf{x}_N) \\
 &= \hat{O}_1 \sqrt{N!} \mathcal{A} \left(\prod_{k=1}^N \psi_{p_k}(\mathbf{x}_k) \right) \\
 &= \sqrt{N!} \mathcal{A} \hat{O}_1 \left(\prod_{k=1}^N \psi_{p_k}(\mathbf{x}_k) \right) \\
 &= \sqrt{N!} \mathcal{A} \sum_{i=1}^N \hat{o}_1(\mathbf{x}_i) \psi_{p_i}(\mathbf{x}_i) \left(\prod_{k \neq i} \psi_{p_k}(\mathbf{x}_k) \right) \\
 &= \sqrt{N!} \mathcal{A} \sum_{i=1}^N \sum_p \langle p | \hat{o}_1 | p_i \rangle \psi_p(\mathbf{x}_i) \left(\prod_{k \neq i} \psi_{p_k}(\mathbf{x}_k) \right) \\
 &= \sum_i \sum_p \langle p | \hat{o}_1 | p_i \rangle \sqrt{N!} \mathcal{A} (\psi_{p_1}(\mathbf{x}_1) \dots \psi_{p_{i-1}}(\mathbf{x}_{i-1}) \dots \psi_p(\mathbf{x}_i) \dots \psi_{p_{i+1}}(\mathbf{x}_{i+1}) \dots \psi_{p_N}(\mathbf{x}_N)) \\
 &= \langle \mathbf{x}_1 \dots \mathbf{x}_N | \sum_i \sum_p \langle p | \hat{o}_1 | p_i \rangle | \Phi_{p_1 \dots p_{i-1} p p_{i+1} \dots p_N} \rangle \\
 &= \langle \mathbf{x}_1 \dots \mathbf{x}_N | \sum_i \sum_p \langle p | \hat{o}_1 | p_i \rangle X_{p_1}^\dagger X_{p_2}^\dagger \dots X_{p_{i-1}}^\dagger X_p^\dagger X_{p_{i+1}}^\dagger \dots X_{p_N}^\dagger | 0 \rangle \\
 &= \langle \mathbf{x}_1 \dots \mathbf{x}_N | \sum_i \sum_p \langle p | \hat{o}_1 | p_i \rangle (-1)^{i-1} X_p^\dagger \left(X_{p_1}^\dagger X_{p_2}^\dagger \dots X_{p_{i-1}}^\dagger X_{p_{i+1}}^\dagger \dots X_{p_N}^\dagger \right) | 0 \rangle \\
 &= \langle \mathbf{x}_1 \dots \mathbf{x}_N | \sum_i \sum_{p,q} \langle p | \hat{o}_1 | q \rangle \delta_{p_i q} (-1)^{i-1} X_p^\dagger \left(X_{p_1}^\dagger X_{p_2}^\dagger \dots X_{p_{i-1}}^\dagger X_{p_{i+1}}^\dagger \dots X_{p_N}^\dagger \right) | 0 \rangle \\
 &= \langle \mathbf{x}_1 \dots \mathbf{x}_N | \sum_{p,q} \langle p | \hat{o}_1 | q \rangle X_p^\dagger \sum_i (-1)^{i-1} \delta_{p_i q} \left(X_{p_1}^\dagger X_{p_2}^\dagger \dots X_{p_{i-1}}^\dagger X_{p_{i+1}}^\dagger \dots X_{p_N}^\dagger \right) | 0 \rangle \\
 &= \langle \mathbf{x}_1 \dots \mathbf{x}_N | \sum_{p,q} \langle p | \hat{o}_1 | q \rangle X_p^\dagger X_q \left(X_{p_1}^\dagger \dots X_{p_N}^\dagger \right) | 0 \rangle \\
 &= \sum_{p,q} \langle p | \hat{o}_1 | q \rangle X_p^\dagger X_q \Phi_{p_1 \dots p_N}(\mathbf{x}_1 \dots \mathbf{x}_N)
 \end{aligned}$$

In the field of chemistry, normally, only the one-body and the two-body interactions need to be considered. For an one-body operator acts on an N -body wavefunction. The single particle operator \hat{o}_1 eats the state q and spits out the new state p , the matrix element $\langle p|\hat{o}_1|q\rangle$ describes the amplitude of such process.

$$\begin{aligned}
 \hat{O}_1 &= \sum_{pq} \langle p|\hat{o}_1|q\rangle X_p^\dagger X_q \\
 \hat{O}_2 &= \frac{1}{2} \sum_{pqrs} \langle pq|\hat{o}_2|rs\rangle X_p^\dagger X_q^\dagger X_s X_r \\
 \hat{O}_k &= \frac{1}{k!} \sum_{\substack{p_1 \cdots p_k \\ q_1 \cdots q_k}} \langle p_1 \cdots p_k|\hat{o}_k|q_1 \cdots q_k\rangle X_{p_1}^\dagger \cdots X_{p_k}^\dagger X_{q_k} \cdots X_{q_1} \\
 &= \left(\frac{1}{k!}\right)^2 \sum_{\substack{p_1 \cdots p_k \\ q_1 \cdots q_k}} \langle p_1 \cdots p_k|\hat{o}_k|q_1 \cdots q_k\rangle_{\mathcal{A}} X_{p_1}^\dagger \cdots X_{p_k}^\dagger X_{q_k} \cdots X_{q_1}
 \end{aligned}$$

For a general k -body operator, it able to convert k single particle states, the matrix elements could also be antisymmetrized to fit the requirements of the Hugenholtz type diagrams, and the normal matrix elements work for the Goldstone type diagrams.

$$\langle p_1 \cdots p_k|\hat{o}_k|q_1 \cdots q_k\rangle_{\mathcal{A}} = \sum_{\pi \in S_k} (-1)^{\# \pi} \langle p_1 \cdots p_k|\hat{o}_k|q_{\pi(1)} \cdots q_{\pi(k)}\rangle$$

It is easy to see that to calculate the result of the action of an operator on a state, a bunch of creation and annihilation operators need to be handled. For example, the operator $X_p^\dagger X_q$ acts on the state vector $|rs\rangle$, the result could be calculate by moving the annihilation operator to the right to form a *normal order*. Such process could be done by using the anticommutation relations. As the result, one state in the original is replaced by the new state p . However this method is cumbersome and inefficient for a large number of operators.

$$\begin{aligned}
 X_p^\dagger X_q |rs\rangle &= X_p^\dagger X_q X_r^\dagger X_s^\dagger |0\rangle \\
 &= X_p^\dagger (\delta_{rq} - X_r^\dagger X_q) X_s^\dagger |0\rangle \\
 &= \delta_{rq} X_p^\dagger X_s^\dagger |0\rangle - X_p^\dagger X_r^\dagger X_q X_s^\dagger |0\rangle \\
 &= \delta_{rq} X_p^\dagger X_s^\dagger |0\rangle - X_p^\dagger X_r^\dagger (\delta_{qs} - X_s^\dagger X_q) |0\rangle \\
 &= \delta_{rq} X_p^\dagger X_s^\dagger |0\rangle - \delta_{qs} X_p^\dagger X_r^\dagger |0\rangle + \underbrace{X_s^\dagger X_q |0\rangle}_0 \\
 &= \delta_{rq} X_p^\dagger X_s^\dagger |0\rangle - \delta_{qs} X_p^\dagger X_r^\dagger |0\rangle \\
 &= \delta_{rq} |ps\rangle + \delta_{sq} |rp\rangle
 \end{aligned}$$

A.3. Wick's theorem

Normally, the problem need to solved has the form of, $M_1 \cdots M_m |0\rangle$, or, $\langle 0| M_1 \cdots M_m |0\rangle$, where the M_i could be either a creation operator or an annihilation operator.

The most important thing is how to efficiently transform the bunch of operators into normal order, moving all annihilation operators to the right side.

$$n[M_1 \cdots M_m] = (-1)^{\# \pi} X_{\pi(1)}^\dagger X_{\pi(2)}^\dagger \cdots X_{\pi(j)}^\dagger X_{\pi(j+1)} \cdots X_{\pi(m)}$$

By the definition, $n[\emptyset] = 1$, the normal product has the following properties.

$$\begin{aligned} n[M] &= M \\ n[n[M_1 \cdots M_m]] &= n[M_1 \cdots M_m] \\ n[M_{\pi(1)} \cdots M_{\pi(m)}] &= (-1)^{\# \pi} n[M_1 \cdots M_m] \end{aligned}$$

To evaluate, the difference between the original operator and the normal ordered on, the *contraction* is defined.

$$\begin{array}{c} M_1 M_2 = M_1 M_2 - n[M_1 M_2] \\ \square \end{array}$$

The contractions between two operators are zero unless for the $X_p X_p^\dagger$ case.


$$\begin{aligned} \begin{array}{c} X_p X_q = 0 \\ \square \end{array} & \quad ; \quad \begin{array}{c} X_p^\dagger X_q = 0 \\ \square \end{array} \quad ; \quad \begin{array}{c} X_p^\dagger X_q^\dagger = 0 \\ \square \end{array} \\ \begin{array}{c} X_p X_q^\dagger = X_p X_q^\dagger - n[X_p X_q^\dagger] = X_p X_q^\dagger + X_q^\dagger X_p = \{X_p, X_q^\dagger\} = \delta_{p,q} \\ \square \end{array} \end{aligned}$$

The contractions could also be operated in a normal ordered product, sorting the contracted terms produces a phase factor of the corresponding permutation π . The result of a contraction is just a number thus could be pick up.

$$\begin{aligned} & n[M_1 \cdots M_{i_1} \cdots M_{i_\lambda} \cdots M_{j_1} \cdots M_{j_\lambda} \cdots M_m] \\ & \quad \begin{array}{c} \square \quad \square \end{array} \\ &= (-1)^{\# \pi} n[M_{i_1} M_{j_1} \cdots M_{i_\lambda} M_{j_\lambda} M_{k_1} \cdots M_{k_\mu}] \\ & \quad \begin{array}{c} \square \quad \square \end{array} \\ &= (-1)^{\# \pi} M_{i_1} M_{j_1} \cdots M_{i_\lambda} M_{j_\lambda} n[M_{k_1} \cdots M_{k_\mu}] \\ & \quad \begin{array}{c} \square \quad \square \end{array} \end{aligned}$$

$$\pi = \begin{pmatrix} 1 & 2 & \cdots & 2\lambda - 1 & 2\lambda & 2\lambda + 1 & \cdots & m \\ i_1 & j_1 & \cdots & i_\lambda & j_\lambda & k_1 & \cdots & k_\mu \end{pmatrix} \quad ; \quad 2\lambda + \mu = m$$

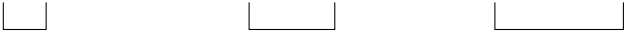
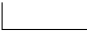
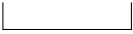






Here is an example.

$$n[X_p X_q X_r^\dagger X_s X_t^\dagger X_u^\dagger] = X_p X_r^\dagger X_q X_t^\dagger n[X_s X_u^\dagger] = -\delta_{pr} \delta_{qt} X_u^\dagger X_s$$


According to the time-independent Wick's theorem, the product of operators could be written into a sum over all possible combinations in the normal ordered product.

$$M_1 \cdots M_m = \sum_{\text{All possible contractions}} n[M_1 \cdots \cdots M_m]$$


In the case with four operators, it could be decomposed into the 1 term with no contraction, the 6 terms with one contractions, the 3 terms with two contractions.

$$\begin{aligned} M_1 M_2 M_3 M_4 &= n[M_1 M_2 M_3 M_4] \\ &+ n[M_1 M_2 M_3 M_4] + n[M_1 M_2 M_3 M_4] + n[M_1 M_2 M_3 M_4] \\ &+ n[M_1 M_2 M_3 M_4] + n[M_1 M_2 M_3 M_4] + n[M_1 M_2 M_3 M_4] \\ &+ n[M_1 M_2 M_3 M_4] + n[M_1 M_2 M_3 M_4] + n[M_1 M_2 M_3 M_4] \end{aligned}$$










In the following case, we can easy find most of the contractions are zero. Only the three terms left. The term with no contraction contains an annihilation operator, it also vanishes as acting on the vacuum state.

$$\begin{aligned}
 X_p^\dagger X_q X_r^\dagger X_s^\dagger &= n[X_p^\dagger X_q X_r^\dagger X_s^\dagger] \\
 &+ n[\underbrace{X_p^\dagger X_q X_r^\dagger X_s^\dagger}] + n[\underbrace{X_p^\dagger X_q X_r^\dagger X_s^\dagger}] + n[\underbrace{X_p^\dagger X_q X_r^\dagger X_s^\dagger}] \\
 &+ n[\underbrace{X_p^\dagger X_q X_r^\dagger X_s^\dagger}] + n[\underbrace{X_p^\dagger X_q X_r^\dagger X_s^\dagger}] + n[\underbrace{X_p^\dagger X_q X_r^\dagger X_s^\dagger}] \\
 &+ n[\underbrace{X_p^\dagger X_q X_r^\dagger X_s^\dagger}] + n[\underbrace{X_p^\dagger X_q X_r^\dagger X_s^\dagger}] + n[\underbrace{X_p^\dagger X_q X_r^\dagger X_s^\dagger}] \\
 &= n[\underbrace{X_p^\dagger X_q X_r^\dagger X_s^\dagger}] + n[\underbrace{X_p^\dagger X_q X_r^\dagger X_s^\dagger}] + n[\underbrace{X_p^\dagger X_q X_r^\dagger X_s^\dagger}] \\
 &= X_q X_r^\dagger n[\underbrace{X_p^\dagger X_s^\dagger}] - X_q X_s^\dagger n[\underbrace{X_p^\dagger X_r^\dagger}] + n[\underbrace{X_p^\dagger X_q X_r^\dagger X_s^\dagger}] \\
 &= \delta_{qr} X_p^\dagger X_s^\dagger + \delta_{qs} X_r^\dagger X_p^\dagger + n[\underbrace{X_p^\dagger X_q X_r^\dagger X_s^\dagger}] \\
 &\Downarrow \\
 X_p^\dagger X_q |rs\rangle &= \delta_{qr} X_p^\dagger X_s^\dagger |0\rangle + \delta_{qs} X_r^\dagger X_p^\dagger |0\rangle = \delta_{qr} |ps\rangle + \delta_{qs} |rp\rangle
 \end{aligned}$$

It is obvious, the attributing terms of the operators acting on the vacuum state are the annihilation fully contracted (a.f.c.). And for the expectation values, the terms need to be fully contracted (f.c.). Otherwise the remaining operators will bring the result of the term to zero.

$$M_1 \cdots M_m |0\rangle = \sum_{\text{a.f.c.}} n[\underbrace{M_1 \cdots \cdots M_m}] |0\rangle$$

$$\langle 0 | M_1 \cdots M_m | 0 \rangle = \langle 0 | \sum_{\text{f.c.}} n[\underbrace{M_1 \cdots \cdots M_m}] | 0 \rangle$$

A.4. Fermi vacuum and hole-particle formalism

In the above, the discussions are based on the true vacuum $|0\rangle$. When dealing with condensed systems, such as molecules, many states are occupied, resulting in a large number of creation operators to be written if the true vacuum state $|0\rangle$ is used as a reference. To simplify the process, a reference state $|\Phi\rangle$ could be used as the new vacuum, *Fermi vacuum*. As a convention, for the state indices, i, j, k, l, m, n, \cdots are for the occupied (occ.) spin-orbitals, a, b, c, d, e, f, \cdots are for the unoccupied

(unocc.) spin-orbitals, p, q, r, s, t, u, \dots are for the generic spin-orbitals. The single excited state could be written as, $|\Phi_i^a\rangle = X_a^\dagger X_i |\Phi\rangle$, it creates a hole on the state i and a particle on the state a .

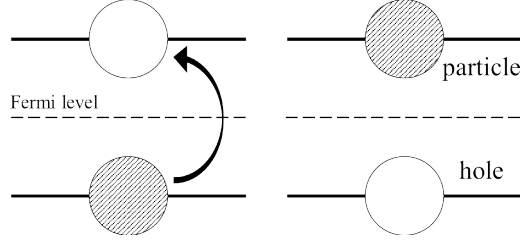


Figure A.1.: The hole and particle are created by single excitation.

The corresponding operators based on the Fermi vacuum are defined as follow, where Y_i^\dagger and Y_a^\dagger create a hole and a particle respectively, Y_i and Y_a annihilate a hole and a particle respectively. Sometimes they are called pseudo-creation and pseudo-annihilation operators.

$$\begin{aligned} \text{occ.} \quad Y_i &= X_i^\dagger \quad ; \quad Y_i^\dagger = X_i \\ \text{unocc.} \quad Y_a &= X_a \quad ; \quad Y_a^\dagger = X_a^\dagger \end{aligned}$$

$p, q \in \text{occ.}$ $p = i, q = j$ $\{Y_i, Y_j\} = \{X_i^\dagger, X_j^\dagger\} = 0$ $\{Y_i^\dagger, Y_j^\dagger\} = \{X_i, X_j\} = 0$ $\{Y_i, Y_j^\dagger\} = \{X_i^\dagger, X_j\} = \delta_{ij}$	$p, q \in \text{unocc.}$ $p = a, q = b$ $\{Y_a, Y_b\} = \{X_a, X_b\} = 0$ $\{Y_a^\dagger, Y_b^\dagger\} = \{X_a^\dagger, X_b^\dagger\} = 0$ $\{Y_a, Y_b^\dagger\} = \{X_a, X_b^\dagger\} = \delta_{ab}$
$p \in \text{occ.} \quad ; \quad q \in \text{unocc.}$ $p = i, q = a$ $\{Y_i, Y_a\} = \{X_i^\dagger, X_a\} = 0$ $\{Y_i^\dagger, Y_a^\dagger\} = \{X_i, X_a^\dagger\} = \delta_{ia} = 0$ $\{Y_i, Y_a^\dagger\} = \{X_i^\dagger, X_a^\dagger\} = 0 = \delta_{ia}$	$p \in \text{unocc.} \quad ; \quad q \in \text{occ.}$ $p = a, q = i$ $\{Y_a, Y_i\} = \{X_a, X_i^\dagger\} = 0$ $\{Y_a^\dagger, Y_i^\dagger\} = \{X_a^\dagger, X_i\} = 0$ $\{Y_a, Y_i^\dagger\} = \{X_a, X_i\} = 0 = \delta_{ai}$

According to the above, the creation and annihilation operators for the Fermi vacuum have same anticommutation relations with the operators for the true vacuum.

$$\{Y_p, Y_q\} = 0 \quad ; \quad \{Y_p^\dagger, Y_q^\dagger\} = 0 \quad ; \quad \{Y_p, Y_q^\dagger\} = \delta_{pq}$$

Use the same logic, the normal order with respect to the Fermi vacuum could be defined, $N[M_1 \cdots M_m]$, where M could be either Y or Y^\dagger . As a definition, $N[\emptyset] = 1$

The contraction with respect to the Fermi vacuum.

$$\overline{M_1 M_2} = M_1 M_2 - N[M_1 M_2]$$

$$\overline{Y_p Y_q} = 0 \quad ; \quad \overline{Y_p^\dagger Y_q} = 0 \quad ; \quad \overline{Y_p^\dagger Y_q^\dagger} = 0 \quad ; \quad \overline{Y_p Y_q^\dagger} = \delta_{p,q}$$

$$M_1 \cdots M_m = \sum_{\text{All possible contractions}} N[\overline{M_1 \cdots M_m}]$$

Here we need to find the rule to contract the vacuum creation and annihilation operators, in the Fermi vacuum picture. Two indicator functions are defined for the state occupation number.

$$\chi(p) = \begin{cases} 1 & p \in \text{occ.} \\ 0 & p \in \text{unocc.} \end{cases} \quad \pi(p) = \begin{cases} 0 & p \in \text{occ.} \\ 1 & p \in \text{unocc.} \end{cases}$$

$$\chi(p) + \pi(p) = 1 \quad ; \quad \chi(p)\pi(p) = 0 \quad ; \quad \chi^2(p) = \chi(p) \quad ; \quad \pi^2(p) = \pi(p)$$

$$\begin{aligned} \overline{X_p Y_q} &= \chi(p) \overline{X_p Y_q} + \pi(p) \overline{X_p Y_q} = \chi(p) \overline{Y_p^\dagger Y_q} + \pi(p) \overline{Y_p Y_q} = 0 \\ \overline{X_p Y_q^\dagger} &= \chi(p) \overline{X_p Y_q^\dagger} + \pi(p) \overline{X_p Y_q^\dagger} = \chi(p) \overline{Y_p^\dagger Y_q^\dagger} + \pi(p) \overline{Y_p Y_q^\dagger} = \pi(p) \delta_{pq} \\ \overline{X_p^\dagger Y_q} &= 0 \\ \overline{X_p^\dagger Y_q^\dagger} &= \chi(p) \overline{X_p^\dagger Y_q^\dagger} + \pi(p) \overline{X_p^\dagger Y_q^\dagger} = \chi(p) \overline{Y_p Y_q^\dagger} + \pi(p) \overline{Y_p^\dagger Y_q^\dagger} = \chi(p) \delta_{pq} \end{aligned}$$

$$\begin{aligned} \overline{Y_p X_q} &= \chi(q) \overline{Y_p X_q} + \pi(q) \overline{Y_p X_q} = \chi(q) \overline{Y_p Y_q^\dagger} + \pi(q) \overline{Y_p Y_q} = \chi(q) \delta_{pq} \\ \overline{Y_p X_q^\dagger} &= \chi(q) \overline{Y_p X_q^\dagger} + \pi(q) \overline{Y_p X_q^\dagger} = \chi(q) \overline{Y_p Y_q} + \pi(q) \overline{Y_p Y_q^\dagger} = \pi(q) \delta_{pq} \\ \overline{Y_p^\dagger X_q} &= \chi(q) \overline{Y_p^\dagger X_q} + \pi(q) \overline{Y_p^\dagger X_q} = \chi(q) \overline{Y_p^\dagger Y_q^\dagger} + \pi(q) \overline{Y_p^\dagger Y_q} = 0 \\ \overline{Y_p^\dagger X_q^\dagger} &= \chi(q) \overline{Y_p^\dagger X_q^\dagger} + \pi(q) \overline{Y_p^\dagger X_q^\dagger} = \chi(q) \overline{Y_p^\dagger Y_q} + \pi(q) \overline{Y_p^\dagger Y_q^\dagger} = 0 \end{aligned}$$

$$\begin{aligned}
 \overline{X_p X_q} &= \chi(p)\chi(q)\overline{X_p X_q} + \chi(p)\pi(q)\overline{X_p X_q} + \pi(p)\chi(q)\overline{X_p X_q} + \pi(p)\pi(q)\overline{X_p X_q} \\
 &= \chi(p)\chi(q)\overline{Y_p^\dagger Y_q^\dagger} + \chi(p)\pi(q)\overline{Y_p^\dagger Y_q} + \pi(p)\chi(q)\overline{Y_p Y_q^\dagger} + \pi(p)\pi(q)\overline{Y_p Y_q} \\
 &= \delta_{pq}\pi(p)\chi(q) = \pi(p)\chi(p) = 0 \\
 \overline{X_p X_q^\dagger} &= \chi(p)\chi(q)\overline{X_p X_q^\dagger} + \chi(p)\pi(q)\overline{X_p X_q^\dagger} + \pi(p)\chi(q)\overline{X_p X_q^\dagger} + \pi(p)\pi(q)\overline{X_p X_q^\dagger} \\
 &= \chi(p)\chi(q)\overline{Y_p^\dagger Y_q} + \chi(p)\pi(q)\overline{Y_p^\dagger Y_q^\dagger} + \pi(p)\chi(q)\overline{Y_p Y_q^\dagger} + \pi(p)\pi(q)\overline{Y_p Y_q} \\
 &= \delta_{pq}\pi(p)\pi(q) = \pi(p)\delta_{pq} \\
 \overline{X_p^\dagger X_q} &= \chi(p)\chi(q)\overline{Y_p Y_q^\dagger} = \chi(p)\delta_{pq} \\
 \overline{X_p^\dagger X_q^\dagger} &= \chi(p)\pi(q)\overline{Y_p Y_q^\dagger} = \delta_{pq}\chi(p)\pi(q) = 0
 \end{aligned}$$

For example, the reference $|\Phi\rangle = |\{p_1 \cdots p_N\}\rangle$, \hat{Z} and \hat{V} are the one-body operator and the two-body operator respectively. For the expectation values, the terms need to be fully contracted.

$$\begin{aligned}
 \langle \Phi | \hat{Z} | \Phi \rangle &= \sum_{p,q} \langle p | \hat{z} | q \rangle \langle \Phi | X_p^\dagger X_q | \Phi \rangle \\
 &= \sum_{p,q} \langle p | \hat{z} | q \rangle \langle \Phi | N[\overline{X_p^\dagger X_q}] | \Phi \rangle = \sum_{p,q} \langle p | \hat{z} | q \rangle \chi(p)\delta_{pq} \\
 &= \sum_{p \in \text{occ.}} \langle p | \hat{z} | p \rangle = \sum_i \langle i | \hat{z} | i \rangle
 \end{aligned}$$

$$\begin{aligned}
 \langle \Phi | \hat{V} | \Phi \rangle &= \frac{1}{2} \sum_{pqrs} \langle pq | \hat{v} | rs \rangle \langle \Phi | X_p^\dagger X_q^\dagger X_s X_r | \Phi \rangle \\
 &= \frac{1}{2} \sum_{pqrs} \langle pq | \hat{v} | rs \rangle \left(\langle \Phi | N[\overline{X_p^\dagger X_q^\dagger X_s X_r}] | \Phi \rangle + \langle \Phi | N[\overline{X_p^\dagger X_q^\dagger X_s X_r}] | \Phi \rangle \right) \\
 &= \frac{1}{2} \sum_{pqrs} \langle pq | \hat{v} | rs \rangle (-\chi(p)\chi(q)\delta_{ps}\delta_{qr} + \chi(p)\chi(q)\delta_{pr}\delta_{qs}) \\
 &= \frac{1}{2} \sum_{p,q \in \text{occ.}} (-\langle pq | \hat{v} | qp \rangle + \langle pq | \hat{v} | pq \rangle) = \frac{1}{2} \sum_{i,j} \langle ij | \hat{v} | ij \rangle_{\mathcal{A}}
 \end{aligned}$$

A.4.1. Decomposition of the operators

In the more general case, the one-body operator Z could be fully contracted, the corresponding term is the Fermi vacuum dependent expectation value $\langle \Phi | \hat{Z} | \Phi \rangle$. And uncontracted part corresponds to the intrinsic one-body interaction term \hat{Z}_N .

$$\begin{aligned}
 \hat{Z} &= \sum_{pq} \langle p | \hat{z} | q \rangle X_p^\dagger X_q \\
 &= \sum_{pq} \langle p | \hat{z} | q \rangle \left(N[X_p^\dagger X_q] + N[\overline{X_p^\dagger X_q}] \right) \\
 &= \sum_{pq} \langle p | \hat{z} | q \rangle N[X_p^\dagger X_q] + \sum_{pq} \langle p | \hat{z} | q \rangle \chi(p) \delta_{pq} \\
 &= \hat{Z}_N + \sum_{p \in \text{occ.}} \langle p | \hat{z} | p \rangle \\
 &= \hat{Z}_N + \langle \Phi | \hat{Z} | \Phi \rangle
 \end{aligned}$$

$$\begin{aligned}
 \hat{V} &= \frac{1}{2} \sum_{pqrs} \langle pq | \hat{v} | rs \rangle X_p^\dagger X_q^\dagger X_s X_r \\
 &= \frac{1}{2} \sum_{pqrs} \langle pq | \hat{v} | rs \rangle \left(N[X_p^\dagger X_q^\dagger X_s X_r] + N[\overline{X_p^\dagger X_q^\dagger X_s X_r}] + N[\overline{X_p^\dagger X_q^\dagger X_s X_r}] \right. \\
 &\quad \left. + N[X_p^\dagger \overline{X_q^\dagger X_s X_r}] + N[X_p^\dagger \overline{X_q^\dagger X_s X_r}] + N[\overline{X_p^\dagger X_q^\dagger X_s X_r}] + N[\overline{X_p^\dagger X_q^\dagger X_s X_r}] \right) \\
 &= \frac{1}{2} \sum_{pqrs} \langle pq | \hat{v} | rs \rangle \left(N[X_p^\dagger X_q^\dagger X_s X_r] - \chi(p) \delta_{ps} N[X_q^\dagger X_r] + \chi(p) \delta_{pr} N[X_q^\dagger X_s] \right. \\
 &\quad \left. + \chi(q) \delta_{qs} N[X_p^\dagger X_r] - \chi(q) \delta_{qr} N[X_p^\dagger X_s] + \chi(q) \chi(q) \delta_{pr} \delta_{qs} - \chi(q) \chi(q) \delta_{ps} \delta_{qr} \right) \\
 &= \frac{1}{2} \sum_{pqrs} \langle pq | \hat{v} | rs \rangle \left(N[X_p^\dagger X_q^\dagger X_s X_r] + \chi(p) (\delta_{pr} N[X_q^\dagger X_s] - \delta_{ps} N[X_q^\dagger X_r]) \right. \\
 &\quad \left. + \chi(q) (\delta_{qs} N[X_p^\dagger X_r] - \delta_{qr} N[X_p^\dagger X_s]) + \chi(q) \chi(q) (\delta_{pr} \delta_{qs} - \delta_{ps} \delta_{qr}) \right) \\
 &= \frac{1}{2} \sum_{pqrs} \langle pq | \hat{v} | rs \rangle N[X_p^\dagger X_q^\dagger X_s X_r] \\
 &\quad + \frac{1}{2} \sum_{qs} \sum_{p \in \text{occ.}} \langle pq | \hat{v} | ps \rangle N[X_q^\dagger X_s] - \frac{1}{2} \sum_{qr} \sum_{p \in \text{occ.}} \langle pq | \hat{v} | rp \rangle N[X_q^\dagger X_r] \\
 &\quad + \frac{1}{2} \sum_{pr} \sum_{q \in \text{occ.}} \langle pq | \hat{v} | rq \rangle N[X_p^\dagger X_r] - \frac{1}{2} \sum_{ps} \sum_{q \in \text{occ.}} \langle pq | \hat{v} | qs \rangle N[X_p^\dagger X_s] \\
 &\quad + \frac{1}{2} \sum_{p, q \in \text{occ.}} (\langle pq | \hat{v} | pq \rangle - \langle pq | \hat{v} | qp \rangle) \\
 &= \hat{V}_N + \underbrace{\sum_{p, q} \sum_i \langle pi | \hat{v} | qi \rangle}_{\hat{G}_N} N[X_p^\dagger X_q] + \langle \Phi | \hat{V} | \Phi \rangle
 \end{aligned}$$

The same method applied on the two-body operator V , resulting the intrinsic two-body term \hat{V}_N , the effective one-body interaction \hat{G}_N , and the expectation value $\langle \Phi | \hat{V} | \Phi \rangle$.

$$\begin{aligned}\hat{G}_N &= \sum_{p,q} \langle p | \hat{g} | q \rangle N[X_p^\dagger X_q] \\ \langle p | \hat{g} | q \rangle &= \sum_i \langle pi | \hat{v} | qi \rangle_{\mathcal{A}}\end{aligned}$$

\hat{G}_N describes the state q converting to the state p with the averaging interaction with all other occupied states, which normally called the mean-field.

$$\begin{aligned}\hat{H} &= \hat{Z} + \hat{V} = \hat{Z}_N + \langle \Phi | \hat{Z} | \Phi \rangle + \hat{V}_N + \hat{G}_N + \langle \Phi | \hat{V} | \Phi \rangle \\ &= (\hat{Z}_N + \hat{G}_N) + \hat{V}_N + \langle \Phi | \hat{Z} + \hat{V} | \Phi \rangle \\ &= \hat{F}_N + \hat{V}_N + \langle \Phi | \hat{H} | \Phi \rangle\end{aligned}$$

Thus, the full Hamiltonian \hat{H} could be decomposed as the intrinsic two-body term, the expectation value $\langle \Phi | \hat{H} | \Phi \rangle$, and the effective one-body interaction \hat{F}_N . Here the single particle operator \hat{f} is called Fock operator.

$$\begin{aligned}\hat{F}_N &= \sum_{p,q} \langle p | \hat{f} | q \rangle N[X_p^\dagger X_q] \quad ; \quad \hat{f} = \hat{z} + \hat{g} \\ \langle p | \hat{f} | q \rangle &= \langle p | \hat{z} | q \rangle + \sum_i \langle pi | \hat{v} | qi \rangle_{\mathcal{A}}\end{aligned}$$

A.5. Configuration interaction

As an approach to the exact wavefunction $|\Psi\rangle$, it could be written as the linear combination over the reference state $|\Phi\rangle$ and all other possible excitation states, or called configurations. The configurations could be coupled by the Hamiltonian.

$$\begin{aligned}|\Psi\rangle &= c_0 |\Phi\rangle + \sum_{n=1}^N \sum_{\substack{i_1 < \dots < i_n \\ a_1 < \dots < a_n}} c_{a_1 \dots a_n}^{i_1 \dots i_n} |\Psi_{i_1 \dots i_n}^{a_1 \dots a_n}\rangle \\ &= c_0 |\Phi\rangle + \sum_{n=1}^N \hat{C}_n |\Phi\rangle \\ &= (c_0 + \hat{C}) |\Phi\rangle \quad ; \quad \hat{C} = \sum_{n=1}^N \hat{C}_n\end{aligned}$$

Here, \hat{C}_n is the n -particle-hole excitation operator.

$$\hat{C}_n = \left(\frac{1}{n!}\right)^2 \sum_{\substack{i_1, \dots, i_n \\ a_1, \dots, a_n}} c_{a_1 \dots a_n}^{i_1 \dots i_n} X_{a_1}^\dagger \cdots X_{a_n}^\dagger X_{i_n} \cdots X_{i_1}$$

For the single excited state $|\Phi_i^a\rangle$.

$$\begin{aligned} \langle \Phi | \hat{Z} | \Phi_i^a \rangle &= \sum_{p,q} \langle p | \hat{z} | q \rangle \langle \Phi | X_p^\dagger X_q X_a^\dagger X_i | \Phi \rangle \\ &= \sum_{p,q} \langle p | \hat{z} | q \rangle \langle \Phi | N[\overbrace{X_p^\dagger X_q X_a^\dagger X_i}] | \Phi \rangle \\ &= \sum_{p,q} \langle p | \hat{z} | q \rangle \chi(p) \pi(q) \delta_{pi} \delta_{qa} = \langle i | \hat{z} | a \rangle \end{aligned}$$

$$\begin{aligned} \langle \Phi | \hat{V} | \Phi_i^a \rangle &= \frac{1}{2} \sum_{pqrs} \langle pq | \hat{v} | rs \rangle \langle \Phi | X_p^\dagger X_q^\dagger X_s X_r X_a^\dagger X_i | \Phi \rangle \\ &= \frac{1}{2} \sum_{pqrs} \langle pq | \hat{v} | rs \rangle \left(\langle \Phi | N[\overbrace{X_p^\dagger X_q^\dagger X_s X_r X_a^\dagger X_i}] | \Phi \rangle + \langle \Phi | N[\overbrace{X_p^\dagger X_q^\dagger X_s X_r X_a^\dagger X_i}] | \Phi \rangle \right. \\ &\quad \left. + \langle \Phi | N[\overbrace{X_p^\dagger X_q^\dagger X_s X_r X_a^\dagger X_i}] | \Phi \rangle + \langle \Phi | N[\overbrace{X_p^\dagger X_q^\dagger X_s X_r X_a^\dagger X_i}] | \Phi \rangle \right) \\ &= \frac{1}{2} \sum_{pqrs} \langle pq | \hat{v} | rs \rangle \left(-\chi(p) \chi(q) \pi(r) \delta_{ps} \delta_{qi} \delta_{ra} + \chi(p) \chi(q) \pi(r) \delta_{pi} \delta_{qs} \delta_{ra} \right. \\ &\quad \left. + \chi(p) \chi(q) \pi(s) \delta_{pr} \delta_{qi} \delta_{sa} - \chi(p) \chi(q) \pi(s) \delta_{pi} \delta_{qr} \delta_{sa} \right) \\ &= \frac{1}{2} \sum_{pqrs} \langle pq | \hat{v} | rs \rangle \left(-\chi(p) \delta_{ps} \delta_{qi} \delta_{ra} + \chi(q) \delta_{pi} \delta_{qs} \delta_{ra} + \chi(p) \delta_{pr} \delta_{qi} \delta_{sa} - \chi(q) \delta_{pi} \delta_{qr} \delta_{sa} \right) \\ &= \frac{1}{2} \sum_{pqrs} \langle pq | \hat{v} | rs \rangle \left(\chi(p) \delta_{qi} (\delta_{pr} \delta_{sa} - \delta_{ps} \delta_{ra}) + \chi(q) \delta_{pi} (\delta_{qs} \delta_{ra} - \delta_{qr} \delta_{sa}) \right) \\ &= \frac{1}{2} \sum_{p \in \text{occ.}} \left(\langle pi | \hat{v} | pa \rangle - \langle pi | \hat{v} | ap \rangle \right) + \frac{1}{2} \sum_{q \in \text{occ.}} \left(\langle iq | \hat{v} | aq \rangle - \langle iq | \hat{v} | qa \rangle \right) \\ &= \sum_j \langle ij | \hat{v} | aj \rangle_{\mathcal{A}} \end{aligned}$$

For the double excited state $|\Phi_{ij}^{ab}\rangle$.

$$\begin{aligned} \langle \Phi | \hat{Z} | \Phi_{ij}^{ab} \rangle &= \sum_{p,q} \langle p | \hat{z} | q \rangle \langle \Phi | X_p^\dagger X_q X_a^\dagger X_i X_q X_b^\dagger X_j | \Phi \rangle \\ &= \sum_{p,q} \langle p | \hat{z} | q \rangle \langle \Phi | X_p^\dagger X_q N[X_a^\dagger X_i X_q X_b^\dagger X_j] | \Phi \rangle = 0 \end{aligned}$$

$$\begin{aligned}
 \langle \Phi | \hat{V} | \Phi_{ij}^{ab} \rangle &= \frac{1}{2} \sum_{pqrs} \langle pq | \hat{v} | rs \rangle \langle \Phi | X_p^\dagger X_q^\dagger X_s X_r X_a^\dagger X_i X_b^\dagger X_j | \Phi \rangle \\
 &= \frac{1}{2} \sum_{pqrs} \langle pq | \hat{v} | rs \rangle \left(\langle \Phi | N[X_p^\dagger X_q^\dagger X_s X_r X_a^\dagger X_i X_b^\dagger X_j] | \Phi \rangle \right. \\
 &\quad + \langle \Phi | N[X_p^\dagger X_q^\dagger X_s X_r X_a^\dagger X_i X_b^\dagger X_j] | \Phi \rangle \\
 &\quad + \langle \Phi | N[X_p^\dagger X_q^\dagger X_s X_r X_a^\dagger X_i X_b^\dagger X_j] | \Phi \rangle \\
 &\quad \left. + \langle \Phi | N[X_p^\dagger X_q^\dagger X_s X_r X_a^\dagger X_i X_b^\dagger X_j] | \Phi \rangle \right) \\
 &= \frac{1}{2} \sum_{pqrs} \langle pq | \hat{v} | rs \rangle (\delta_{pi} \delta_{qj} - \delta_{pj} \delta_{qi}) (\delta_{ra} \delta_{sb} - \delta_{rb} \delta_{sa}) \\
 &= \langle ij | \hat{v} | ab \rangle_{\mathcal{A}}
 \end{aligned}$$

In principle, it is possible to construct the exact Hamiltonian matrix according to the above method block by block. And diagonalized the full matrix to get the exact state vectors. Such ideal case is the full configuration interaction (FCI). However, in practice, only a few lower exciton are selected, like CISD only considers the single and double excitation.

$$\begin{array}{c}
 \Phi \text{ (0)} \quad \Phi_i^a \text{ (S)} \quad \Phi_{ij}^{ab} \text{ (D)} \quad \Phi_{ijk}^{abc} \text{ (T)} \quad \dots \quad \dots \\
 \begin{array}{c}
 0 \\
 S \\
 D \\
 T \\
 \vdots \\
 \vdots
 \end{array}
 \left(\begin{array}{cccccc}
 \mathbf{H}_{00} & \mathbf{H}_{0S} & \mathbf{H}_{0D} & \mathbf{H}_{0T} & \dots & \dots \\
 \mathbf{H}_{S0} & \mathbf{H}_{SS} & \mathbf{H}_{SD} & \mathbf{H}_{ST} & \dots & \dots \\
 \mathbf{H}_{D0} & \mathbf{H}_{DS} & \mathbf{H}_{DD} & \mathbf{H}_{DT} & \dots & \dots \\
 \mathbf{H}_{T0} & \mathbf{H}_{TS} & \mathbf{H}_{TD} & \mathbf{H}_{TT} & \dots & \dots \\
 \vdots & \vdots & \vdots & \vdots & \ddots & \vdots \\
 \vdots & \vdots & \vdots & \vdots & \dots & \dots
 \end{array} \right)
 \end{array}$$

A.6. Many-body perturbation theory

The many-body perturbation theories (MBPT), like the Rayleigh-Schrödinger perturbation theory, are another approaching to the exact state. For example \hat{K} is the full operator, but hard to solve, where the $|\Psi\rangle$ and the k are the exact eigenstate and eigenvalue respectively. The \hat{K} could be decomposed into two parts, the unperturbed part is easy to solve with giving a complete set $\{\Phi_n\}$ and the corresponding eigenvalues $\{\kappa_n\}$.

$$\begin{aligned}\hat{K}|\Psi\rangle &= k|\Psi\rangle \quad ; \quad \hat{K} = \underbrace{\hat{K}_0}_{\text{unperturbed operator}} + \underbrace{\hat{W}}_{\text{perturbation}} \\ \hat{K}_0|\Phi_n\rangle &= \kappa_n|\Phi_n\rangle \quad ; \quad n = 0, 1, \dots \quad ; \quad \langle\Phi_m|\Phi_n\rangle = \delta_{mn}\end{aligned}$$

Here the wave operator $\hat{\Omega}$ is defined, which is able to convert the unperturbed reference state $|\Phi_0\rangle$ to the exact state, with the intermediate normalization condition, $\langle\Psi|\Phi_0\rangle = \langle\Phi_0|\Phi_0\rangle = 1$. It is easy to know $\hat{\Omega}$ should be a function of the perturbation \hat{W} .

$$|\Psi\rangle = \hat{\Omega}|\Phi_0\rangle$$

For the energy correction, the reaction operator $\hat{\tau}$ is deduced, then the exact energy could be written as the unperturbed reference energy and the expectation value of the reaction operator with respect to the reference.

$$\begin{aligned}\hat{K}|\Psi\rangle &= k|\Psi\rangle \\ (\hat{K}_0 + \hat{W})|\Psi\rangle &= k|\Psi\rangle \\ \langle\Phi_0|\hat{K}_0|\Psi\rangle + \langle\Phi_0|\hat{W}|\Psi\rangle &= k\langle\Phi_0|\Psi\rangle \\ \kappa_0 + \langle\Phi_0|\hat{W}|\Psi\rangle &= k \\ \kappa_0 + \langle\Phi_0|\hat{W}\hat{\Omega}|\Phi_0\rangle &= k \\ k = \kappa_0 + \langle\Phi_0|\hat{\tau}|\Phi_0\rangle \quad ; \quad \hat{\tau} &= \hat{W}\hat{\Omega}\end{aligned}$$

It is true that, in many cases, the wavefunction and the energy is expanded in series, and then deduce the expression for each order. But this approach is cumbersome and lacks systematicity.

A.6.1. Reduced resolvent

Here the Hilbert space is split to the subspaces of the reference state and the others, $\mathcal{H} = \mathcal{H}_P \oplus \mathcal{H}_Q$, where the reference state $|\Phi_0\rangle$ spans \mathcal{H}_P and $|\Phi_{n \neq 0}\rangle$ span \mathcal{H}_Q . Then the corresponding projection operators \hat{P} and \hat{Q} could be defined. The resolvent of \hat{K} is defined as follow, $\hat{\mathcal{R}}(\kappa, \hat{K})$. Here the α will not appear in the final representation, it is used to guarantee the existence of the inverse.

$$\begin{aligned}\hat{P} &= |\Phi_0\rangle\langle\Phi_0| \quad ; \quad \hat{Q} = 1 - \hat{P} = \sum_{n \neq 0} |\Phi_n\rangle\langle\Phi_n| \\ \hat{\mathcal{R}}(\kappa, \hat{K}) &= \hat{Q} \left[\alpha \hat{P} + \hat{Q}(\kappa - \hat{K})\hat{Q} \right]^{-1} \hat{Q}\end{aligned}$$

$$\hat{P} = \left(\begin{array}{c|c} 1 & 0 \\ \hline 0 & 0 \end{array} \right) \quad ; \quad \hat{Q} = \left(\begin{array}{c|c} 0 & 0 \\ \hline 0 & \mathbf{I}_Q \end{array} \right) \quad ; \quad \hat{K} = \left(\begin{array}{c|c} \mathbf{K}_{PP} & \mathbf{K}_{PQ} \\ \hline \mathbf{K}_{QP} & \mathbf{K}_{QQ} \end{array} \right)$$

$$\begin{aligned} \alpha \hat{P} + \hat{Q}(\kappa - \hat{K})\hat{Q} &= \begin{pmatrix} \alpha & 0 \\ 0 & 0 \end{pmatrix} + \begin{pmatrix} 0 & 0 \\ 0 & \mathbf{I}_Q \end{pmatrix} \begin{pmatrix} \kappa - \mathbf{K}_{PP} & -\mathbf{K}_{PQ} \\ -\mathbf{K}_{QP} & \kappa \mathbf{I}_Q - \mathbf{K}_{QQ} \end{pmatrix} \begin{pmatrix} 0 & 0 \\ 0 & \mathbf{I}_Q \end{pmatrix} \\ &= \begin{pmatrix} \alpha & 0 \\ 0 & \kappa \mathbf{I}_Q - \mathbf{K}_{QQ} \end{pmatrix} \end{aligned}$$

$$\hat{\mathcal{R}}(\kappa, \hat{K}) = \begin{pmatrix} 0 & 0 \\ 0 & \mathbf{I}_Q \end{pmatrix} \begin{pmatrix} \alpha^{-1} & 0 \\ 0 & (\kappa \mathbf{I}_Q - \mathbf{K}_{QQ})^{-1} \end{pmatrix} \begin{pmatrix} 0 & 0 \\ 0 & \mathbf{I}_Q \end{pmatrix} = \begin{pmatrix} 0 & 0 \\ 0 & (\kappa \mathbf{I}_Q - \mathbf{K}_{QQ})^{-1} \end{pmatrix}$$

Form the above matrices representations of the operators is easy to know. The resolvent $\hat{\mathcal{R}}(\kappa, \hat{K})$ is the inverse of the operator $\hat{Q}(\kappa - \hat{K})\hat{Q}$ in the Q space, where $\hat{Q}(\kappa - \hat{K})\hat{Q}\hat{\mathcal{R}}(\kappa, \hat{K}) = \hat{Q}$ (\hat{Q} is the identity in the Q space). This is a reason, the resolvent has a short notation as $\frac{\hat{Q}}{\kappa - \hat{K}}$. It is worth to know, if κ is an eigenvalue of $\hat{K}_{QQ} = \hat{Q}\hat{K}\hat{Q}$, then $\hat{\mathcal{R}}(\kappa, \hat{K})$ does not exist.

Here we need to define a trial function $|\Psi_\kappa\rangle$, with intermediate normalization condition, $\langle \Phi_0 | \Psi_\kappa \rangle = 1$

$$|\Psi_\kappa\rangle = |\Phi_0\rangle + \hat{\mathcal{R}}(\kappa, \hat{K})\hat{K}|\Phi_0\rangle$$

To solve the Schrödinger equation, $\hat{K}|\Psi\rangle = k|\Psi\rangle$, is equivalent to $(k - \hat{K})|\Psi\rangle = 0$, the equation can be treated as a special case of a function with the value of zero, which is $(\kappa - \hat{K})|\Psi_\kappa\rangle$.

$$\begin{aligned} (\kappa - \hat{K})|\Psi_\kappa\rangle &= \hat{P}(\kappa - \hat{K})|\Psi_\kappa\rangle + \hat{Q}(\kappa - \hat{K})|\Psi_\kappa\rangle \\ &= \hat{P}(\kappa - \hat{K})|\Psi_\kappa\rangle + \hat{Q}(\kappa - \hat{K})|\Phi_0\rangle + \hat{Q}(\kappa - \hat{K})\hat{\mathcal{R}}(\kappa, \hat{K})\hat{K}|\Phi_0\rangle \\ &= \hat{P}(\kappa - \hat{K})|\Psi_\kappa\rangle + \kappa\hat{Q}|\Phi_0\rangle - \hat{Q}\hat{K}|\Phi_0\rangle + \hat{Q}\hat{K}|\Phi_0\rangle \\ &= \hat{P}(\kappa - \hat{K})|\Psi_\kappa\rangle = |\Phi_0\rangle \langle \Phi_0 | \kappa - \hat{K} | \Psi_\kappa \rangle \\ &= \kappa |\Phi_0\rangle \underbrace{\langle \Phi_0 | \Psi_\kappa \rangle}_1 - |\Phi_0\rangle \underbrace{\langle \Phi_0 | \hat{K} | \Psi_\kappa \rangle}_{f(\kappa)} \\ &= (\kappa - f(\kappa)) |\Phi_0\rangle \end{aligned}$$

The fix points of f , $f(\kappa) = \kappa$, give the eigenvalues of \hat{K} , and the function returns the Schrödinger equation.

$$f(\kappa) = \langle \Phi_0 | \hat{K} | \Psi_\kappa \rangle = \langle \Phi_0 | \hat{K} + \hat{K}\hat{\mathcal{R}}(\kappa, \hat{K})\hat{K} | \Phi_0 \rangle$$

In the case of $\kappa = k$, then $(k - \hat{K})|\Psi\rangle = 0$ and $f(k) = k$. because of $|\Psi\rangle = |\Phi_0\rangle + \hat{\mathcal{R}}(k, \hat{K})\hat{K}|\Phi_0\rangle$, and the definition of the wave operator, $|\Psi\rangle = \hat{\Omega}|\Phi_0\rangle$.

$$\hat{\Omega} = \hat{P} + \hat{\mathcal{R}}(k, \hat{K})\hat{K}\hat{P}$$

Thus in general,

$$\begin{aligned}\hat{\Omega}_\kappa &= \hat{P} + \hat{\mathcal{R}}(\kappa, \hat{K})\hat{K}\hat{P} \\ &= \hat{P} + \hat{\mathcal{R}}(\kappa, \hat{K})(\hat{K}_0 + \hat{W})\hat{P} \\ &= \hat{P} + \hat{\mathcal{R}}(\kappa, \hat{K})\hat{K}_0\hat{P} + \hat{\mathcal{R}}(\kappa, \hat{K})\hat{W}\hat{P} \\ &= \hat{P} + \hat{\mathcal{R}}(\kappa, \hat{K})\hat{K}_0|\Phi_0\rangle\langle\Phi_0| + \hat{\mathcal{R}}(\kappa, \hat{K})\hat{W}\hat{P} \\ &= \hat{P} + \kappa_0\hat{\mathcal{R}}(\kappa, \hat{K})\hat{P} + \hat{\mathcal{R}}(\kappa, \hat{K})\hat{W}\hat{P} \\ &= \hat{P} + \hat{\mathcal{R}}(\kappa, \hat{K})\hat{W}\hat{P}\end{aligned}$$

Here define the resolvent of the unperturbed operator.

$$\hat{R}_0 = \hat{\mathcal{R}}(\kappa_0, \hat{K}_0)$$

Then the original resolvent $\hat{\mathcal{R}}(\kappa, \hat{K})$, could be written in terms of \hat{R}_0 . For simple the notation, $\hat{W}'_\kappa = \hat{W} - \kappa + \kappa_0$ is defined. And the inverse of the difference between two matrices is given, $(\mathbf{A} - \mathbf{B})^{-1} = \mathbf{A}^{-1} + \mathbf{A}^{-1}\mathbf{B}(\mathbf{A} - \mathbf{B})^{-1}$. As the result the original resolvent could be written as the infinite series of \hat{R}_0 .

$$\begin{aligned}\hat{\mathcal{R}}(\kappa, \hat{K}) &= \hat{Q} \left[\alpha\hat{P} + \hat{Q}(\kappa - \hat{K})\hat{Q} \right]^{-1} \hat{Q} \\ &= \hat{Q} \left[\alpha\hat{P} + \hat{Q}(\kappa_0 - \hat{K}_0 + \kappa - \kappa_0 - \hat{W})\hat{Q} \right]^{-1} \hat{Q} \\ &= \hat{Q} \left[\underbrace{\alpha\hat{P} + \hat{Q}(\kappa_0 - \hat{K}_0)\hat{Q}}_{\mathbf{A}} - \underbrace{\hat{Q}\hat{W}'_\kappa\hat{Q}}_{\mathbf{B}} \right]^{-1} \hat{Q} \\ &= \hat{Q} \left[\underbrace{\alpha\hat{P} + \hat{Q}(\kappa_0 - \hat{K}_0)\hat{Q}}_{\mathbf{A}^{-1}} \right]^{-1} \hat{Q} + \hat{Q}\mathbf{A}^{-1}\hat{Q}\hat{W}'_\kappa\hat{Q}(\mathbf{A} - \mathbf{B})^{-1}\hat{Q} \\ &= \hat{R}_0 + \hat{R}_0\hat{W}'_\kappa\hat{\mathcal{R}}(\kappa, \hat{K}) \\ &= \hat{R}_0 + \left(\hat{R}_0\hat{W}'_\kappa \right) \hat{R}_0 + \left(\hat{R}_0\hat{W}'_\kappa \right)^2 \hat{\mathcal{R}}(\kappa, \hat{K}) \\ &= \sum_{n=0}^{\infty} \left(\hat{R}_0\hat{W}'_\kappa \right)^n \hat{R}_0\end{aligned}$$

Then the corresponding wave operator and the reactive operator could be given in

terms of \hat{R}_0 .

$$\begin{aligned}\hat{\Omega}_\kappa &= \hat{P} + \sum_{n=0}^{\infty} \left(\hat{R}_0 \hat{W}'_\kappa \right)^n \hat{R}_0 \hat{W} \hat{P} \\ \hat{\tau}_\kappa &= \hat{P} \hat{W} \hat{P} + \sum_{n=0}^{\infty} \hat{P} \hat{W} \left(\hat{R}_0 \hat{W}'_\kappa \right)^n \hat{R}_0 \hat{W} \hat{P}\end{aligned}$$

For $\kappa = k$, the exact state $|\Psi\rangle$ and the exact energy k could also be written as the series of \hat{R}_0 .

$$\begin{aligned}|\Psi\rangle &= \hat{\Omega}_{\kappa=k} |\Phi_0\rangle = |\Phi_0\rangle + \sum_{n=0}^{\infty} \left(\hat{R}_0 \hat{W}'_k \right)^n \hat{R}_0 \hat{W} |\Phi_0\rangle \\ k &= \kappa_0 + \langle \Phi_0 | \hat{\tau}_{\kappa=k} | \Phi_0 \rangle = \underbrace{\kappa_0}_{k^{(0)}} + \underbrace{\langle \Phi_0 | \hat{W} | \Phi_0 \rangle}_{k^{(1)}} + \underbrace{\sum_{n=0}^{\infty} \langle \Phi_0 | \hat{W} \left(\hat{R}_0 \hat{W}'_k \right)^n \hat{R}_0 \hat{W} | \Phi_0 \rangle}_{k^{(2)}, \dots}\end{aligned}$$

It is clear, $k = \sum_{n=0}^{\infty} k^{(n)}$, thus $\hat{W}' = \hat{W}'_{\kappa=k} = \hat{W} - k + \kappa_0 = \hat{W} - \sum_{n=1}^{\infty} k^{(n)}$. Here need to notice, the higher order corrections necessarily include lower order corrections.

In general, the exact state could be written as the series of the states with n -order permutation.

$$\begin{aligned}|\Psi\rangle &= |\Psi^{(0)}\rangle + |\Psi^{(1)}\rangle + |\Psi^{(2)}\rangle + \dots = \sum_{n=0}^{\infty} |\Psi^{(n)}\rangle \\ k &= k^{(0)} + k^{(1)} + k^{(2)} + \dots = \sum_{n=0}^{\infty} k^{(n)}\end{aligned}$$

For the zero-order,

$$\begin{aligned}|\Psi^{(0)}\rangle &= |\Phi_0\rangle \quad ; \quad \hat{\Omega}^{(0)} = \hat{P} \\ k^{(0)} &= \kappa_0 \quad ; \quad \hat{\tau}^{(0)} = 0\end{aligned}$$

For the first-order,

$$\begin{aligned}|\Psi^{(1)}\rangle &= \hat{R}_0 \hat{W} |\Phi_0\rangle \quad ; \quad \hat{\Omega}^{(1)} = \hat{R}_0 \hat{W} \hat{P} \\ k^{(1)} &= \langle \Phi_0 | \hat{W} | \Phi_0 \rangle \quad ; \quad \hat{\tau}^{(1)} = \hat{P} \hat{W} \hat{P}\end{aligned}$$

For the second-order,

$$\begin{aligned}|\Psi^{(2)}\rangle &= \hat{R}_0 \left(\hat{W} - k^{(1)} \right) \hat{R}_0 \hat{W} |\Phi_0\rangle = \hat{R}_0 \hat{W} \hat{R}_0 \hat{W} |\Phi_0\rangle - \langle \Phi_0 | \hat{W} | \Phi_0 \rangle \hat{R}_0^2 \hat{W} |\Phi_0\rangle \\ k^{(2)} &= \langle \Phi_0 | \hat{W} \hat{R}_0 \hat{W} | \Phi_0 \rangle\end{aligned}$$

For the third-order,

$$\begin{aligned}
 |\Psi^{(3)}\rangle &= \left(\hat{R}_0(\hat{W} - k^{(1)})\right)^2 \hat{R}_0 \hat{W} |\Phi_0\rangle + \left(\hat{R}_0(-k^{(2)})\right)^1 \hat{R}_0 \hat{W} |\Phi_0\rangle \\
 &= \left(\hat{R}_0 \hat{W}\right)^3 |\Phi_0\rangle - k^{(1)} \hat{R}_0^2 \hat{W} \hat{R}_0 \hat{W} |\Phi_0\rangle - k^{(1)} \hat{R}_0 \hat{W} \hat{R}_0^2 \hat{W} |\Phi_0\rangle \\
 &\quad + k^{(1)2} \hat{R}_0^3 \hat{W} |\Phi_0\rangle - k^{(2)} \hat{R}_0^2 \hat{W} |\Phi_0\rangle \\
 &= \left(\hat{R}_0 \hat{W}\right)^3 |\Phi_0\rangle - \langle\Phi_0|\hat{W}|\Phi_0\rangle \left(\hat{R}_0^2 \hat{W} \hat{R}_0 \hat{W} |\Phi_0\rangle + \hat{R}_0 \hat{W} \hat{R}_0^2 \hat{W} |\Phi_0\rangle\right) \\
 &\quad + \langle\Phi_0|\hat{W}|\Phi_0\rangle^2 \hat{R}_0^3 \hat{W} - \langle\Phi_0|\hat{W} \hat{R}_0 \hat{W}|\Phi_0\rangle \hat{R}_0^2 \hat{W} |\Phi_0\rangle \\
 k^{(3)} &= \langle\Phi_0|\hat{W} \hat{R}_0 (\hat{W} - k^{(1)}) \hat{R}_0 \hat{W}|\Phi_0\rangle \\
 &= \langle\Phi_0|\hat{W} (\hat{R}_0 \hat{W})^2 |\Phi_0\rangle - \langle\Phi_0|\hat{W}|\Phi_0\rangle \langle\Phi_0|\hat{W} \hat{R}_0^2 \hat{W}|\Phi_0\rangle
 \end{aligned}$$

For the four-order,

$$\begin{aligned}
 k^{(4)} &= \langle\Phi_0|\hat{W} \left(\hat{R}_0(\hat{W} - k^{(1)})\right)^2 \hat{R}_0 \hat{W}|\Phi_0\rangle - k^{(2)} \langle\Phi_0|\hat{W} \hat{R}_0^2 \hat{W}|\Phi_0\rangle \\
 &= \langle\Phi_0|\hat{W} (\hat{R}_0 \hat{W})^3 |\Phi_0\rangle - \langle\Phi_0|\hat{W}|\Phi_0\rangle \left(\langle\Phi_0|\hat{W} \hat{R}_0^2 \hat{W} \hat{R}_0 \hat{W}|\Phi_0\rangle + \langle\Phi_0|\hat{W} \hat{R}_0 \hat{W} \hat{R}_0^2 \hat{W}|\Phi_0\rangle\right) \\
 &\quad + \langle\Phi_0|\hat{W}|\Phi_0\rangle^2 \langle\Phi_0|\hat{W} \hat{R}_0^3 \hat{W}|\Phi_0\rangle - \langle\Phi_0|\hat{W} \hat{R}_0 \hat{W}|\Phi_0\rangle \langle\Phi_0|\hat{W} \hat{R}_0^2 \hat{W}|\Phi_0\rangle
 \end{aligned}$$

To give the exact expression of \hat{R}_0 , Here, $|\Phi\rangle$ is an arbitrary state. The acting of \hat{R}_0 , gives the linear combination in the Q space, where c_n are the coefficients.

$$\begin{aligned}
 \hat{R}_0 |\Phi\rangle &= (\hat{P} + \hat{Q}) \hat{R}_0 |\Phi\rangle = \underbrace{\hat{P} \hat{R}_0}_0 |\Phi\rangle + \hat{Q} \hat{R}_0 |\Phi\rangle \\
 &= \sum_{n \neq 0} |\Phi_n\rangle \langle\Phi_n| \hat{R}_0 |\Phi\rangle = \sum_{n \neq 0} c_n |\Phi_n\rangle \quad ; \quad c_n = \langle\Phi_n| \hat{R}_0 |\Phi\rangle
 \end{aligned}$$

On the other hand, \hat{R}_0 is the inverse of $\hat{Q} (\kappa_0 - \hat{K}_0) \hat{Q}$ in the Q space.

$$\begin{aligned}
 \hat{Q} |\Phi\rangle &= \hat{Q} (\kappa_0 - \hat{K}_0) \hat{R}_0 |\Phi\rangle \\
 &= \sum_{n \neq 0} |\Phi_n\rangle \langle\Phi_n| (\kappa_0 - \hat{K}_0) \hat{R}_0 |\Phi\rangle \\
 &= \sum_{n \neq 0} |\Phi_n\rangle (\kappa_0 - \kappa_n) \langle\Phi_n| \hat{R}_0 |\Phi\rangle \\
 \sum_{n \neq 0} |\Phi_n\rangle \langle\Phi_n| \Phi\rangle &= \sum_{n \neq 0} c_n (\kappa_0 - \kappa_n) |\Phi_n\rangle \\
 \Rightarrow c_n &= \frac{\langle\Phi_n| \Phi\rangle}{(\kappa_0 - \kappa_n)}
 \end{aligned}$$

Then the expression of the c_n are given, substitute back into the original formula, it could find the \hat{R}_0 are like the projection operator \hat{Q} , but with suppression from denominator. The states with a larger energy difference with respect to the reference state have less component. And the k -power of \hat{R}_0 could also be given.

$$\begin{aligned}\hat{R}_0 |\Phi\rangle &= \sum_{n \neq 0} c_n |\Phi_n\rangle = \sum_{n \neq 0} \frac{\langle \Phi_n | \Phi \rangle}{(\kappa_0 - \kappa_n)} |\Phi_n\rangle = \sum_{n \neq 0} \frac{|\Phi_n\rangle \langle \Phi_n|}{(\kappa_0 - \kappa_n)} |\Phi\rangle \\ \Rightarrow \hat{R}_0 &= \sum_{n \neq 0} \frac{|\Phi_n\rangle \langle \Phi_n|}{(\kappa_0 - \kappa_n)} \quad ; \quad \hat{R}_0^k = \sum_{n \neq 0} \frac{|\Phi_n\rangle \langle \Phi_n|}{(\kappa_0 - \kappa_n)^k}\end{aligned}$$

Thus for the first-order,

$$\begin{aligned}|\Psi^{(1)}\rangle &= \hat{R}_0 \hat{W} |\Phi_0\rangle = \sum_{n \neq 0} \frac{|\Phi_n\rangle \langle \Phi_n | \hat{W} | \Phi_0 \rangle}{\kappa_0 - \kappa_n} \\ k^{(1)} &= \langle \Phi_0 | \hat{W} | \Phi_0 \rangle .\end{aligned}$$

For the second-order,

$$\begin{aligned}|\Psi^{(2)}\rangle &= \sum_{m, n \neq 0} \frac{|\Phi_m\rangle \langle \Phi_m | \hat{W} | \Phi_n \rangle \langle \Phi_n | \hat{W} | \Phi_0 \rangle}{(\kappa_0 - \kappa_m)(\kappa_0 - \kappa_n)} \\ &\quad - \langle \Phi_0 | \hat{W} | \Phi_0 \rangle \sum_{m, n \neq 0} \frac{|\Phi_m\rangle \langle \Phi_m | \Phi_n \rangle \langle \Phi_n | \hat{W} | \Phi_0 \rangle}{(\kappa_0 - \kappa_m)(\kappa_0 - \kappa_n)} \\ &= \sum_{m, n \neq 0} \frac{|\Phi_m\rangle \langle \Phi_m | \hat{W} | \Phi_n \rangle \langle \Phi_n | \hat{W} | \Phi_0 \rangle}{(\kappa_0 - \kappa_m)(\kappa_0 - \kappa_n)} - \langle \Phi_0 | \hat{W} | \Phi_0 \rangle \sum_{n \neq 0} \frac{|\Phi_n\rangle \langle \Phi_n | \hat{W} | \Phi_0 \rangle}{(\kappa_0 - \kappa_n)^2} .\end{aligned}$$

A.7. Coupled cluster theory

From the above expression we can find that, the n -order perturbed wavefunction and the $n + 1$ -order perturbed energy contain a term with $(\hat{R}_0 \hat{W})^n$, this term is called the principle term and the rest terms are called the renormalization terms.

$$\begin{aligned}|\Psi^{(n)}\rangle &= \underbrace{(\hat{R}_0 \hat{W})^n}_{\text{principal term}} |\Phi_0\rangle + \text{renormalization terms} \\ k^{(n+1)} &= \underbrace{\langle \Phi_0 | \hat{W} (\hat{R}_0 \hat{W})^n | \Phi_0 \rangle}_{\text{principal term}} + \text{renormalization terms}\end{aligned}$$

According to the linked cluster theorem, for the wavefunction, the unlinked components in the principle term could cancel with the renormalization terms, leaving

the linked components in the principle term only. For the energy, the disconnected components in the principle term could cancel with the renormalization terms, leaving the connected components in the principle term only. Here the *connected* has the same meaning as daily languages, which all perturbation vertices are binding together, are connected. The *linked* component could be disconnected with several pieces, however each piece should have external legs, which is not allowed to be fully contracted with in any piece.

$$\begin{aligned} |\Psi^{(n)}\rangle &= \left\{ \left(\hat{R}_0 \hat{W} \right)^n \right\}_L |\Phi_0\rangle \\ k^{(n+1)} &= \langle \Phi_0 | \left\{ \hat{W} \left(\hat{R}_0 \hat{W} \right)^n \right\}_C |\Phi_0\rangle \end{aligned}$$

The exact wavefunction could be written in terms of the linked components of the perturbation, where L indicates the component is linked, r indicates the number of the connected pieces in the component.

$$\begin{aligned} |\Psi\rangle &= |\Phi_0\rangle + \sum_{n=1}^{\infty} \left\{ \left(\hat{R}_0 \hat{W} \right)^n \right\}_L |\Phi_0\rangle \\ &= |\Phi_0\rangle + \sum_{n=1}^{\infty} \sum_{r=1}^n \left\{ \left(\hat{R}_0 \hat{W} \right)^n \right\}_{L,r} |\Phi_0\rangle \end{aligned}$$

The sum of the connected components of the perturbation could be defined as the operator \hat{T} , called cluster operator.

$$\sum_{n=1}^{\infty} \left\{ \left(\hat{R}_0 \hat{W} \right)^n \right\}_{L,r=1} |\Phi_0\rangle = \sum_{n=1}^{\infty} \left\{ \left(\hat{R}_0 \hat{W} \right)^n \right\}_C |\Phi_0\rangle = \hat{T} |\Phi_0\rangle$$

It could be proved that, the sum of other linked but disconnected components with r pieces, could be written in terms of the cluster operator as well.

$$\sum_{n=r}^{\infty} \left\{ \left(\hat{R}_0 \hat{W} \right)^n \right\}_{L,r} = \frac{1}{r!} \hat{T}^r |\Phi_0\rangle$$

Then the exact wavefunction $|\Psi\rangle$ could be written as the action of the cluster operator series on the reference state, which final given the coupled-cluster expression.

$$\begin{aligned} |\Psi\rangle &= |\Phi_0\rangle + \sum_{n=1}^{\infty} \sum_{r=1}^n \left\{ \left(\hat{R}_0 \hat{W} \right)^n \right\}_{L,r} |\Phi_0\rangle \\ &= |\Phi_0\rangle + \sum_{r=1}^{\infty} \sum_{n=r}^{\infty} \left\{ \left(\hat{R}_0 \hat{W} \right)^n \right\}_{L,r} |\Phi_0\rangle \\ &= |\Phi_0\rangle + \sum_{r=1}^{\infty} \frac{1}{r!} \hat{T}^r |\Phi_0\rangle \\ &= e^{\hat{T}} |\Phi_0\rangle \end{aligned}$$

The cluster operator could be decomposed by the number excitations. Here k indicates the connected components with $2k$ external lines, represented the kp - kh excitation.

$$\hat{T} = \sum_{k=1} \hat{T}_k \quad ; \quad \hat{T}_k = \sum_{n=1}^{\infty} \left\{ \left(\hat{R}_0 \hat{W} \right)^n \right\}_{C,k} \quad ; \quad \hat{T}_k = \frac{1}{k!} \langle a_1 \cdots a_k | \hat{t}_k | i_1 \cdots i_k \rangle \hat{E}_{i_1 \cdots i_k}^{a_1 \cdots a_k}$$

The truncation could be made according to the excitations. For example, coupled cluster single-double-triple (CCSDT) contains the single, double, triple excitations.

$$\begin{aligned} \text{CCSD} & : \quad \hat{T} = \hat{T}_1 + \hat{T}_2 \\ \text{CCSDT} & : \quad \hat{T} = \hat{T}_1 + \hat{T}_2 + \hat{T}_3 \\ \text{CCSDTQ} & : \quad \hat{T} = \hat{T}_1 + \hat{T}_2 + \hat{T}_3 + \hat{T}_4 \end{aligned}$$

Comparing the CI expression by the excitation operator \hat{C}_n , and the CC expression by the cluster operator \hat{T}_n .

$$\begin{aligned} |\Psi\rangle &= \left(1 + \hat{C}_1 + \hat{C}_2 + \hat{C}_3 + \hat{C}_4 + \cdots \right) |\Phi_0\rangle \\ &= e^{1 + \hat{T}_1 + \hat{T}_2 + \hat{T}_3 + \hat{T}_4 + \cdots} |\Phi_0\rangle \\ &= \left[1 + (1 + \hat{T}_1 + \hat{T}_2 + \hat{T}_3 + \hat{T}_4 + \cdots) \right. \\ &\quad + \frac{1}{2}(1 + \hat{T}_1 + \hat{T}_2 + \hat{T}_3 + \hat{T}_4 + \cdots)^2 \\ &\quad + \frac{1}{6}(1 + \hat{T}_1 + \hat{T}_2 + \hat{T}_3 + \hat{T}_4 + \cdots)^3 \\ &\quad \left. + \frac{1}{24}(1 + \hat{T}_1 + \hat{T}_2 + \hat{T}_3 + \hat{T}_4 + \cdots)^4 + \cdots \right] |\Phi_0\rangle \end{aligned}$$

The CI operator for the same type excitation could have cluster operators with different type excitations. For example, \hat{C}_2 could be the one-time double CC excitation, or the two-times single CC excitation.

$$\begin{aligned} \hat{C}_1 &= \hat{T}_1 \\ \hat{C}_2 &= \hat{T}_2 + \frac{1}{2}\hat{T}_1^2 \\ \hat{C}_3 &= \hat{T}_3 + \hat{T}_1\hat{T}_2 + \frac{1}{6}\hat{T}_1^3 \\ \hat{C}_4 &= \hat{T}_4 + \frac{1}{2}\hat{T}_2^2 + \hat{T}_1\hat{T}_3 + \frac{1}{2}\hat{T}_1^2\hat{T}_2 + \frac{1}{24}\hat{T}_1^4 \\ &\vdots \end{aligned}$$

For the reference state based on the Hartree–Fock method $|\Phi_0^{\text{HF}}\rangle$, the MBPT order for the above terms are given, which is easy to know, CC expression is more effective to cover the low order corrections. In general CCSD is better than CISD, and CCSDT is far better than CISDT and close to CISDTQ.

Table A.1.: The comparison with CI and CC of the MBPT orders for each terms.

		MBPT order	
		Wavefunction	Energy
\hat{C}_1	\hat{T}_1	2	4
\hat{C}_2	\hat{T}_2	1	2
	$\frac{1}{2}\hat{T}_1^2$	4	5
\hat{C}_3	\hat{T}_3	2	4
	$\hat{T}_1\hat{T}_2$	3	5
	$\frac{1}{6}\hat{T}_1^3$	6	8
\hat{C}_4	\hat{T}_4	3	5
	$\frac{1}{2}\hat{T}_2^2$	4	6
	$\hat{T}_1\hat{T}_3$	2	4
	$\frac{1}{2}\hat{T}_1^2\hat{T}_2$	5	7
	$\frac{1}{24}\hat{T}_1^4$	8	10

B. Supporting information for reactive force-field fitting

B.1. The data structure of ReaxFF parameters files

```

1 Reactive MD-force field
2      41 ! Number of general parameters (Equation)
3      50.0000 ! p_boc1 Overcoordination parameter 4c
4      9.5469 ! p_boc2 Overcoordination parameter 4d
5      .....
6      .....
7      0.0000 ! n.u. not used n/a
8      5 ! Nr of atoms; AtomSymbol; r_s; valency; mass; r_vdw; epsilon(
9      Dij); gamma; r_pi; valency_e;
10      alpha; gamma_w; valency_boc; p_ovun5; n.u.; chi; eta;
11      p_hbond;
12      r_pi_pi; p_lp2; n.u.; b_o_131; b_o_132; b_o_133; n.u.; n
13      .u.;
14      p_ovun2; p_val3; n.u.; valency_val; p_val5; rcore2;
15      ecore2; acore2;;; lgcij; lgre;
16 C      1.3825 4.0000 12.0000 1.9133 0.1853 0.9000 1.1359
17      4.0000
18      9.7602 2.1346 4.0000 33.2433 79.5548 5.8678 7.0000
19      0.0000
20      1.2104 0.0000 199.0303 8.6991 34.7289 13.3894 0.8563
21      0.0000
22      -2.8983 2.5000 1.0564 4.0000 2.9663 0.0000 0.0000
23      0.0000
24 ...
25      13 ! Nr of bonds; at1; at2; De_s; De_p; De_pp; p_be1; p_bo5; v13cor
26      ; p_bo6; p_ovun1;
27      p_be2; p_bo3; p_bo4; n.u.; p_bo1; p_bo2; ovc;n.u.;
28      1 1 156.5953 100.0397 80.0000 -0.8157 -0.4591 1.0000 37.7369
29      0.4235
30      0.4527 -0.1000 9.2605 1.0000 -0.0750 6.8316 1.0000

```

```

0.0000
21 1 2 170.2316 0.0000 0.0000 -0.5931 0.0000 1.0000 6.0000
0.7140
22 5.2267 1.0000 0.0000 1.0000 -0.0500 6.8315 0.0000
0.0000
23 ....
24 10 ! Nr of off-diagonal terms; at1; at2; D; r_vdW; alpha; r_s; r_p;
r_pp; lgcij
25 1 2 0.1219 1.4000 9.8442 1.1203 -1.0000 -1.0000 0.0000
26 2 3 0.1285 1.8410 10.7276 1.3619 -1.0000 -1.0000 0.0000
27 ....
28 46 ! Nr of angles; at1; at2; at3; theta_00; p_val1; p_val2; p_coa1;
p_val7; p_pen1; p_val4
29 1 1 1 67.2326 22.0695 1.6286 0.0000 1.7959 15.4141 1.8089
30 1 1 2 65.2527 14.3185 6.2977 0.0000 0.5645 0.0000 1.1530
31 .....
32 28 ! Nr of torsions; at1; at2; at3; at4; V1; V2; V3; p_tor1; p_cot1
; n.u.; n.u.
33 1 1 1 1 -0.2500 11.5822 0.1879 -4.7057 -2.2047 0.0000
0.0000
34 1 1 1 2 -0.2500 31.2596 0.1709 -4.6391 -1.9002 0.0000
0.0000
35 .....
36 1 ! Nr of hydrogen bonds; at1; at2; at3; r0_hb; p_hb1; p_hb2;
p_hb3
37 5 2 5 1.9682 -4.4628 1.7976 3.0000
    
```

Listing B.1: A typical ReaxFF parameters file.

Table B.1.: The parameters blocks in the ReaxFF parameters files.

Line	Definitions
1	The title of parameter file
2	The number of general parameters
3-7	The general parameters
8-11	The number of atom types
12-16	The atomic parameters
17-18	The number of bond parameters
19-23	The bond parameters
24	The number of off-diagonal parameters
25-27	The off-diagonal parameters
28	The number of angle parameters
29-31	The angle parameters
32	The number of torsions parameters
33-35	The torsions parameters
36	The number of hydrogen bonds parameters
37	The hydrogen bonds parameters

There are seven parameter blocks in a ReaxFF parameters files (*.ff) to define general, atomic, bond, off-diagonal, angle, torsion, and hydrogen bond terms. The "!" character indicates a comment. Basically there are two different type of files, the normal type (4 lines' atomic parameters for a element), and the `lgvdw` type with the low-gradient correction of the long-range London Dispersion (5 lines' atomic parameters for a element). The definitions of parameters are shown in Listing B.2, which were double checked based on the source code of LAMMPS VER.15APR2020. Be careful, the implementations of the ReaxFF have some tiny differences in various software (*e.g.*, LAMMPS, ADF), thus the definition of parameters may have some discrepancy.

1	GeneralTerms		
2	0	! Number of general parameters	(Equation)
3	1	! p_boc1 Overcoordination parameter	4c
4	2	! p_boc2 Overcoordination parameter	4d
5	3	! p_coa2 Valency angle conjugation parameter	15
6	4	! p_trip4 Triple bond stabilization parameter	20
7	5	! p_trip3 Triple bond stabilization parameter	20
8	6	! p_lp3(kc2) C2-correction	19
9	7	! p_ovun6 Undercoordination parameter	12
10	8	! p_trip2 Triple bond stabilization parameter	20
11	9	! p_ovun7 Undercoordination parameter	12
12	10	! p_ovun8 Undercoordination parameter	12
13	11	! p_trip1 Triple bond stabilization energy	20
14	12	! swa Lower Taper-radius	21
15	13	! swb Upper Taper-radius	21
16	14	! n.u. not used	n/a
17	15	! p_val6 Valency undercoordination	13c
18	16	! p_lp1 Valency angle/lone pair parameter	8
19	17	! p_val9 Valency angle parameter	13f
20	18	! p_val10 Valency angle parameter	13g
21	19	! n.u. not used	n/a
22	20	! p_pen2 Double bond/angle parameter	14a
23	21	! p_pen3 Double bond/angle parameter: overcoord	14b
24	22	! p_pen4 Double bond/angle parameter: overcoord	14b
25	23	! n.u. not used	n/a
26	24	! p_tor2 Torsion/B0 parameter	16b
27	25	! p_tor3 Torsion overcoordination	16c
28	26	! p_tor4 Torsion overcoordination	16c
29	27	! n.u. not used	n/a
30	28	! p_cot2 Conjugation	17b
31	29	! p_vdW1 VdW shielding	23b
32	30	! cutoff*100 Cutoff for bond order (* 100)	3a,b
33	31	! p_coa4 Valency angle conjugation parameter	15
34	32	! p_ovun4 Overcoordination parameter	11b

35	33	! p_ovun3	Overcoordination parameter	11b
36	34	! p_val8	Valency/lone pair parameter	13d
37	35	! n.u.	not used	n/a
38	36	! n.u.	not used	n/a
39	37	! n.u.	not used	n/a
40	38	! gp37	1: remove delta_j for non-C-C-C angles	13d
41	39	! p_coa3	Valency angle conjugation parameter	15
42	40	! n.u.	not used	n/a
43	41	! n.u.	not used	n/a
44				
45		AtomTerms		
46	0	AtomSymbol	AtomSymbol	n/a
47	1	r_s	Sigma bond covalent radius	2
48	2	valency	Valency	3a, 4b, 5, 9a
49	3	mass	Atomic mass	9a
50	4	r_vdw	van der Waals radius	23a
51	5	epsilon(Dij)	van der Waals dissociation energy	23a
52	6	gamma	gammaEEM; EEM shielding	24
53	7	r_pi	Pi bond covalent radius	2
54	8	valency_e	Number of valence electrons	7, 8, 9
55	0	alpha	van der Waals parameter	23b
56	1	gamma_w	van der Waals shielding	23b
57	2	valency_boc	Valency for 1,3-B0 correction	16c, 13c
58	3	p_ovun5	Undercoordination energy	12
59	4	n.u.	not used	n/a
60	5	chi	EEM electronegativity	24, 25
61	6	eta	EEM hardness	24, 25
62	7	p_hbond	Donor or acceptor switch in H-bonds(int);	
63			1 for H,	
64			2 for hbonding atoms (O,S,P,N),	
65			0 for others	n/a
66	0	r_pi_pi	Double pi bond covalent radius	2
67	1	p_lp2	Lone pair energy	10
68	2	n.u.	Atomic heat of formation?	n/a
69	3	b_o_131	Bond order correction	4e,f
70	4	b_o_132	Bond order correction	4e,f
71	5	b_o_133	Bond order correction	4e,f
72	6	n.u.	not used	n/a
73	7	n.u.	not used	n/a
74	0	p_ovun2	Valence angle parameter	12
75	1	p_val3	Valence angle parameter	13b -> 13a
76	2	n.u.	not used	n/a
77	3	valency_val	Number of lone pairs	3b
78	4	p_val5	Valence angle parameter	13b
79	5	rcore2	Inner wall vdW repulsion parameter	23c
80	6	ecore2	Inner wall vdW repulsion parameter	23c

81	7	acore2	Inner wall vdW repulsion parameter	23c
82	0	lgcij	Lg dispersion parameter	23d
83	1	lgre	VdW Radius for Lg dispersion correction	23d
84				
85		BondTerms		
86	0	atom_1(j)		
87	1	atom_2(k)		
88	2	De_s	Sigma-bond dissociation energy	6, 11a
89	3	De_p	Pi-bond dissociation energy	6
90	4	De_pp	Double pi-bond dissociation energy	6
91	5	p_be1	Bond energy parameter	6
92	6	p_bo5	Double pi bond parameter	2
93	7	v13cor	1,3-Bond order correction	3b
94	8	p_bo6	Double pi bond order	2
95	9	p_ovun1	Overcoordination penalty	11a
96	0	p_be2	Bond energy parameter	6
97	1	p_bo3	Pi bond order parameter	2
98	2	p_bo4	Pi bond order parameter	2
99	3	n.u.	not used	n/a
100	4	p_bo1	Sigma bond order	2
101	5	p_bo2	Sigma bond order	2
102	6	ovc	Uncorrected BO overcoordination	3a
103	7	n.u.	not used	n/a
104				
105		OffDiagonalTerms		
106	0	atom_1(j)		
107	1	atom_2(k)		
108	2	D	VdW energy	23a
109	3	r_vdW	VdW radius	23a
110	4	alpha	VdW parameter	23a
111	5	r_s	Sigma bond length	2
112	6	r_p	Pi bond length	2
113	7	r_pp	PiPi bond length	2
114	8	lgcij	Lg dispersion parameter	23d
115				
116		AngleTerms		
117	0	atom_1(j)		
118	1	atom_2(k)		
119	2	atom_3(m)		
120	3	theta_00	180o-(equilibrium angle)	13g
121	4	p_val1	Valence angle parameter	13a
122	5	p_val2	Valence angle parameter	13a
123	6	p_coa1	Valence conjugation	15
124	7	p_val7	Undercoordination	13c
125	8	p_pen1	Penalty energy	14b->14a
126	9	p_val4	Valence angle parameter	13b

127				
128	TorsionTerms			
129	0	atom_1(j)		
130	1	atom_2(k)		
131	2	atom_3(m)		
132	3	atom_4(n)		
133	4	V1	V1-torsion barrier	16a
134	5	V2	V2-torsion barrier	16a
135	6	V3	V3-torsion barrier	16a
136	7	p_tor1	Torsion angle parameter	16a
137	8	p_cot1	Conjugation energy	17a
138	9	n.u.	not used	n/a
139	10	n.u.	not used	n/a
140				
141	HydrogenBondTerms			
142	0	atom_1(j)		
143	1	atom_2(k)		
144	2	atom_3(m)		
145	3	r0_hb	Hydrogen bond equilibrium distance	18
146	4	p_hb1	Hydrogen bond energy	18
147	5	p_hb2	Hydrogen bond/bond order	18
148	6	p_hb3	Hydrogen bond parameter	18

Listing B.2: The definition for the parameters and the corresponding original equations.

B.2. LAMMMPS

B.2.1. Installation

Large-scale Atomic/Molecular Massively Parallel Simulator (LAMMMPS) is an open source molecular dynamics code commonly used in material science simulation. The codes are written in C++, and have a very clear hierarchical class structure, thus just it's easy to implement new functions without change other modules. The meticulous document is aviliable on <https://lammps.sandia.gov/doc/Manual.html>.

For the installation, the source code could be download either from the website or GITHUB.

```
1 git clone -b stable https://github.com/lammps/lammps.git
```

To compile LAMMMPS, the following command could be used. The typical MPI wrapped compilers are listed in Table B.2. It is worth noting that, if the computer

is using Inter CPU, using Intel compiler could gain some speed up (around 50%).

```

1 unzip lammmps-master.zip
2 cd lammmps-master
3 mkdir bin
4 cd src
5
6 ## Some packages required by ReaxFF
7 make yes-KOKKOS
8 make yes-MANYBODY
9 make yes-MOLECULE
10 make yes-user-reaxc
11
12 ## For OpenMPI (using Makefile.mpi)
13 make -j 4 mpi # compiling by 4 cores
14
15 ## For IntelMPI (using Makefile.intel_cpu_intelmpi)
16 cd MAKE
17 cp OPTIONS/Makefile.intel_cpu_intelmpi Makefile.impi
18 cd ..
19 make -j 4 impi # compiling by 4 cores
20
21 cp lmp_* ../bin
22 echo "export PATH=$PATH:YourPathWayToLAMMPS/bin" >> .bashrc

```

Table B.2.: The typical MPI libraries and compilers and the corresponding compiler wrappers.

Wrappers	Compiler	Language(s)	MPI Library
Generic			
mpicc mpicxx mpifc	gcc, cc g++ gfortran	C C/C++ Fortran77/Fortran 95	OpenMPI/IntelMPI
GNU			
mpigcc mpigxx mpif77 mpif90	gcc g++ gfortran gfortran	C C/C++ Fortran 77 Fortran 95	OpenMPI/IntelMPI
Intel			
mpiicc mpiicpc mpiifort	icc icpc ifort	C C++ Fortran77/Fortran 95	IntelMPI

B.2.2. The structures of normal LAMMPS input files

For running a normal LAMMPS job, a control file (*.in) and a data file containing the structure and force field parameters (*.data) are required. As an example of the data file shown in Listing B.3, in the beginning, we define the number of atoms and atom types (1 – 6), together with a simulation box which holds all atoms (7 – 10). LAMMPS could run periodic and non-periodic simulations. For non-periodic simulations, the box should be sized in a way that all atoms are included, but the useless empty space will slow the calculations. For periodic simulations, the setting numbers relate to the unit cell. Then the types of atoms are defined by their masses (11 – 15), and it will be better to sort the sequence by the number of atoms, the most frequent atom type comes first. The definition of the atoms are followed (16 – 21). Possible parameters of a normal force field could be attached behind.

```

1 Created by PDB2lmpData on Wed Aug 12 22:02:58 2020 # Just a title
2 # Don't delete the blank line or add more
3 28 atoms # The number of atoms
4 # Don't delete the blank line or add more
5 2 atom types # The number of atom types
6 # Don't delete the blank line or add more
7 0.000000 18.000000000000 xlo xhi # Simulation box X axis
8 0.000000 18.000000000000 ylo yhi # Simulation box Y axis
9 0.000000 50.000000000000 zlo zhi # Simulation box Z axis
10 # Don't delete the blank line or add more
11 Masses
12 # Don't delete the blank line or add more
13 1 12.011 # The mass of the first type atom
14 2 1.008 # The mass of the second type atom
15 # Don't delete the blank line or add more
16 Atoms #full: atom-ID, molecule-ID, atom-type, q, x, y, z; The Atom
    format is 'full'
17
18 1 1 2 0.00 6.609000000000 9.421000000000 15.362000000000 #H
19 2 1 1 0.00 6.692000000000 9.317000000000 17.037000000000 #C
20 3 1 1 0.00 6.654000000000 9.326000000000 18.260000000000 #C
21 4 1 1 0.00 6.627000000000 9.327000000000 19.675000000000 #C

```

Listing B.3: A typical data file for a LAMMPS job.

For running a job in MPI, the absolute path to `lmp_*` binary executable file need to be given. The `-np` parameter controls the number of cores to run (the number processes, MPI rank), but if the job runs on a cluster, usually it does not need to be specified, the batch system (*e.g.*, SLURM, PBS) could set it automatically.

```

1 mpirun -np 4 /YourPathWayToLAMMPS/bin/lmp_mpi -i lmp.in &> log &

```

After a task ends normally, the outputs (`log`, `log.lammps`) should give similar informations, the trajectory file (`*.trj`) records snapshots of frames containing the positions and velocities information.

B.2.3. Simulations with reactive force fields (ReaxFF)

The reactive force fields (ReaxFF) offer the unique capability to describe bond breaking and formation, which normal force fields can not, but they are also more expensive than the normal one. For a ReaxFF simulation, the additional two files are needed, the ReaxFF parameters file (`*.ff`, *e.g.*, Listing B.1) and the additional ReaxFF module control file (`lmp_control`, *e.g.*, Listing B.4) which controls the force field.

```

1 simulation_name      test  ! output files will carry this name + their
   specific ext
2 tabulate_long_range 10000 ! denotes the granularity of long range
   tabulation, 0 means no tabulation
3 energy_update_freq  1
4
5 nbrhood_cutoff      7.5   ! near neighbors cutoff for bond calculations
   in A
6 hbond_cutoff        6.0   ! cutoff distance for hydrogen bond
   interactions
7 bond_graph_cutoff   0.3   ! bond strength cutoff for bond graphs
8 thb_cutoff          0.001 ! cutoff value for three body interactions
9
10 write_freq          10000 ! write trajectory after so many steps
11 traj_title          test  ! (no white spaces)
12 atom_info           1     ! 0: no atom info, 1: print basic atom info
   in the trajectory file
13 atom_forces         1     ! 0: basic atom format, 1: print force on
   each atom in the trajectory file
14 atom_velocities     0     ! 0: basic atom format, 1: print the velocity
   of each atom in the trajectory file
15 bond_info           0     ! 0: do not print bonds, 1: print bonds in
   the trajectory file
16 angle_info          0     ! 0: do not print angles, 1: print angles in
   the trajectory file

```

Listing B.4: A ReaxFF module control file for the ReaxFF simulation.

Furthermore, the LAMMPS control file also need to be modified according to the requirements as an example shown in Listing B.5. Here, the names of the ReaxFF module control file (`lmp_control`) and the ReaxFF parameters file (`AuSCH_2013.ff`) are specified in the line 13 and 14 respectively.

```

1 processors 3 2 2      # define processors - the simulation
2                      # box will be divided as such
3
4 units              real # define units
5 atom_style         full
6 dimension          3
7 boundary           s s s # we don't use periodic calculations
8                      # here
9
10 read_data          input.data # load input structure
11
12 # load some stuff regarding the force field
13 pair_style          reax/c lmp_control
14 pair_coeff          * * AuSCH_2013.ff      Au C H S
15 neighbor            3 bin
16 neigh_modify        every 10 delay 0 check yes
17 thermo_modify       lost ignore
18
19 velocity            all create 100 19931024 dist gaussian
20
21 fix fixTem_1        all temp/berendsen 300 300 1
22 fix fixNVE_1        all nve
23 fix fixReax         all qeq/reax 1 0.0 10.0 1e-6 reax/c
24
25 timestep 0.5         # time step of the calculations
26 thermo 1000         # when to write thermo info
27
28 # settings how to save the trajectory
29 dump d1 all custom 500 output.lammpstrj id type x y z vx vy vz fx fy fz
30      q element
31 dump_modify d1 element Au C H S
32 dump_modify d1 format 4 %6.8g
33 dump_modify d1 format 5 %6.8g
34 dump_modify d1 format 6 %6.8g
35
36 run 10000            # run calculation

```

Listing B.5: A LAMMPS control file for the ReaxFF simulation.

B.3. C_{20} mechanical learning test results

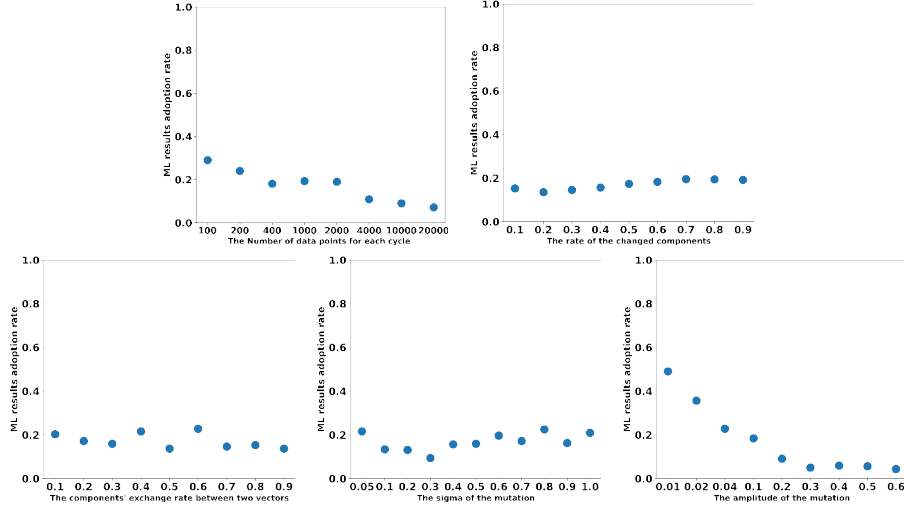


Figure B.1.: For the C_{20} system, the adoption rates of the optimized seed vectors by the RFR model for various number of generated parameter vectors (top left), the rate of the changed components (top right), the various rate of components exchange (bottom left), the mutation standard deviation σ (bottom center), and the mutation amplitude factor μ (bottom right).

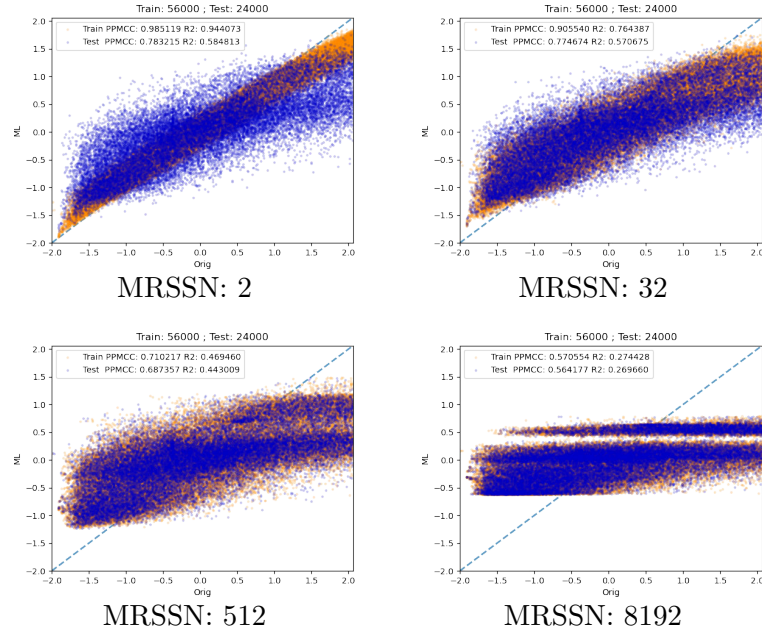


Figure B.2.: For C_{20} , the comparison between the actual scores and the scores predicted by the RFR model with the minimum required sample splitting number (MRSSN) of 2 (top left), 32 (top right), 512 (bottom left), and 8192 (bottom right). The yellow and the blue points represent the training and the test data.

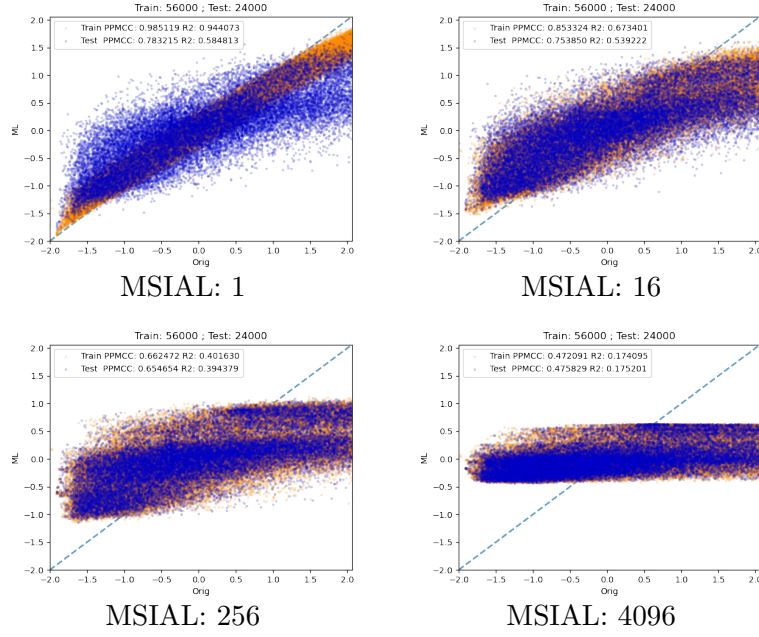


Figure B.3.: For C_{20} , the comparison between the actual scores and the scores predicted by the RFR model with the minimum samples in a leaf (MSIAL) for 1 (top left), 16 (top right), 256 (bottom left), and 4096 (bottom right). The yellow and the blue points represent the training and the test data respectively.

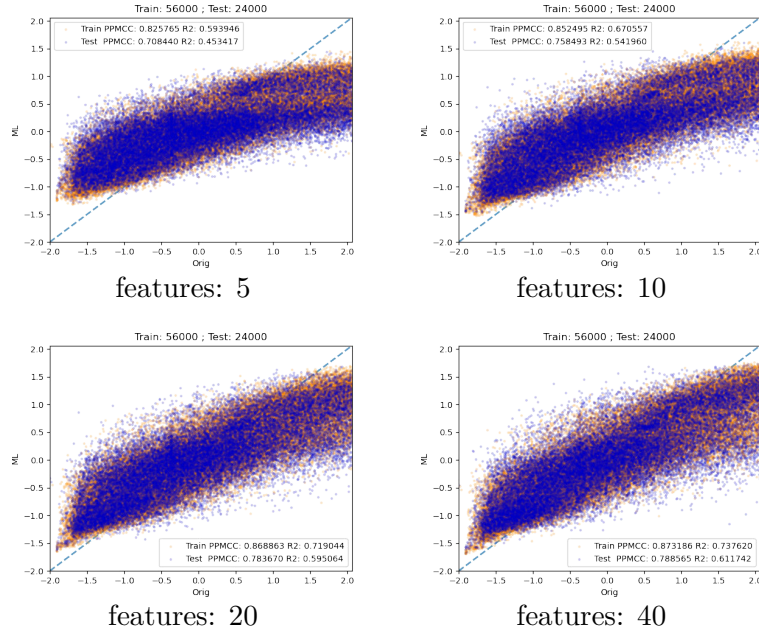


Figure B.4.: For C_{20} , the comparison between the actual scores and the scores predicted by the RFR model with 5 (top left), 10 (top right), 20 (bottom left), and 40 (bottom right) features. The yellow and the blue points represent the training and the test data respectively.

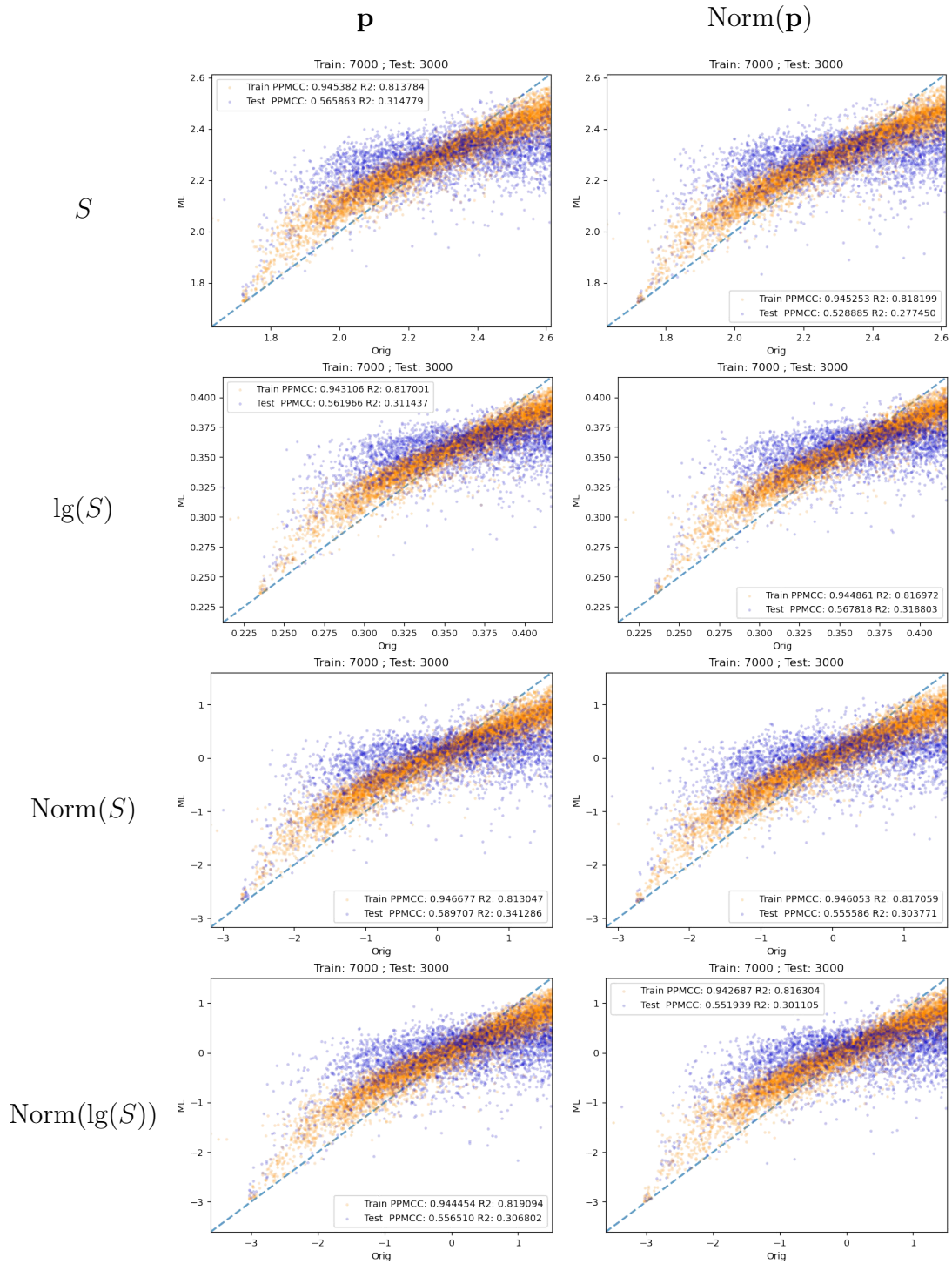


Figure B.5.: For the C_{20} system, the comparison between the actual scores and the scores predicted by the RFR model. In the first column, the vectors' components remained in the original value, in the second column, the vectors' components were normalized correspondingly. The original scores (the first row), the logarithmic score (the second row), the normalized scores (the third row), and the normalized logarithmic scores (the fourth row) were used for training and testing. The yellow and the blue points represent the training and the test data respectively.

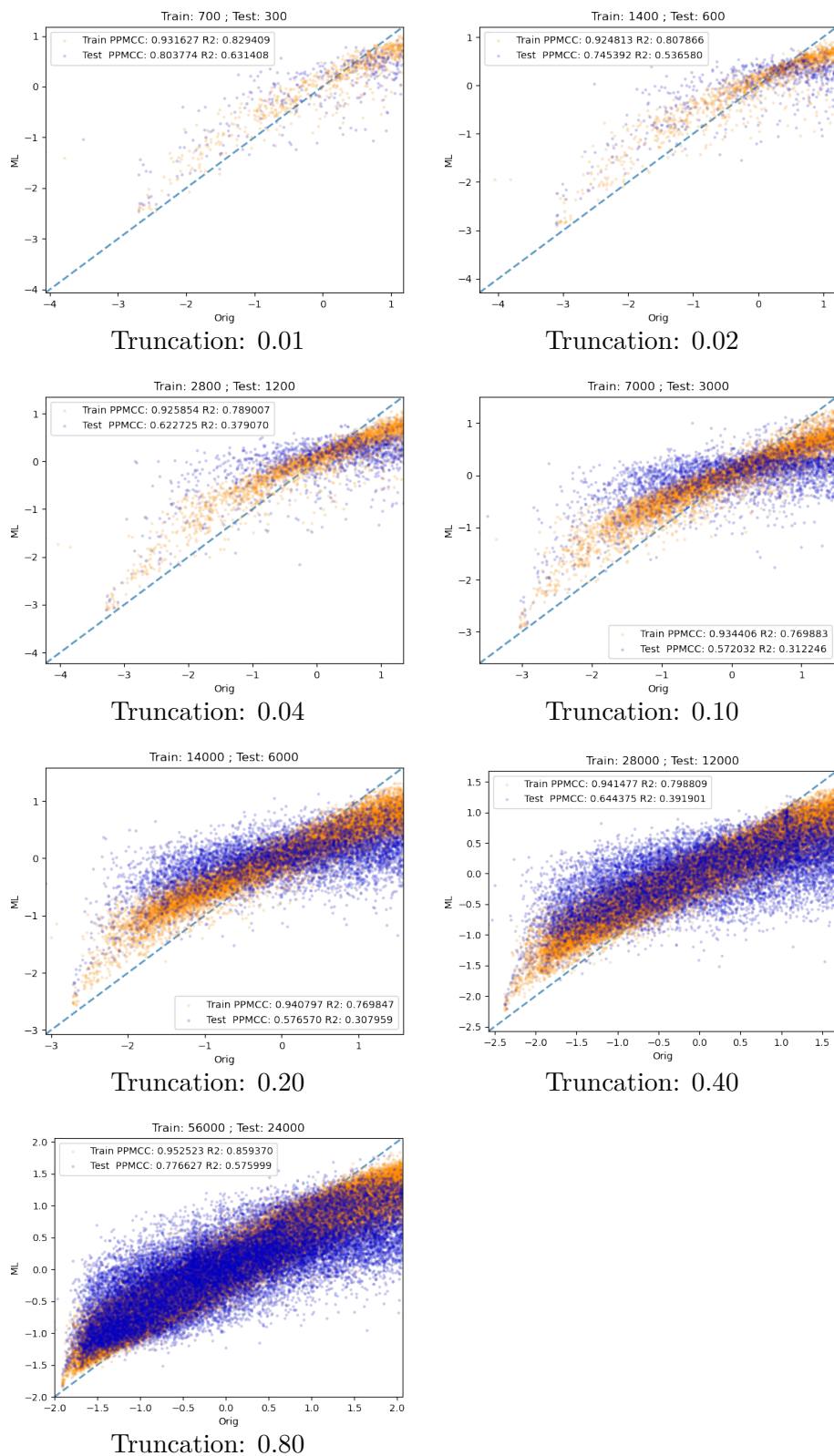


Figure B.6.: For the C_{20} system, the comparison between the actual scores and the scores predicted by the RFR model. Here the yellow and the blue points represent the training and the test data respectively. The data truncation ratios were 0.01, 0.02, 0.04, 0.10, 0.20, 0.40, 0.80, respectively.

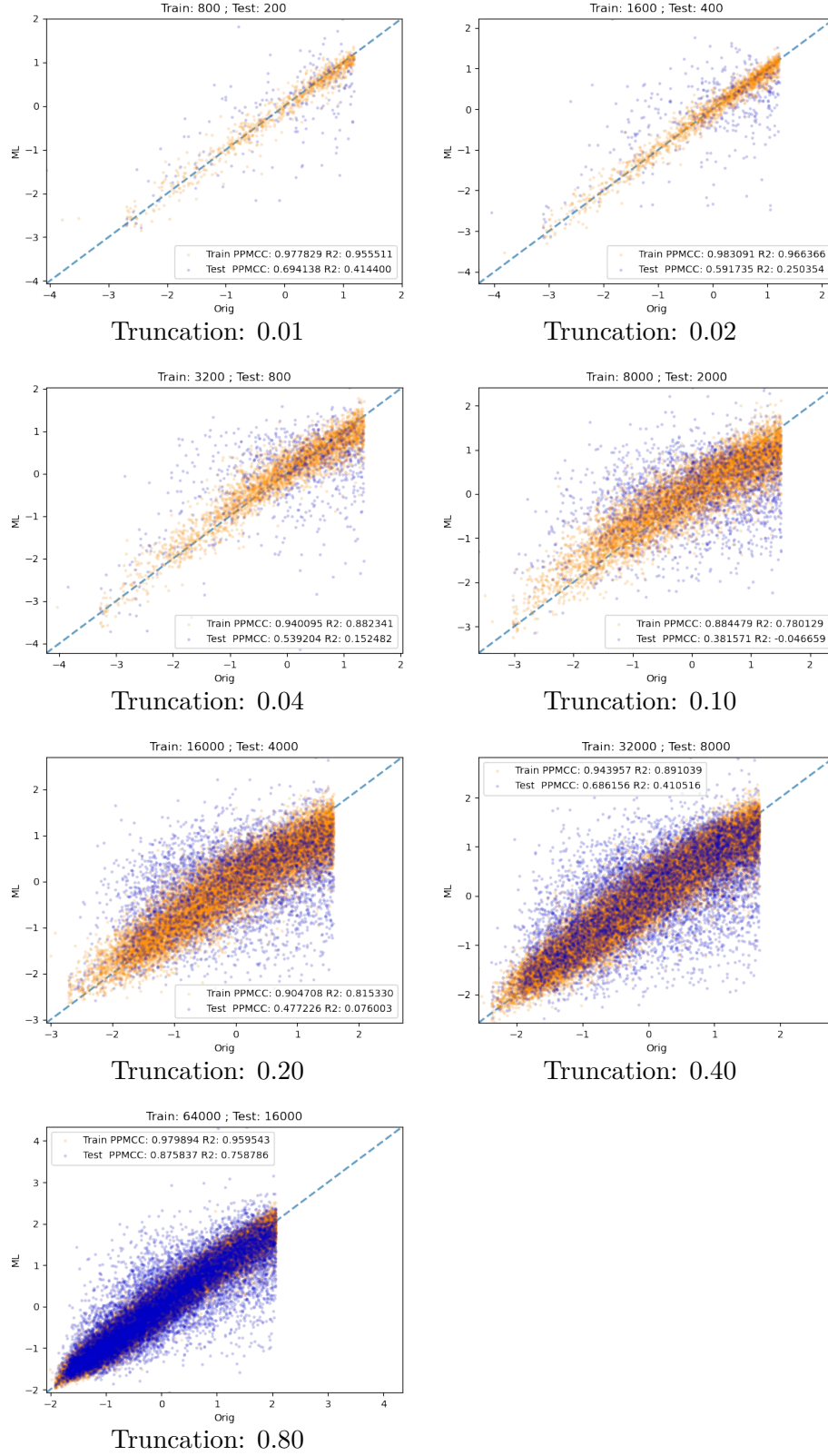


Figure B.7.: For the C_{20} system, the comparison between the actual scores and the scores predicted by the neural network model consisted of ten hidden layers with dimension 88, 176, 176, 176, 176, 88, 44, 22, 11, 5. Here the yellow and the blue points represent the training and the test data respectively. The data truncation ratios were 0.01, 0.02, 0.04, 0.10, 0.20, 0.40, 0.80, respectively.

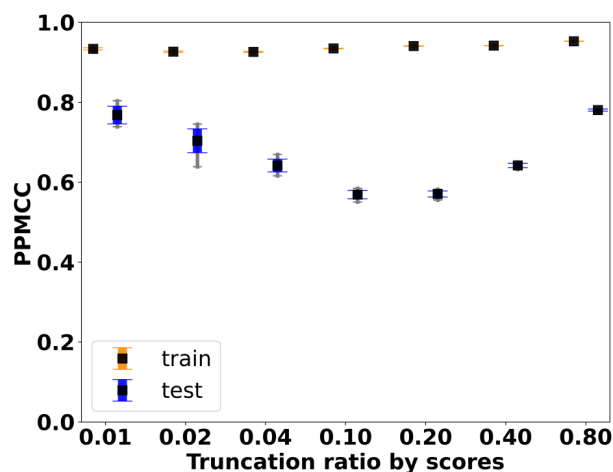


Figure B.8.: For the C_{20} system, the comparison between the actual scores and the scores predicted by the RFR model. Ten duplicates were calculated for each condition and the accuracy of the models evaluated by PPMCC. The black square in the centre represents the mean, the bar represents the standard deviation and the thin grey line represents the maximum and minimum values.

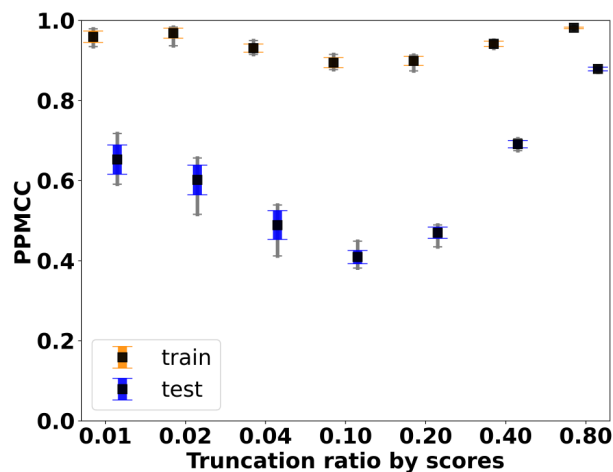


Figure B.9.: For the C_{20} system, the comparison between the actual scores and the scores predicted by the neural network model consisted of ten hidden layers with dimension 88, 176, 176, 176, 176, 88, 44, 22, 11, 5. Ten duplicates were calculated for each condition and the accuracy of the models evaluated by PPMCC. The black square in the centre represents the mean, the bar represents the standard deviation and the thin grey line represents the maximum and minimum values.

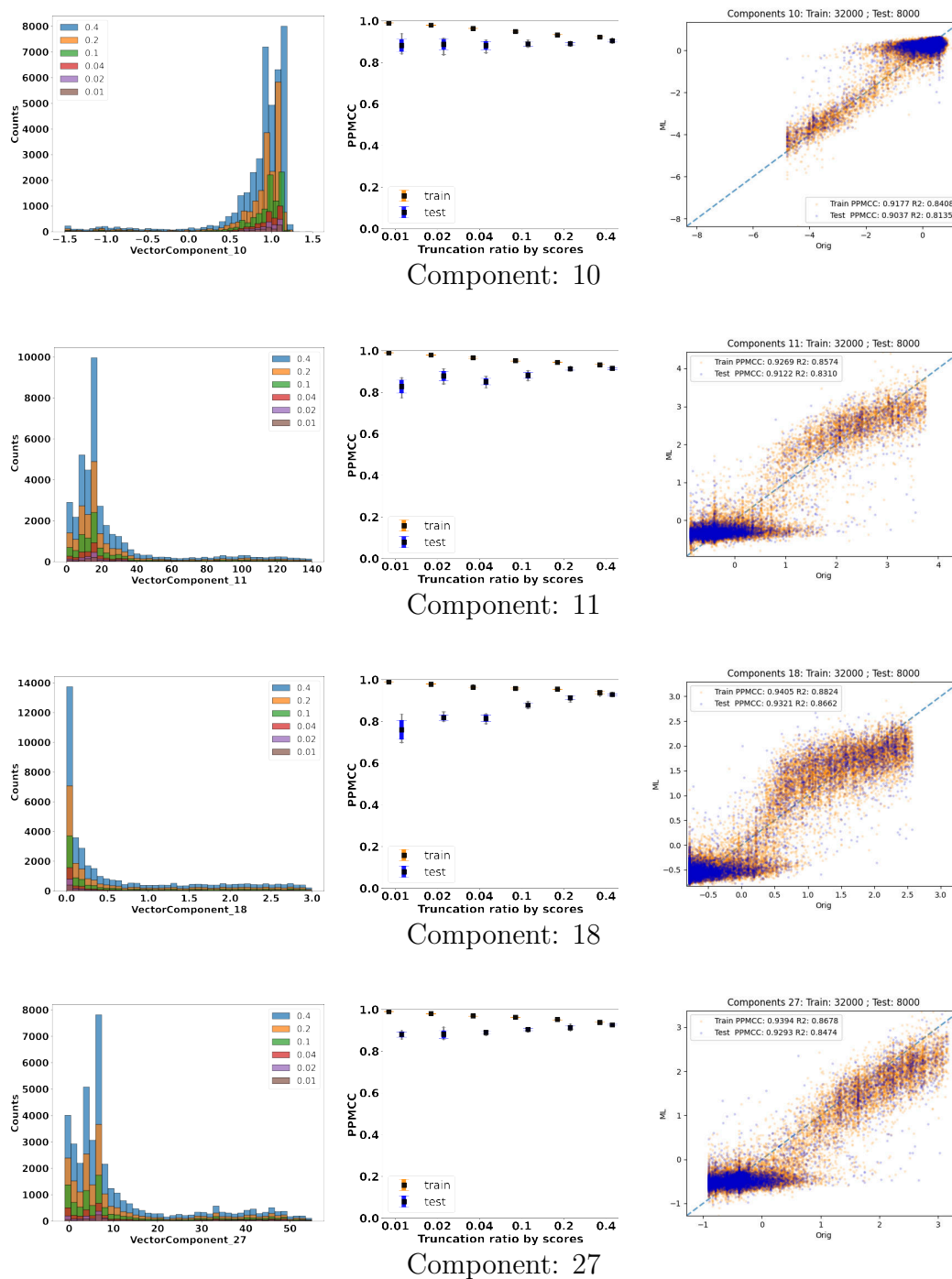


Figure B.10.: For the C_{20} system, the histogram of the components' values under different truncation ratios (the left column). The accuracy of the CAEs evaluated by PPMCC based on the ten duplicates. The code dimension is set as 22. The sample data sets were truncated by scores with various ratios. (the middle column). The predicted values by CAEs verse the original for the training set (orange) and the test set for the data truncation of 0.4 (blue, the right column).

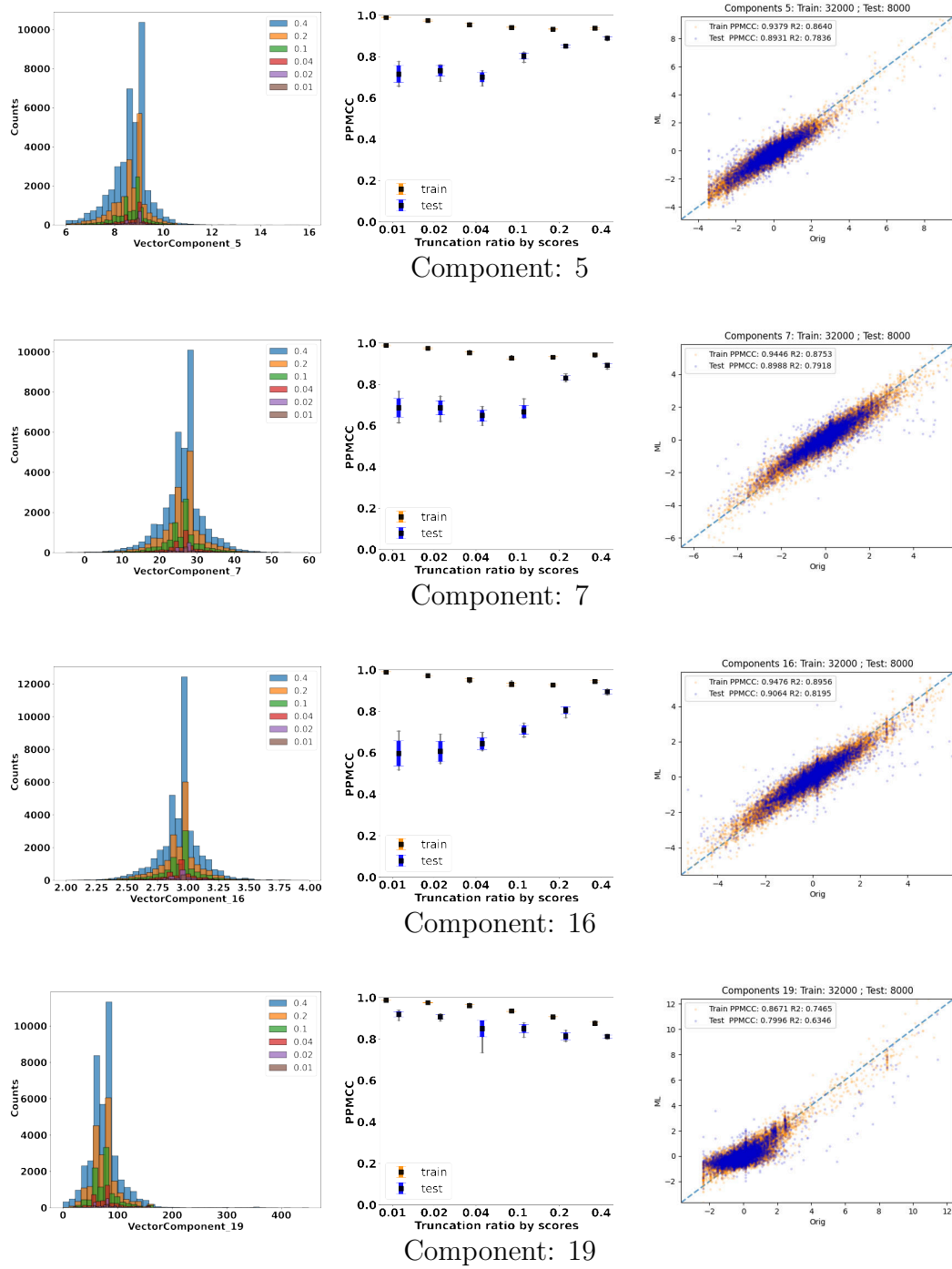


Figure B.11.: For the C_{20} system, the histogram of the components' values under different truncation ratios (the left column). The accuracy of the CAEs evaluated by PPMCC based on the ten duplicates. The code dimension is set as 22. The sample data sets were truncated by scores with various ratios. (the middle column). The predicted values by CAEs verse the original for the training set (orange) and the test set for the data truncation of 0.4 (blue, the right column).

B.4. Components segmentation for a 4,4'-bis(thiol)benzil system

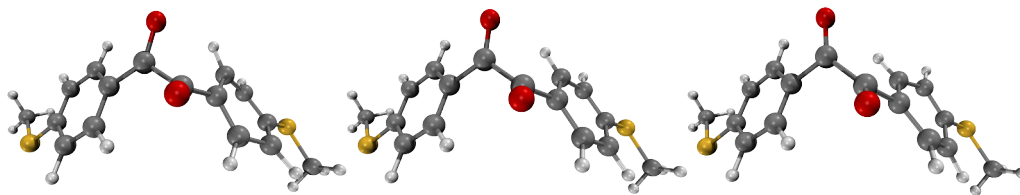


Figure B.12.: Ball-and-stick models of 4,4'-bis(thiol)benzil. Frames are obtained by scanning the O-C-C-O dihedral angle. The correspondence between atoms and colors, carbon (gray); hydrogen (white); oxygen (red); sulfur (yellow).

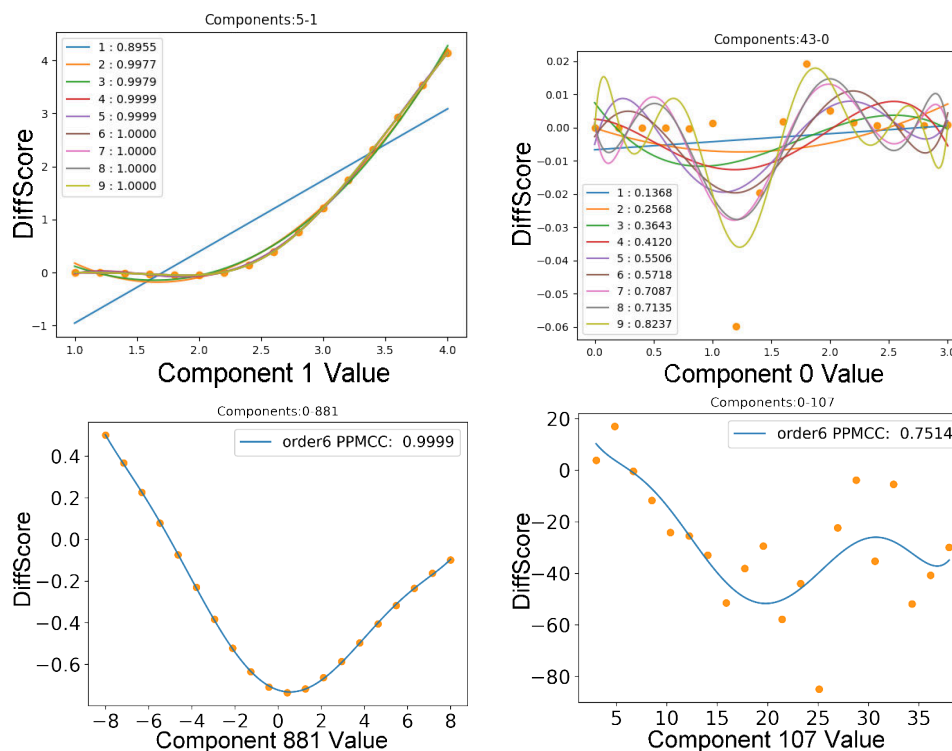


Figure B.13.: The scatter plots of $\Delta S(\mathbf{p}^{(5)}; \mathbf{p}^{(1)})$ (top left) and $\Delta S(\mathbf{p}^{(43)}; \mathbf{p}^{(0)})$ (top right), which were fitted by polynomial functions of degrees from one to nine. The scatter plots of $\Delta S(\mathbf{p}^{(0)}; \mathbf{p}^{(881)})$ (bottom left) and $\Delta S(\mathbf{p}^{(0)}; \mathbf{p}^{(107)})$ (bottom right), which were fitted by a polynomial functions of degree five. The performance of fitting was measured by PPMCC. Here, $\Delta S(\mathbf{p}^{(A)}; \mathbf{p}^{(B)})$ is the differences of the score function along the component $\mathbf{p}^{(B)}$ when the component $\mathbf{p}^{(A)}$ is slightly changed.

C. Supporting information for TEMPO

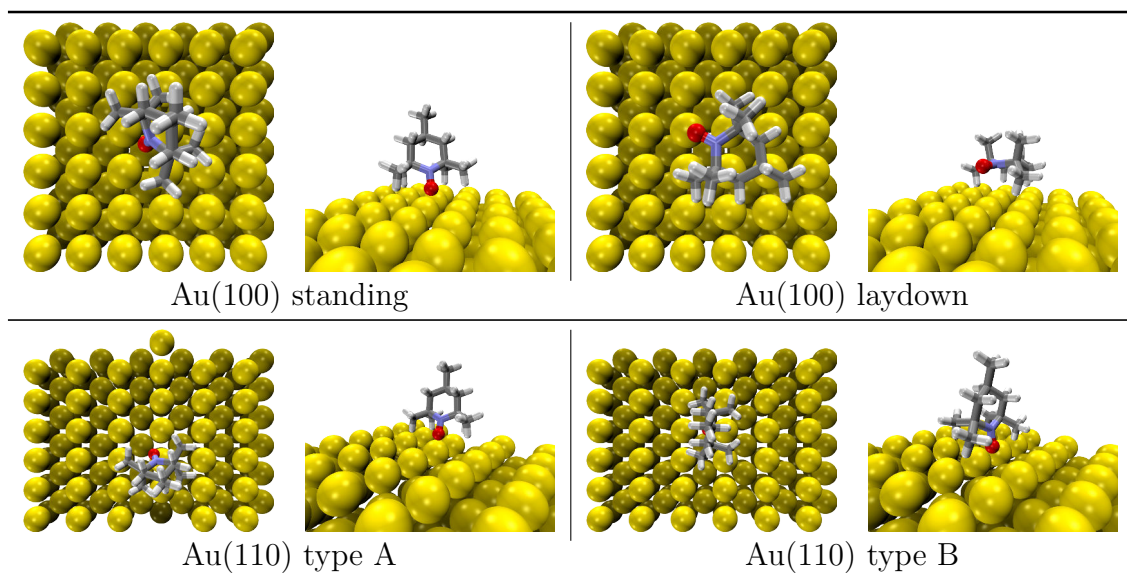
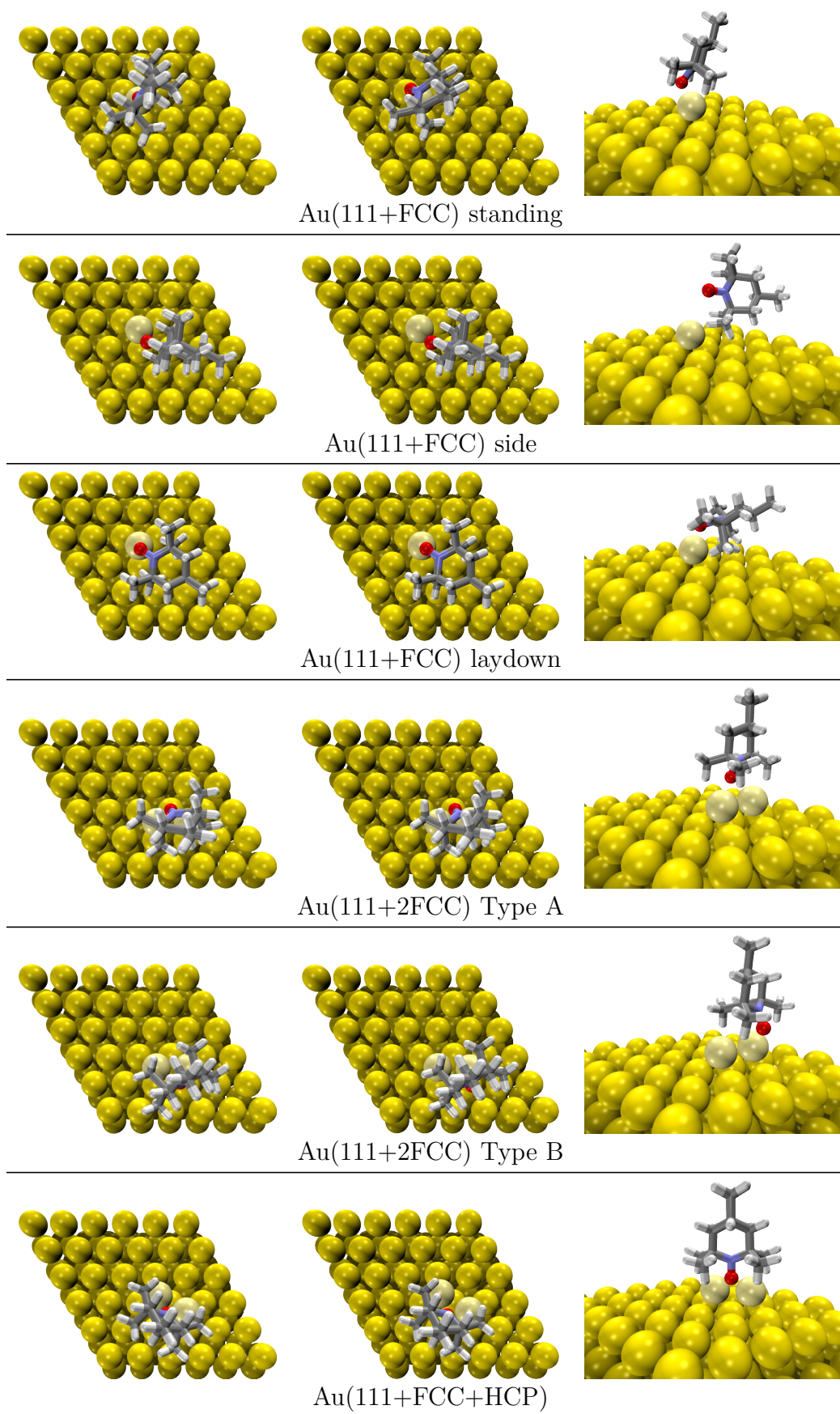


Figure C.1.: The optimized TEMPO structures on the Au(100) and the Au(110) surfaces from the top and the side views.

Table C.1.: The binding energies of the optimized TEMPO molecules on the different adsorbed positions of the Au(100) and the Au(110) surfaces.

Config.	E_{Binding} (kJ/mol)	E_{D3} (kJ/mol)	E_{SCF} (kJ/mol)	spin
Au(100) standing	−108.1021	−97.4309	−10.6713	1.0132
Au(100) laydown	−135.3399	−155.2642	19.9242	0.0000
Au(110) type A	−120.3847	−101.8016	−18.5831	−0.9390
Au(110) type B	−118.5708	−104.7637	−13.8167	0.7929



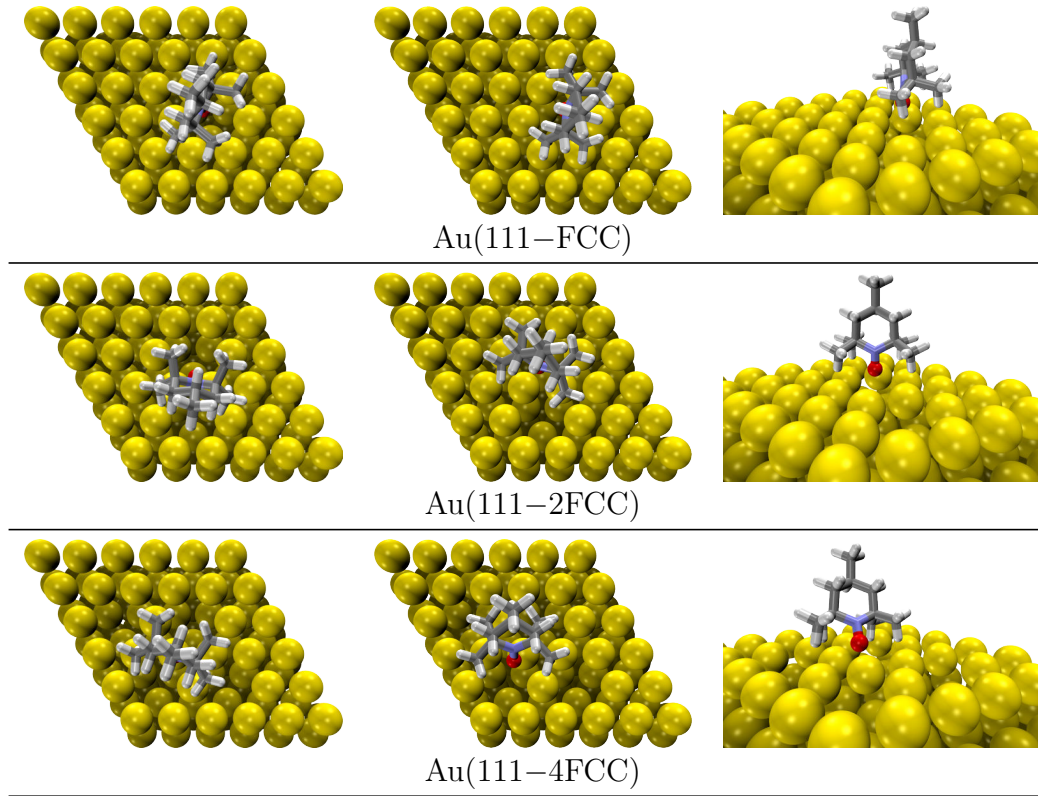


Figure C.2.: The initial TEMPO structure on the various defective Au(111) surfaces (the left column), the optimized structures from the top view (the middle column) and from the side view (the right column). Here the + sign and the – sign represent adding or removing gold atoms from the corresponding positions.

Table C.2.: The binding energies of the optimized TEMPO molecules on the different defective Au(111) surfaces.

Config.	E_{Binding} (kJ/mol)	E_{D3} (kJ/mol)	E_{SCF} (kJ/mol)	spin
Au(111+FCC) standing	–115.2517	–58.5762	–56.6658	0.7481
Au(111+FCC) side	–62.2716	–74.0911	11.8195	0.0001
Au(111+FCC) laydown	–139.1415	–89.6638	–49.4777	0.7034
Au(111+2FCC) Type A	–90.4357	–62.8023	–27.6334	0.1066
Au(111+2FCC) Type B	–95.6941	–64.6162	–31.0779	0.2920
Au(111+FCC+HCP)	–75.4226	–71.5149	–3.9077	0.0000
Au(111–FCC)	–114.2097	–105.7479	–8.4618	0.7198
Au(111–2FCC)	–108.2758	–99.0711	–9.2047	0.7345
Au(111–4FCC)	–116.3902	–99.5632	–16.8174	0.4207

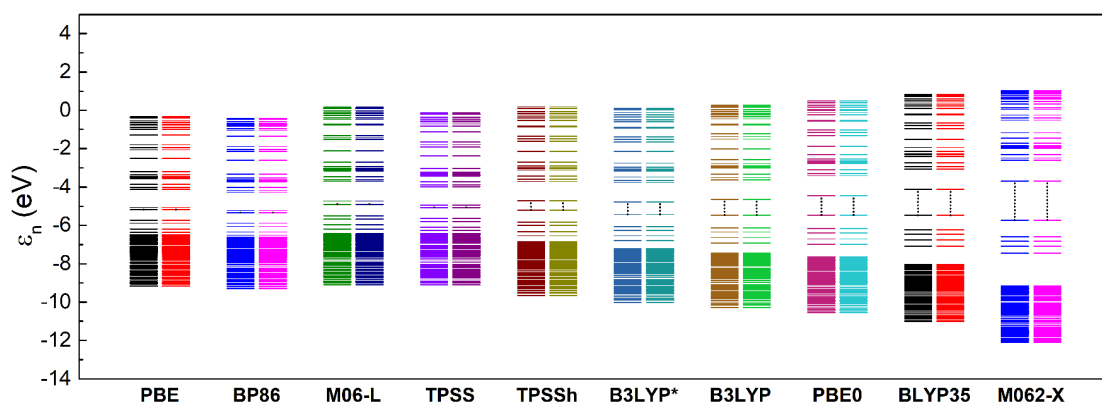


Figure C.3.: Kohn-Sham orbital energy levels of the Au_{20} cluster calculated by different functionals, where the left side for α electrons, the right side for β electrons, the black vertical dashes indicate gaps.

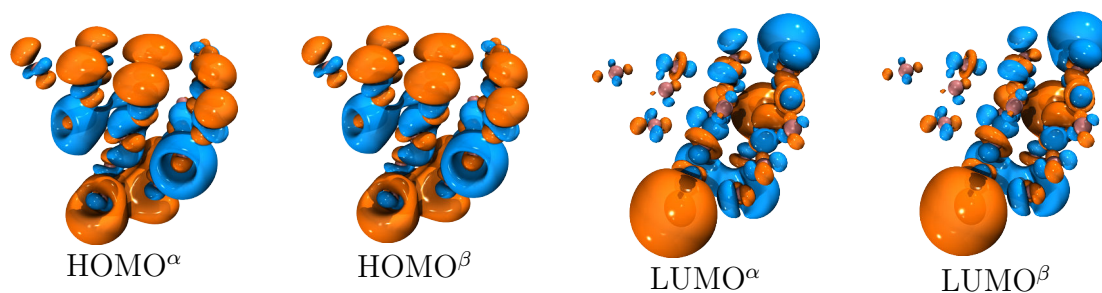


Figure C.4.: The molecular orbital isosurfaces for the Au_{20} cluster based on PBE KS-DFT.

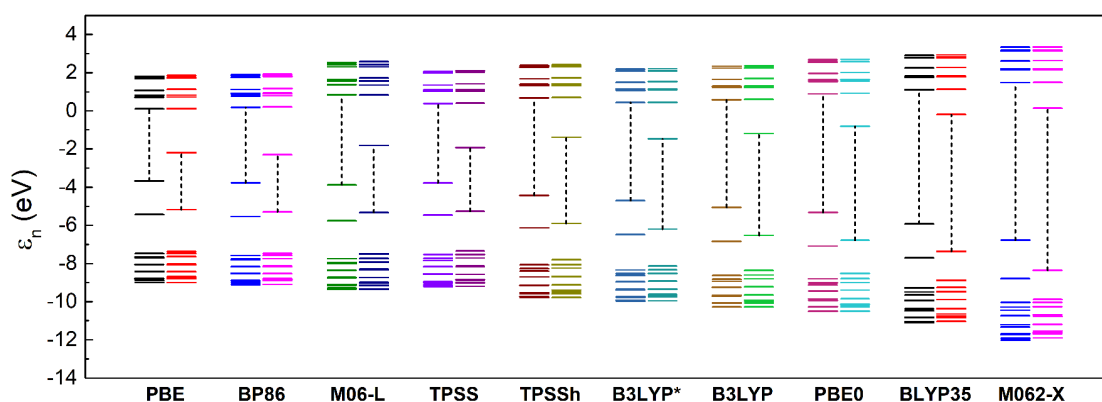


Figure C.5.: Kohn-Sham orbital energy levels of TEMPO calculated by different functionals where the left side for α electrons, the right side for β electrons, the black vertical dashes indicate gaps.

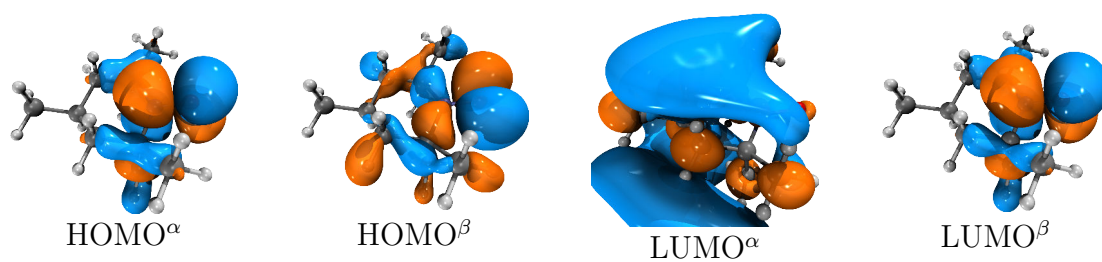


Figure C.6.: The molecular orbital isosurfaces for the TEMPO molecule based on PBE KS-DFT.

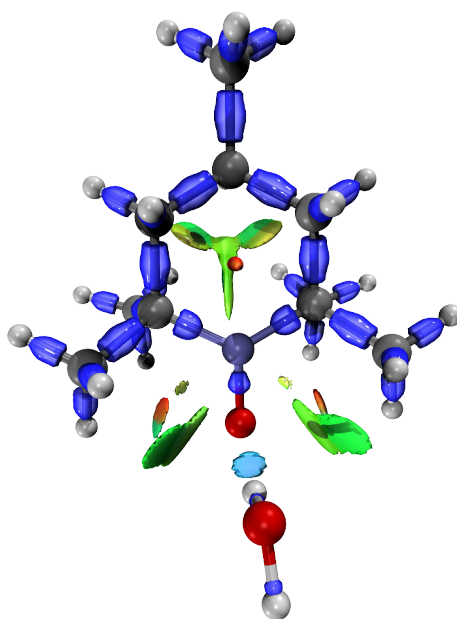
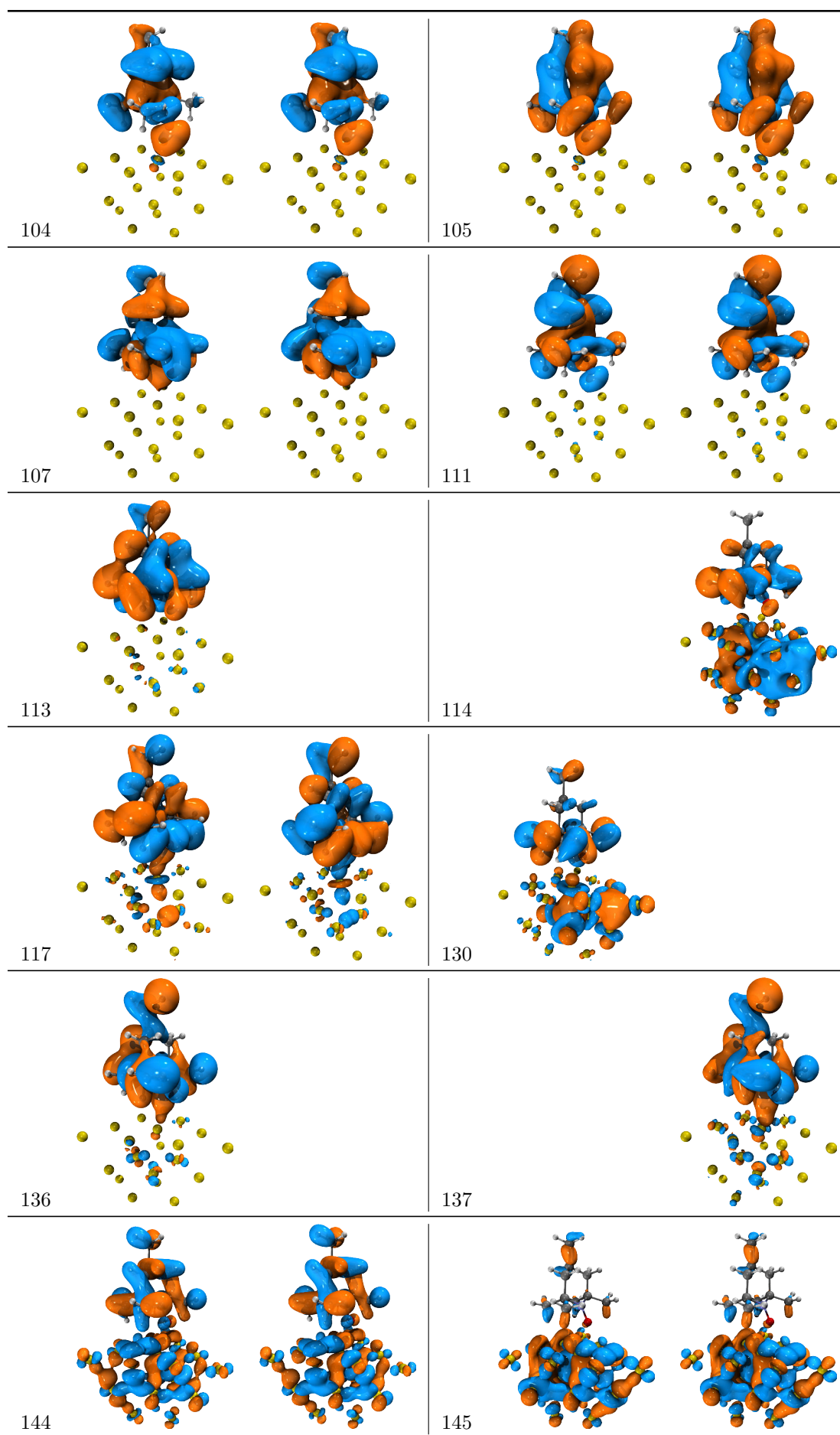


Figure C.7.: The IRI isosurfaces of the complex of TEMPO and H_2O colored by $\text{sign}(\lambda_2)\rho$.



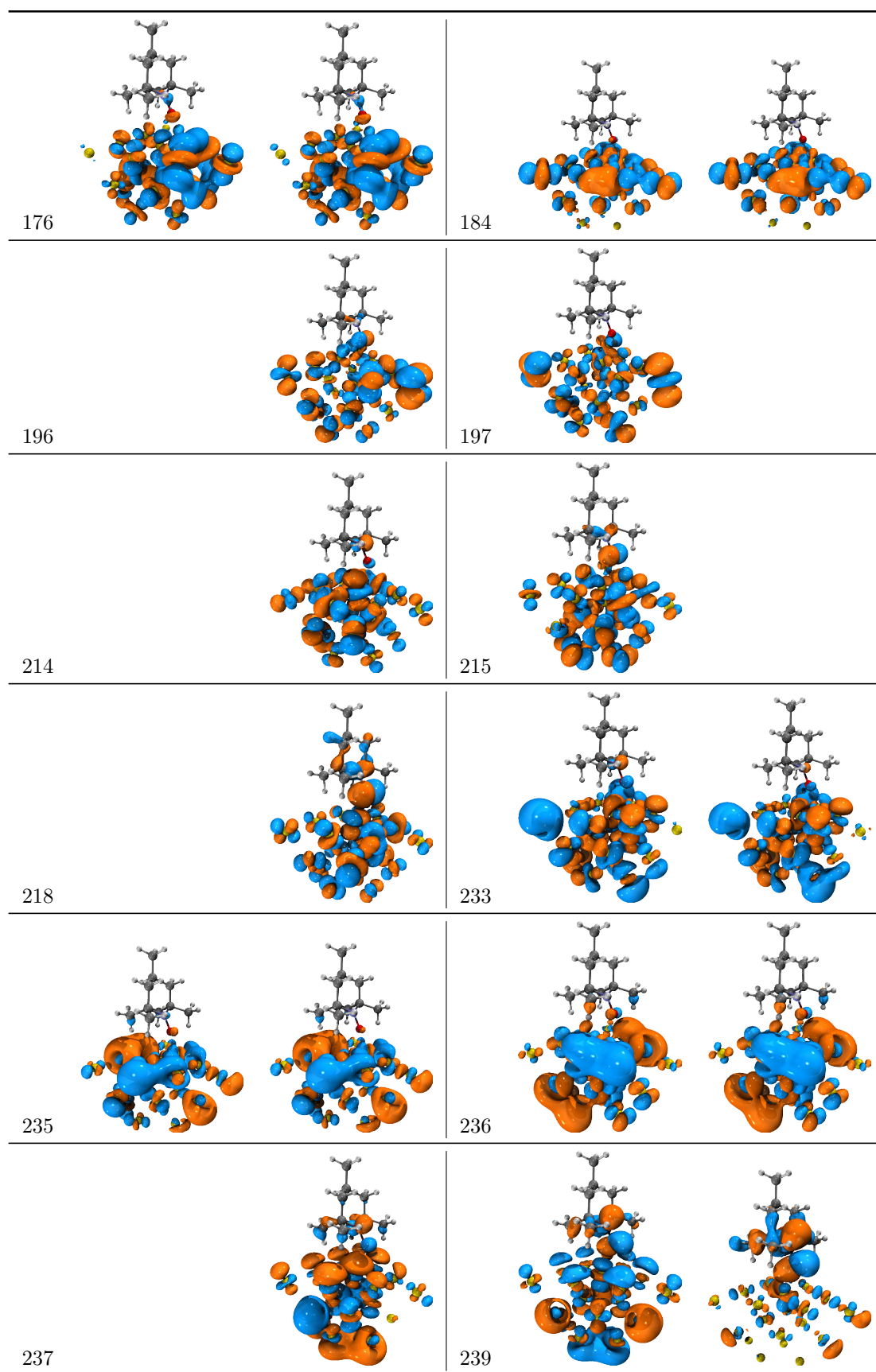


Figure C.8.: The molecular orbital isosurfaces for the TEMPO-Au₂₀ complex based on PBE KS-DFT.

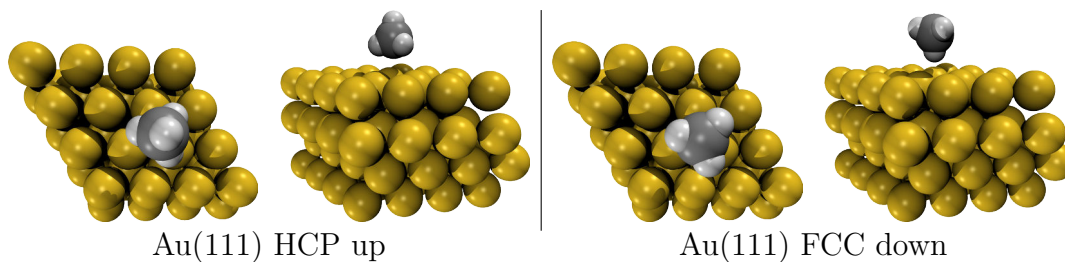


Figure C.9.: The optimized CH_4 structures on the HCP position and the FCC position of the Au(111) surface from the top and the side views.

Table C.3.: The binding energies of the optimized CH_4 molecules on the Au(111) surface with the different adsorbed position.

Position	E_{Binding} (kJ/mol)	E_{D3} (kJ/mol)	E_{DFT} (kJ/mol)
HCP(up)	−21.0025	−23.2375	2.2350
FCC(down)	−17.3581	−19.2430	1.8850

Table C.4.: The binding energies of the optimized anchoring molecules on the Au(111) surface.

Molecule	E_{Binding} (kJ/mol)	E_{D3} (kJ/mol)	E_{DFT} (kJ/mol)	spin
Piperidinyloxy(standing)	−119.1444	−91.4275	−27.7168	1.3141
Piperidinyloxy(laydown)	−100.3990	−88.7337	−11.6653	0.3142
PhS(standing)	−200.3601	−86.0282	−114.3319	0.0000
PhS(laydown)	−230.6645	−118.9210	−111.7434	0.0000
PhSH(standing)	−47.7963	−112.5868	64.7904	0.0000
PhSH(laydown)	−124.5978	−117.6561	−6.9416	0.0021
tmchS	−270.1320	−148.3307	−121.8013	0.0000
tmchSH	−147.2365	−142.3969	−4.8396	0.0000
tmchOH	−107.1449	−115.5286	8.3837	0.0000
tmchNH2	−140.5091	−134.1397	−6.3694	0.0000
cyhexS	−271.5637	−121.1344	−150.4292	0.0000
cyhexSH	−111.6513	−96.9697	−14.6816	0.0000
cyhexOH	−84.1467	−86.7934	2.6467	0.0000
cyhexNH2	−126.1290	−102.0708	−24.0582	0.0000
cyhexCOOH	−77.5030	−78.9829	1.4799	0.0000
cyhexCOO [−]	173.6340	−58.4305	232.0645	0.0000

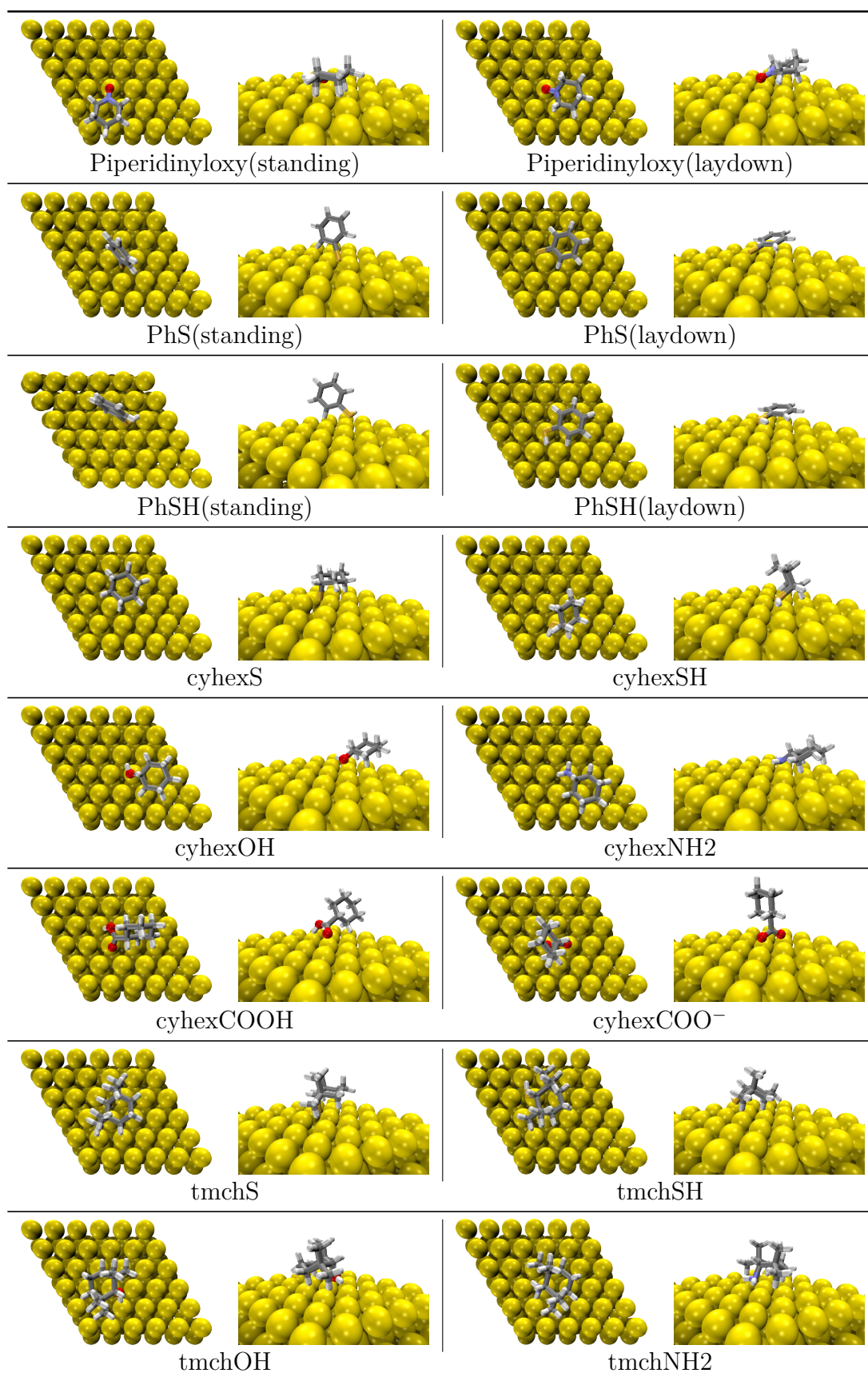
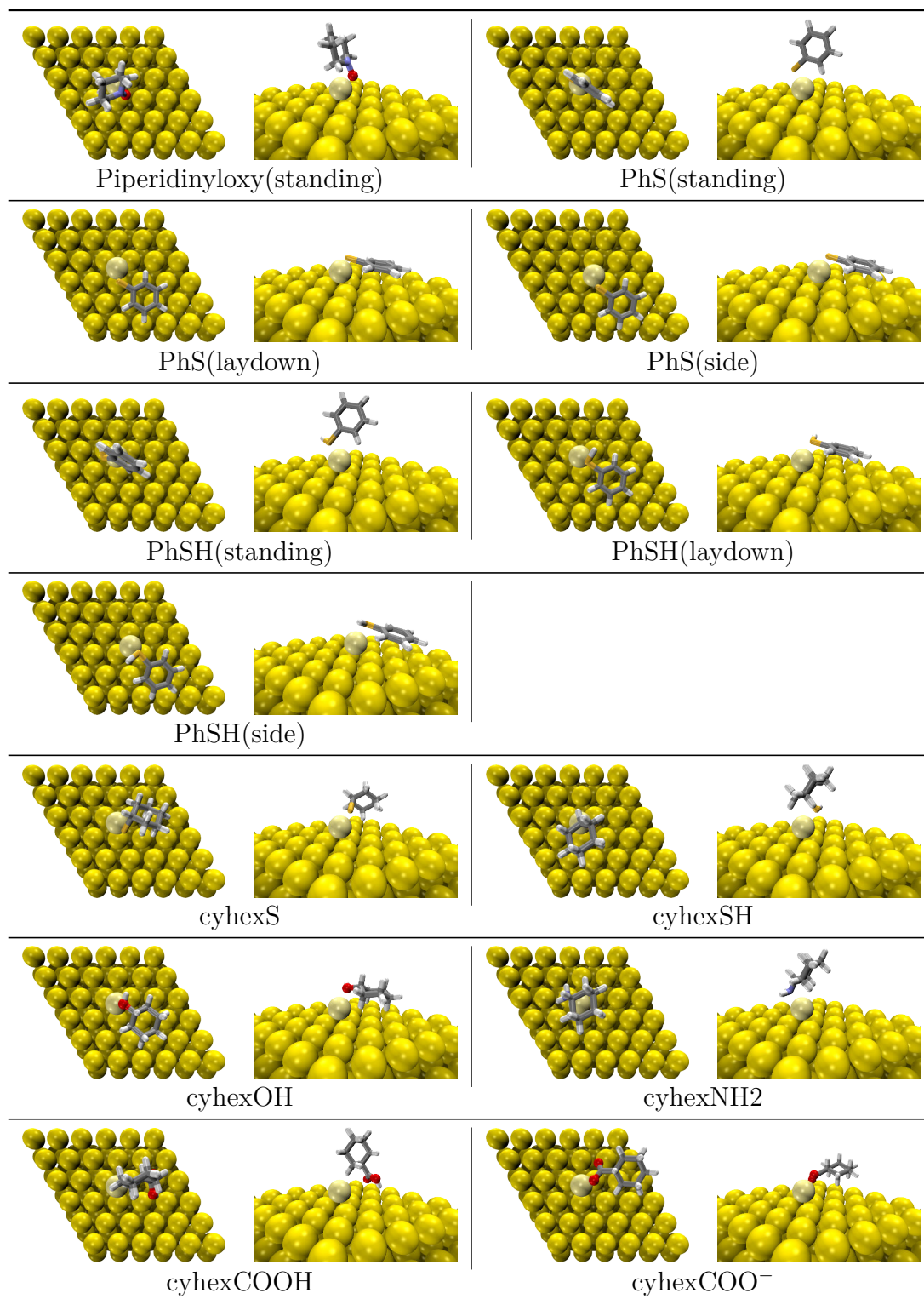


Figure C.10.: The optimized structures of the other molecules with the conventional anchoring groups on the Au(111) surface from the top and the side views.



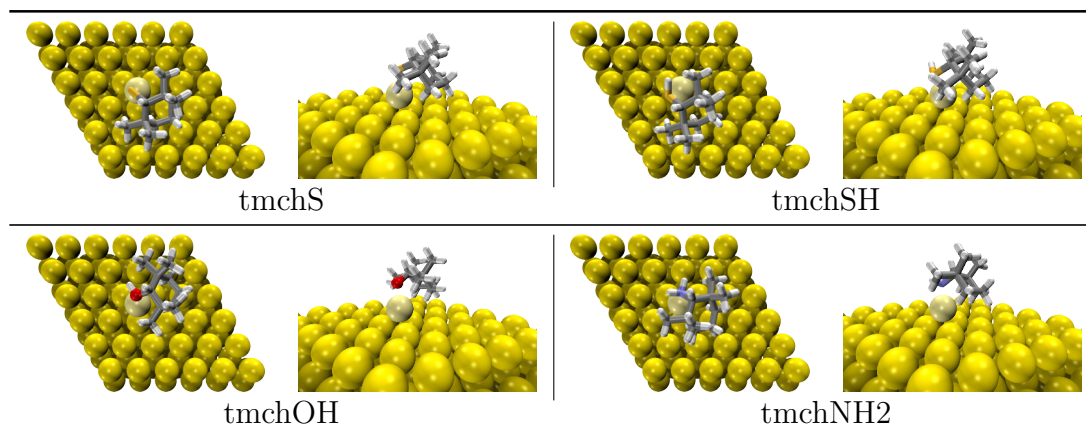


Figure C.11.: The optimized structures of the other molecules with the conventional anchoring groups on the Au(111+FCC) surface from the top and the side views.

Table C.5.: The binding energies of the optimized anchoring molecules on the Au(111+FCC) surface.

Molecule	E_{Binding} (kJ/mol)	E_{D3} (kJ/mol)	E_{DFT} (kJ/mol)	spin
Piperidinyloxy(standing)	-89.9201	-27.9093	-62.0108	0.0271
PhS(standing)	-201.3220	-29.3383	-171.9837	0.0000
PhS(laydown)	-260.0050	-102.4635	-157.5415	0.0000
PhS(side)	-247.3000	-96.8992	-150.4008	0.0000
PhSH(standing)	-101.2344	-35.1737	-66.0606	0.0000
PhSH(laydown)	-158.1619	-96.2586	-61.9033	0.0000
PhSH(side)	-153.1528	-91.2037	-61.9491	0.0000
cyhexS	-253.0700	-71.9964	-181.0736	0.0006
cyhexSH	-121.7908	-40.7457	-81.0451	0.0000
cyhexOH	-113.4388	-82.5528	-30.8859	0.0000
cyhexNH2	-127.5279	-38.9222	-88.6057	0.0000
cyhexCOOH	-71.4630	-60.2136	-11.2494	0.0000
cyhexCOO ⁻	126.9663	-104.1318	231.0981	0.0000
tmchS	-277.1855	-100.0340	-177.1515	0.0012
tmchSH	-183.6243	-105.0214	-78.6029	0.0000
tmchOH	-124.4457	-98.5318	-25.9140	0.0000
tmchNH2	-180.8553	-98.7537	-82.1017	0.0000

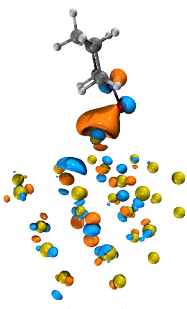
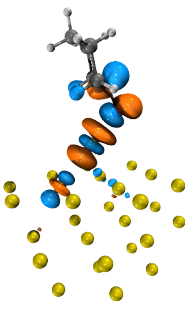
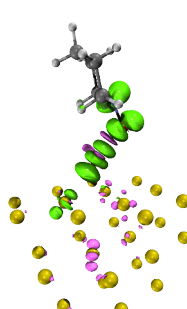
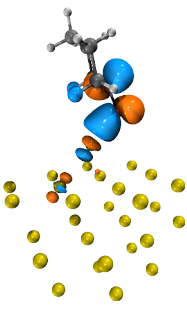
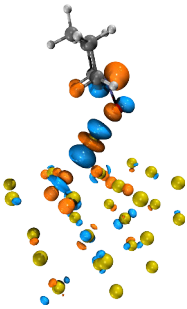
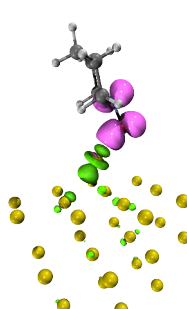

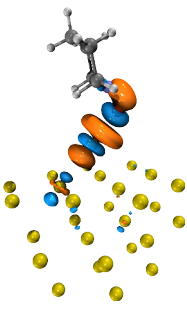
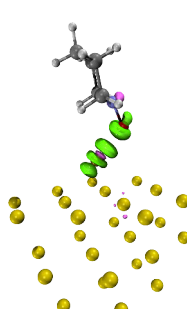
Pair	Acceptor orbital	Donor orbital	NOCV pair density
1	 orbital 1	 orbital 1397	
700	 orbital 1398	 orbital 2794	
701	 orbital 1399	 orbital 2793	

Figure C.12.: The NOCV orbital pairs' isosurfaces with the value of 0.04 and the corresponding density isosurfaces with the value of 0.0015 for the piperidinyloxy-Au₂₈ complex, where the green and the magenta indicate the decreasing and the increasing of the density.

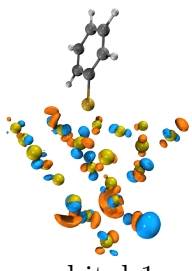
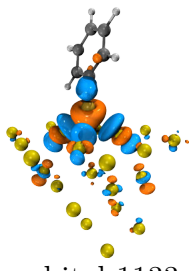
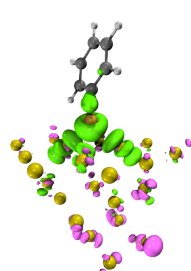
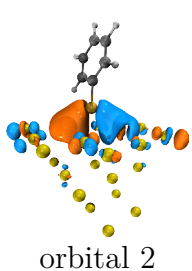
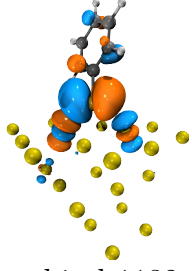
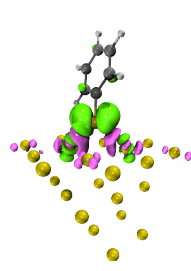
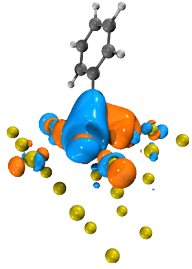
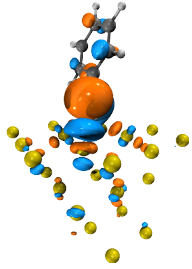
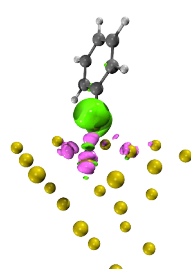
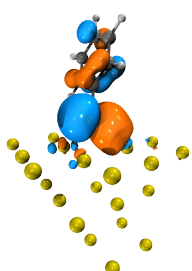
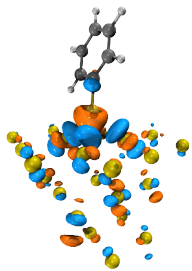
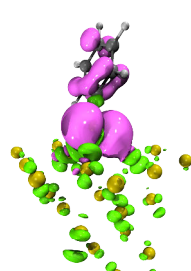
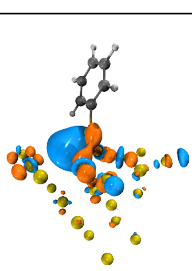
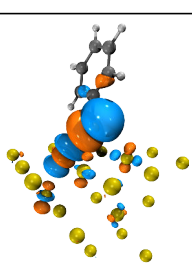
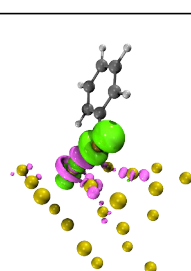
Pair	Acceptor orbital	Donor orbital	NOCV pair density
1	 orbital 1	 orbital 1133	
2	 orbital 2	 orbital 1132	
3	 orbital 3	 orbital 1131	
568	 orbital 1134	 orbital 2266	
569	 orbital 1135	 orbital 2265	

Figure C.13.: The NOCV orbital pairs' isosurfaces with the value of 0.04 and the corresponding density isosurfaces with the value of 0.0015 for the PhS-Au₂₂ complex, where the green and the magenta indicate the decreasing and the increasing of the density.

Table C.6.: The significant NOCV orbital pairs of the piperidinyloxy-Au₂₈ complex.

Alpha NOCV orbital pairs							
Pair	E (kJ/mol)	Orbital	Eigenvalue	E	Orbital	Eigenvalue	E
1	-71.9648	1	0.53181	-425.8894	1397	-0.53181	-290.5370
2	-8.3680	2	0.15021	-408.3166	1396	-0.15021	-352.5438
Beta NOCV orbital pairs							
Pair	E (kJ/mol)	Orbital	Eigenvalue	E	Orbital	Eigenvalue	E
700	-56.0656	1398	0.55579	-532.2466	2794	-0.55579	-431.4122
701	-20.9618	1399	0.18834	-401.0364	2793	-0.18834	-289.7838
702	-6.2342	1400	0.10577	-399.8649	2792	-0.10577	-340.7450

Table C.7.: The significant NOCV orbital pairs of the PhS-Au₂₂ complex.

Alpha NOCV orbital pairs							
Pair	E (kJ/mol)	Orbital	Eigenvalue	E	Orbital	Eigenvalue	E
1	-100.9181	1	0.75086	-461.1605	1133	-0.75086	-326.7286
2	-80.3328	2	0.39516	-434.8431	1132	-0.39516	-231.5844
3	-42.8023	3	0.31647	-431.7051	1131	-0.31647	-296.4782
Beta NOCV orbital pairs							
Pair	E (kJ/mol)	Orbital	Eigenvalue	E	Orbital	Eigenvalue	E
568	-229.9526	1134	0.98430	-639.0223	2266	-0.98430	-405.4296
569	-71.5464	1135	0.40077	-417.1030	2265	-0.40077	-238.6135

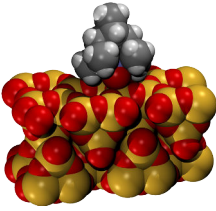
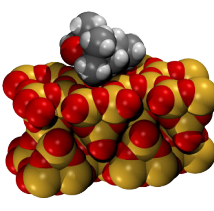
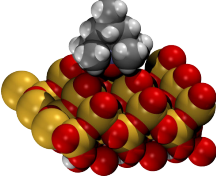
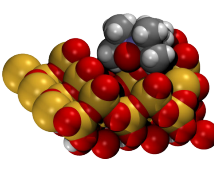
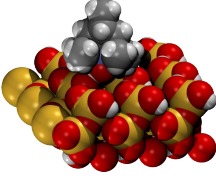
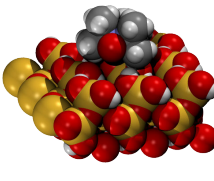
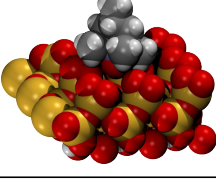
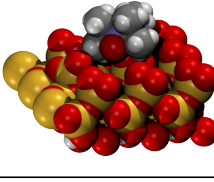
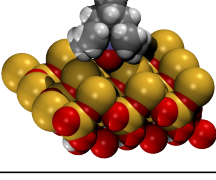
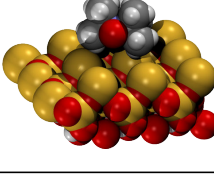
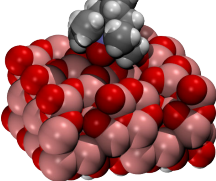
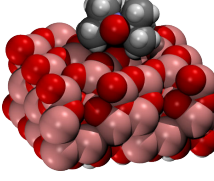
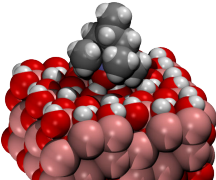
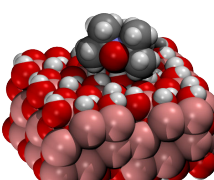
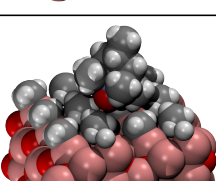
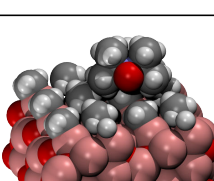
Surfaces	TEMPO(Stand)	TEMPO(Laydown)
Reconstructed-SiO ₂		
Dehydro- α -SiO ₂ (100)		
Hydro- α -SiO ₂ (100)		
Ox- α -SiO ₂ (100)		
Red- α -SiO ₂ (100)		
Dehydro- α -Al ₂ O ₃ (001)		
Hydro- α -Al ₂ O ₃ (001)		
Methyl- α -Al ₂ O ₃ (001)		

Figure C.14.: The optimized TEMPO structures on the various SiO₂ and Al₂O₃ surfaces.

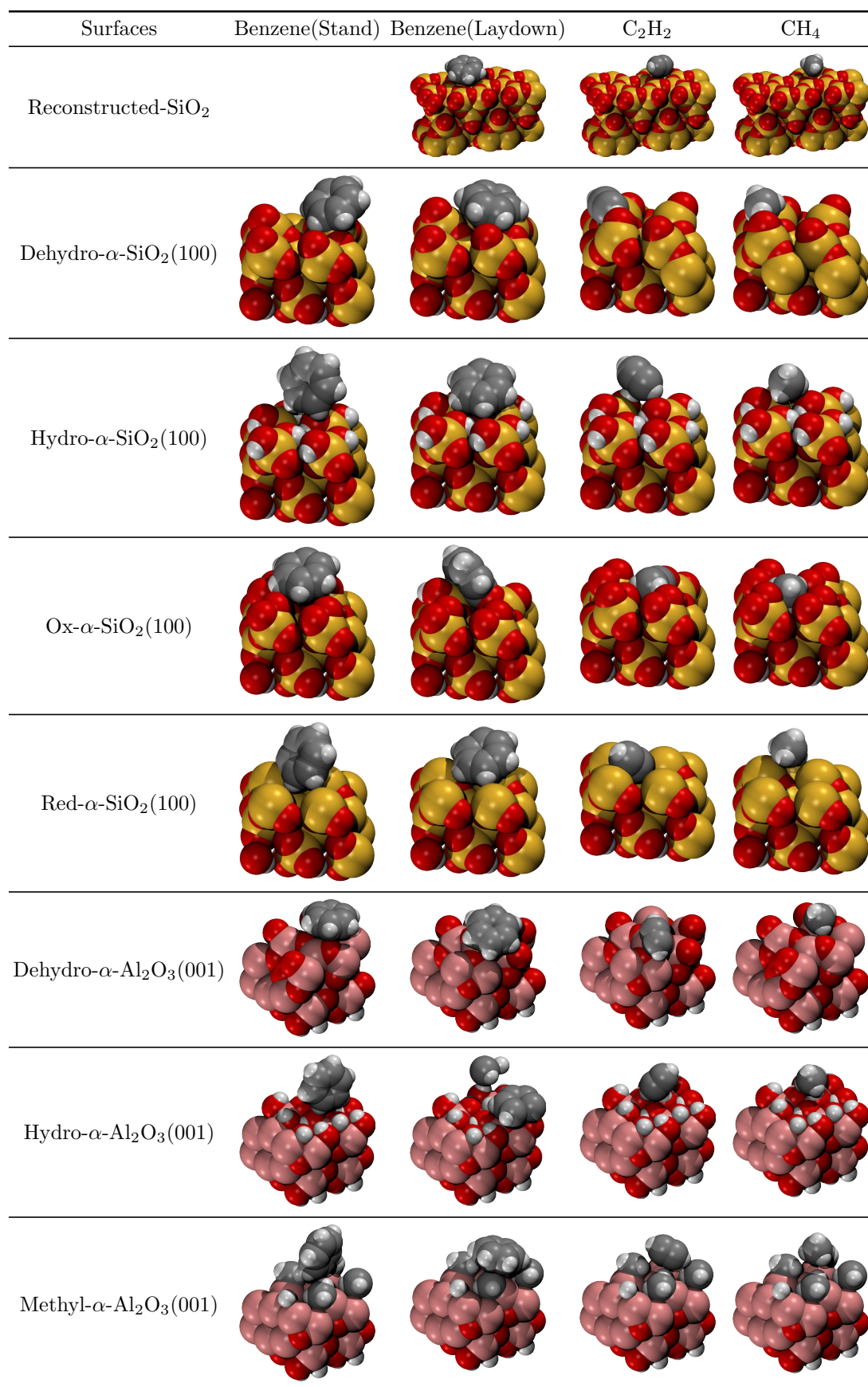


Figure C.15.: The optimized structures of benzene, C₂H₂, and CH₄ on the various SiO₂ and Al₂O₃ surfaces.

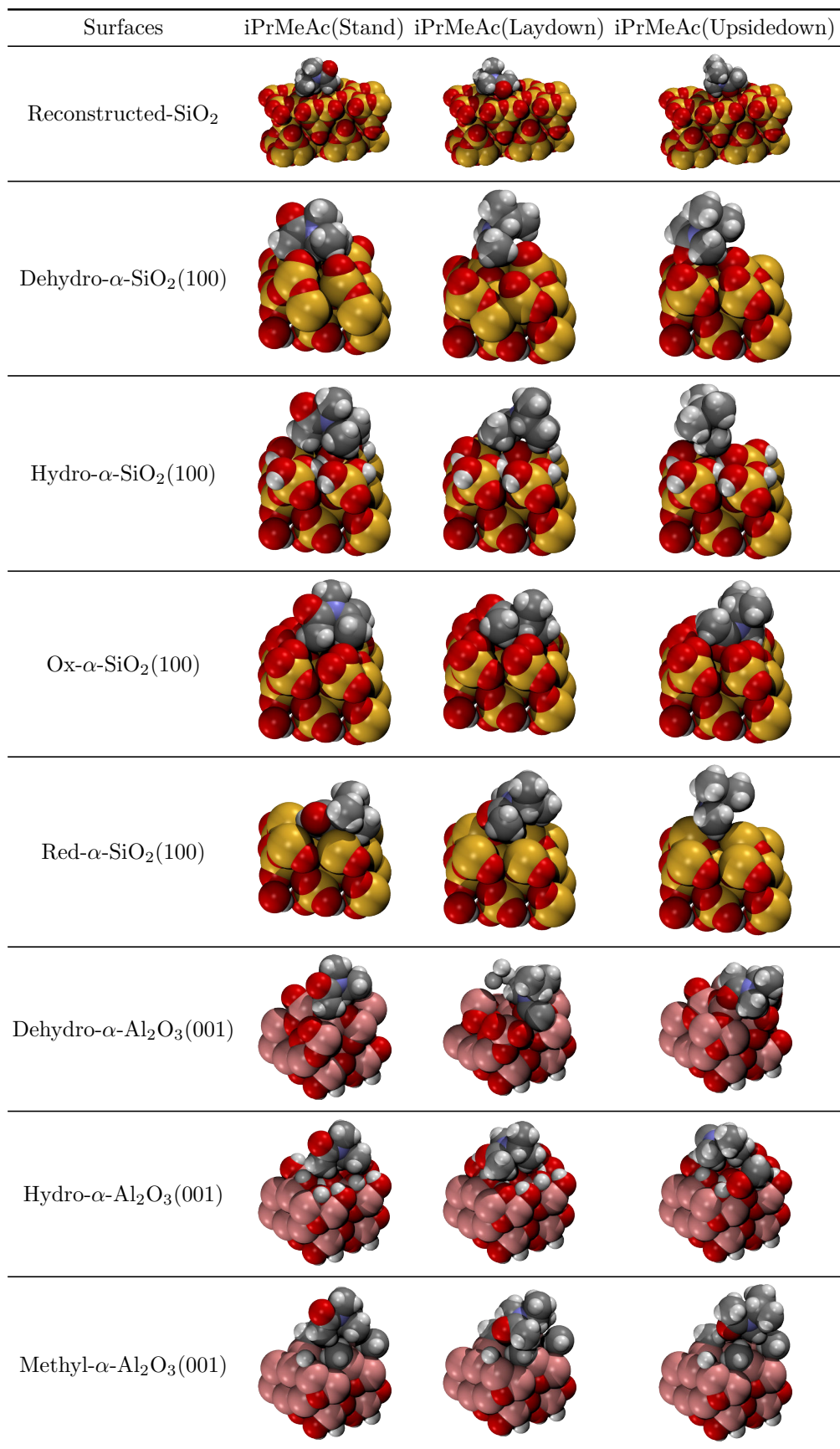


Figure C.16.: The optimized structures of iPrMeAc on the various SiO₂ and Al₂O₃ surfaces.

Table C.8.: The binding energies of the optimized fragment molecules on the various SiO₂ and Al₂O₃ surfaces.

E_{Binding} (kJ/mol)	TEMPO(Stand)	TEMPO(Laydown)		
Reconstructed-SiO ₂	-38.6069	-51.5298		
Dehydro- α -SiO ₂ (100)	-181.9004	-259.1962		
Hydro- α -SiO ₂ (100)	-75.2343	-40.1010		
Ox- α -SiO ₂ (100)	-193.6178	-217.7626		
Red- α -SiO ₂ (100)	-23.2640	-28.7413		
Dehydro- α -Al ₂ O ₃ (001)	-107.9080	-156.0642		
Hydro- α -Al ₂ O ₃ (001)	-89.6031	-69.4767		
Methyl- α -Al ₂ O ₃ (001)	-37.8832	-42.2582		
E_{Binding} (kJ/mol)	Benzene(Stand)	Benzene(Laydown)	C ₂ H ₂	CH ₄
Reconstructed-SiO ₂		-35.7349	-13.7072	-12.7860
Dehydro- α -SiO ₂ (100)	-195.0833	-220.7494	-156.3809	-59.3626
Hydro- α -SiO ₂ (100)	-15.5812	-48.9357	-35.0931	-13.0256
Ox- α -SiO ₂ (100)	-32.2886	-722.1088	-393.6034	-24.9451
Red- α -SiO ₂ (100)	-24.9154	-31.8544	-27.3831	-8.8999
Dehydro- α -Al ₂ O ₃ (001)	-91.0915	-357.7030	-343.3606	-63.4849
Hydro- α -Al ₂ O ₃ (001)	-38.1048	-59.5105	-34.6883	-16.5557
Methyl- α -Al ₂ O ₃ (001)	-23.4602	-32.9857	-17.1864	-10.2940
E_{Binding} (kJ/mol)	iPrMeAc(Stand)	iPrMeAc(Laydown)	iPrMeAc(Upsidedown)	
Reconstructed-SiO ₂	-32.1724	-41.3751	-26.7038	
Dehydro- α -SiO ₂ (100)	-94.7335	-424.1171	-353.8059	
Hydro- α -SiO ₂ (100)	-31.2296	-94.5057	-71.2171	
Ox- α -SiO ₂ (100)	-481.9829	-375.2978	-420.4038	
Red- α -SiO ₂ (100)	-54.6064	-38.2890	-85.4775	
Dehydro- α -Al ₂ O ₃ (001)	-89.7579	-501.5975	-489.9981	
Hydro- α -Al ₂ O ₃ (001)	-56.6472	-97.4252	-98.3861	
Methyl- α -Al ₂ O ₃ (001)	-30.3068	-42.1646	-29.7828	

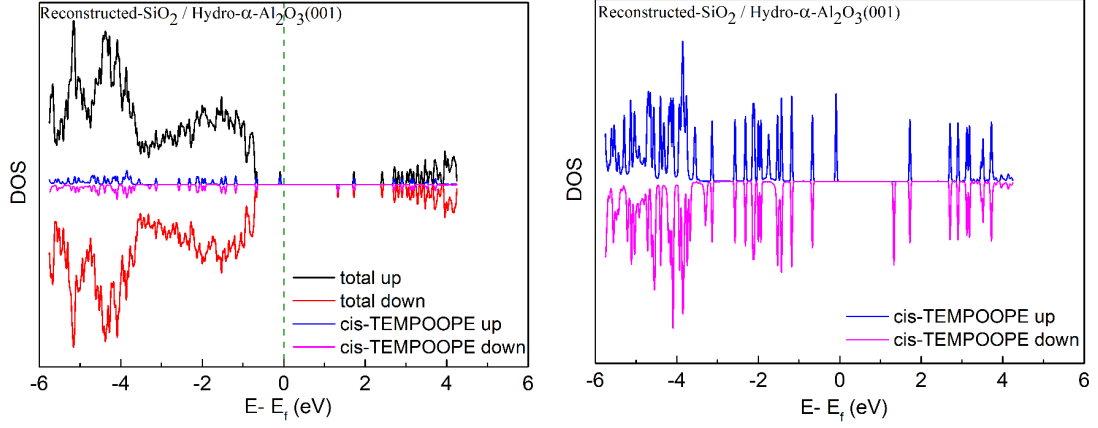


Figure C.17.: The DOS (left) and the PDOS (right) of *cis*-TEMPO-OPE embedded between the reconstructed-SiO₂ and the hydro-α-Al₂O₃ layers based on PBE KS-DFT.

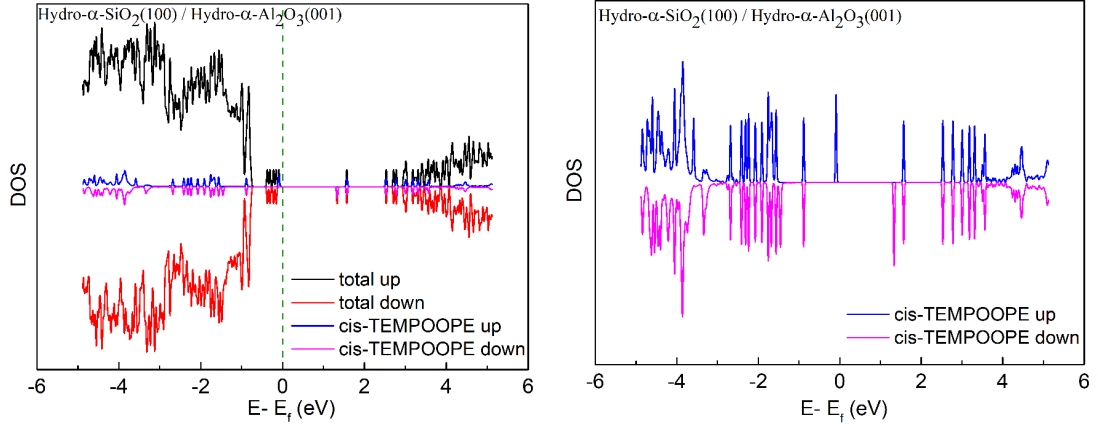


Figure C.18.: The DOS (left) and the PDOS (right) of *cis*-TEMPO-OPE embedded between the hydro-SiO₂ and the hydro-α-Al₂O₃ layers based on PBE KS-DFT.

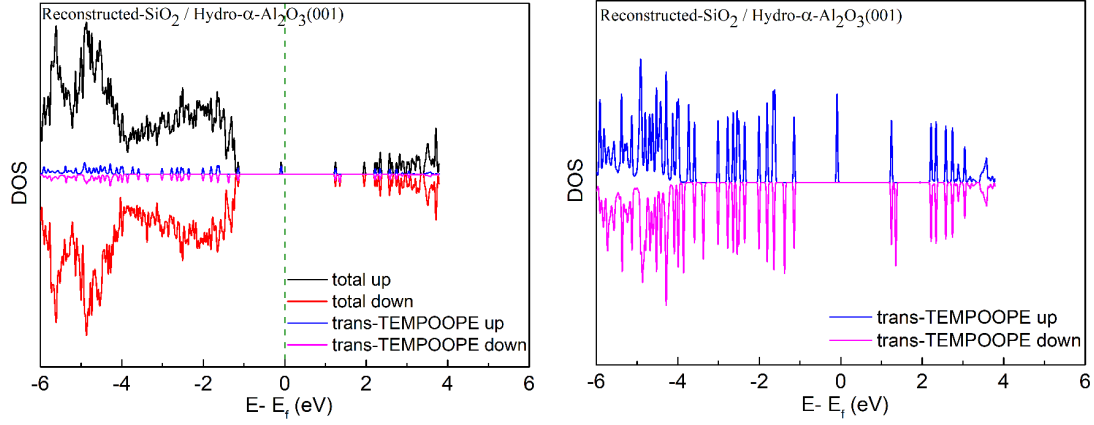


Figure C.19.: The DOS (left) and the PDOS (right) of *trans*-TEMPO–OPE embedded between the reconstructed-SiO₂ and the hydro- α -Al₂O₃ layers based on PBE KS-DFT.

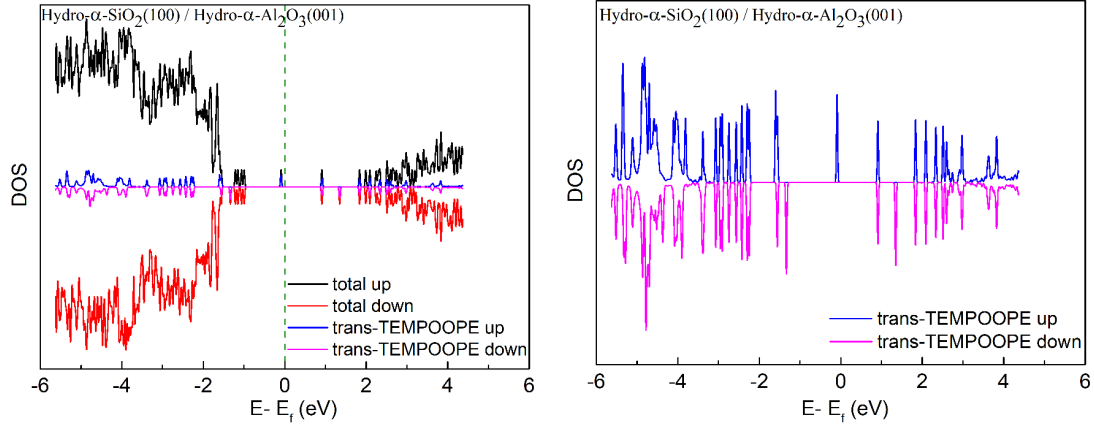


Figure C.20.: The DOS (left) and the PDOS (right) of *trans*-TEMPO–OPE embedded between the hydro-SiO₂ and the hydro- α -Al₂O₃ layers based on PBE KS-DFT.

D. Supporting information for CoDAE

Table D.1.: The bond length of Co and coordinated atoms for the open-form and the closed-form under two temperature points.

Co-X (\AA)	Open(100K)		Closed(100K)		Open(400K)		Closed(380K)	
	N	O	N	O	N	O	N	O
	1.923	1.861	1.938	1.868	2.030	1.880	1.962	1.897
	1.945	1.863	1.944	1.892	2.050	1.900	2.075	1.913
		1.873		1.894		1.905		1.982
		1.885		1.901		1.950		2.001
		1.907				2.020		
		1.920				2.060		
Average	1.934	1.885	1.941	1.889	2.040	1.953	2.019	1.948
σ	0.016	0.024	0.004	0.014	0.014	0.073	0.080	0.051

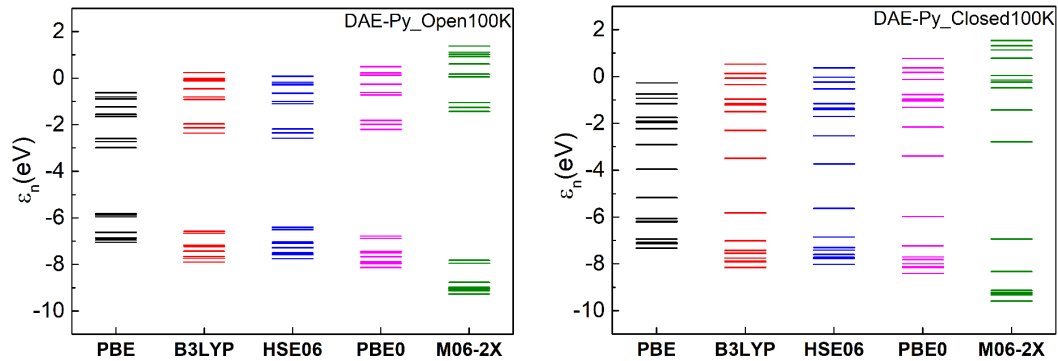


Figure D.1.: Kohn-Sham orbital energy levels calculated by different functionals of DAEpy in the open-form (left) and the closed-form (right) at 100 K.

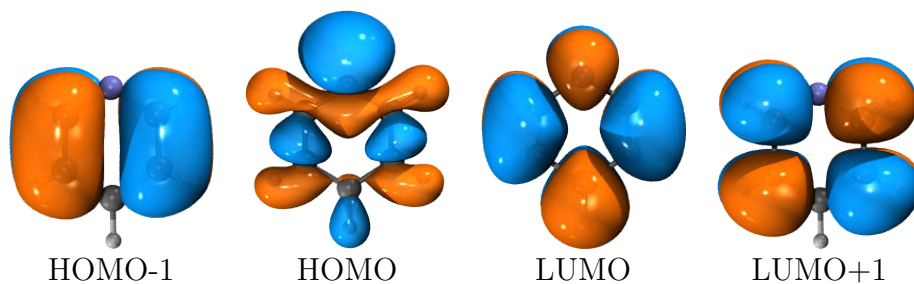


Figure D.2.: The molecular orbital isosurfaces of pyridine based on the B3LYP calculated wavefunctions

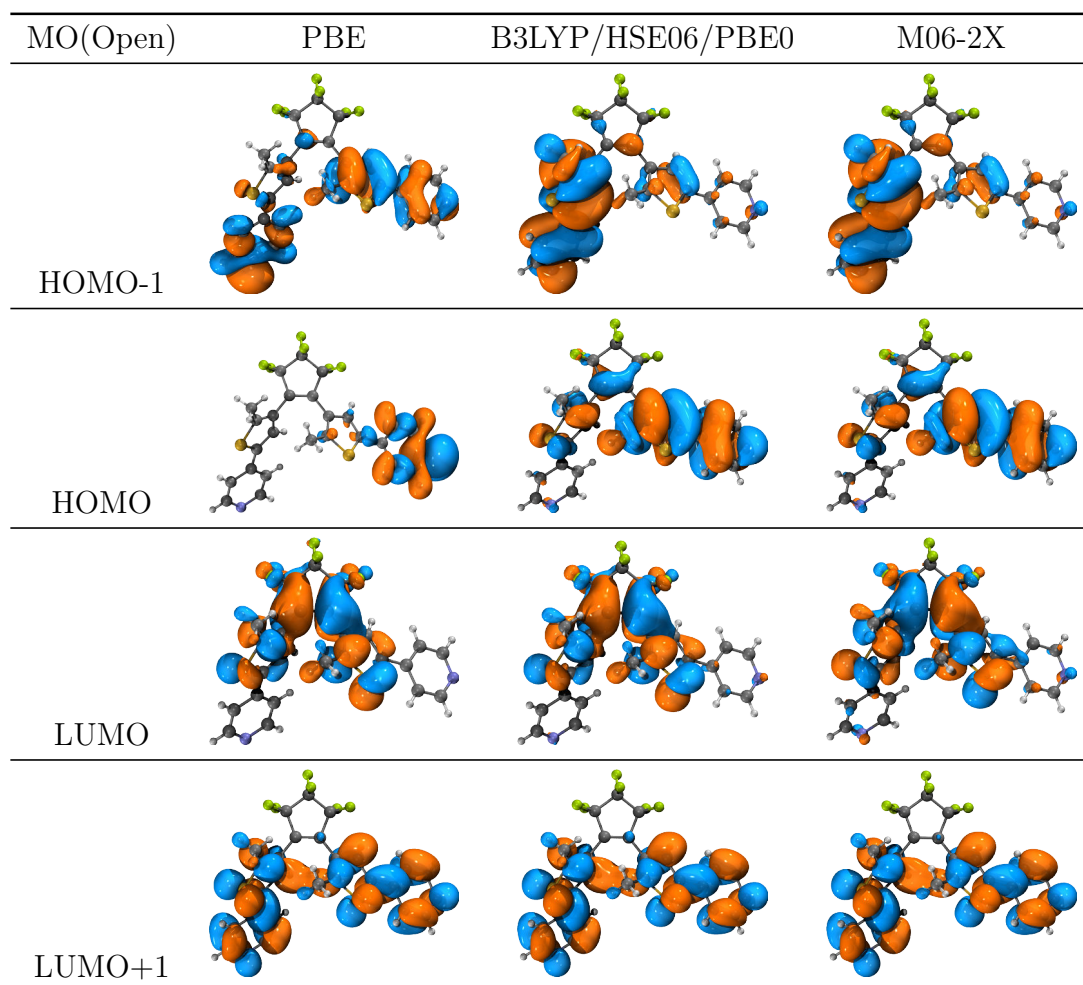


Figure D.3.: The molecular orbital isosurfaces of DAEpy in the 100 K open molecular structure calculated by different functionals

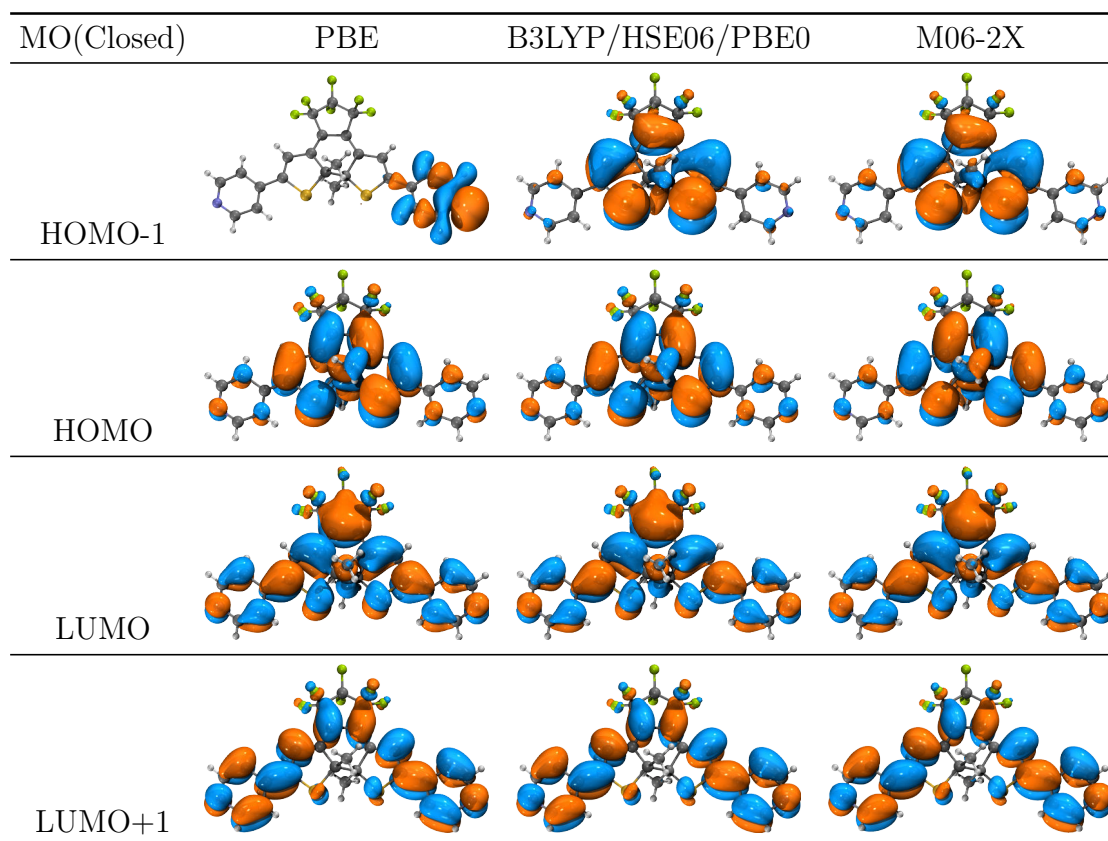


Figure D.4.: The molecular orbital isosurfaces of DAEpy in the 100 K closed molecular structure calculated by different functionals

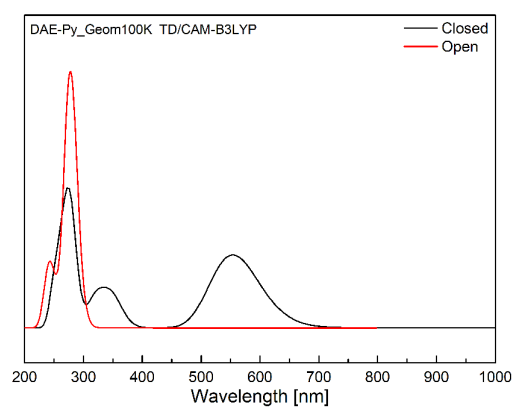


Figure D.5.: The UV-vis spectroscopy of the closed-form and the open-form DAEpy simulated by the TD-DFT under CAM-B3LYP.

Table D.2.: The HOMO, LUMO energy levels, and the gap of DAEpy(F6) and DAEpy(H6) calculated by B3LYP.

	(eV)	HOMO	LUMO	Gap
DAEpy(F6) (Open 100K)		−6.5735	−2.3609	4.2126
DAEpy(F6) (Close 100K)		−5.8192	−3.4929	2.3263
DAEpy(H6) (Open 100K)		−5.9016	−1.7674	4.1342
DAEpy(H6) (Close 100K)		−5.0121	−2.7054	2.3067

Table D.3.: The ionization potential (IP), the electron affinity (EA), the on-site Coulomb repulsion ($U^{(v)}$) of the closed-form and the open-form DAEpy calculated by different functionals.

	DAEpy(Open)			DAEpy(Closed)		
(eV)	IP	EA	$U^{(v)}$	IP	EA	$U^{(v)}$
PBE	7.458	1.256	6.202	6.920	2.363	4.557
TPSSh	7.647	1.047	6.600	6.967	2.282	4.685
B3LYP	7.817	1.089	6.728	7.100	2.319	4.781
HSE06	7.850	1.107	6.743	7.129	2.367	4.762
PBE0	7.908	1.064	6.843	7.141	2.348	4.793
M06-2X	8.374	0.961	7.414	7.435	2.320	5.115

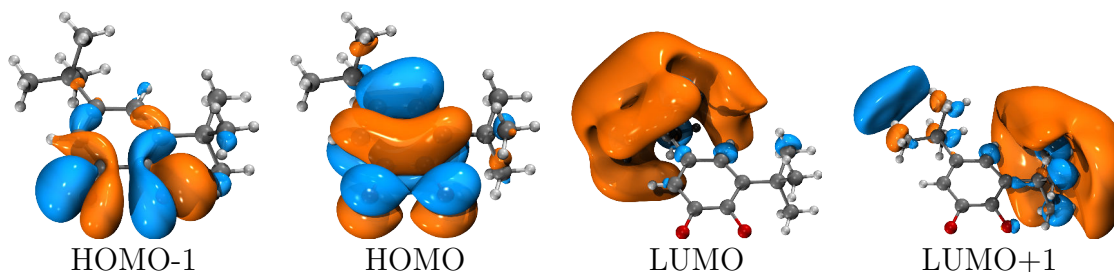


Figure D.6.: The molecular orbital isosurfaces of $L=(Cat^{2-})$.

Table D.4.: The spin density on the cobalt center and the ligands, and the energy difference with respect to the stablest configuration based on PBE KS-DFT.

PBE	<i>ls</i> -geom: Mulliken spin; $E - E_I$				<i>hs</i> -geom: Mulliken spin; $E - E_{VII}$			
Guess	Co	L1	L2	ΔE (eV)	Co	L1	L2	ΔE (eV)
I	0.13	0.43	0.43	0.0000	0.11	0.45	0.45	-0.8044
II				Unconv.	2.79	1.03	1.03	0.0065
III				Unconv.	2.46	0.72	-0.25	0.0129
IV				2.7225	1.30	0.80	0.80	-0.2022
V	0.13	0.43	0.43	0.0000	0.11	0.45	0.45	-0.8043
VI	0.13	0.43	0.43	0.0000	0.11	0.45	0.45	-0.8044
VII				6.6775	2.79	1.04	1.04	0.0000
VIII				Unconv.	2.46	-0.25	0.72	0.0129
IX	0.13	0.43	0.43	0.0000	0.11	0.45	0.45	-0.8044

Table D.5.: The spin density on the cobalt center and the ligands, and the energy difference with respect to the stablest configuration based on M06-L KS-DFT.

M06-L	<i>ls</i> -geom: Mulliken spin; $E - E_I$				<i>hs</i> -geom: Mulliken spin; $E - E_{VII}$			
Guess	Co	L1	L2	ΔE (eV)	Co	L1	L2	ΔE (eV)
I	0.07	0.46	0.46	0.0000	0.04	0.48	0.48	-0.1874
II				Unconv.	2.90	1.00	1.00	0.0906
III	1.88	0.61	0.61	1.4947	2.82	0.79	-0.70	0.1825
IV	1.88	0.61	0.61	1.4947	1.30	0.81	0.81	0.2235
V	0.07	0.46	0.46	0.0000	2.57	-0.80	-0.80	0.4847
VI	0.07	0.46	0.46	0.0000	0.04	0.48	0.48	-0.1874
VII				Unconv.	2.90	0.99	0.99	0.0000
VIII				Unconv.	2.82	-0.70	0.79	0.1825
IX	0.07	0.46	0.46	0.0000	2.57	-0.80	-0.80	0.4869

Table D.6.: The spin density on the cobalt center and the ligands, and the energy difference with respect to the stablest configuration based on TPSSh KS-DFT.

TPSSh	<i>ls</i> -geom: Mulliken spin; $E - E_I$				<i>hs</i> -geom: Mulliken spin; $E - E_{VII}$			
Guess	Co	L1	L2	ΔE (eV)	Co	L1	L2	ΔE (eV)
I	0.07	0.47	0.47	0.0000	0.04	0.48	0.48	-0.1597
II	2.86	1.01	1.01	1.9825	2.83	1.04	1.04	0.0079
III	1.85	0.63	0.63	1.5330	2.76	0.97	-0.80	0.0986
IV	1.85	0.63	0.63	1.5330	1.24	0.85	0.85	0.1422
V	0.07	0.47	0.47	0.0000	1.97	-0.45	-0.47	0.7912
VI	0.07	0.47	0.47	0.0000	-0.66	0.84	0.84	1.0670
VII	2.87	1.00	1.00	1.9636	2.84	1.03	1.03	0.0000
VIII	1.85	0.63	0.63	1.5330	2.76	-0.80	-0.80	0.0986
IX				1.6230	2.61	-0.83	-0.83	0.2746

Table D.7.: The spin density on the cobalt center and the ligands, and the energy difference with respect to the stablest configuration based on B3LYP* KS-DFT.

B3LYP*	<i>ls</i> -geom: Mulliken spin; $E - E_I$				<i>hs</i> -geom: Mulliken spin; $E - E_{VII}$			
Guess	Co	L1	L2	ΔE (eV)	Co	L1	L2	ΔE (eV)
I	0.06	0.47	0.47	0.0000	0.02	0.49	0.49	-0.1433
II	2.84	1.01	1.01	1.9392	2.80	1.04	1.04	0.0095
III	1.27	0.89	0.89	1.5193	2.74	0.98	-0.81	0.1141
IV	1.33	0.79	0.79	1.3129	1.18	0.87	0.87	0.1321
V	0.06	0.47	0.47	0.0000	1.82	-0.36	-0.36	0.7716
VI	0.06	0.47	0.47	0.0000	-0.73	0.88	0.88	1.1725
VII	2.85	1.00	1.00	1.9252	2.81	1.04	1.04	0.0000
VIII	1.81	0.65	0.65	1.4877	2.74	-0.81	0.98	0.1141
IX				1.5986	2.60	-0.83	-0.83	0.3043

Table D.8.: The spin density on the cobalt center and the ligands, and the energy difference with respect to the stablest configuration based on B3LYP KS-DFT.

B3LYP	<i>ls</i> -geom: Mulliken spin; $E - E_I$				<i>hs</i> -geom: Mulliken spin; $E - E_{VII}$			
Guess	Co	L1	L2	ΔE (eV)	Co	L1	L2	ΔE (eV)
I	0.04	0.48	0.48	0.0000	0.01	0.50	0.50	0.1377
II	2.86	1.01	1.01	1.7208	2.81	1.05	1.05	0.0069
III	1.81	0.64	0.64	1.4160	2.76	1.00	-0.84	0.1084
IV	1.81	0.64	0.64	1.4160	1.10	0.92	0.92	0.2643
V	0.04	0.48	0.48	0.0000	1.87	-0.38	-0.38	0.9816
VI	0.04	0.48	0.48	0.0000	-0.94	1.02	1.02	1.2407
VII	2.86	1.00	1.00	1.7055	2.81	1.05	1.05	0.0000
VIII				Unconv.	2.76	-0.84	1.00	0.1084
IX	1.73	-0.33	-0.33	1.5266	2.65	-0.86	-0.86	0.2609

Table D.9.: The spin density on the cobalt center and the ligands, and the energy difference with respect to the stablest configuration based on HSE06 KS-DFT.

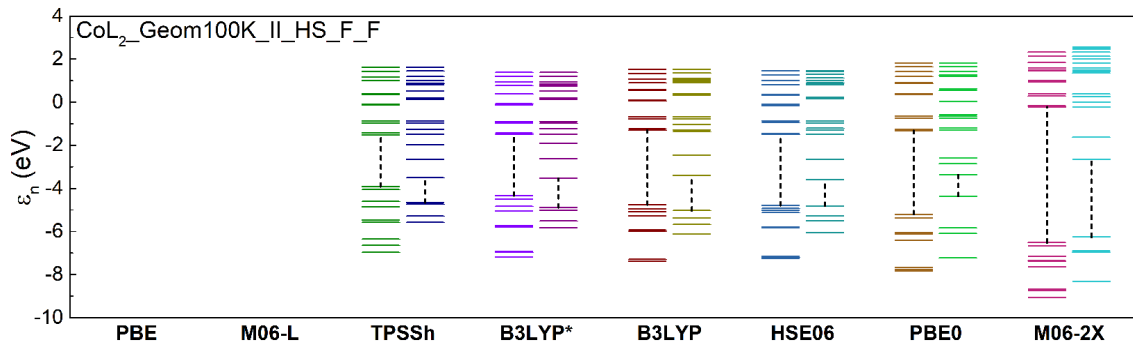
HSE06	<i>ls</i> -geom: Mulliken spin; $E - E_I$				<i>hs</i> -geom: Mulliken spin; $E - E_{VII}$			
Guess	Co	L1	L2	ΔE (eV)	Co	L1	L2	ΔE (eV)
I	0.03	0.49	0.49	0.0000	0.00	0.50	0.50	0.5094
II	2.91	0.99	0.99	1.3996	2.83	1.05	1.05	0.0048
III	1.85	0.63	0.63	1.2526	2.79	1.01	-0.86	0.1048
IV	1.85	0.63	0.63	1.2526	1.07	0.95	0.95	0.4470
V	0.03	0.49	0.49	0.0000	2.68	-0.87	-0.87	0.3255
VI	0.03	0.49	0.49	0.0000				Unconv.
VII	2.91	0.99	0.99	1.3812	2.84	1.04	1.04	0.0000
VIII				Unconv.	2.79	-0.86	1.01	0.1048
IX	1.81	0.37	-0.37	1.3629	2.70	-0.88	-0.88	0.2388

Table D.10.: The spin density on the cobalt center and the ligands, and the energy difference with respect to the stablest configuration based on PBE0 KS-DFT.

PBE0	<i>ls</i> -geom: Mulliken spin; $E - E_I$				<i>hs</i> -geom: Mulliken spin; $E - E_{VII}$			
Guess	Co	L1	L2	ΔE (eV)	Co	L1	L2	ΔE (eV)
I	0.03	0.49	0.49	0.0000	0.00	0.50	0.50	0.6072
II	2.83	0.87	-0.79	1.3060	2.83	1.05	1.05	0.0044
III	2.90	0.99	0.99	1.4702	2.79	1.02	-0.86	0.1048
IV	1.86	0.63	0.63	1.2285	1.06	0.96	0.96	0.4819
V	1.83	-0.36	-0.36	1.3275	1.97	-0.43	-0.43	1.2410
VI	0.03	0.49	0.49	0.0000	-0.99	1.04	1.04	1.3070
VII	3.18	0.82	0.82	1.8110	2.83	1.05	1.05	0.0000
VIII				Unconv.	2.79	-0.86	1.02	0.1048
IX	1.82	-0.37	-0.37	1.3448	2.70	-0.88	-0.88	0.2358

Table D.11.: The spin density on the cobalt center and the ligands, and the energy difference with respect to the stablest configuration based on M06-2X KS-DFT.

M06-2X	<i>ls</i> -geom: Mulliken spin; $E - E_I$				<i>hs</i> -geom: Mulliken spin; $E - E_{VII}$			
Guess	Co	L1	L2	ΔE (eV)	Co	L1	L2	ΔE (eV)
I	-0.01	0.51	0.51	0.0000	-0.02	0.51	0.51	1.5174
II	2.90	1.00	1.00	0.6074	2.82	1.06	1.06	0.0019
III	2.80	0.97	-0.87	0.7597	2.79	1.05	-0.91	0.0768
IV	0.93	0.98	0.98	5.2711	0.94	1.01	1.01	0.7264
V	0.86	-0.95	0.98	5.3084	1.96	-0.43	-0.43	1.8767
VI	-0.79	0.96	0.96	5.3693	-0.99	1.04	1.04	1.7465
VII	2.90	1.00	1.00	0.6074	2.82	1.05	1.05	0.0000
VIII	2.80	-0.87	0.97	0.7635	2.79	-0.91	1.05	0.0768
IX	2.75	-0.93	-0.93	2.9920	2.75	-0.92	-0.92	0.1563


Figure D.7.: Kohn-Sham orbital energy levels of the *high-spin* configuration calculated by different functionals of CoL_2 based on the the *low-spin* molecular structure (100K).

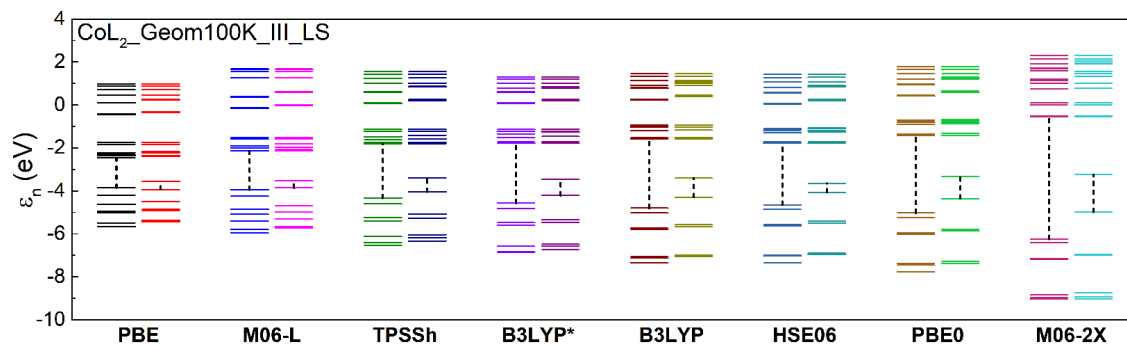


Figure D.8.: Kohn–Sham orbital energy levels of the *low-spin* configuration calculated by different functionals of CoL₂ based on the the *low-spin* molecular structure (100K).

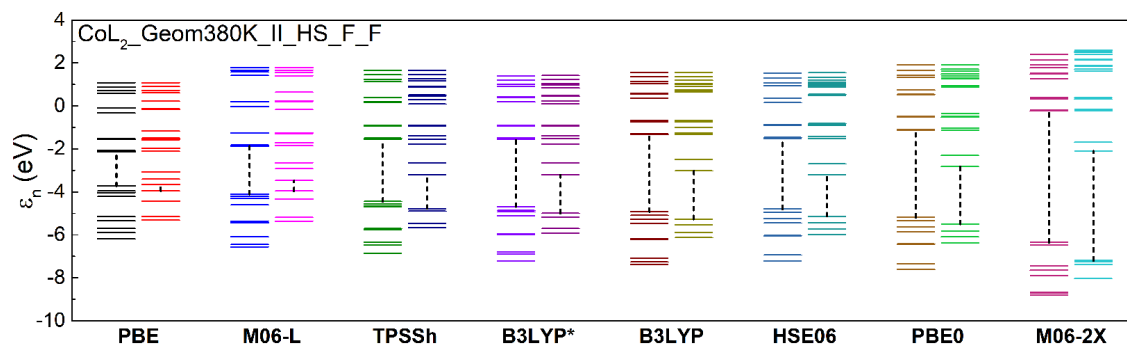


Figure D.9.: Kohn–Sham orbital energy levels of the *high-spin* configuration calculated by different functionals of CoL₂ based on the the *high-spin* molecular structure (380K).

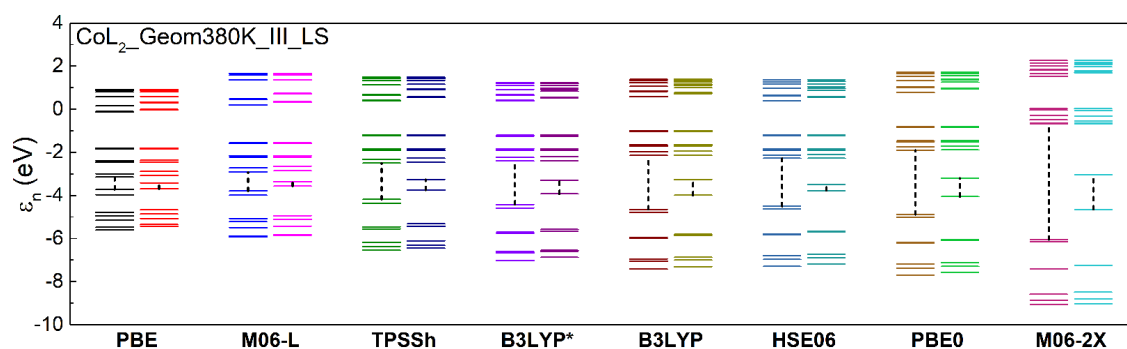


Figure D.10.: Kohn–Sham orbital energy levels of the *low-spin* configuration calculated by different functionals of CoL₂ based on the the *high-spin* molecular structure (380K).

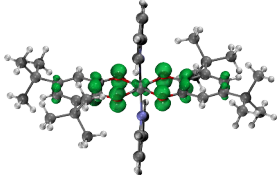
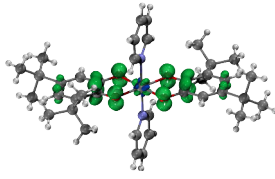
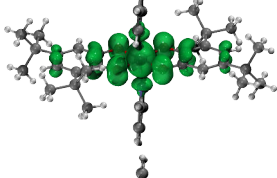
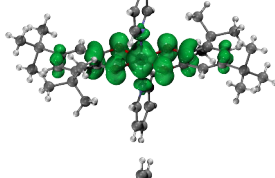
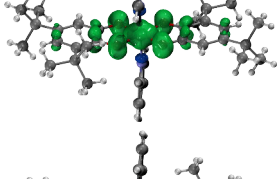
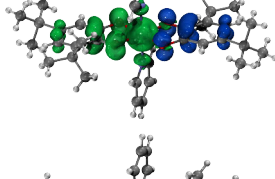
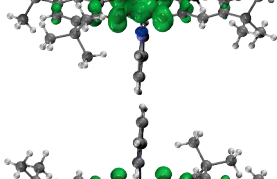
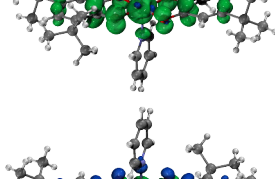
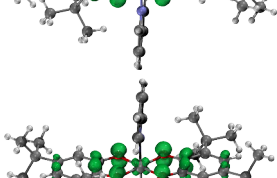
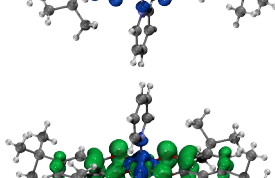
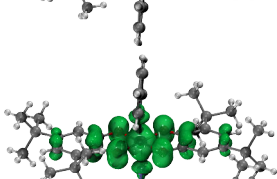
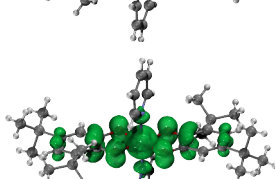
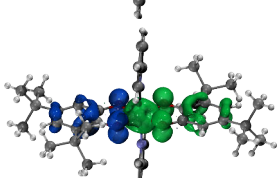
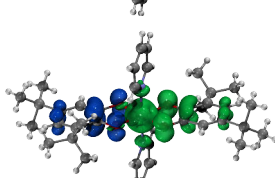
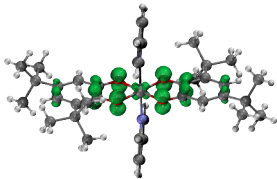
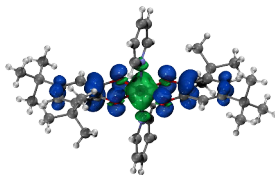
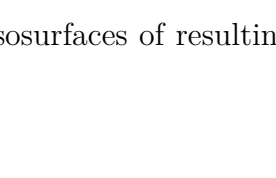
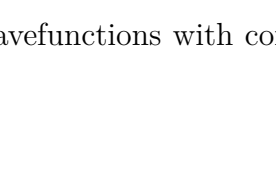
Guess	<i>ls</i> -geom(100K)	<i>hs</i> -geom(380K)
I(LS) $ls\text{-Co}^{\text{III}}(\text{Cat}^{2-})(\text{SQ}^-)$		
II $hs\text{-Co}^{\text{III}}(\text{Cat}^{2-})(\text{SQ}^-)_{\text{FM}}$		
III $hs\text{-Co}^{\text{III}}(\text{Cat}^{2-})(\text{SQ}^-)_{\text{AFM}}$		
IV $ls\text{-Co}^{\text{II}}(\text{SQ}^-)_{\text{FM}}(\text{SQ}^-)_{\text{FM}}$		
V $ls\text{-Co}^{\text{II}}(\text{SQ}^-)_{\text{FM}}(\text{SQ}^-)_{\text{AFM}}$		
VI $ls\text{-Co}^{\text{II}}(\text{SQ}^-)_{\text{AFM}}(\text{SQ}^-)_{\text{AFM}}$		
VII(HS) $hs\text{-Co}^{\text{II}}(\text{SQ}^-)_{\text{FM}}(\text{SQ}^-)_{\text{FM}}$		
VIII $hs\text{-Co}^{\text{II}}(\text{SQ}^-)_{\text{AFM}}(\text{SQ}^-)_{\text{FM}}$		
IX $hs\text{-Co}^{\text{II}}(\text{SQ}^-)_{\text{AFM}}(\text{SQ}^-)_{\text{AFM}}$		

Figure D.11.: The spin density isosurfaces of resulting wavefunctions with corresponding initial guesses.

	Coordinate Structures	Spin desity
Open(Co1 Asymm)		
Open(Co2 Symm)		
Closed(Co1 Symm)		
Closed(Co2 Symm)		

Figure D.12.: The spin density isosurfaces of the *low-spin* wavefunctions of $ls\text{-Co}^{\text{III}}(\text{Cat}^{2-})(\text{SQ}^-)$ in the 100 K molecular structures calculated by B3LYP KS-DFT.

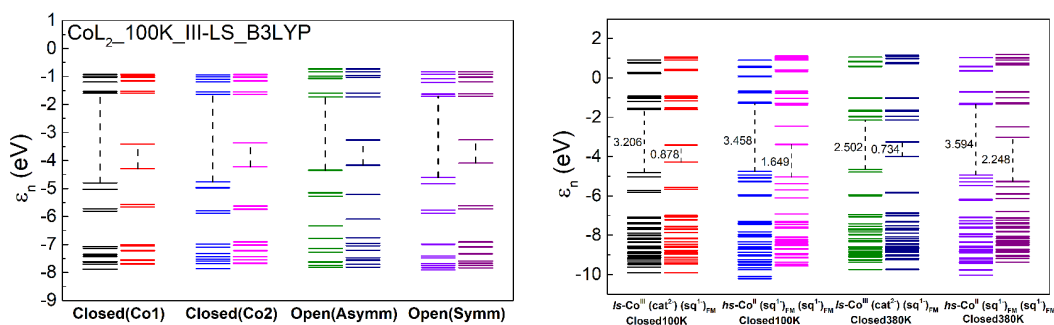


Figure D.13.: Kohn–Sham orbital energy levels of the stable *low-spin* configuration $ls\text{-Co}^{\text{III}}(\text{Cat}^{2-})(\text{SQ}^-)$ in the 100 K molecular structures calculated by B3LYP (left). The energy levels of the stable *low/high-spin* configuration in the 100 K/380 K closed molecular structures calculated by B3LYP KS-DFT (right).

Table D.12.: The energy difference of the positive one charged CoL_2 in the *low-spin* (100K) closed molecular structure started from the possible initial guesses with reference to the stablest configuration, $E - E_{\text{GS}}$ (eV).

Guess	PBE	BP86	TPSS	M06-L	TPSSh	B3LYP	HSE06	PBE0	M06-2X
I ⁺	0.0962	0.0942	0.0675	0.0463	0.0276	0.0158	0.0132	0.0122	0.0053
II ⁺	0.0000	0.0000	0.0000	0.0000	0.0000	0.0000	0.0000	0.0000	0.0000
III ⁺	2.7249	2.8288	2.7686	2.0998	2.4334	2.2199	1.8773	1.8235	-3.8727
IV ⁺	1.6046	1.6424	1.6152	1.4785	1.4725	2.2345	2.0218	1.9683	-3.7817
V ⁺	0.0962	0.0942	0.0675	0.0463	0.0276	2.1484	2.1775	2.1217	-3.6719
VI ⁺	1.6046	1.6424	1.6151	1.5264	1.4725	1.3688	1.8965	1.8458	-3.8732
VII ⁺	0.0962	0.0942	0.0675	0.0463	0.0276	1.4087	1.2401	1.2165	-3.9087

Table D.13.: The energy difference of the positive one charged CoL_2 in the *high-spin* (380K) closed molecular structure started from the possible initial guesses with reference to the stablest configuration, $E - E_{\text{GS}}$ (eV).

Guess	PBE	BP86	TPSS	M06-L	TPSSh	B3LYP	HSE06	PBE0	M06-2X
I ⁺	0.0441	0.0430	0.0280	0.0182	0.0093	0.0052	0.0026	0.0020	Unconv.
II ⁺	0.0000	0.0000	0.0000	0.0000	0.0000	0.0000	0.0000	0.0000	0.0000
III ⁺	1.4881	1.5912	1.5332	0.9732	1.1817	0.9795	0.6025	0.5417	-5.0653
IV ⁺	0.9132	0.9608	Unconv.	0.8517	Unconv.	0.7986	0.4753	0.4241	-3.3880
V ⁺	0.0441	0.0430	0.0280	0.0182	0.0093	0.6533	0.3512	0.3124	-4.9086
VI ⁺	0.9132	Unconv.	Unconv.	Unconv.	0.7625	0.7986	0.5488	0.4241	Unconv.
VII ⁺	0.0441	0.0430	0.0280	0.6798	0.8061	0.6433	0.3394	0.2992	Unconv.

Table D.14.: The energy difference of the negative one charged CoL_2 in the *low-spin* (100K) closed molecular structure started from the possible initial guesses with reference to the stablest configuration, $E - E_{\text{GS}}$ (eV).

Guess	PBE	BP86	TPSS	M06-L	TPSSh	B3LYP	HSE06	PBE0	M06-2X
I ⁻	0.0000	0.0000	0.0000	0.0000	0.0000	0.0000	0.0000	0.0000	0.0000
II ⁻	2.1168	2.2061	2.1451	1.6170	1.8207	1.6745	1.3653	1.3251	-4.3751
III ⁻	Unconv.	1.1273	1.1590	1.1484	1.1171	Unconv.	0.9853	Unconv.	0.8518
IV ⁻	0.0000	0.0000	0.0000	0.0000	0.0000	0.0000	0.0000	0.0000	1.0577
V ⁻	2.1168	2.2061	2.1393	1.6170	1.8207	1.6745	1.3653	1.3251	-4.3751
VI ⁻	1.1041	1.1273	1.1590	1.1484	1.1171	1.1008	0.9853	1.2335	Unconv.

Table D.15.: The energy difference of the negative one charged CoL_2 in the *high-spin* (380K) closed molecular structure started from the possible initial guesses with reference to the stablest configuration, $E - E_{\text{GS}}$ (eV).

Guess	PBE	BP86	TPSS	M06-L	TPSSh	B3LYP	HSE06	PBE0	M06-2X
I ⁻	0.0000	0.0000	0.0000	0.0000	0.0000	0.0000	0.0000	0.0000	0.0000
II ⁻	0.5414	0.6299	0.5403	0.0464	0.1990	0.0624	-0.2512	-0.2776	-2.6481
III ⁻	0.2877	0.3118	0.3056	0.2352	0.4923	Unconv.	0.0638	Unconv.	-1.8075
IV ⁻	0.0000	0.0000	0.0000	0.0000	0.0000	Unconv.	Unconv.	0.0000	Unconv.
V ⁻	0.5414	0.6299	0.5403	0.0464	0.1990	0.0624	Unconv.	-0.2776	-4.4365
VI ⁻	0.2877	0.3118	0.3056	0.2352	0.4807	Unconv.	0.0484	0.0399	-2.4288

Table D.16.: The results of the converged configurations for the negative one charged CoL_2 in the *low-spin* (100 K) closed molecular structures by possible initial guesses.

Initial Guess	Result
I ⁻ : $ls\text{-Co}^{\text{III}}(\text{Cat}^{2-})(\text{Cat}^{2-})$	I ⁻ : $ls\text{-Co}^{\text{III}}(\text{Cat}^{2-})(\text{Cat}^{2-})$
II ⁻ : $hs\text{-Co}^{\text{III}}(\text{Cat}^{2-})(\text{Cat}^{2-})$	III ⁻ : $ls\text{-Co}^{\text{II}}(\text{Cat}^{2-})(\text{SQ}^-)_{\text{FM}}$
III ⁻ : $ls\text{-Co}^{\text{II}}(\text{Cat}^{2-})(\text{SQ}^-)_{\text{FM}}$	III ⁻ : $ls\text{-Co}^{\text{II}}(\text{Cat}^{2-})(\text{SQ}^-)_{\text{FM}}$
IV ⁻ : $ls\text{-Co}^{\text{II}}(\text{Cat}^{2-})(\text{SQ}^-)_{\text{AFM}}$	I ⁻ : $ls\text{-Co}^{\text{III}}(\text{Cat}^{2-})(\text{Cat}^{2-})$
V ⁻ : $hs\text{-Co}^{\text{II}}(\text{Cat}^{2-})(\text{SQ}^-)_{\text{FM}}$	III ⁻ : $ls\text{-Co}^{\text{II}}(\text{Cat}^{2-})(\text{SQ}^-)_{\text{FM}}$
VI ⁻ : $hs\text{-Co}^{\text{II}}(\text{Cat}^{2-})(\text{SQ}^-)_{\text{AFM}}$	III ⁻ : $ls\text{-Co}^{\text{II}}(\text{Cat}^{2-})(\text{SQ}^-)_{\text{FM}}$

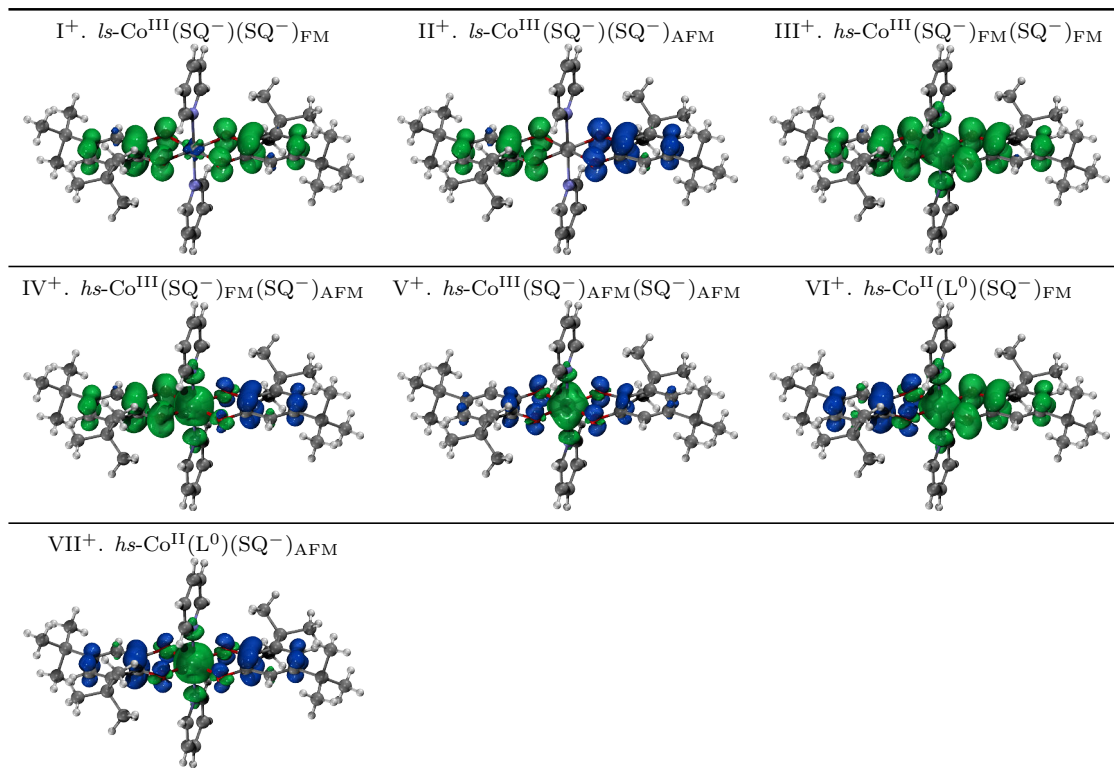


Figure D.14.: The resulting spin density isosurfaces of the converged wavefunctions of the positive one charged CoL_2 in the *high-spin* (380 K) closed molecular structures.

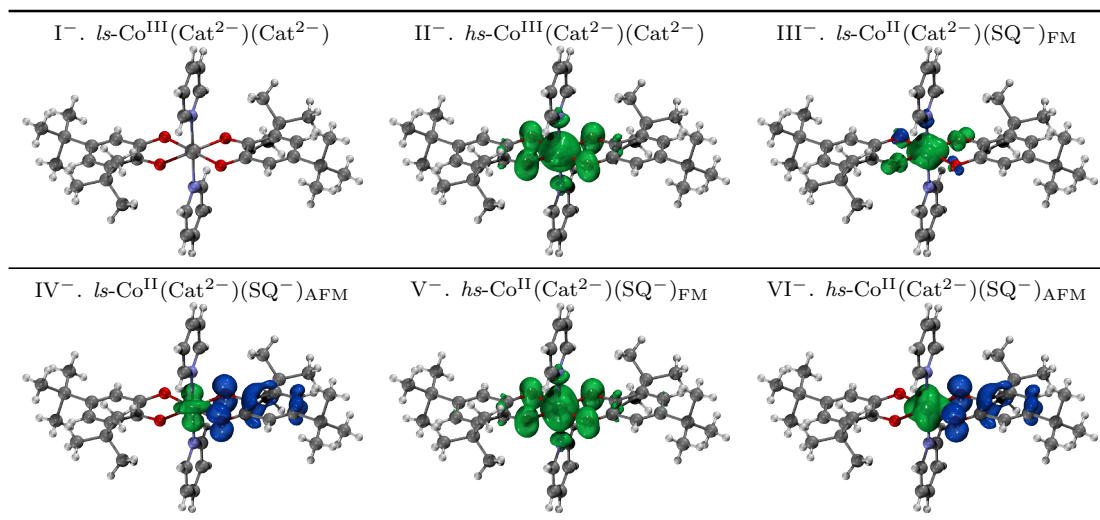


Figure D.15.: The resulting spin density isosurfaces of the converged wavefunctions of the negative one charged CoL_2 in the *high-spin* (380 K) closed molecular structures.

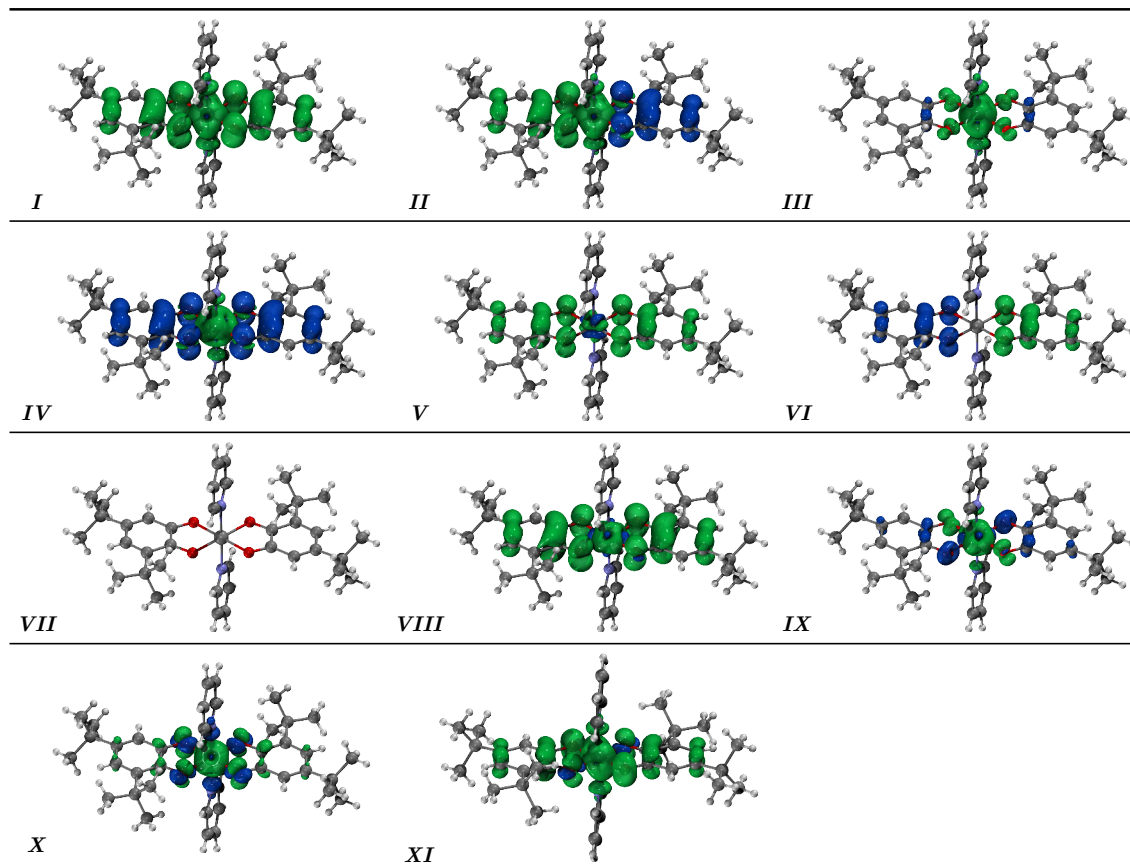


Figure D.16.: The resulting spin density isosurfaces of CoL_2 started from possible initial guesses by PBE+U ($U = 6$ eV).

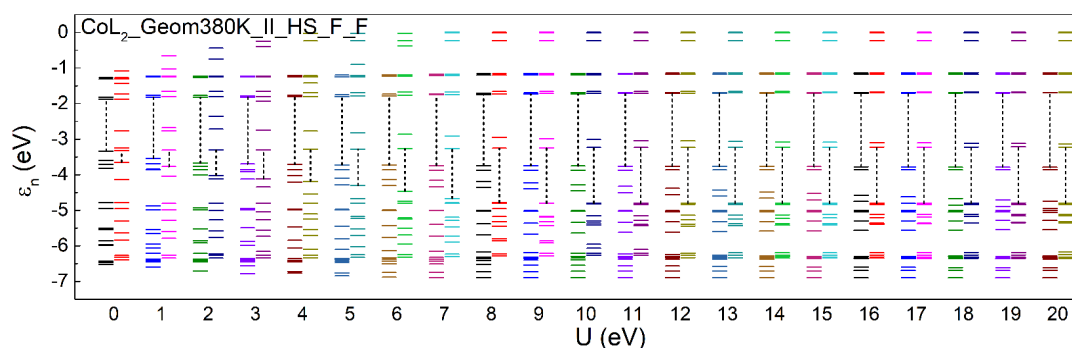


Figure D.17.: The orbital energy levels versus Hubbard U of the *high-spin* configuration $hs\text{-Co}^{\text{II}}(\text{SQ}^-)_{\text{FM}}(\text{SQ}^-)_{\text{FM}}$ in the the *high-spin* (380 K) molecular structure.

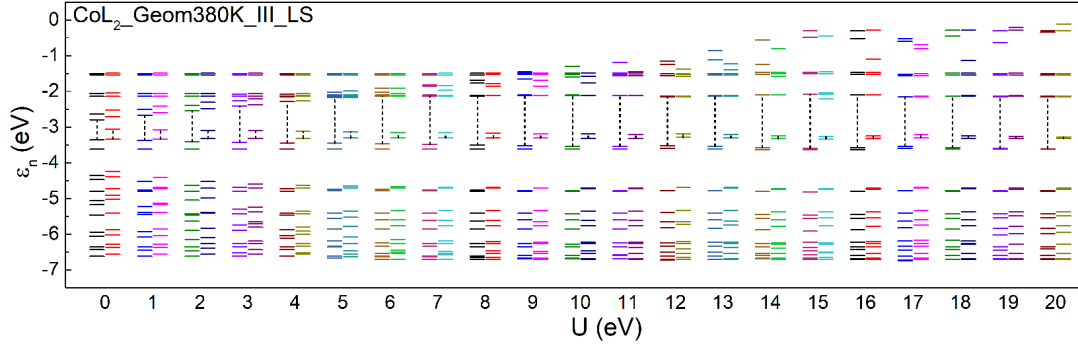


Figure D.18.: The orbital energy levels versus Hubbard U of the *low-spin* configuration $ls\text{-Co}^{\text{III}}(\text{Cat}^{2-})(\text{SQ}^-)$ in the the *high-spin* (380 K) molecular structure.

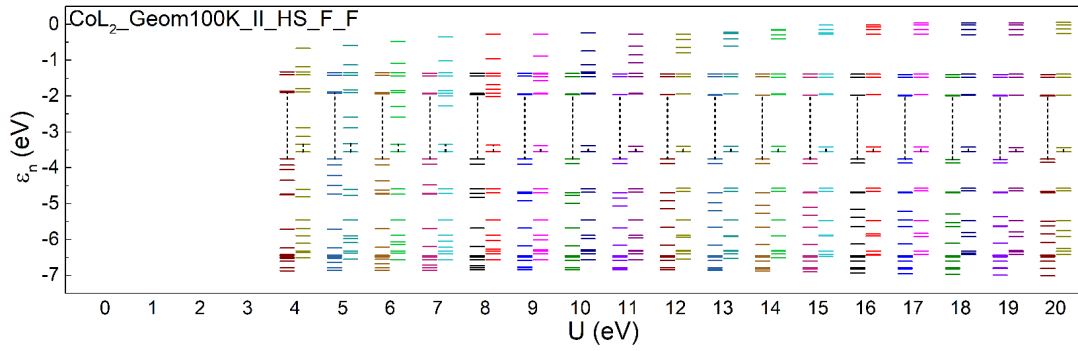


Figure D.19.: The orbital energy levels versus Hubbard U of the *high-spin* configuration $hs\text{-Co}^{\text{II}}(\text{SQ}^-)_{\text{FM}}(\text{SQ}^-)_{\text{FM}}$ in the the *low-spin* (100 K) molecular structure.

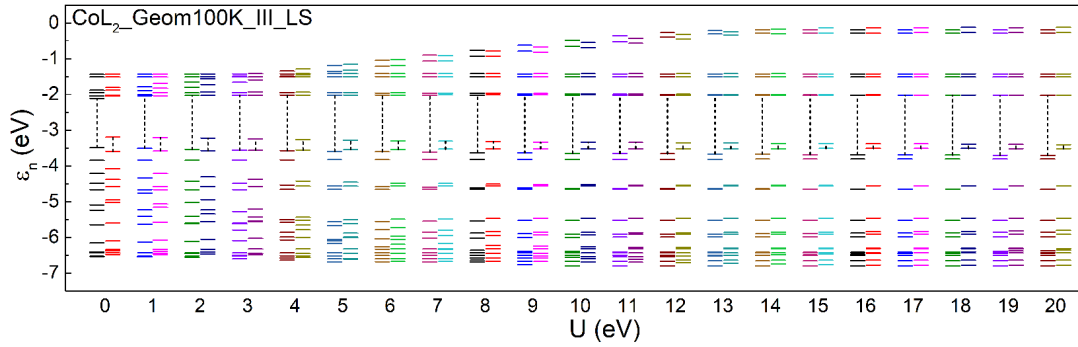


Figure D.20.: The orbital energy levels versus Hubbard U of the *low-spin* configuration $ls\text{-Co}^{\text{III}}(\text{Cat}^{2-})(\text{SQ}^-)$ in the the *low-spin* (100 K) molecular structure.

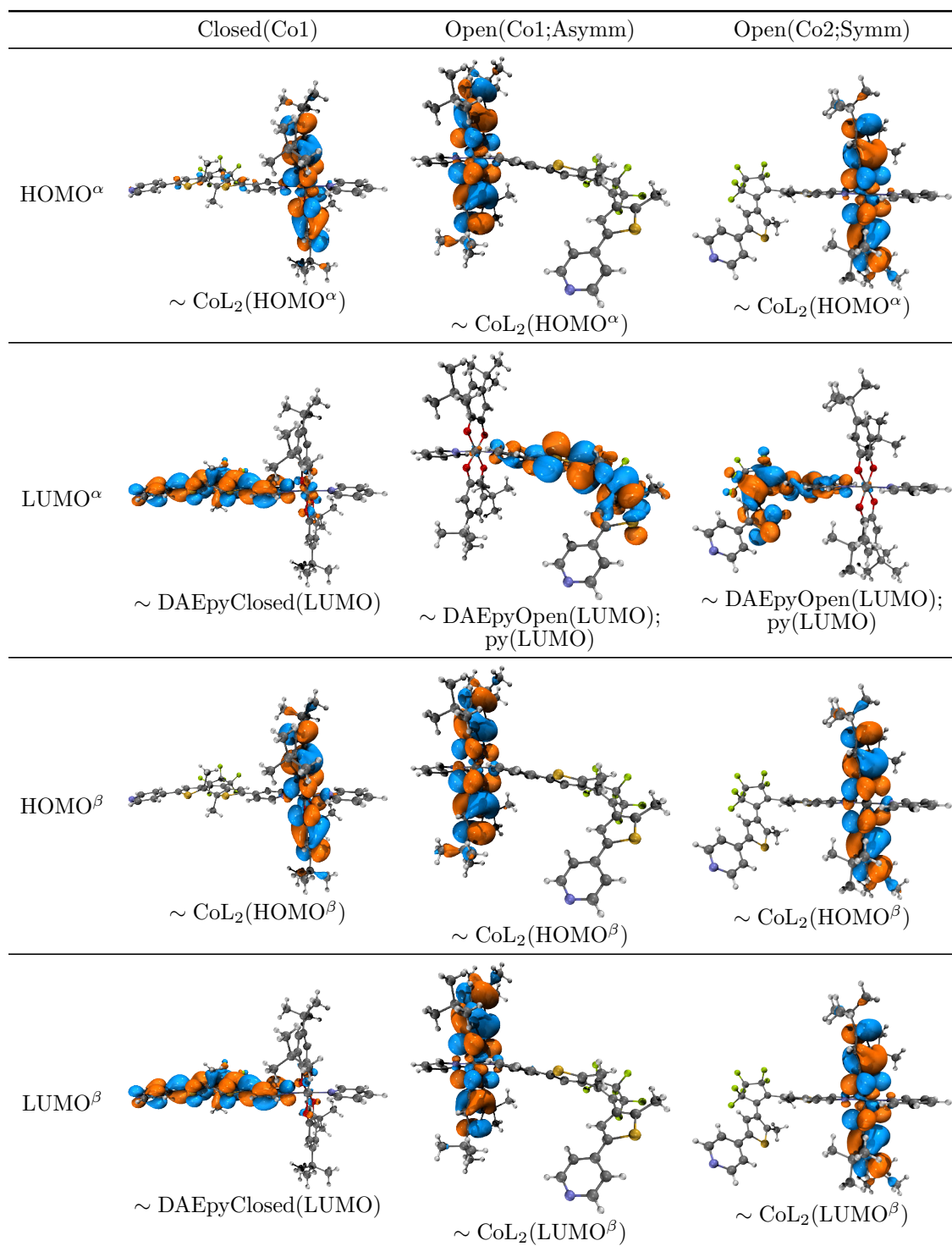


Figure D.21.: The molecular orbital isosurfaces of the *low-spin* CoL₂DAEpy complexes in low temperature molecular structures (100 K) based on PBE KS-DFT.

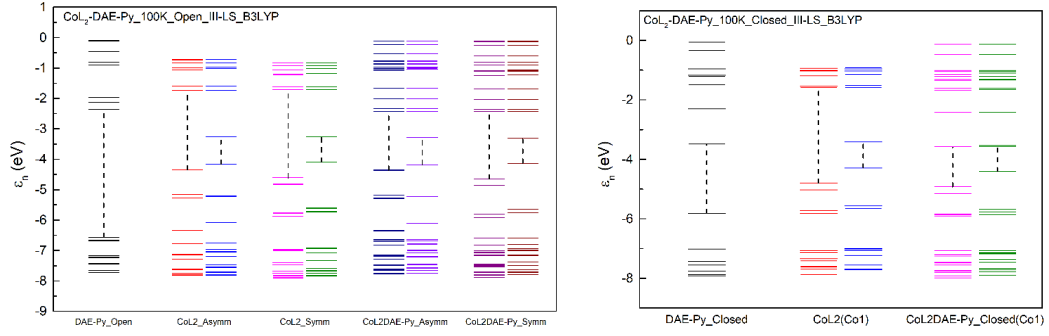


Figure D.22.: Kohn–Sham orbital energy levels of the *low-spin* configuration for the CoL₂DAEpy complex by B3LYP in the low temperature (100 K) open molecular structure (left) and the closed molecular structure (right).

Table D.17.: The HOMO–LUMO gaps of the CoL₂DAEpy complexes in the *low-spin* (100 K) molecular structure based on the different functionals.

Gap (eV)	Closed(Co1)		Open(Co1;Asymm)		Open(Co2;Symm)	
Functionl	α	β	α	β	α	β
PBE	0.1091	0.2016	0.7023	0.3429	0.7170	0.3532
BP86	0.1102	0.1992	0.7070	0.3374	0.7219	0.3483
TPSS	0.1260	0.1322	0.8136	0.3323	0.8180	0.3467
M06-L	0.1989	0.1039	0.9897	0.2868	0.9627	0.3069
TPSSh	0.7214	0.4278	1.5606	0.5886	1.4550	0.6240
B3PW91	1.3176	0.7989	2.2041	0.8359	1.9200	0.9129
B3LYP	1.3377	0.8237	2.2096	0.8264	1.9282	0.8991
CAM-B3LYP	3.7922	2.2006	4.7228	2.1051	4.1424	3.1250
HSE03	0.9652	0.3733	1.8523	0.3916	1.5072	0.4781
HSE06	0.9434	0.3616	1.8297	0.3842	1.4966	0.4672
PBE0	1.6656	0.9938	2.5799	0.9581	2.1481	1.1002
M06-2X	3.4703	1.7418	4.2567	1.6803	3.7688	2.6341

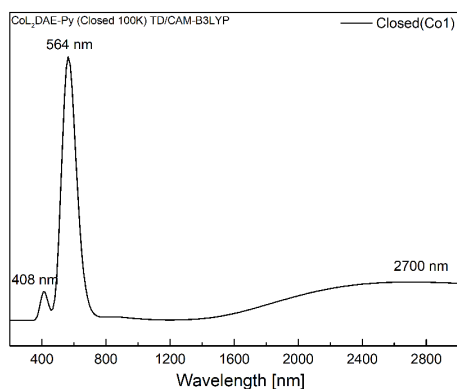


Figure D.23.: The UV-vis spectroscopy of the *low-spin* CoL₂DAEpy complex in the low temperature (100 K) closed (Co1) molecular structure simulated by CAM-B3LYP TD-DFT.

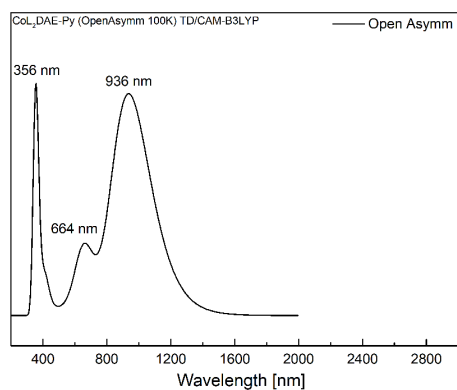


Figure D.24.: The UV-vis spectroscopy of the *low-spin* CoL₂DAEpy complex in the low temperature (100 K) open (Co1;Asymm) molecular structure simulated by CAM-B3LYP TD-DFT.

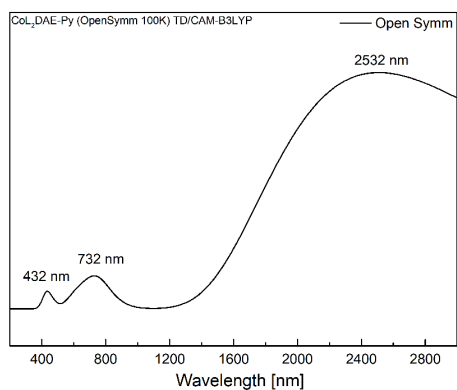


Figure D.25.: The UV-vis spectroscopy of the *low-spin* CoL₂DAEpy complex in the low temperature (100 K) open (Co2;Symm) molecular structure simulated by CAM-B3LYP TD-DFT.

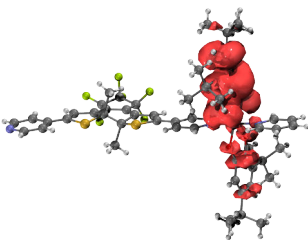
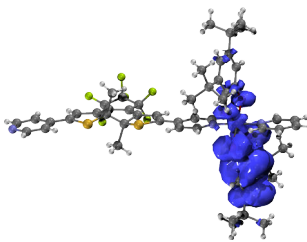
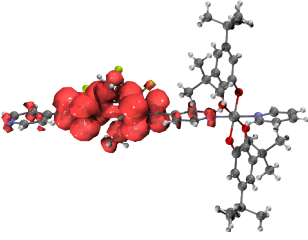
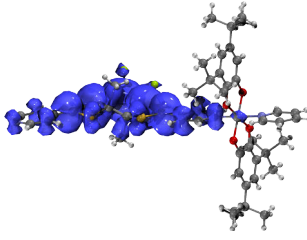
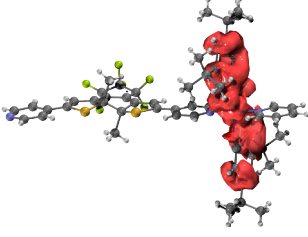
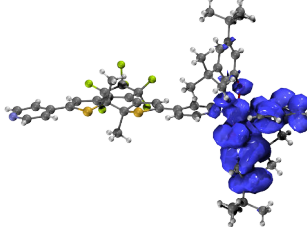
Excited State Info.		Hole	Electron
E.S.	1		
E (eV)	0.4592		
λ (nm)	2699.99		
f	0.0553		
$\langle S^2 \rangle$	0.770		
E.S.	16		
E (eV)	2.1982		
λ (nm)	564.03		
f	0.3728		
$\langle S^2 \rangle$	0.767		
E.S.	30		
E (eV)	3.0124		
λ (nm)	411.59		
f	0.0290		
$\langle S^2 \rangle$	1.031		

Figure D.26.: The information of the excited states and the corresponding hole-electron distributions of the *low-spin* CoL₂DAEpy complex (100 K) in the closed (Co1) molecular structure. $\langle S^2 \rangle$ indicates the multiplicity of the excitation: singlet = 0.0; doublet = 0.75; triplet = 2.0

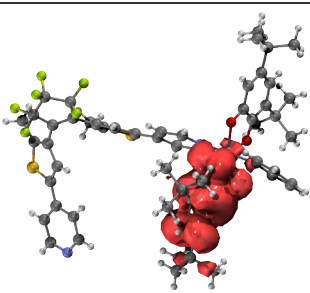
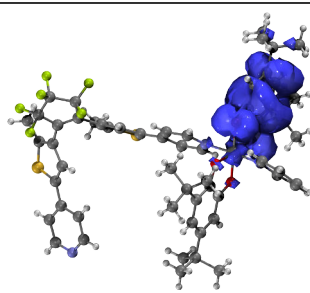
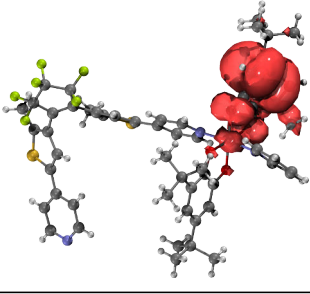
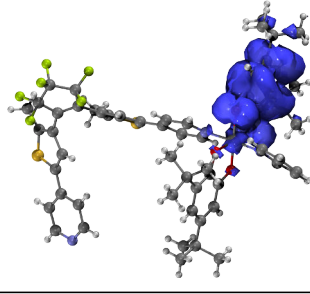
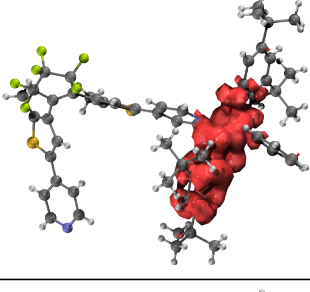
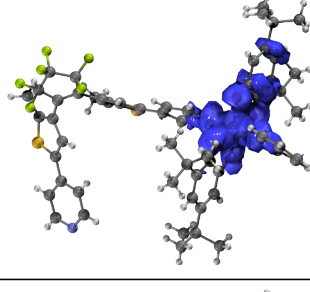
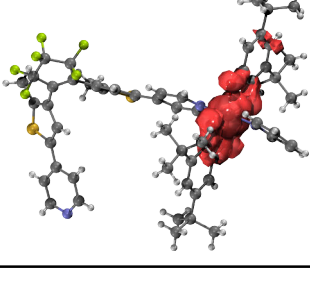
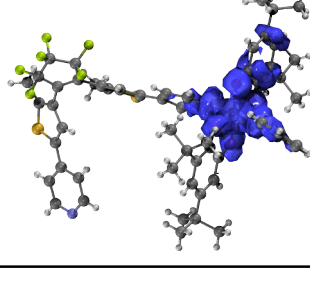
		Hole	Electron
E.S.	1		
E (eV)	1.3236		
λ (nm)	936.70		
f	0.0217		
$\langle S^2 \rangle$	0.772		
E.S.	7		
E (eV)	1.8697		
λ (nm)	663.11		
f	0.0067		
$\langle S^2 \rangle$	0.868		
E.S.	28		
E (eV)	3.4569		
λ (nm)	358.66		
f	0.0097		
$\langle S^2 \rangle$	0.784		
E.S.	29		
E (eV)	3.5088		
λ (nm)	353.35		
f	0.0132		
$\langle S^2 \rangle$	0.776		

Figure D.27.: The information of the excited states and the corresponding hole-electron distributions of the *low-spin* CoL₂DAEpy complex (100 K) in the open (Co1;Asymm) molecular structure.

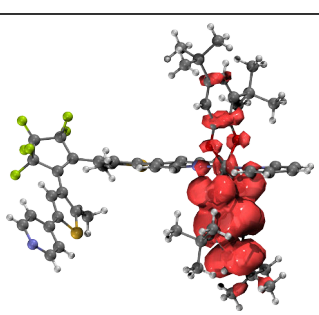
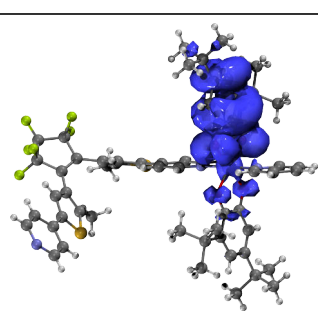
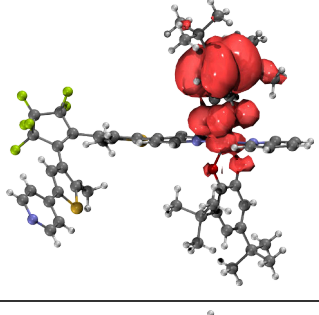
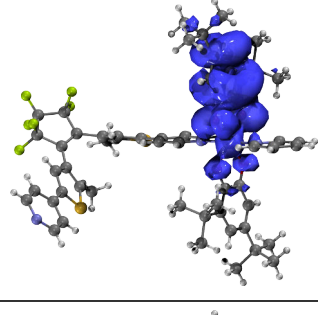
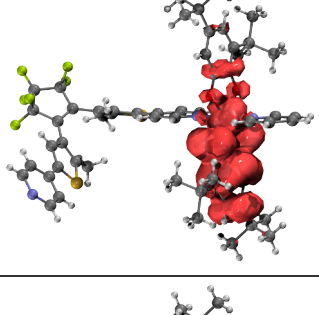
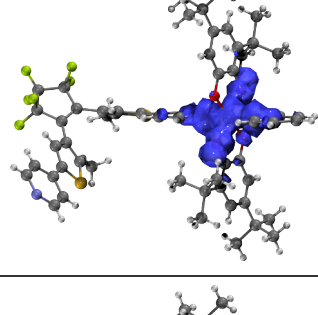
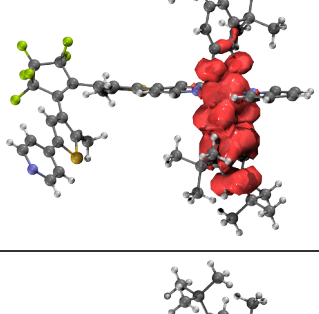
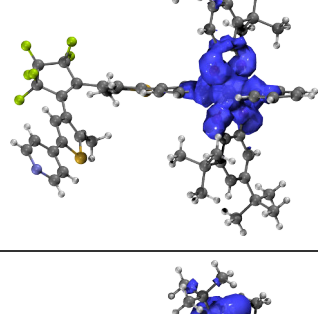
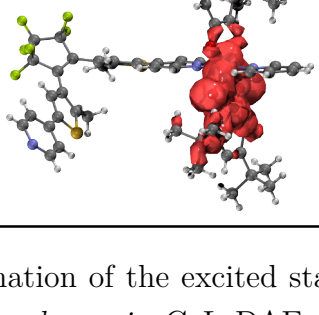
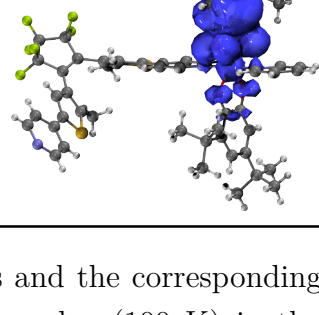
		Hole	Electron
E.S.	1		
E (eV)	0.4944		
λ (nm)	2507.87		
f	0.0473		
$\langle S^2 \rangle$	0.77		
E.S.	5		
E (eV)	1.6483		
λ (nm)	752.21		
f	0.0053		
$\langle S^2 \rangle$	0.946		
E.S.	9		
E (eV)	1.9078		
λ (nm)	649.87		
f	0.0023		
$\langle S^2 \rangle$	0.913		
E.S.	23		
E (eV)	2.8347		
λ (nm)	437.38		
f	0.0025		
$\langle S^2 \rangle$	0.871		
E.S.	25		
E (eV)	2.9968		
λ (nm)	413.72		
f	0.0011		
$\langle S^2 \rangle$	0.775		

Figure D.28.: The information of the excited states and the corresponding hole-electron distributions of the *low-spin* CoL₂DAEpy complex (100 K) in the open (Co₂;Symm) molecular structure.

Table D.18.: The Mulliken spin on the fragments and the corresponding IP or EA of the CoL₂DAEpy complexes in the *low-spin* open (Co1;Asymm) molecular structure started from the different initial guesses by B3LYP.

	Co		L1		L2		DAEpy		IP/EA (eV)
	charge	spin	charge	spin	charge	spin	charge	spin	
1^P	0.31	−0.01	−0.19	0.98	−0.14	−0.97	0.53	0.00	5.354
2^P	0.31	0.01	−0.20	0.99	−0.13	0.98	0.53	0.01	5.371
3^P	0.31	−0.01	−0.19	0.98	−0.14	−0.97	0.53	0.00	5.354
4ⁿ	0.35	0.00	−1.04	0.00	−1.01	0.00	0.31	0.00	2.093
5ⁿ	0.33	0.05	−0.51	0.78	−0.80	0.18	−0.34	0.88	1.306
6ⁿ	0.35	0.00	−1.00	0.13	−1.00	0.00	0.27	−0.14	2.103

Table D.19.: The Mulliken spin on the fragments and the corresponding IP or EA of the CoL₂DAEpy complexes in the *low-spin* open (Co2;Symm) molecular structure started from the different initial guesses by B3LYP.

	Co		L1		L2		DAEpy		IP/EA (eV)
	charge	spin	charge	spin	charge	spin	charge	spin	
1^P	0.32	0.00	−0.16	0.98	−0.16	−0.98	0.52	0.00	5.235
2^P	0.32	0.01	−0.16	0.99	−0.16	0.99	0.52	0.01	5.249
3^P	0.32	0.00	−0.16	0.98	−0.16	−0.98	0.52	0.00	5.235
4ⁿ	0.36	0.00	−1.06	0.00	−1.05	0.00	0.38	0.00	2.184
5ⁿ	0.34	0.03	−0.65	0.47	−0.64	0.49	−0.37	0.90	1.325
6ⁿ	0.36	0.00	−1.03	0.03	−1.03	0.03	0.33	−0.05	2.188

Table D.20.: The Mulliken spin on the fragments and the corresponding IP or EA of the CoL₂DAEpy complexes in the *low-spin* closed (Co1) molecular structure started from the different initial guesses by B3LYP.

	Co		L1		L2		DAEpy		IP/EA (eV)
	charge	spin	charge	spin	charge	spin	charge	spin	
1^P	0.32	0.00	−0.16	0.98	−0.16	−0.98	0.51	0.00	5.489
2^P	0.32	0.01	−0.16	0.99	−0.16	0.99	0.51	0.01	5.504
3^P	0.32	0.00	−0.16	0.98	−0.16	−0.98	0.51	0.00	5.489
4ⁿ	0.36	0.00	−0.91	0.00	−0.90	0.00	0.07	0.00	2.605
5ⁿ	0.34	0.04	−0.65	0.47	−0.63	0.50	−0.47	1.00	2.505
6ⁿ	0.35	0.04	−0.83	0.25	−0.83	0.25	−0.08	−0.54	2.692

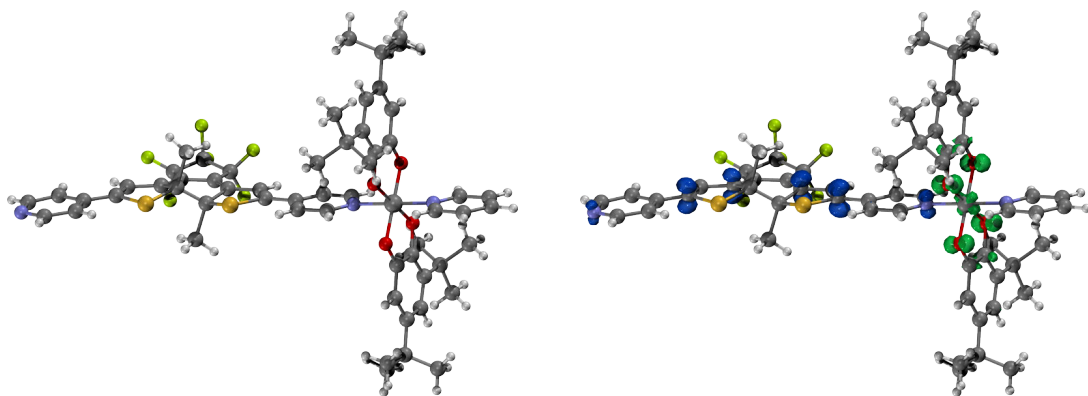

 Closed-Shell: $ls\text{-Co}^{\text{III}}(\text{Cat}^{2-})(\text{Cat}^{2-})(\text{DAEpy}^0)$ Diradical: $ls\text{-Co}^{\text{III}}(\text{Cat}^{2-})(\text{SQ}^-)(\text{DAEpy}^-)_{\text{AFM}}$

Figure D.29.: The spin density isosurfaces of the *low-spin* (100 K) closed (Co1) type $[\text{CoL}_2\text{DAEpy}]^-$ complex in the closed-shell state (left) or the diradical state (right).

Table D.21.: The energy difference of FM-coupled and AFM-coupling between the different adjacent CoL_2 pairs under the various functionals.

$E_{\text{FM}} - E_{\text{AFM}} (\text{cm}^{-1})$	PBE	TPSS	M06-L	TPSSh
Closed(Co1-Co2)	1.1195e-01	-1.0316e-01	-1.1195e-01	-8.1220e-02
Closed(Co1-Co1)	0.0000e+00	0.0000e+00	0.0000e+00	0.0000e+00
Closed(Co2-Co2)	6.3863e-01	3.2488e-01	7.4606e-02	3.0730e-02
Closed(Co1-DAEpy-Co2)	3.1318e+00	-2.5371e+00	2.1954e-01	6.3637e-02
Open(sCo2-sCo2)	6.5331e-03	-4.6135e-02	3.2907e-02	-6.5895e-02
Open(asCo1-sCo2-t1)	2.1777e-03	2.2584e-03	0.0000e+00	0.0000e+00
$E_{\text{FM}} - E_{\text{AFM}} (\text{cm}^{-1})$	B3LYP*	B3LYP	CAM-B3LYP	
Closed(Co1-Co2)	-7.9042e-02	-7.2429e-02	-3.9287e-01	
Closed(Co1-Co1)	0.0000e+00	-3.2921e-02	0.0000e+00	
Closed(Co2-Co2)	2.1938e-02	-1.5405e-02	-2.1938e-02	
Closed(Co1-DAEpy-Co2)	2.8471e-02	1.7583e-02	1.5405e-02	
Open(sCo2-sCo2)	-4.8313e-02	-5.2668e-02	-3.7343e-02	
Open(asCo1-asCo1-t1)		0.0000e+00		
Open(asCo1-asCo1-t2)		-2.1779e-03		
Open(asCo1-asCo1-t3)		0.0000e+00		
Open(asCo1-sCo2-t1)	0.0000e+00	0.0000e+00		
Open(asCo1-sCo2-t2)		0.0000e+00		
Open(asCo1-sCo2-t3)		0.0000e+00		
$E_{\text{FM}} - E_{\text{AFM}} (\text{cm}^{-1})$	HSE06	PBE0	M06-2X	
Closed(Co1-Co2)	-9.2189e-02	-6.5815e-02	-6.5331e-03	
Closed(Co1-Co1)	0.0000e+00	0.0000e+00	0.0000e+00	
Closed(Co2-Co2)	-8.7753e-02	-3.2907e-02	4.1699e-02	
Closed(Co1-DAEpy-Co2)	2.1938e-02	2.2019e-02	0.0000e+00	
Open(sCo2-sCo2)	-8.1220e-02	-6.8073e-02	5.7104e-02	

Table D.22.: The CoL₂ pair along the *a* axis in the *low-spin* (100 K) closed molecular structure was placed in a (26Å×26Å×18Å) unit cell. The energy difference of FM-coupled and AFM-coupling configurations ($\Delta E = E_{\text{FM}} - E_{\text{AFM}}$), by PBE with an 800 eV kinetic energy cutoff versus Hubbard U (the first group), by PBE+U (U=6 eV) versus kinetic energy cutoff (the second group), by PBE+U (U=6 eV) with an 800 eV kinetic energy cutoff versus the cell size (the third group), by HSE06 versus kinetic energy cutoff (the fourth group).

U (eV)	ΔE (eV)	E_{cut} (eV)	ΔE (eV)	Cell Enlarge	ΔE (eV)	E_{cut} (eV)	ΔE (eV)
0	-1.360e-05	560	-1.841e-05	1.00	-1.830e-05	400	-1.107e-05
1	-1.384e-05	640	-1.826e-05	1.05	-1.805e-05	450	-1.083e-05
2	-1.426e-05	680	-1.821e-05	1.10	-1.800e-05	500	-1.104e-05
3	-1.526e-05	720	-1.838e-05	1.15	-1.787e-05	550	-1.132e-05
4	-1.601e-05	800	-1.835e-05	1.20	-1.798e-05	600	-1.036e-05
5	-1.715e-05	880	-1.835e-05	1.25	-1.775e-05	650	-1.101e-05
6	-1.829e-05	920	-1.841e-05	1.30	-1.763e-05	700	-1.153e-05
7	-1.948e-05	960	-1.824e-05	1.40	-1.795e-05	750	-1.107e-05
8	-2.098e-05	1000	-1.826e-05	1.45	-1.761e-05	800	-1.110e-05
9	-2.183e-05	1040	-1.824e-05			850	-9.840e-06
10	-2.276e-05	1120	-1.840e-05			900	-1.102e-05
11	-2.131e-05					950	-1.070e-05
12	-1.100e-06					1000	-1.019e-05
						1050	-1.144e-05
						1100	-1.112e-05
						1150	-1.015e-05
						1200	-1.112e-05

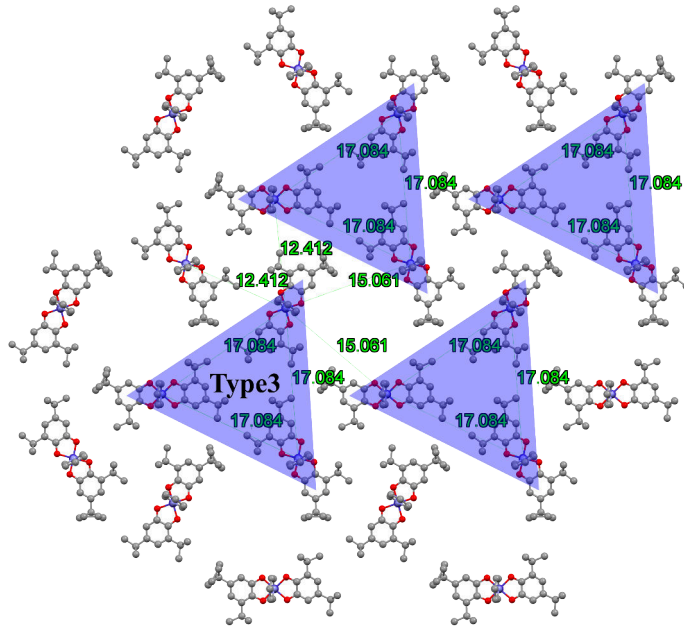


Figure D.30.: The asymmetric CoL₂ layer in **o-CoDAE** under 100 K, the type 3 pairs (asCo1–asCo1-t3) could only form a local conductive triangle.

E. Supporting information for CoBO₄

Table E.1.: The structure of the reduced BO layer in a VASP input form.

Reduced BO Layer			
1.0			
6.2115726471	0.0000000000	0.0000000000	
-2.0924469771	3.3599957430	0.0000000000	
-4.5504452798	-5.8467494930	21.4998577467	
C	H	O	S
10	8	4	4
Direct			
0.011723587	0.959605910	0.746594689	
0.761936843	0.771395709	0.766692155	
0.238555777	0.115692390	0.849373516	
0.047319401	0.139319200	0.865695915	
0.420389354	0.413369605	0.967135419	
0.572937533	0.572894272	0.028572915	
0.946008439	0.846948493	0.130013694	
0.754773052	0.870579236	0.146336315	
0.231391064	0.214871980	0.229016289	
0.981603748	0.026651417	0.249114753	
0.970972859	0.792407534	0.705119474	
0.071966879	0.241616837	0.743394935	
0.617319102	0.748587758	0.734871071	
0.702943996	0.490687069	0.770402993	
0.290382988	0.495576885	0.225304364	
0.376008730	0.237680074	0.260838017	
0.921360113	0.744647159	0.252313487	
0.022352233	0.193848988	0.290589791	
0.223205520	0.975931996	0.791170964	
0.813958488	0.024404286	0.825994323	
0.179368480	0.961859718	0.169715163	
0.770125147	0.010347006	0.204538457	
0.525914005	0.278754253	0.908663352	
0.106143998	0.327357922	0.944399939	
0.887181966	0.658902305	0.051308866	
0.467413867	0.707513575	0.087045192	

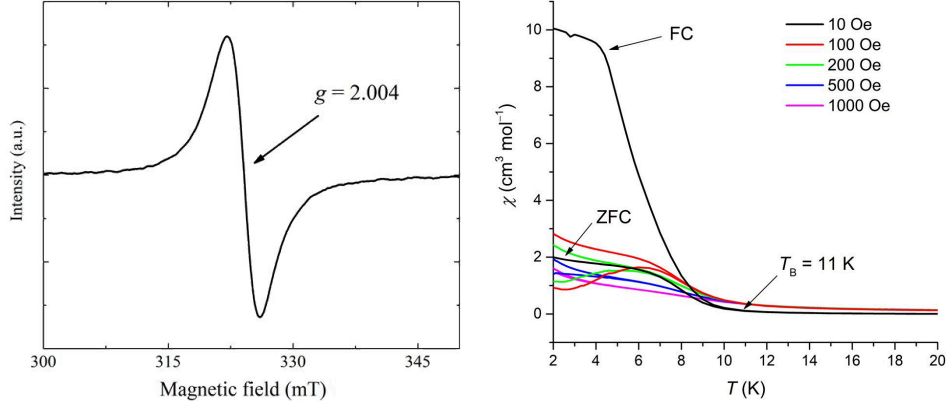


Figure E.1.: The room temperature EPR signal of **CoBO₄** aroused by the BO radical (left). The field cooling (FC) and zero field cooling (ZFC) temperature dependent magnetic susceptibility (χ) of **CoBO₄** at 10, 100, 200, 500 and 1000 Oe magnetic field (right).

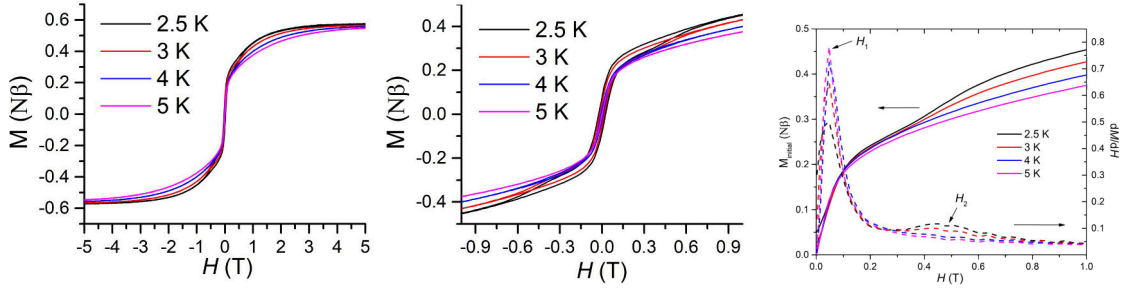


Figure E.2.: The magnetization curves of **CoBO₄** at 2.5, 3, 4 and 5 K in the magnetic field of -5 – $+5$ T (left) and an enlarged view (middle). The derivative of magnetization with respect to the magnetic field in the range of 0 – 1 T (right).

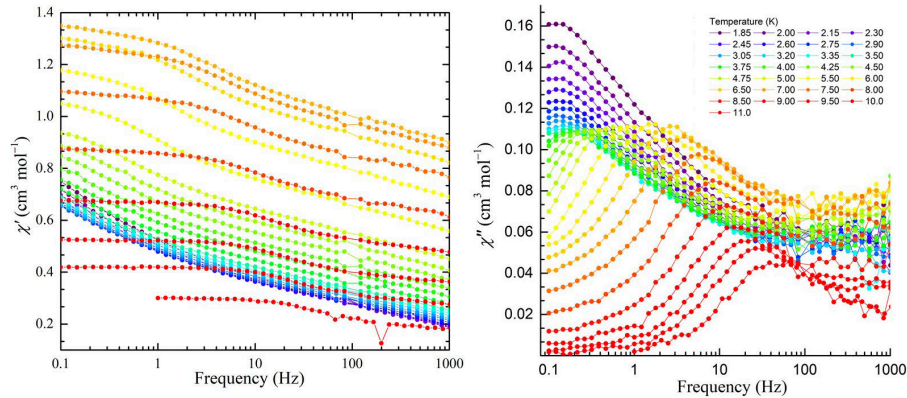


Figure E.3.: The frequency dependent in-phase (χ' ; left) and out-of-phase magnetic susceptibility (χ'' ; right) in the temperature range of 1.85–11.0 K in a zero field.

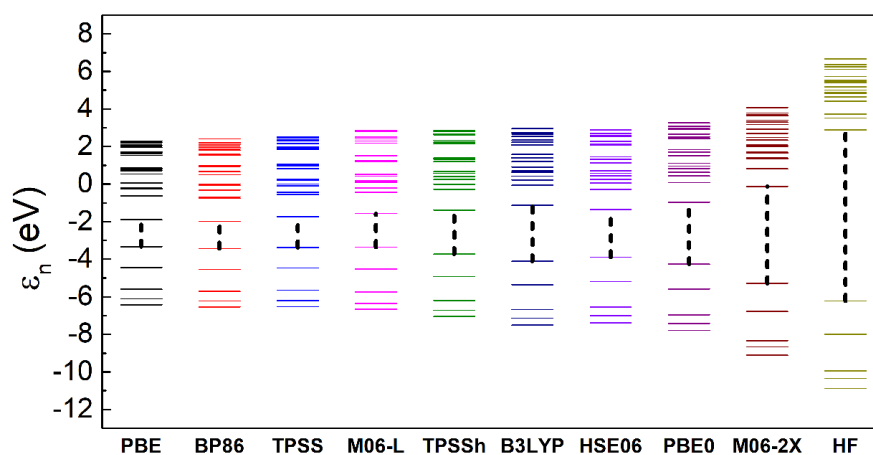


Figure E.4.: Kohn-Sham orbital energy levels of a neutral BO monomer calculated by different functionals (black vertical dashes indicate gaps).

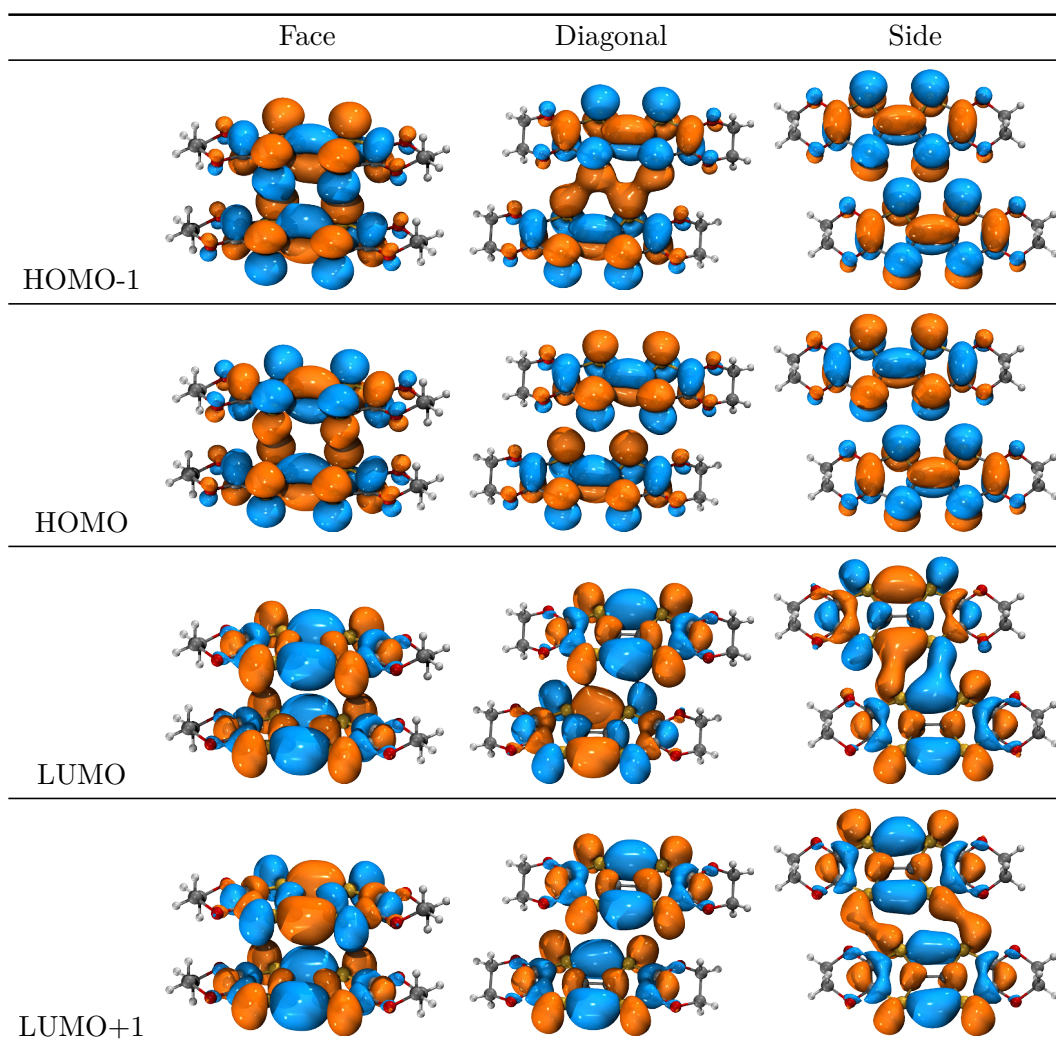


Figure E.5.: The molecular orbital isosurfaces for the three types of neutral BO dimer ($[\text{BO}_2]^0$) based on B3LYP KS-DFT.

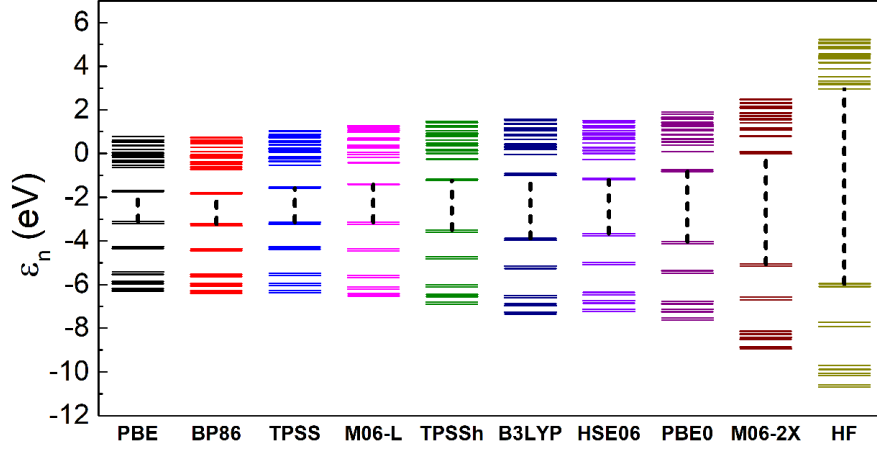


Figure E.6.: Kohn-Sham orbital energy levels of a neutral face-type BO dimer ($[\text{BO}_2]_{\text{face}}^0$) calculated by different functionals (black vertical dashes indicate gaps).

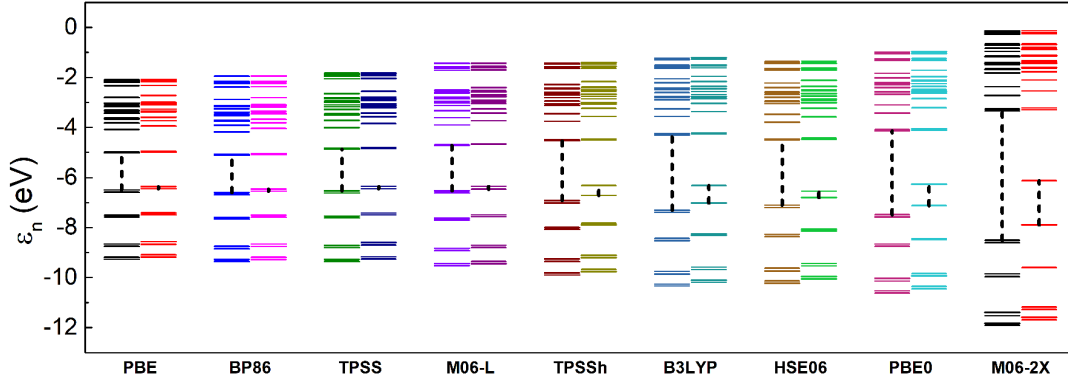


Figure E.7.: Kohn-Sham orbital energy levels of a positive one charged face-type BO dimer ($[\text{BO}_2]_{\text{face}}^{1+}$) calculated by different functionals (the left side is alpha orbital level and the right side is beta orbital energy level, black vertical dashes indicate gaps).

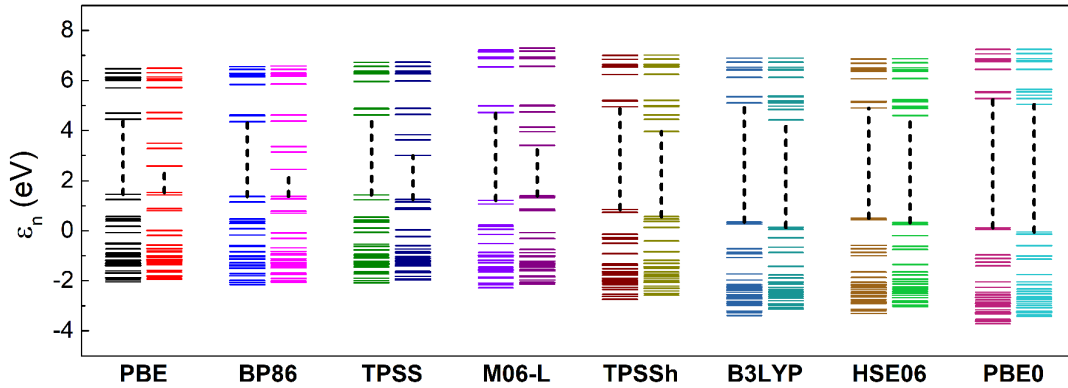


Figure E.8.: Kohn-Sham orbital energy levels of $[\text{Co}(\text{pdms})_2]^{2-}$ calculated by different functionals.

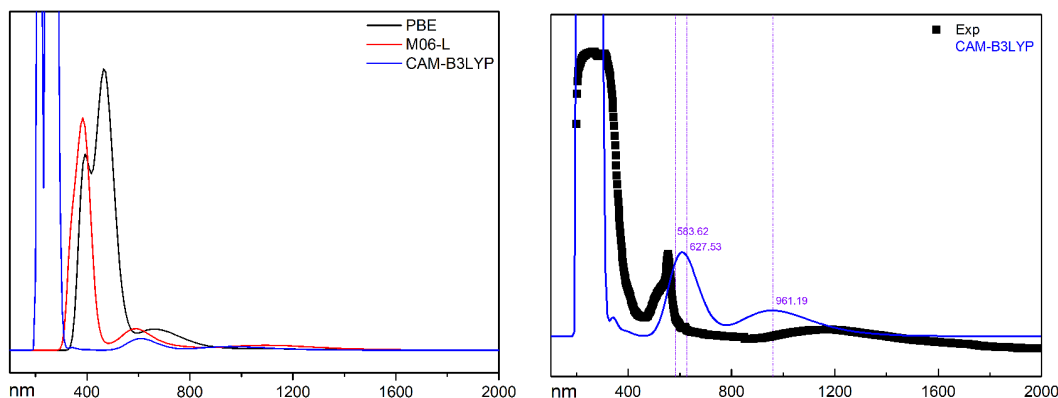


Figure E.9.: The UV-vis spectroscopy of $[\text{Co}(\text{pdms})_2]^{2-}$ simulated by the TD-DFT under the selected functionals (left) and the comparison with the experimental data (right). Measured (black) and calculated (blue) solid-state UV-Vis-NIR spectrum of $(\text{HNEt}_3)_2[\text{Co}(\text{pdms})_2]$. The absorbance at 1200 nm, which was calculated by CAM-B3LYP at 960 nm, mainly corresponds to the $d-d$ electron transition on cobalt ion.

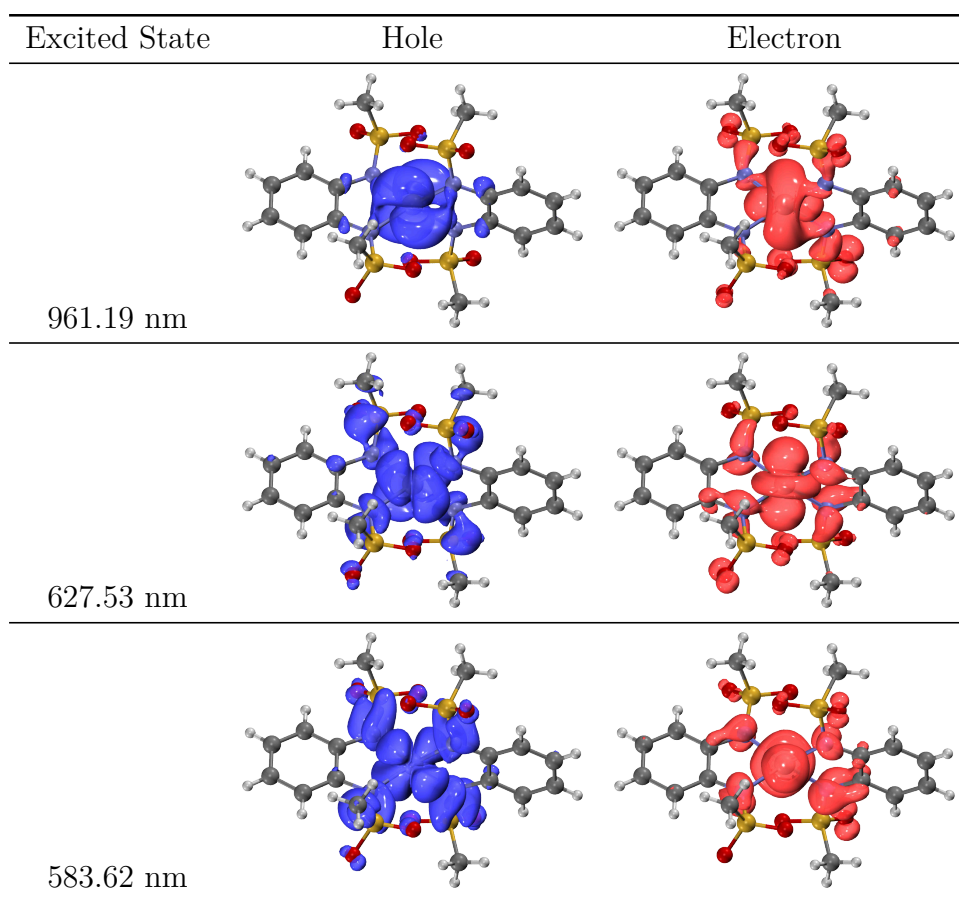


Figure E.10.: The hole-electron distributions of corresponding excitations (an electron leaves hole and goes to electron) by CAM-B3LYP for $[\text{Co}(\text{pdms})_2]^{2-}$.

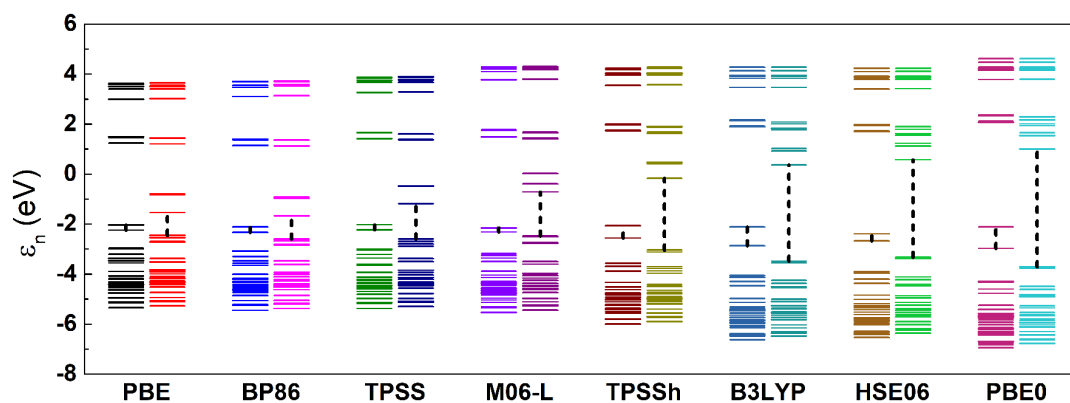


Figure E.11.: Kohn-Sham orbital energy levels of $[\text{Co}(\text{pdms})_2]^-$ calculated by different functionals.

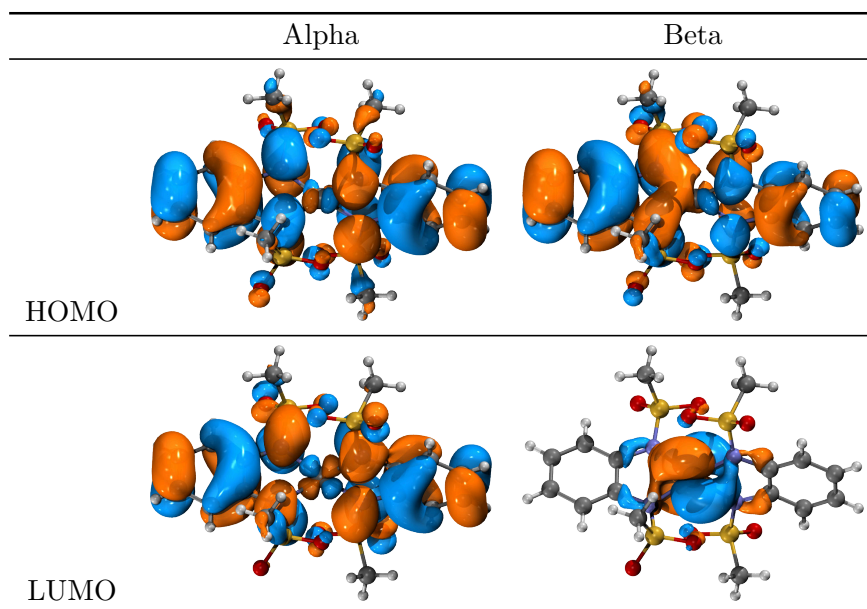


Figure E.12.: Molecular orbitals of AFM configured $[\text{Co}(\text{pdms})_2]^-$ based on B3LYP KS-DFT.

Table E.2.: The energy difference of AFM-coupled and FM-coupling between the Co^{2+} ion with the $(\text{pdms})^-$ radical.

$E_{\text{FM}} - E_{\text{AFM}}$ (eV)			
PBE	0.3018	TPSSh	0.2618
BP86	0.3323	B3LYP	0.2106
TPSS	0.3359	HSE06	0.1794
M06-L	0.1283	PBE0	0.1801

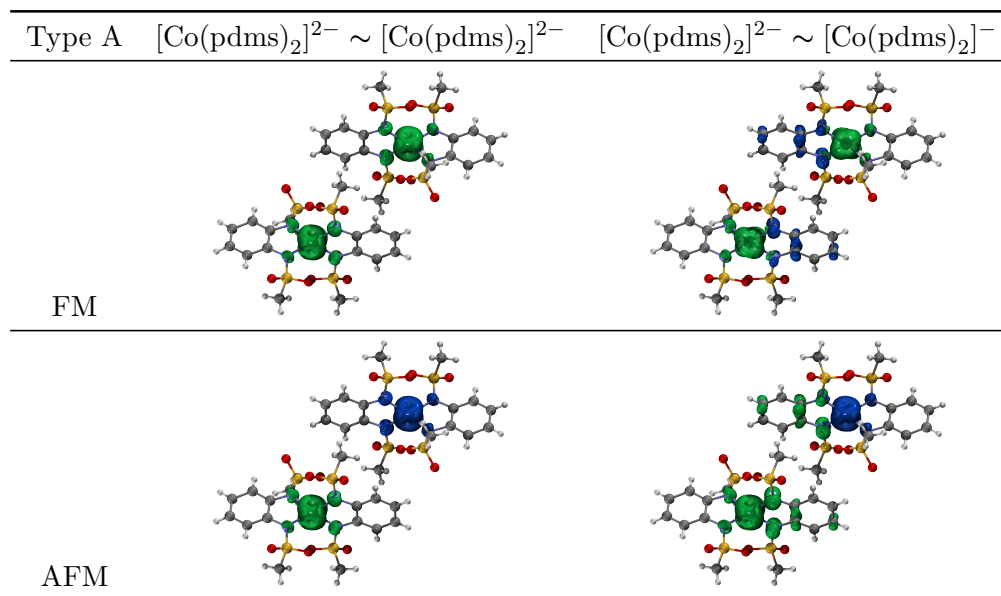


Figure E.13.: The spin density of Type A $[\text{Co}(\text{pdms})_2]$ dimer with four electronic configurations based on B3LYP KS-DFT.

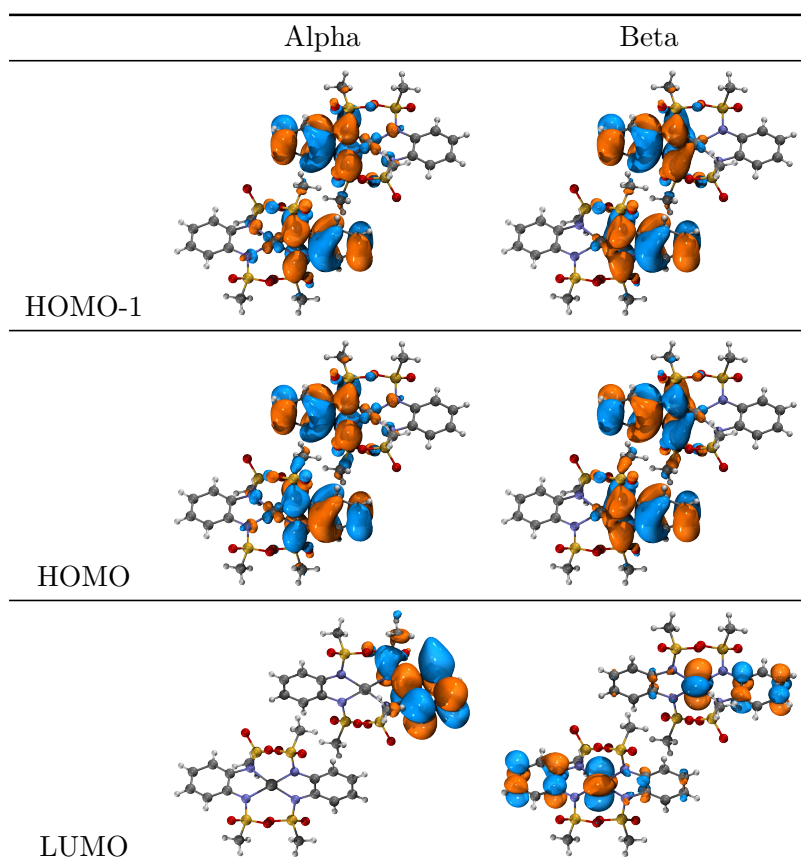


Figure E.14.: The molecular orbitals of Type A $[\text{Co}(\text{pdms})_2]$ dimer with four electronic configurations based on B3LYP KS-DFT.

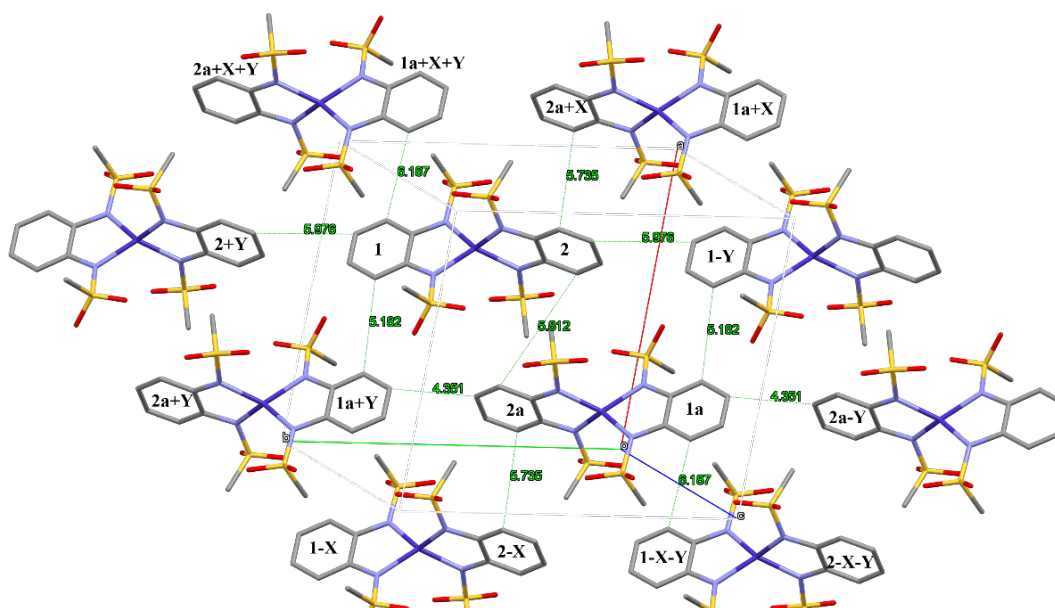


Figure E.15.: The short contacts between adjacent pdms units.

Table E.3.: isotropic coupling constant $J_{\text{pdms-pdms}}$ calculated from pdms^- dimer.

	$J(\text{cm}^{-1})$	PBE	TPSSh	B3LYP	PBE0	M06-2X	HF	
1	1a+X+Y	-5.972	-2.873	-2.743	-2.329	-3.681	-0.911	(C)
1	1a+Y	1.536	1.549	1.398	1.321	1.183	0.564	(D)
1	2a	-139.915	0.257	0.121	0.077	0.029	-0.033	
1	2a+X+Y	-33.716	-0.020	0.024	0.055	-0.066	0.079	
1	2	8.669	5.188	5.515	4.776	2.243	4.117	
1	2+Y	-0.891	-0.250	-0.299	-0.103	-0.428	0.105	
2	1a+X	-34.541	-0.149	-0.068	-0.018	0.007	0.079	
2	1-Y	-0.891	-0.250	-0.299	-0.103	-0.428	0.103	
2	2a+X	0.957	1.043	1.042	1.071	1.045	0.996	(B)
2	2a	-7.256	-4.315	-4.260	-3.735	-5.331	-1.903	(A)

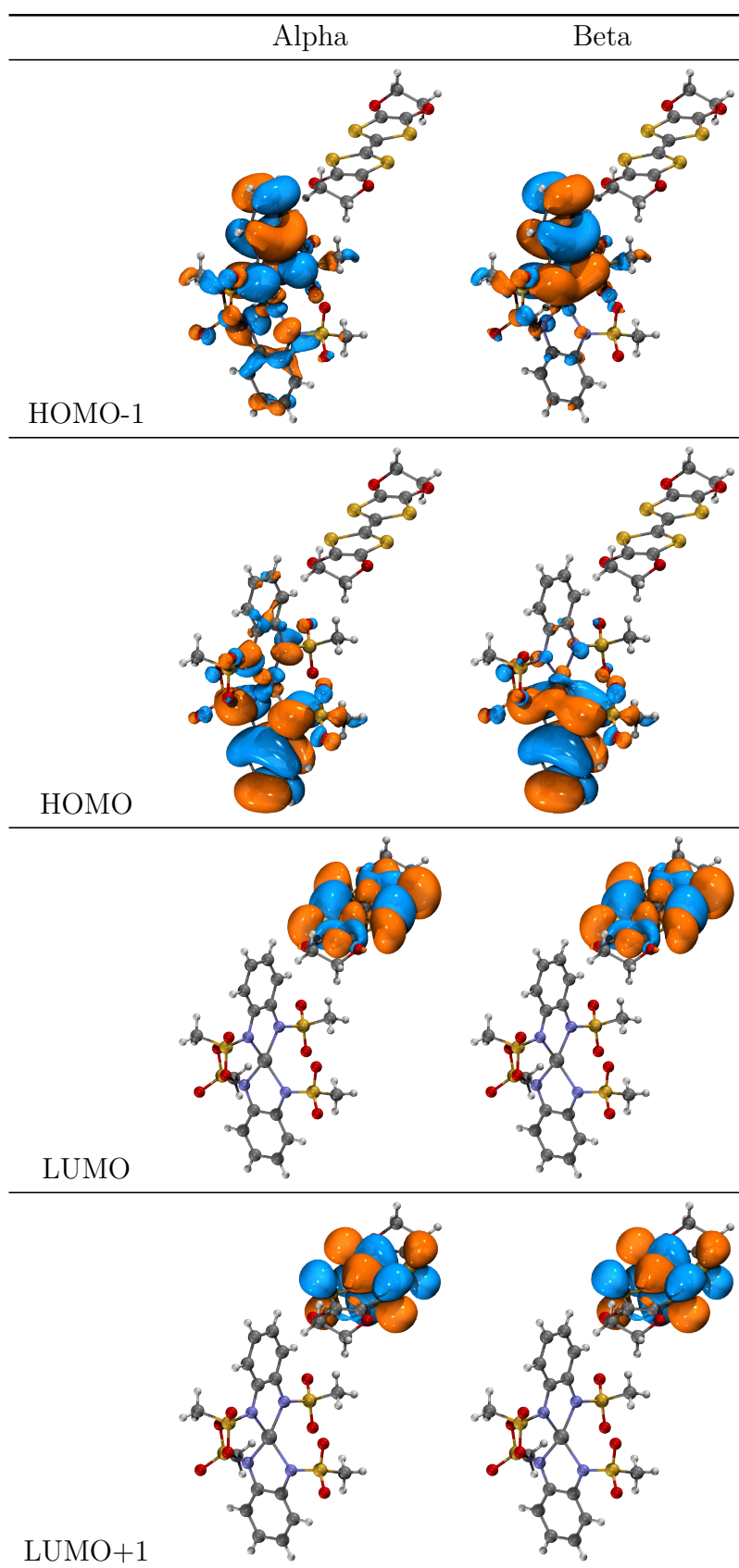


Figure E.16.: Molecular orbitals of $[\text{Co}(\text{pdms})_2]^{2-} \sim [\text{BO}]^0$ complex based on B3LYP KS-DFT.

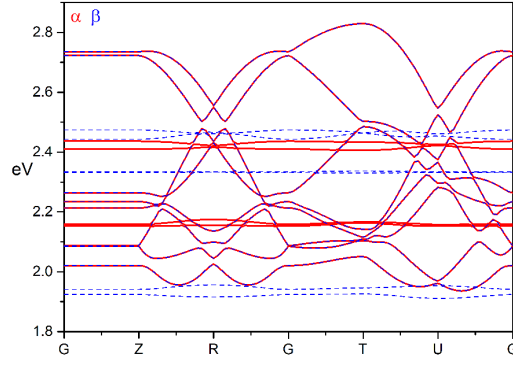


Figure E.17.: The band structure of **CoBO₄** based on PBE KS-DFT. G(0, 0, 0), Z(0, 0, 0.5), R(0.5, -0.5, 0.5), T(0, 0.5, -0.5), U(0.5, 0, -0.5).

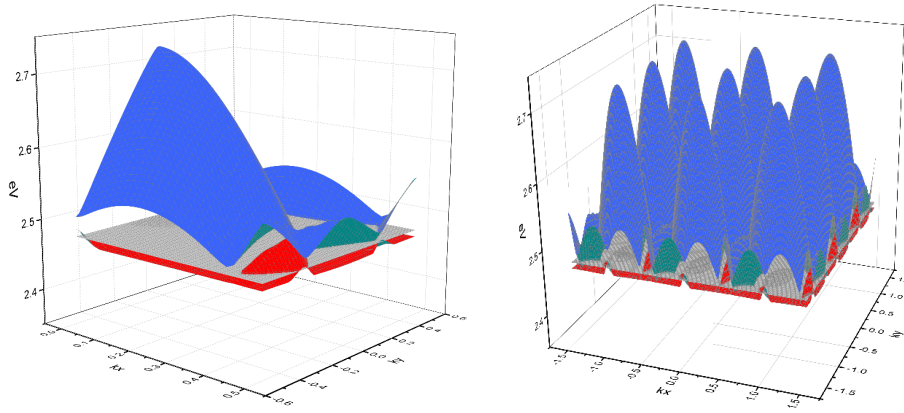


Figure E.18.: The 2D band dispersion near the Fermi surface of **CoBO₄** ($k_z = 0$, red: hole band, blue: electron band, gray: Fermi surface) in a primitive (left) and an extended cell (right).

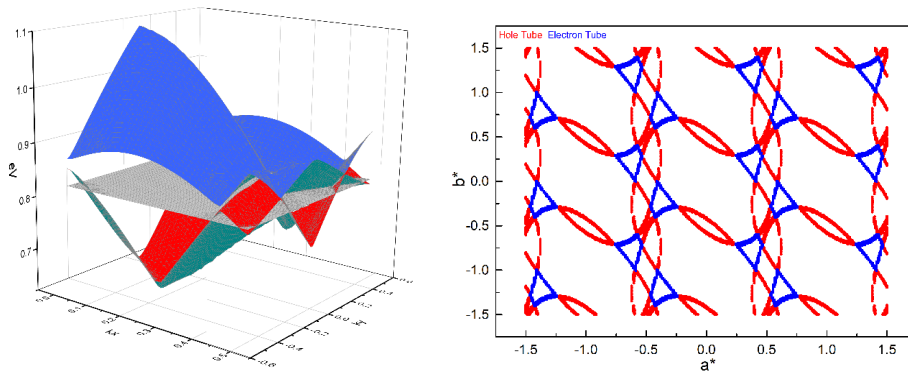


Figure E.19.: The 2D band dispersion near the Fermi surface of **[BO₈]⁴⁺@CoBO₄** layer ($k_z = 0$, red: hole band, blue: electron band, gray: Fermi surface) in a primitive cell (left). The cross-section of the hole band (red) and electron band (blue) with the Fermi surface respectively (right).

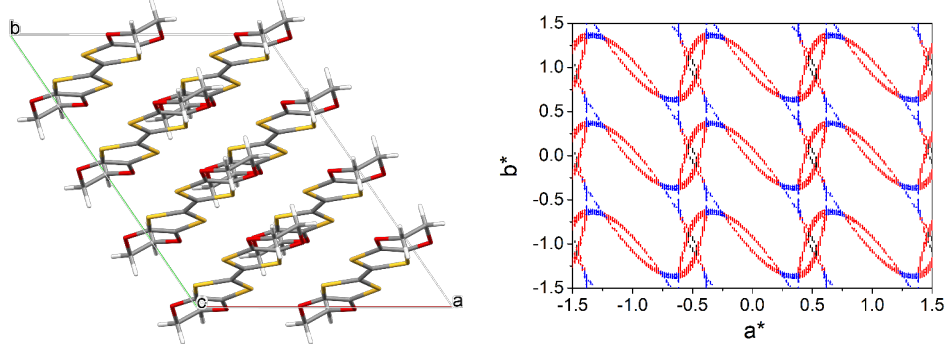


Figure E.20.: The supercell of charged BO octamer base on the reduced structure($[\text{BO}_8]^{4+}$, left). The Fermi surface profile in the a^*b^* plane with $k_z = 0$ base on PBE results, where the squares represent the data points (right).

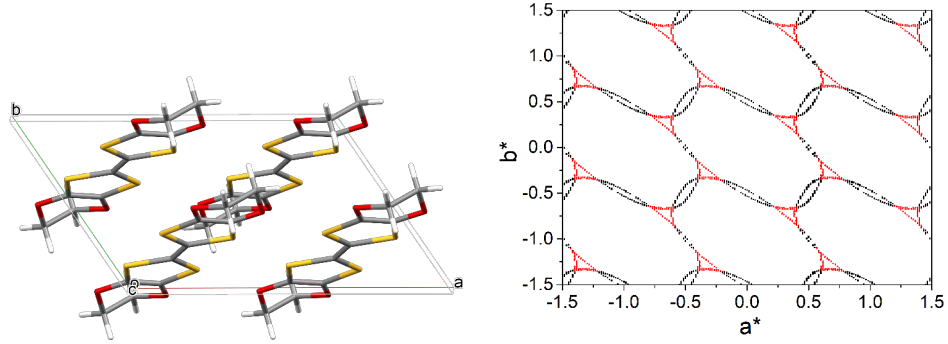


Figure E.21.: The supercell of charged BO tetramer base on the reduced structure($[\text{BO}_4]^{2+}$, left). The Fermi surface profile in the a^*b^* plane with $k_z = 0$ base on PBE results, where the squares represent the data points (right).

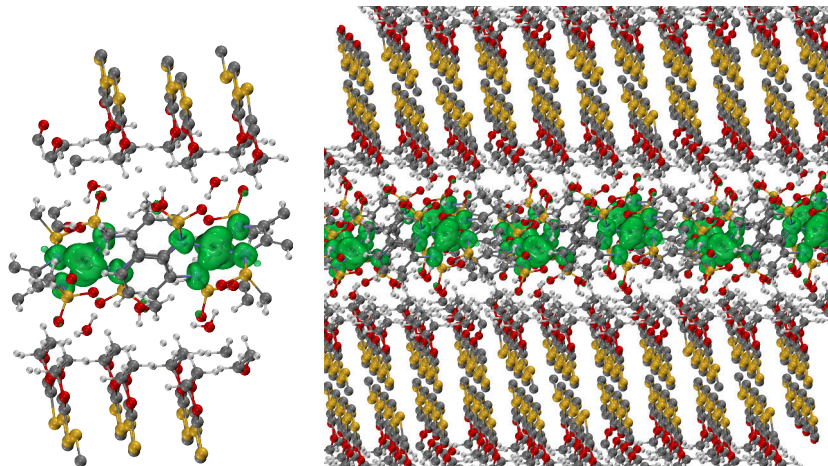


Figure E.22.: The spin density of CoBO_4 .

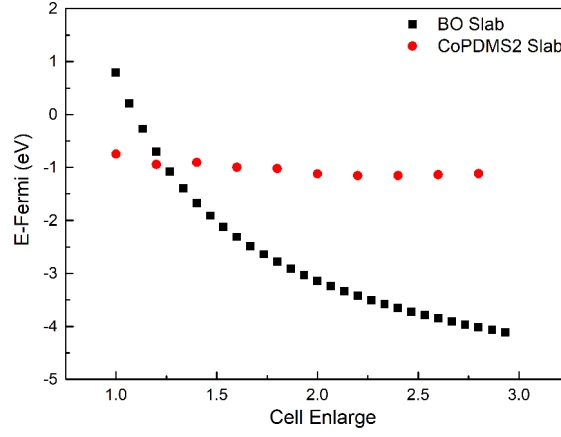


Figure E.23.: The Fermi level of $[\text{BO}_8]^{4+}@\text{CoBO}_4$ layer and $[\text{Co}(\text{pdms})_2]_2^{4-}@\text{CoBO}_4$ layer altered by unit cell size without changing the geometry of molecule.

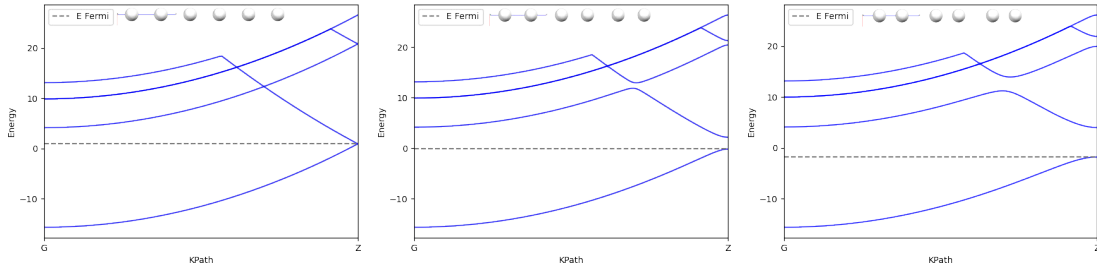


Figure E.24.: A illustration of the Peierls distortion in 1D hydrogen atoms chain.

F. List of publications

F.1. Published

1. Yongbing Shen, Hiroshi Ito, Haitao Zhang, Hideki Yamochi, Seiu Katagiri, Shinji K. Yoshina, Akihiro Otsuka, Manabu Ishikawa, Goulven Cosquer, Kaiji Uchida, Carmen Herrmann, Takefumi Yoshida, Brian K. Breedlove, and Masahiro Yamashita, Simultaneous manifestation of metallic conductivity and single-molecule magnetism in a layered molecule-based compound, *Chem. Sci.* **2020**, 11, 11154. (Chapter 6 is based on this work)
2. Martin Sebastian Zöllner, Rukan Nasri, Haitao Zhang, and Carmen Herrmann, Design Considerations for Oligo(p-phenyleneethynylene) Organic Radicals in Molecular Junctions, *J. Phys. Chem. C* **2021**, 125, 1208.
3. Yongbing Shen, Hiroshi Ito, Haitao Zhang, Hideki Yamochi, Goulven Cosquer, Carmen Herrmann, Toshiaki Ina, Shinji K. Yoshina, Brian K. Breedlove, Akihiro Otsuka, Manabu Ishikawa, Takefumi Yoshida, and Masahiro Yamashita, Emergence of Metallic Conduction and Cobalt(II)-Based Single-Molecule Magnetism in the Same Temperature Range, *J. Am. Chem. Soc.* **2021**, 143, 4891. (Chapter 6 is related to this work)
4. Yongbing Shen, Kuniyoshi Sugimoto, Satoshi Yamashita, Takefumi Yoshida, Yasuhiro Nakazawa, Brian K. Breedlove, Haitao Zhang, and Masahiro Yamashita, Melamine-induced synthesis of a structurally perfect kagomé antiferromagnet, *Chem. Commun.* **2022**, 58, 3763.

F.2. In preparation

1. Michael Deffner, Philipp Bahlke, Haitao Zhang, Maike Mücke, Jonny Proppe, Ignacio Franco, and Carmen Herrmann, Learning Conductance: Gaussian Process Regression for Molecular Electronics, to be submitted.
2. Haitao Zhang, Carmen Herrmann, The adsorption of radicals on gold surfaces, in preparation. (based on Chapter 4)

G. List of chemicals

No hazardous chemicals according to the Globally Harmonised System of Classification and Labelling of Chemicals (GHS) regulation have been used within the scope of this thesis.

Bibliography

- [1] G. E. Moore. “Cramming More Components Onto Integrated Circuits”. In: *Proceedings of the IEEE* 86.1 (1998), pp. 82–85. DOI: 10.1109/jproc.1998.658762.
- [2] M. M. Waldrop. “The chips are down for Moore’s law”. In: *Nature* 530.7589 (2016), pp. 144–7. DOI: 10.1038/530144a.
- [3] Juan C. Ranuárez, M. J. Deen, and Chih-Hung Chen. “A review of gate tunneling current in MOS devices”. In: *Microelectronics Reliability* 46.12 (2006), pp. 1939–1956. DOI: 10.1016/j.microrel.2005.12.006.
- [4] Leonard F. Register, Elyse Rosenbaum, and Kevin Yang. “Analytic model for direct tunneling current in polycrystalline silicon-gate metal–oxide–semiconductor devices”. In: *Applied Physics Letters* 74.3 (1999), pp. 457–459. DOI: 10.1063/1.123060.
- [5] Giorgos Fagas et al. “Energy Challenges for ICT”. In: *ICT - Energy Concepts for Energy Efficiency and Sustainability*. Ed. by Giorgos Fagas Paul et al. IntechOpen, 2017. Chap. 1. DOI: 10.5772/66678.
- [6] Burn J. Lin. “The ending of optical lithography and the prospects of its successors”. In: *Microelectronic Engineering* 83.4-9 (2006), pp. 604–613. DOI: 10.1016/j.mee.2005.12.017.
- [7] Vivek Bakshi. *EUV lithography*. 2009.
- [8] Daniel Loss and David P. DiVincenzo. “Quantum computation with quantum dots”. In: *Physical Review A* 57.1 (1998), pp. 120–126. DOI: 10.1103/PhysRevA.57.120.
- [9] M. N. Leuenberger and D. Loss. “Quantum computing in molecular magnets”. In: *Nature* 410.6830 (2001), pp. 789–93. DOI: 10.1038/35071024.
- [10] Charles H. Bennett. “Notes on Landauer’s principle, reversible computation, and Maxwell’s Demon”. In: *Studies in History and Philosophy of Science Part B: Studies in History and Philosophy of Modern Physics* 34.3 (2003), pp. 501–510. DOI: 10.1016/s1355-2198(03)00039-x.

-
- [11] L. L. Yan et al. “Single-Atom Demonstration of the Quantum Landauer Principle”. In: *Phys Rev Lett* 120.21 (2018), p. 210601. DOI: 10.1103/PhysRevLett.120.210601.
- [12] G. Burkard, H. A. Engel, and D. Loss. “Spintronics and quantum dots for quantum computing and quantum communication”. In: *Fortschritte Der Physik-Progress of Physics* 48.9-11 (2000), pp. 965–986. DOI: Doi10.1002/1521-3978(200009)48:9/11<965::Aid-Prop965>3.0.Co;2-V.
- [13] D. G. Cory, A. F. Fahmy, and T. F. Havel. “Ensemble quantum computing by NMR spectroscopy”. In: *Proc Natl Acad Sci U S A* 94.5 (1997), pp. 1634–9. DOI: 10.1073/pnas.94.5.1634.
- [14] G. Binasch et al. “Enhanced magnetoresistance in layered magnetic structures with antiferromagnetic interlayer exchange”. In: *Phys Rev B Condens Matter* 39.7 (1989), pp. 4828–4830. DOI: 10.1103/physrevb.39.4828.
- [15] S. N. Piramanayagam. “Perpendicular recording media for hard disk drives”. In: *Journal of Applied Physics* 102.1 (2007). DOI: 10.1063/1.2750414.
- [16] Arie Aviram and Mark A. Ratner. “Molecular rectifiers”. In: *Chemical Physics Letters* 29.2 (1974), pp. 277–283. DOI: 10.1016/0009-2614(74)85031-1.
- [17] Yuki Komoto et al. “Single-molecule junctions for molecular electronics”. In: *Journal of Materials Chemistry C* 4.38 (2016), pp. 8842–8858. DOI: 10.1039/c6tc03268k.
- [18] Y. Kim et al. “Characteristics of amine-ended and thiol-ended alkane single-molecule junctions revealed by inelastic electron tunneling spectroscopy”. In: *ACS Nano* 5.5 (2011), pp. 4104–11. DOI: 10.1021/nn200759s.
- [19] T. Sendler et al. “Light-Induced Switching of Tunable Single-Molecule Junctions”. In: *Adv Sci (Weinh)* 2.5 (2015), p. 1500017. DOI: 10.1002/advs.201500017.
- [20] S. Schmaus et al. “Giant magnetoresistance through a single molecule”. In: *Nat Nanotechnol* 6.3 (2011), pp. 185–9. DOI: 10.1038/nnano.2011.11.
- [21] R. Hayakawa et al. “Large Magnetoresistance in Single-Radical Molecular Junctions”. In: *Nano Lett* 16.8 (2016), pp. 4960–7. DOI: 10.1021/acs.nanolett.6b01595.
- [22] Y. Kim et al. “Charge transport characteristics of diarylethene photoswitching single-molecule junctions”. In: *Nano Lett* 12.7 (2012), pp. 3736–42. DOI: 10.1021/nl3015523.
- [23] Y. Kim et al. “Benzenedithiol: a broad-range single-channel molecular conductor”. In: *Nano Lett* 11.9 (2011), pp. 3734–8. DOI: 10.1021/nl201777m.

- [24] L. Venkataraman et al. “Dependence of single-molecule junction conductance on molecular conformation”. In: *Nature* 442.7105 (2006), pp. 904–7. DOI: 10.1038/nature05037.
- [25] C. R. Arroyo et al. “Signatures of quantum interference effects on charge transport through a single benzene ring”. In: *Angew Chem Int Ed Engl* 52.11 (2013), pp. 3152–5. DOI: 10.1002/anie.201207667.
- [26] H. Ohnishi, Y. Kondo, and K. Takayanagi. “Quantized conductance through individual rows of suspended gold atoms”. In: *Nature* 395.6704 (1998), pp. 780–783. DOI: Doi10.1038/27399.
- [27] D. Xiang et al. “Mechanically controllable break junctions for molecular electronics”. In: *Adv Mater* 25.35 (2013), pp. 4845–67. DOI: 10.1002/adma.201301589.
- [28] F. Kuemmeth et al. “Carbon nanotubes for coherent spintronics”. In: *Materials Today* 13.3 (2010), pp. 18–26. DOI: 10.1016/s1369-7021(10)70030-4.
- [29] S. Takahashi et al. “Coherent manipulation and decoherence of s=10 single-molecule magnets”. In: *Phys Rev Lett* 102.8 (2009), p. 087603. DOI: 10.1103/PhysRevLett.102.087603.
- [30] L. Poggini et al. “Chemisorption of nitronyl-nitroxide radicals on gold surface: an assessment of morphology, exchange interaction and decoherence time”. In: *Nanoscale* 13.16 (2021), pp. 7613–7621. DOI: 10.1039/d1nr00640a.
- [31] Herman J. C. Berendsen. *Simulating the Physical World: Hierarchical Modeling from Quantum Mechanics to Fluid Dynamics*. Cambridge: Cambridge University Press, 2007. DOI: 10.1017/CB09780511815348.
- [32] A. Szabo and N.S. Ostlund. *Modern Quantum Chemistry: Introduction to Advanced Electronic Structure Theory*. Dover Publications, 2012.
- [33] D. Sholl and J.A. Steckel. *Density Functional Theory: A Practical Introduction*. Wiley, 2009.
- [34] James J. P. Stewart. “Optimization of parameters for semiempirical methods VI: more modifications to the NDDO approximations and re-optimization of parameters”. In: *Journal of molecular modeling* 19.1 (2013), pp. 1–32. DOI: 10.1007/s00894-012-1667-x.
- [35] C. Herrmann et al. “Ghost transmission: How large basis sets can make electron transport calculations worse”. In: *J Chem Phys* 132.2 (2010), p. 024103. DOI: 10.1063/1.3283062.
- [36] D. A. Case et al. “The Amber biomolecular simulation programs”. In: *J Comput Chem* 26.16 (2005), pp. 1668–88. DOI: 10.1002/jcc.20290.

- [37] B. R. Brooks et al. "CHARMM: the biomolecular simulation program". In: *J Comput Chem* 30.10 (2009), pp. 1545–614. DOI: 10.1002/jcc.21287.
- [38] William L. Jorgensen, David S. Maxwell, and Julian Tirado-Rives. "Development and Testing of the OPLS All-Atom Force Field on Conformational Energetics and Properties of Organic Liquids". In: *Journal of the American Chemical Society* 118.45 (1996), pp. 11225–11236. DOI: 10.1021/ja9621760.
- [39] Adri C. T. van Duin et al. "ReaxFF: A Reactive Force Field for Hydrocarbons". In: *The Journal of Physical Chemistry A* 105.41 (2001), pp. 9396–9409. DOI: 10.1021/jp004368u.
- [40] N. Hansen, S. D. Muller, and P. Koumoutsakos. "Reducing the time complexity of the derandomized evolution strategy with covariance matrix adaptation (CMA-ES)". In: *Evol Comput* 11.1 (2003), pp. 1–18. DOI: 10.1162/106365603321828970.
- [41] A. Collauto et al. "A slow relaxing species for molecular spin devices: EPR characterization of static and dynamic magnetic properties of a nitronyl nitroxide radical". In: *Journal of Materials Chemistry* 22.41 (2012). DOI: 10.1039/c2jm35076a.
- [42] V. A. Ivanov et al. "Spintronics and spintronics materials". In: *Russian Chemical Bulletin* 53.11 (2004), pp. 2357–2405. DOI: 10.1007/s11172-005-0135-5.
- [43] S.D. Bader and S.S.P. Parkin. "Spintronics". In: *Annual Review of Condensed Matter Physics* 1.1 (2010), pp. 71–88. DOI: 10.1146/annurev-conmatphys-070909-104123.
- [44] Y. Shen et al. "Simultaneous manifestation of metallic conductivity and single-molecule magnetism in a layered molecule-based compound". In: *Chem Sci* 11.41 (2020), pp. 11154–11161. DOI: 10.1039/d0sc04040a.
- [45] J.J. Sakurai and J. Napolitano. *Modern Quantum Mechanics*. Cambridge University Press, 2020.
- [46] M. Born and R. Oppenheimer. "Zur Quantentheorie der Molekeln". In: *Annalen der Physik* 389.20 (1927), pp. 457–484. DOI: 10.1002/andp.19273892002.
- [47] Antonio J. C. Varandas et al. "A double many-body expansion of the two lowest-energy potential surfaces and nonadiabatic coupling for H₃". In: *The Journal of Chemical Physics* 86.11 (1987), pp. 6258–6269. DOI: 10.1063/1.452463.

- [48] D. J. Thouless. “Stability conditions and nuclear rotations in the Hartree-Fock theory”. In: *Nuclear Physics* 21 (1960), pp. 225–232. DOI: 10.1016/0029-5582(60)90048-1.
- [49] C. C. J. Roothaan. “Self-Consistent Field Theory for Open Shells of Electronic Systems”. In: *Reviews of Modern Physics* 32.2 (1960), pp. 179–185. DOI: 10.1103/RevModPhys.32.179.
- [50] W. J. Hehre, R. Ditchfield, and J. A. Pople. “Self—Consistent Molecular Orbital Methods. XII. Further Extensions of Gaussian—Type Basis Sets for Use in Molecular Orbital Studies of Organic Molecules”. In: *The Journal of Chemical Physics* 56.5 (1972), pp. 2257–2261. DOI: 10.1063/1.1677527.
- [51] J. C. Slater. “Atomic Shielding Constants”. In: *Physical Review* 36.1 (1930), pp. 57–64. DOI: 10.1103/PhysRev.36.57.
- [52] Norbert Schuch and Frank Verstraete. “Computational complexity of interacting electrons and fundamental limitations of density functional theory”. In: *Nature Physics* 5.10 (2009), pp. 732–735. DOI: 10.1038/nphys1370.
- [53] S. Pall et al. “Heterogeneous parallelization and acceleration of molecular dynamics simulations in GROMACS”. In: *J Chem Phys* 153.13 (2020), p. 134110. DOI: 10.1063/5.0018516.
- [54] M. K. Gilson and H. X. Zhou. “Calculation of protein-ligand binding affinities”. In: *Annu Rev Biophys Biomol Struct* 36 (2007), pp. 21–42. DOI: 10.1146/annurev.biophys.36.040306.132550.
- [55] P. Sledz and A. Caflisch. “Protein structure-based drug design: from docking to molecular dynamics”. In: *Curr Opin Struct Biol* 48 (2018), pp. 93–102. DOI: 10.1016/j.sbi.2017.10.010.
- [56] J. D. Durrant and J. A. McCammon. “Molecular dynamics simulations and drug discovery”. In: *BMC Biol* 9 (2011), p. 71. DOI: 10.1186/1741-7007-9-71.
- [57] J. Zhang, Y. Liang, and Y. Zhang. “Atomic-level protein structure refinement using fragment-guided molecular dynamics conformation sampling”. In: *Structure* 19.12 (2011), pp. 1784–95. DOI: 10.1016/j.str.2011.09.022.
- [58] G. Srinivas, D. E. Discher, and M. L. Klein. “Self-assembly and properties of diblock copolymers by coarse-grain molecular dynamics”. In: *Nat Mater* 3.9 (2004), pp. 638–44. DOI: 10.1038/nmat1185.
- [59] D. Furman et al. “Enhanced Particle Swarm Optimization Algorithm: Efficient Training of ReaxFF Reactive Force Fields”. In: *J Chem Theory Comput* 14.6 (2018), pp. 3100–3112. DOI: 10.1021/acs.jctc.7b01272.

- [60] H. R. Larsson, A. C. van Duin, and B. Hartke. “Global optimization of parameters in the reactive force field ReaxFF for SiOH”. In: *J Comput Chem* 34.25 (2013), pp. 2178–89. DOI: 10.1002/jcc.23382.
- [61] M. Dittner et al. “Efficient global optimization of reactive force-field parameters”. In: *J Comput Chem* 36.20 (2015), pp. 1550–61. DOI: 10.1002/jcc.23966.
- [62] B. M. Rice et al. “Parameterizing complex reactive force fields using multiple objective evolutionary strategies (MOES): Part 2: transferability of ReaxFF models to C-H-N-O energetic materials”. In: *J Chem Theory Comput* 11.2 (2015), pp. 392–405. DOI: 10.1021/ct5007899.
- [63] J. P. Larentzos et al. “Parameterizing complex reactive force fields using multiple objective evolutionary strategies (MOES). Part 1: ReaxFF models for cyclotrimethylene trinitramine (RDX) and 1,1-diamino-2,2-dinitroethene (FOX-7)”. In: *J Chem Theory Comput* 11.2 (2015), pp. 381–91. DOI: 10.1021/ct500788c.
- [64] A. Jaramillo-Botero, S. Naserifar, and 3rd Goddard W. A. “General Multi-objective Force Field Optimization Framework, with Application to Reactive Force Fields for Silicon Carbide”. In: *J Chem Theory Comput* 10.4 (2014), pp. 1426–39. DOI: 10.1021/ct5001044.
- [65] G. Shchygol et al. “ReaxFF Parameter Optimization with Monte-Carlo and Evolutionary Algorithms: Guidelines and Insights”. In: *J Chem Theory Comput* 15.12 (2019), pp. 6799–6812. DOI: 10.1021/acs.jctc.9b00769.
- [66] E. Iype et al. “Parameterization of a reactive force field using a Monte Carlo algorithm”. In: *J Comput Chem* 34.13 (2013), pp. 1143–54. DOI: 10.1002/jcc.23246.
- [67] Nils Müller and Tobias Glasmachers. “Challenges in High-Dimensional Reinforcement Learning with Evolution Strategies”. In: *Parallel Problem Solving from Nature – PPSN XV*. Springer International Publishing, pp. 411–423.
- [68] Conference Paper. 2021. DOI: 10.1145/3449726.3459575.
- [69] Yann LeCun, Yoshua Bengio, and Geoffrey Hinton. “Deep learning”. In: *Nature* 521.7553 (2015), pp. 436–444. DOI: 10.1038/nature14539.
- [70] H. Nakata and S. Bai. “Development of a new parameter optimization scheme for a reactive force field based on a machine learning approach”. In: *J Comput Chem* 40.23 (2019), pp. 2000–2012. DOI: 10.1002/jcc.25841.

- [71] Feng Guo et al. “Intelligent-ReaxFF: Evaluating the reactive force field parameters with machine learning”. In: *Computational Materials Science* 172 (2020), p. 109393. DOI: <https://doi.org/10.1016/j.commatsci.2019.109393>.
- [72] L. Y. Xue et al. “ReaxFF-MPNN machine learning potential: a combination of reactive force field and message passing neural networks”. In: *Phys Chem Chem Phys* 23.35 (2021), pp. 19457–19464. DOI: [10.1039/d1cp01656c](https://doi.org/10.1039/d1cp01656c).
- [73] Mert Y. Sengul et al. “INDEEDopt: a deep learning-based ReaxFF parameterization framework”. In: *npj Computational Materials* 7.1 (2021), p. 68. DOI: [10.1038/s41524-021-00534-4](https://doi.org/10.1038/s41524-021-00534-4).
- [74] G. Kresse and J. Hafner. “Ab initio molecular dynamics for liquid metals”. In: *Phys Rev B Condens Matter* 47.1 (1993), pp. 558–561. DOI: [10.1103/physrevb.47.558](https://doi.org/10.1103/physrevb.47.558).
- [75] M. J. Frisch G. et al. “Gaussian 16, Revision C.01”. In: (2016).
- [76] Aidan P. Thompson et al. “LAMMPS - a flexible simulation tool for particle-based materials modeling at the atomic, meso, and continuum scales”. In: *Computer Physics Communications* 271 (2022). DOI: [10.1016/j.cpc.2021.108171](https://doi.org/10.1016/j.cpc.2021.108171).
- [77] F. Pedregosa et al. “Scikit-learn: Machine Learning in Python”. In: *Journal of Machine Learning Research* ().
- [78] Conference Paper. 1995. DOI: [10.1109/ICDAR.1995.598994](https://doi.org/10.1109/ICDAR.1995.598994).
- [79] Leo Breiman. “Random Forests”. In: *Machine Learning* 45.1 (2001), pp. 5–32. DOI: [10.1023/A:1010933404324](https://doi.org/10.1023/A:1010933404324).
- [80] Carl Edward Rasmussen. “Gaussian Processes in Machine Learning”. In: *Advanced Lectures on Machine Learning: ML Summer Schools 2003, Canberra, Australia, February 2 - 14, 2003, Tübingen, Germany, August 4 - 16, 2003, Revised Lectures*. Ed. by Olivier Bousquet, Ulrike von Luxburg, and Gunnar Rätsch. Berlin, Heidelberg: Springer Berlin Heidelberg, 2004, pp. 63–71. DOI: [10.1007/978-3-540-28650-9_4](https://doi.org/10.1007/978-3-540-28650-9_4).
- [81] D. C. Cireşan et al. “Deep, Big, Simple Neural Nets for Handwritten Digit Recognition”. In: *Neural Computation* 22.12 (2010), pp. 3207–3220. DOI: [10.1162/NECO_a_00052](https://doi.org/10.1162/NECO_a_00052).
- [82] Warren S. McCulloch and Walter Pitts. “A logical calculus of the ideas immanent in nervous activity”. In: *The bulletin of mathematical biophysics* 5.4 (1943), pp. 115–133. DOI: [10.1007/BF02478259](https://doi.org/10.1007/BF02478259).

-
- [83] A. Lazarevic and Z. Obradovic. “Effective pruning of neural network classifier ensembles”. In: *IJCNN’01. International Joint Conference on Neural Networks. Proceedings (Cat. No.01CH37222)*. Vol. 2, 796–801 vol.2. DOI: 10.1109/IJCNN.2001.939461.
- [84] Robert Kirk DeLisle and Steven L. Dixon. “Induction of Decision Trees via Evolutionary Programming”. In: *Journal of Chemical Information and Computer Sciences* 44.3 (2004), pp. 862–870. DOI: 10.1021/ci034188s.
- [85] Jürgen Braun and Michael Griebel. “On a Constructive Proof of Kolmogorov’s Superposition Theorem”. In: *Constructive Approximation* 30.3 (2009), p. 653. DOI: 10.1007/s00365-009-9054-2.
- [86] Mark A. Kramer. “Nonlinear principal component analysis using autoassociative neural networks”. In: *AIChE Journal* 37.2 (1991), pp. 233–243. DOI: 10.1002/aic.690370209.
- [87] Martín Abadi et al. “TensorFlow: Large-scale machine learning on heterogeneous systems”. In: *Software available from tensorflow.org*. (2015).
- [88] Salah Rifai et al. “Contractive auto-encoders: Explicit invariance during feature extraction”. In: *Icml*.
- [89] S. T. Roweis and L. K. Saul. “Nonlinear dimensionality reduction by locally linear embedding”. In: *Science* 290.5500 (2000), pp. 2323–6. DOI: 10.1126/science.290.5500.2323.
- [90] R. Karbauskaite, O. Kurasova, and G. Dzemyda. “Selection of the number of neighbours of each data point for the locally linear embedding algorithm”. In: *Information Technology and Control* 36.4 (2007), pp. 359–364.
- [91] B. W. Kernighan and S. Lin. “An efficient heuristic procedure for partitioning graphs”. In: *The Bell System Technical Journal* 49.2 (1970), pp. 291–307. DOI: 10.1002/j.1538-7305.1970.tb01770.x.
- [92] James M. Tour, Masatoshi Kozaki, and Jorge M. Seminario. “Molecular Scale Electronics: A Synthetic/Computational Approach to Digital Computing”. In: *Journal of the American Chemical Society* 120.33 (1998), pp. 8486–8493. DOI: 10.1021/ja9808090.
- [93] Kazunobu Sato et al. “Novel Applications of ESR/EPR: Quantum Computing/Quantum Information Processing”. In: *EPR of Free Radicals in Solids II: Trends in Methods and Applications*. Ed. by Anders Lund and Masaru Shiotani. Dordrecht: Springer Netherlands, 2012, pp. 163–204. DOI: 10.1007/978-94-007-4887-3_4.

- [94] S. Yamamoto et al. “Adiabatic quantum computing with spin qubits hosted by molecules”. In: *Phys Chem Chem Phys* 17.4 (2015), pp. 2742–9. DOI: 10.1039/c4cp04744c.
- [95] J. N. Nelson et al. “CNOT gate operation on a photogenerated molecular electron spin-qubit pair”. In: *J Chem Phys* 152.1 (2020), p. 014503. DOI: 10.1063/1.5128132.
- [96] L. Koblitz et al. “Fast photodriven electron spin coherence transfer: a quantum gate based on a spin exchange J-jump”. In: *J Am Chem Soc* 134.30 (2012), pp. 12430–3. DOI: 10.1021/ja305650x.
- [97] Y. Wu et al. “Covalent Radical Pairs as Spin Qubits: Influence of Rapid Electron Motion between Two Equivalent Sites on Spin Coherence”. In: *J Am Chem Soc* 140.40 (2018), pp. 13011–13021. DOI: 10.1021/jacs.8b08105.
- [98] Tomohiro Yoshino et al. “ESR and ¹H-,¹⁹F-ENDOR/TRIPLE Study of Fluorinated Diphenylnitroxides as Synthetic Bus Spin-Qubit Radicals with Client Qubits in Solution”. In: *The Journal of Physical Chemistry Letters* 2.5 (2011), pp. 449–453. DOI: 10.1021/jz101650z.
- [99] E. R. Canarie, S. M. Jahn, and S. Stoll. “Quantitative Structure-Based Prediction of Electron Spin Decoherence in Organic Radicals”. In: *J Phys Chem Lett* 11.9 (2020), pp. 3396–3400. DOI: 10.1021/acs.jpcclett.0c00768.
- [100] Kazunobu Sato et al. “Molecular electron-spin quantum computers and quantum information processing: pulse-based electron magnetic resonance spin technology applied to matter spin-qubits”. In: *Journal of Materials Chemistry* 19.22 (2009). DOI: 10.1039/b819556k.
- [101] H. Mao et al. “Controlling the Dynamics of Three Electron Spin Qubits in a Donor-Acceptor-Radical Molecule Using Dielectric Environment Changes”. In: *J Phys Chem Lett* 12.9 (2021), pp. 2213–2218. DOI: 10.1021/acs.jpcclett.1c00077.
- [102] J. H. Olshansky et al. “Selectively Addressable Photogenerated Spin Qubit Pairs in DNA Hairpins”. In: *J Am Chem Soc* 142.7 (2020), pp. 3346–3350. DOI: 10.1021/jacs.9b13398.
- [103] J. N. Nelson et al. “Effect of Electron-Nuclear Hyperfine Interactions on Multiple-Quantum Coherences in Photogenerated Covalent Radical (Qubit) Pairs”. In: *J Phys Chem A* 122.49 (2018), pp. 9392–9402. DOI: 10.1021/acs.jpca.8b07556.

- [104] P. Glenn Barkley, Joseph P. Hornak, and Jack H. Freed. “Surface-suppressed electron resonance spectroscopies”. In: *The Journal of Chemical Physics* 84.3 (1986), pp. 1886–1900. DOI: 10.1063/1.450437.
- [105] M. Lucarini and L. Pasquato. “ESR spectroscopy as a tool to investigate the properties of self-assembled monolayers protecting gold nanoparticles”. In: *Nanoscale* 2.5 (2010), pp. 668–76. DOI: 10.1039/b9nr00384c.
- [106] C. P. Liu et al. “Interactions of nitroxide radicals with dendrimer-entrapped Au-8-clusters: a fluorescent nanosensor for intracellular imaging of ascorbic acid”. In: *Journal of Materials Chemistry B* 3.2 (2015), pp. 191–197. DOI: 10.1039/c4tb01657b.
- [107] C. Aliaga et al. “On the interactions of TEMPO radicals with gold nanostructures”. In: *New Journal of Chemistry* 42.12 (2018), pp. 9764–9770. DOI: 10.1039/c7nj04714b.
- [108] J. Guin et al. “Biomimetic carbene-catalyzed oxidations of aldehydes using TEMPO”. In: *Angew Chem Int Ed Engl* 47.45 (2008), pp. 8727–30. DOI: 10.1002/anie.200802735.
- [109] Amarajothi Dhakshinamoorthy, Mercedes Alvaro, and Hermenegildo Garcia. “Aerobic Oxidation of Benzylic Alcohols Catalyzed by Metal–Organic Frameworks Assisted by TEMPO”. In: *ACS Catalysis* 1.1 (2010), pp. 48–53. DOI: 10.1021/cs1000703.
- [110] J. Qu et al. “Synthesis and properties of DNA complexes containing 2,2,6,6-tetramethyl-1-piperidinoxy (TEMPO) moieties as organic radical battery materials”. In: *Chemistry* 14.11 (2008), pp. 3250–9. DOI: 10.1002/chem.200800021.
- [111] P. J. Wright and A. M. English. “Scavenging with TEMPO* to identify peptide- and protein-based radicals by mass spectrometry: advantages of spin scavenging over spin trapping”. In: *J Am Chem Soc* 125.28 (2003), pp. 8655–65. DOI: 10.1021/ja0291888.
- [112] O. Swiech, R. Bilewicz, and E. Megiel. “TEMPO coated Au nanoparticles: synthesis and tethering to gold surfaces”. In: *Rsc Advances* 3.17 (2013), pp. 5979–5986. DOI: 10.1039/c3ra23106b.
- [113] Olga Swiech et al. “Gold Nanoparticles Tethered to Gold Surfaces Using Nitroxyl Radicals”. In: *The Journal of Physical Chemistry C* 115.15 (2011), pp. 7347–7354. DOI: 10.1021/jp200842u.

- [114] U. Yxklinten, J. Hartford, and T. Holmquist. “Atoms embedded in an electron gas: the generalized gradient approximation”. In: *Physica Scripta* 55.4 (1997), pp. 499–506. DOI: 10.1088/0031-8949/55/4/022.
- [115] G. Zhang and C. B. Musgrave. “Comparison of DFT methods for molecular orbital eigenvalue calculations”. In: *J Phys Chem A* 111.8 (2007), pp. 1554–61. DOI: 10.1021/jp061633o.
- [116] S. Grimme et al. “A consistent and accurate ab initio parametrization of density functional dispersion correction (DFT-D) for the 94 elements H-Pu”. In: *J Chem Phys* 132.15 (2010), p. 154104. DOI: 10.1063/1.3382344.
- [117] Jiří Čížek. “On the Correlation Problem in Atomic and Molecular Systems. Calculation of Wavefunction Components in Ursell-Type Expansion Using Quantum-Field Theoretical Methods”. In: *The Journal of Chemical Physics* 45.11 (1966), pp. 4256–4266. DOI: 10.1063/1.1727484.
- [118] I. W. Bulik, T. M. Henderson, and G. E. Scuseria. “Can Single-Reference Coupled Cluster Theory Describe Static Correlation?” In: *J Chem Theory Comput* 11.7 (2015), pp. 3171–9. DOI: 10.1021/acs.jctc.5b00422.
- [119] D. Rappoport and F. Furche. “Property-optimized gaussian basis sets for molecular response calculations”. In: *J Chem Phys* 133.13 (2010), p. 134105. DOI: 10.1063/1.3484283.
- [120] D. Andrae et al. “Energy-adjusted ab initio pseudopotentials for the second and third row transition elements”. In: *Theoretica Chimica Acta* 77.2 (1990), pp. 123–141. DOI: 10.1007/bf01114537.
- [121] J. P. Perdew, K. Burke, and M. Ernzerhof. “Generalized Gradient Approximation Made Simple”. In: *Phys Rev Lett* 77.18 (1996), pp. 3865–3868. DOI: 10.1103/PhysRevLett.77.3865.
- [122] G. Kresse and J. Hafner. “Ab initio molecular-dynamics simulation of the liquid-metal-amorphous-semiconductor transition in germanium”. In: *Phys Rev B Condens Matter* 49.20 (1994), pp. 14251–14269. DOI: 10.1103/physrevb.49.14251.
- [123] G. Kresse and J. Furthmüller. “Efficiency of ab-initio total energy calculations for metals and semiconductors using a plane-wave basis set”. In: *Computational Materials Science* 6.1 (1996), pp. 15–50. DOI: 10.1016/0927-0256(96)00008-0.
- [124] G. Kresse and J. Furthmüller. “Efficient iterative schemes for ab initio total-energy calculations using a plane-wave basis set”. In: *Phys Rev B Condens Matter* 54.16 (1996), pp. 11169–11186. DOI: 10.1103/physrevb.54.11169.

- [125] P. E. Blochl. "Projector augmented-wave method". In: *Phys Rev B Condens Matter* 50.24 (1994), pp. 17953–17979. DOI: 10.1103/physrevb.50.17953.
- [126] T. Lu and F. Chen. "Multiwfn: a multifunctional wavefunction analyzer". In: *J Comput Chem* 33.5 (2012), pp. 580–92. DOI: 10.1002/jcc.22885.
- [127] William Humphrey, Andrew Dalke, and Klaus Schulten. "VMD: Visual molecular dynamics". In: *Journal of Molecular Graphics* 14.1 (1996), pp. 33–38. DOI: 10.1016/0263-7855(96)00018-5.
- [128] Marc Benard. "A study of Hartree–Fock instabilities in $\text{Cr}_2(\text{O}_2\text{CH})_4$ and $\text{Mo}_2(\text{O}_2\text{CH})_4$ ". In: *The Journal of Chemical Physics* 71.6 (1979), pp. 2546–2556. DOI: 10.1063/1.438609.
- [129] R. Hoffmann and CORNELL UNIV ITHACA NY BAKER LAB. *Solids and Surfaces: A Chemist's View of Bonding in Extended Structures*. VCH Publishers, 1988.
- [130] M. P. Mitoraj, A. Michalak, and T. Ziegler. "A Combined Charge and Energy Decomposition Scheme for Bond Analysis". In: *J Chem Theory Comput* 5.4 (2009), pp. 962–75. DOI: 10.1021/ct800503d.
- [131] M. P. Mitoraj et al. "Applications of the ETS-NOCV method in descriptions of chemical reactions". In: *J Mol Model* 17.9 (2011), pp. 2337–52. DOI: 10.1007/s00894-011-1023-6.
- [132] E. R. Johnson et al. "Revealing noncovalent interactions". In: *J Am Chem Soc* 132.18 (2010), pp. 6498–506. DOI: 10.1021/ja100936w.
- [133] Tian Lu and Qinxue Chen. "Interaction Region Indicator: A Simple Real Space Function Clearly Revealing Both Chemical Bonds and Weak Interactions**". In: *Chemistry–Methods* 1.5 (2021), pp. 231–239. DOI: 10.1002/cmtd.202100007.
- [134] R. F. W. Bader and H. Essén. "The characterization of atomic interactions". In: *The Journal of Chemical Physics* 80.5 (1984), pp. 1943–1960. DOI: 10.1063/1.446956.
- [135] R. Hayakawa, T. Chikyow, and Y. Wakayama. "Vertical resonant tunneling transistors with molecular quantum dots for large-scale integration". In: *Nanoscale* 9.31 (2017), pp. 11297–11302. DOI: 10.1039/c7nr02463k.
- [136] Hoon-Seok Seo et al. "Multilevel Operation of Resonant Tunneling with Binary Molecules in a Metal–Insulator–Semiconductor Configuration". In: *The Journal of Physical Chemistry C* 118.12 (2014), pp. 6467–6472. DOI: 10.1021/jp411386s.

- [137] R. Hayakawa et al. “Photoisomerization-induced manipulation of single-electron tunneling for novel Si-based optical memory”. In: *ACS Appl Mater Interfaces* 5.21 (2013), pp. 11371–6. DOI: 10.1021/am403616m.
- [138] Ryoma Hayakawa et al. “Single-Electron Tunneling through Molecular Quantum Dots in a Metal-Insulator-Semiconductor Structure”. In: *Advanced Functional Materials* 21.15 (2011), pp. 2933–2937. DOI: 10.1002/adfm.201100220.
- [139] Senthil Kumar Karuppannan et al. “Room-temperature tunnel magnetoresistance across biomolecular tunnel junctions based on ferritin”. In: *Journal of Physics: Materials* 4.3 (2021). DOI: 10.1088/2515-7639/abfa79.
- [140] Akitoshi Ishizaka and Yasuhiro Shiraki. “Low Temperature Surface Cleaning of Silicon and Its Application to Silicon MBE”. In: *Journal of The Electrochemical Society* 133.4 (2019), pp. 666–671. DOI: 10.1149/1.2108651.
- [141] Wei Gao et al. “Interfacial adhesion between graphene and silicon dioxide by density functional theory with van der Waals corrections”. In: *Journal of Physics D: Applied Physics* 47.25 (2014). DOI: 10.1088/0022-3727/47/25/255301.
- [142] D. Zagorac et al. “Recent developments in the Inorganic Crystal Structure Database: theoretical crystal structure data and related features”. In: *J Appl Crystallogr* 52.Pt 5 (2019), pp. 918–925. DOI: 10.1107/S160057671900997X.
- [143] C. B. Fan et al. “Significant Enhancement of C2 H2 /C2 H4 Separation by a Photochromic Diarylethene Unit: A Temperature- and Light-Responsive Separation Switch”. In: *Angew Chem Int Ed Engl* 56.27 (2017), pp. 7900–7906. DOI: 10.1002/anie.201702484.
- [144] Tsuyoshi Tsujioka and Hayato Kondo. “Organic bistable molecular memory using photochromic diarylethene”. In: *Applied Physics Letters* 83.5 (2003), pp. 937–939. DOI: 10.1063/1.1597966.
- [145] R. Hayakawa et al. “Optically and electrically driven organic thin film transistors with diarylethene photochromic channel layers”. In: *ACS Appl Mater Interfaces* 5.9 (2013), pp. 3625–30. DOI: 10.1021/am400030z.
- [146] Ersan Demiralp and William A. Goddard. “Conduction properties of the organic superconductor $-(BEDT-TTF)_2Cu(NCS)_2$ based on Hubbard unrestricted Hartree-Fock band calculations”. In: *Physical Review B* 56.18 (1997), pp. 11907–11919. DOI: 10.1103/PhysRevB.56.11907.
- [147] H. J. Kulik et al. “Density functional theory in transition-metal chemistry: a self-consistent Hubbard U approach”. In: *Phys Rev Lett* 97.10 (2006), p. 103001. DOI: 10.1103/PhysRevLett.97.103001.

-
- [148] A. Floris et al. “Vibrational properties of MnO and NiO from DFT+U-based density functional perturbation theory”. In: *Physical Review B* 84.16 (2011). DOI: 10.1103/PhysRevB.84.161102.
- [149] R. A. Marcus. “On the Theory of Oxidation-Reduction Reactions Involving Electron Transfer. I”. In: *The Journal of Chemical Physics* 24.5 (1956), pp. 966–978. DOI: 10.1063/1.1742723.
- [150] E. Apra et al. “NWChem: Past, present, and future”. In: *J Chem Phys* 152.18 (2020), p. 184102. DOI: 10.1063/5.0004997.
- [151] H. K. Onnes. “Further experiments with liquid helium. D. On the change of the electrical resistance of pure metals at very low temperatures, etc. V. The disappearance of the resistance of mercury (Reprinted from Proceedings of the Koninklijke Nederlandse Akademie van Wetenschappen, vol 14, pg 113–115, 1911)”. In: *Proceedings of the Koninklijke Nederlandse Akademie Van Wetenschappen* 100.3-4 (1997), pp. 156–158.
- [152] W. Meissner and R. Ochsenfeld. “Ein neuer Effekt bei Eintritt der Supraleitfähigkeit”. In: *Die Naturwissenschaften* 21.44 (1933), pp. 787–788. DOI: 10.1007/bf01504252.
- [153] J. Bardeen, L. N. Cooper, and J. R. Schrieffer. “Microscopic Theory of Superconductivity”. In: *Physical Review* 106.1 (1957), pp. 162–164. DOI: 10.1103/PhysRev.106.162.
- [154] J. Bardeen, L. N. Cooper, and J. R. Schrieffer. “Theory of Superconductivity”. In: *Physical Review* 108.5 (1957), pp. 1175–1204. DOI: 10.1103/PhysRev.108.1175.
- [155] D. Jérôme et al. “Superconductivity in a synthetic organic conductor (TMTSF)₂PF₆”. In: *Journal de Physique Lettres* 41.4 (1980), pp. 95–98. DOI: 10.1051/jphyslet:0198000410409500.
- [156] R. P. Groff, A. Suna, and R. E. Merrifield. “Temperature Dependence of Conductivity of Tetrathiafulvalene-Tetracyanoquinodimethane (TTF-TCNQ) Single Crystals”. In: *Physical Review Letters* 33.7 (1974), pp. 418–421. DOI: 10.1103/PhysRevLett.33.418.
- [157] R. Sessoli et al. “Magnetic bistability in a metal-ion cluster”. In: *Nature* 365.6442 (1993), pp. 141–143. DOI: 10.1038/365141a0.
- [158] S. Thiele et al. “Electrically driven nuclear spin resonance in single-molecule magnets”. In: *Science* 344.6188 (2014), pp. 1135–8. DOI: 10.1126/science.1249802.

- [159] C. Schlegel et al. “Direct observation of quantum coherence in single-molecule magnets”. In: *Phys Rev Lett* 101.14 (2008), p. 147203. DOI: 10.1103/PhysRevLett.101.147203.
- [160] D. Aravena and E. Ruiz. “Spin dynamics in single-molecule magnets and molecular qubits”. In: *Dalton Trans* 49.29 (2020), pp. 9916–9928. DOI: 10.1039/d0dt01414a.
- [161] A. Lunghi et al. “The role of anharmonic phonons in under-barrier spin relaxation of single molecule magnets”. In: *Nat Commun* 8 (2017), p. 14620. DOI: 10.1038/ncomms14620.
- [162] M. Atzori et al. “Quantum Coherence Times Enhancement in Vanadium(IV)-based Potential Molecular Qubits: the Key Role of the Vanadyl Moiety”. In: *J Am Chem Soc* 138.35 (2016), pp. 11234–44. DOI: 10.1021/jacs.6b05574.
- [163] L. Sorace, C. Benelli, and D. Gatteschi. “Lanthanides in molecular magnetism: old tools in a new field”. In: *Chem Soc Rev* 40.6 (2011), pp. 3092–104. DOI: 10.1039/c0cs00185f.
- [164] J. L. Liu, Y. C. Chen, and M. L. Tong. “Symmetry strategies for high performance lanthanide-based single-molecule magnets”. In: *Chem Soc Rev* 47.7 (2018), pp. 2431–2453. DOI: 10.1039/c7cs00266a.
- [165] H. Zhang et al. “Low coordinated mononuclear erbium(iii) single-molecule magnets with C_{3v} symmetry: a method for altering single-molecule magnet properties by incorporating hard and soft donors”. In: *Dalton Trans* 47.2 (2018), pp. 302–305. DOI: 10.1039/c7dt04053a.
- [166] Y. Kamihara et al. “Iron-based layered superconductor: LaOFeP”. In: *J Am Chem Soc* 128.31 (2006), pp. 10012–3. DOI: 10.1021/ja063355c.
- [167] A. A. Kordyuk. “Iron-based superconductors: Magnetism, superconductivity, and electronic structure (Review Article)”. In: *Low Temperature Physics* 38.9 (2012), pp. 888–899. DOI: 10.1063/1.4752092.
- [168] G. Serrano et al. “Quantum dynamics of a single molecule magnet on superconducting Pb(111)”. In: *Nat Mater* 19.5 (2020), pp. 546–551. DOI: 10.1038/s41563-020-0608-9.
- [169] W Wernsdorfer. “From micro- to nano-SQUIDS: applications to nanomagnetism”. In: *Superconductor Science and Technology* 22.6 (May 2009), p. 064013. DOI: 10.1088/0953-2048/22/6/064013.
- [170] Y. Rechkemmer et al. “A four-coordinate cobalt(II) single-ion magnet with coercivity and a very high energy barrier”. In: *Nat Commun* 7 (2016), p. 10467. DOI: 10.1038/ncomms10467.

- [171] Soner Steiner et al. “Calculation of the magnetic anisotropy with projected-augmented-wave methodology and the case study of disorderedFe1–xCox-alloys”. In: *Physical Review B* 93.22 (2016). DOI: 10.1103/PhysRevB.93.224425.
- [172] E. F. Valeev et al. “Effect of electronic polarization on charge-transport parameters in molecular organic semiconductors”. In: *J Am Chem Soc* 128.30 (2006), pp. 9882–6. DOI: 10.1021/ja061827h.
- [173] Christophe Iung Enric Canadell Marie-Liesse Doublet. *Orbital Approach to the Electronic Structure of Solids*. 2012. DOI: 10.1093/acprof:oso/9780199534937.001.0001.
- [174] E. Scriven and B. J. Powell. “Toward the parametrization of the Hubbard model for salts of bis(ethylenedithio)tetrathiafulvalene: a density functional study of isolated molecules”. In: *J Chem Phys* 130.10 (2009), p. 104508. DOI: 10.1063/1.3080543.
- [175] Edan Scriven and B. J. Powell. “Effective Coulomb interactions within BEDT-TTF dimers”. In: *Physical Review B* 80.20 (2009). DOI: 10.1103/PhysRevB.80.205107.
- [176] Louis Noodleman. “Valence bond description of antiferromagnetic coupling in transition metal dimers”. In: *The Journal of Chemical Physics* 74.10 (1981), pp. 5737–5743. DOI: 10.1063/1.440939.
- [177] E. Canadell and M. H. Whangbo. “Conceptual Aspects of Structure Property Correlations and Electronic Instabilities, with Applications to Low-Dimensional Transition-Metal Oxides”. In: *Chemical Reviews* 91.5 (1991), pp. 965–1034. DOI: DOI10.1021/cr00005a015.
- [178] S. Horiuchi et al. “Quantum ferroelectricity in charge-transfer complex crystals”. In: *Nat Commun* 6 (2015), p. 7469. DOI: 10.1038/ncomms8469.
- [179] R. Rösslhuber et al. “Phase coexistence at the first-order Mott transition revealed by pressure-dependent dielectric spectroscopy of κ -(BEDT–TTF)₂–Cu₂(CN)₃”. In: *Physical Review B* 103.12 (2021). DOI: 10.1103/PhysRevB.103.125111.

Acknowledgements

First and foremost, I would like to thank my supervisor Prof. Dr. Carmen Herrmann for the opportunity to enter the field of theoretical chemistry four years ago. I am particularly grateful for her guidance through my work on this thesis. Her wealth of knowledge and experience always gives me inspiration and guidance. Full academic freedom gave me the opportunity to learn acquire new knowledge and to explore my area of interest, but she always pulled me back when I went astray. Thank you for letting me see the beauty of quantum chemistry.

Additionally, I would like to thank my PhD committee members Prof. Dr. Gabriel Bester, Prof. Dr. Andrew Torda, and Dr. Tobias Vossmeier for their interest in my work.

I would like to take this opportunity to express my immense gratitude to our group members that really helped to accomplish my research. Dr. Michael Deffner, thanks for proofreading my thesis and the valuable discussions, especially about machine learning, which always bring me new ideas. Dr. Alexander Voigt, thanks for helping me write down my first line of python, and for showing the charm of POV-Ray and Tetris. Dr. Philipp Bahlke, thanks for sharing the knowledge in electronic correlation and the delicious home-brewed beer. Dr. Martin Zöllner, thanks for the textbooks, which gave me a better understanding of the relativistic effect. Dr. Susanne Kröncke, thanks for sharing the skills about poster making and attending the conference with me where we learned a lot. Rukan Nasri, thanks for helping my first step in Hamburg and the university. Dr. Sumit Naskar, Dr. Torben Steenbock, Aida Saghatchi, Lawrence Rybakowski, Ursula Rastetter, Michaela Schneeberger, Karen Schaefer, Eduard Hahn, Conrad Stork, Benjamin Bolbrinker, Michael Jaruszewski who have given their invaluable support and assistance.

The thesis would not be complete without the help of our collaborators, I would like to thank Dr. Ryoma Hayakawa, Dr. Zhaoyang Li, and Dr. Yongbing Shen for providing the fascinating experimental results which have taught me a lot.

Moreover, I also thank people that work more from the background. The IT service of the chemistry department, especially Christian Schmidt and Sören Ziehe, who always help us solve hardware and software problems and provide an excellent

office environment. The high performance computing centre of the university (RRZ) and the North-German Supercomputing Alliance (HLRN), which provide computational resources. Dr. Thomas Orgis and Dr. Hinnerk Stüben, who maintain the facilities and offer the excellent technical support. I want to thank Susanne Breidohr and Ingke Klemm for helping me deal with all administrative affairs.

Meanwhile, the financial support from the Deutsche Forschungsgemeinschaft (DFG) is gratefully acknowledged.

Apart from academy, I am very grateful to my family and friends for their support and encouragement, which has allowed me to pursue my ideals without any apprehension. Special thanks to our friend, Nancy Fiebig, she has been giving us the plenty of happiness and good memory in this city. Last but not least, I want to thank my beloved Kuyi, for her love, support, and patience, to give me the courage to face the unknown.

Declaration on Oath

Hiermit erkläre ich an Eides statt, dass ich die vorliegende Dissertationsschrift selbst verfasst und keine anderen als die angegebenen Quellen und Hilfsmittel benutzt habe.

I hereby declare on oath that this doctoral dissertation is written independently and solely by my own based on the original work of my PhD and has not been used other than the acknowledged resources and aids. The submitted written version corresponds to the version on the electronic storage medium.

I declare that the present dissertation was prepared maintaining the Rules of Good Scientific Practice of the German Research Foundation and it has never been submitted in the present form or similar to any other University or board of examiners.



Haitao Zhang

31/05/2022

Date